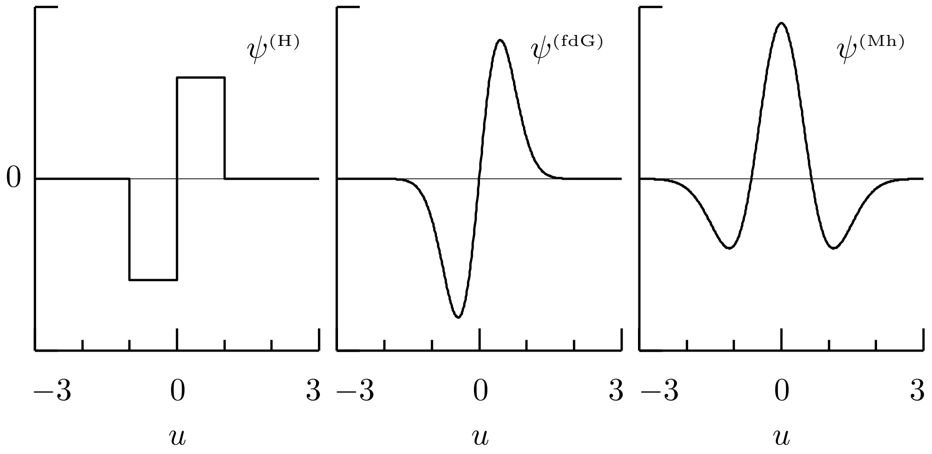

Figure 3. Three wavelets. From left to right, we have one version of the Haar wavelet; a wavelet that is related to the first derivative of the Gaussian probability density function (PDF); and the Mexican hat wavelet, which is related to the second derivative of the Gaussian PDF.

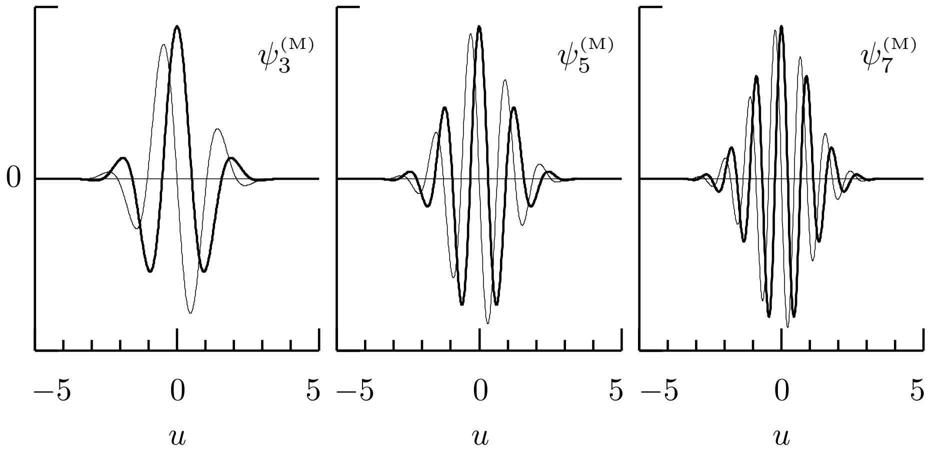

Figure 5. Three Morlet wavelets $\psi_{\omega_0}^{(\mathrm{M})}(\cdot)$. These wavelets are complex-valued, so their real and imaginary parts are plotted using, respectively, thick and thin curves. The parameter ω_0 controls the frequency of the complex exponential that is then modulated by a function whose shape is dictated by the standard Gaussian PDF. As ω_0 increases from 3 to 7, the number of oscillations within the effective width of the Gaussian PDF increases.

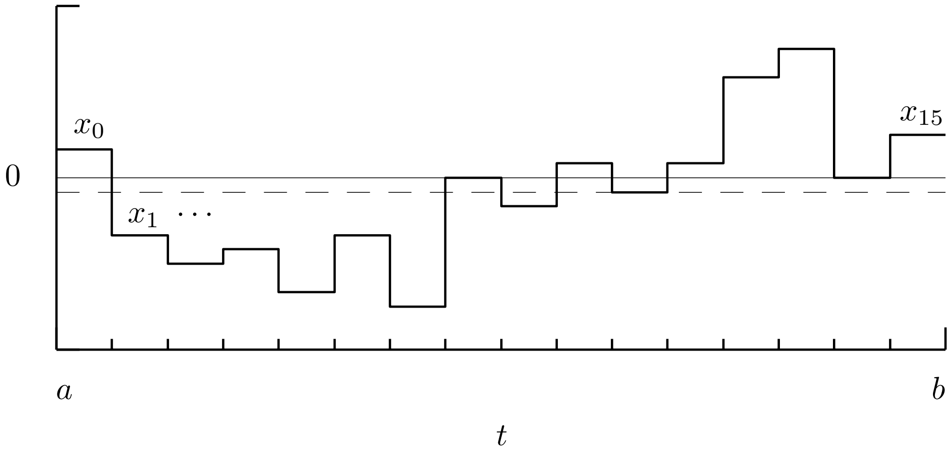

Figure 6. Step function $x(\cdot)$ successively taking on the values $x_0, x_1, \ldots, x_{15}$ over a partitioning of the interval $[a, b]$ into 16 equal subintervals. As defined by Equation (5), the average value of $x(\cdot)$ over $[a, b]$ is just the sample mean of all 16 x_j's (the dashed line indicates this average).

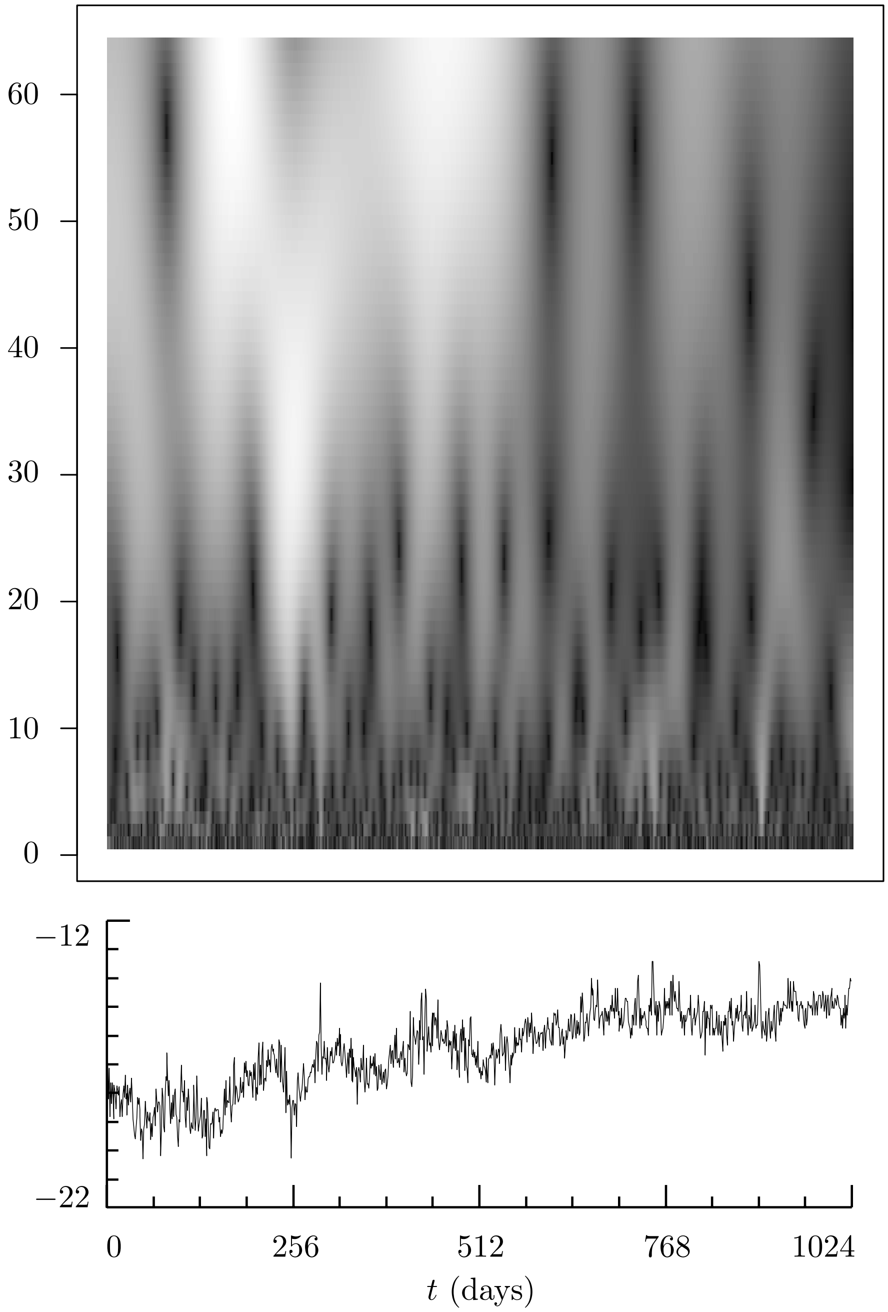

Figure 8. Average daily fractional frequency deviates for cesium beam atomic clock 571 (bottom plot) and its Mexican hat CWT. The fractional frequency deviates are recorded in parts in 10^{13} (a deviation of -15 parts in 10^{13} means that clock 571 lost about 129.6 billionths of a second in one day with respect to the US Naval Observatory master clock to which it was being compared). The vertical axis of the CWT plot is scale (ranging from 1 to 64 days), while the horizontal axis is the same as on the lower plot. The CWT plot is grey-scaled coded so that large magnitudes correspond to bright spots (regions where the plot is dark indicate scales and days at which the clock performed well).

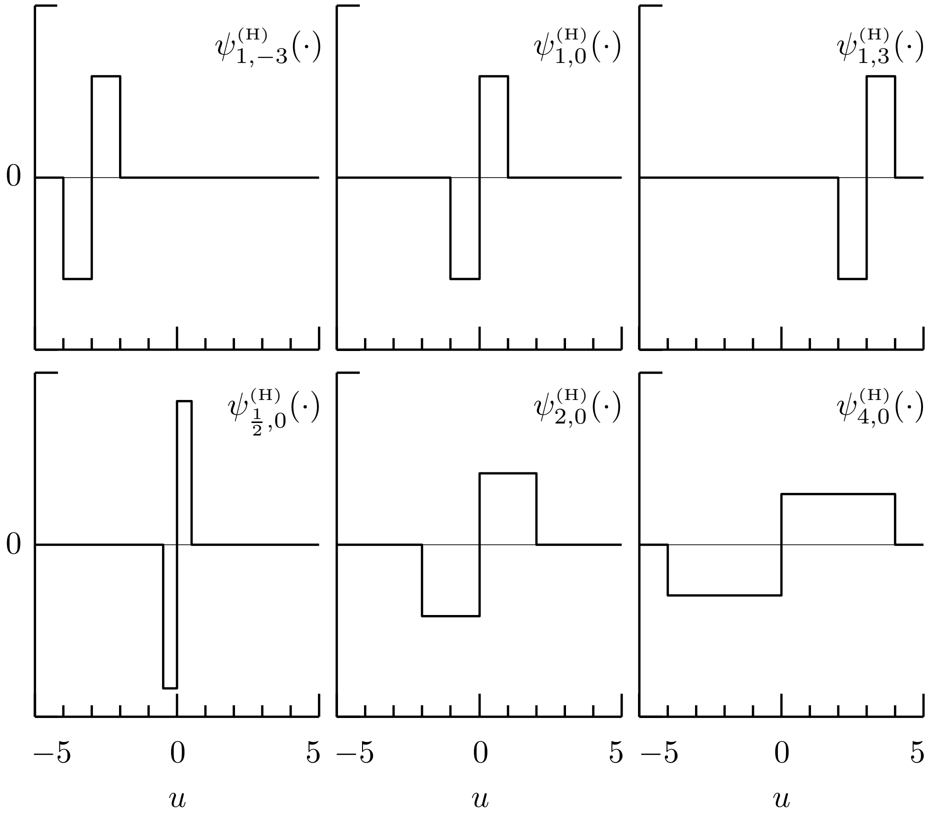

Figure 10. Shifted and rescaled versions of the Haar wavelet $\psi^{(\mathrm{H})}(\cdot)$. The plots above show $\psi^{(\mathrm{H})}_{\lambda,t}(\cdot)$, which can be used to measure how much adjacent averages of a signal $x(\cdot)$ over a scale of length λ change at time t. The top row of plots shows the effect of keeping λ fixed at unity while t is varied; in the bottom row t is fixed at zero while λ is varied.

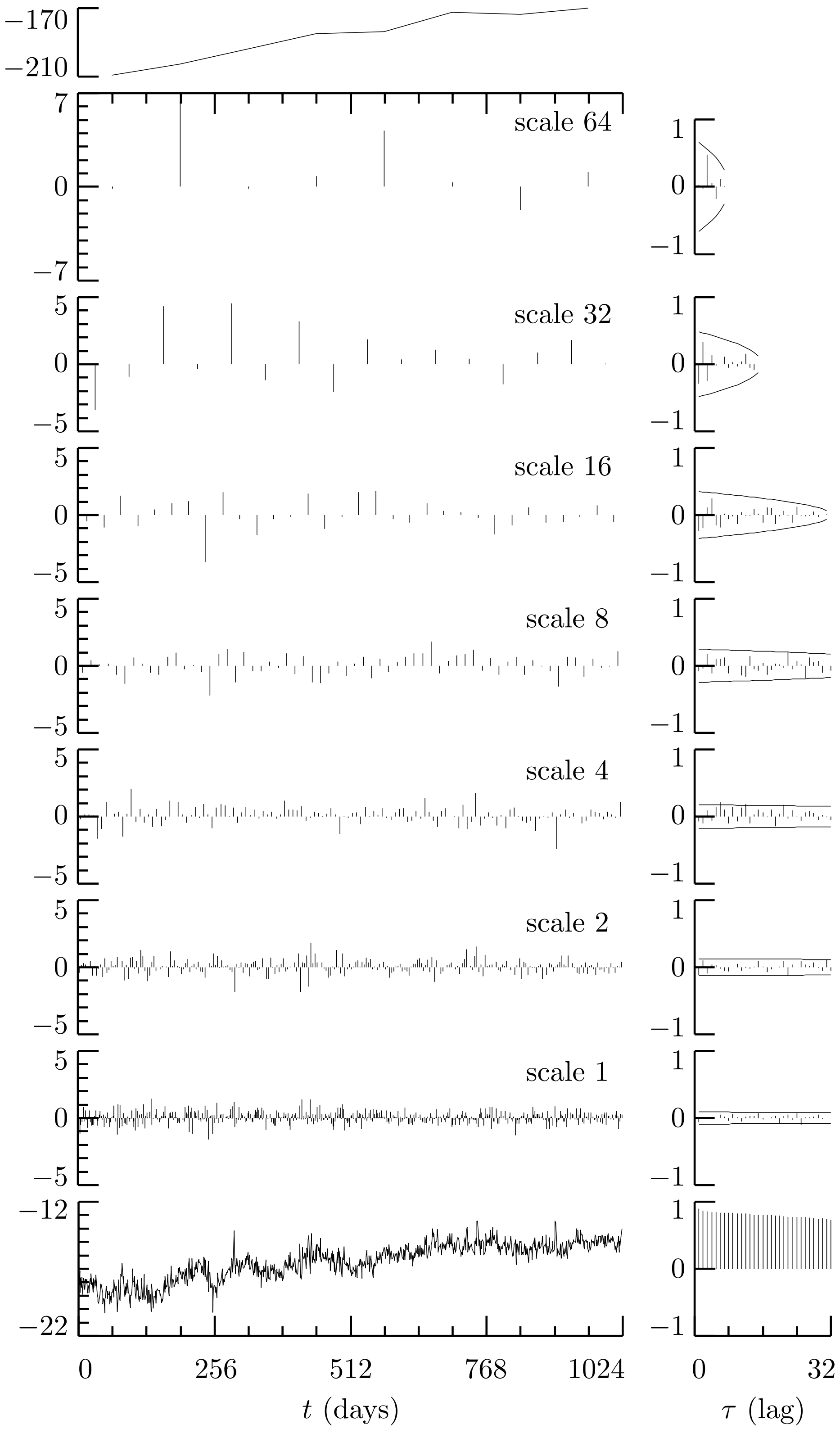

Figure 14. Haar DWT coefficients for clock 571 and sample ACSs.

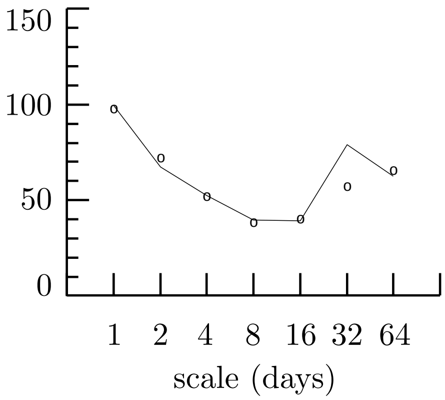

Figure 16. Energy analysis for clock 571 based on Haar DWT wavelet coefficients (curve) and Haar MODWT wavelet coefficients (o's).

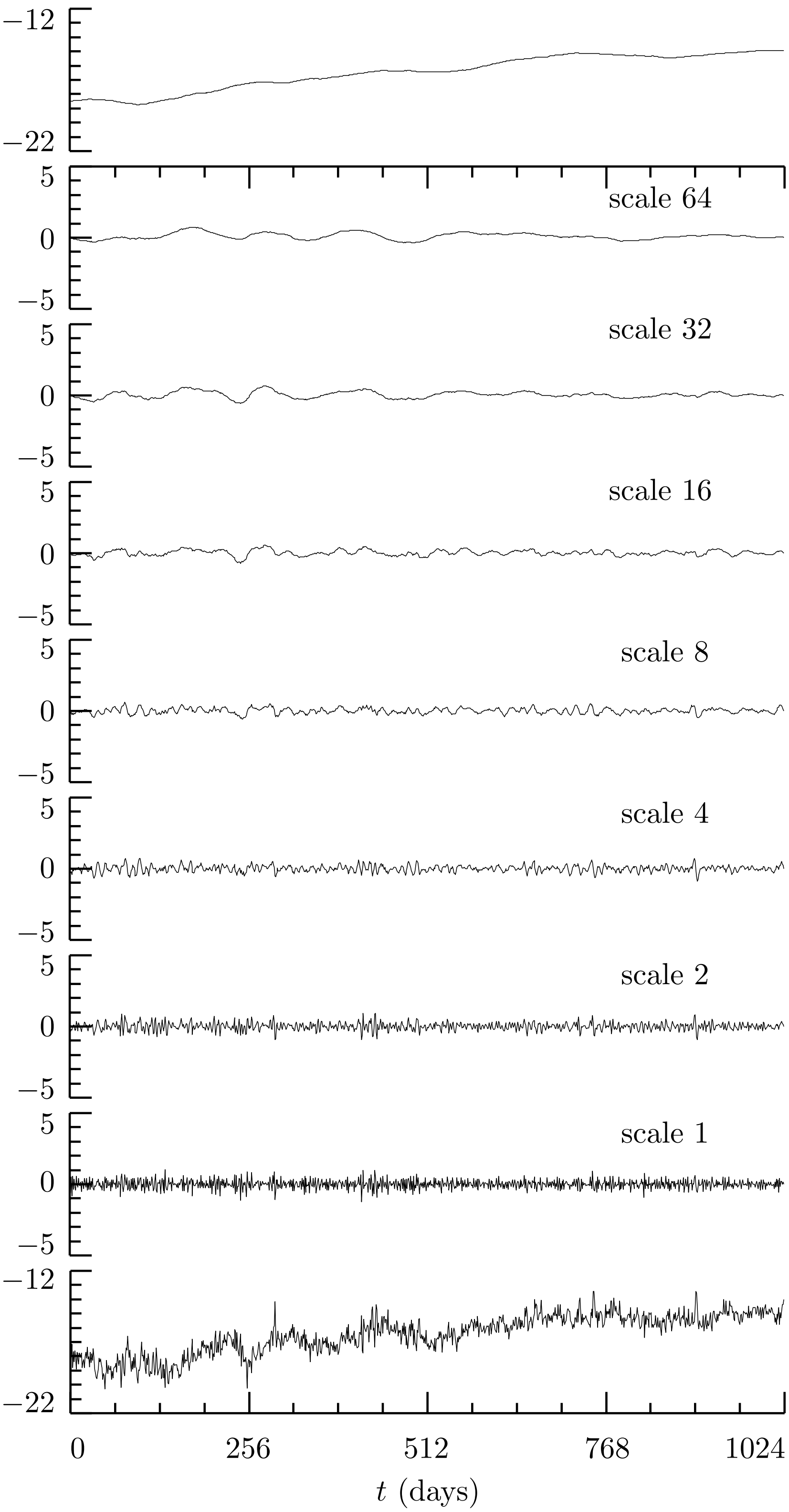

Figure 18. Haar MODWT coefficients for clock 571.

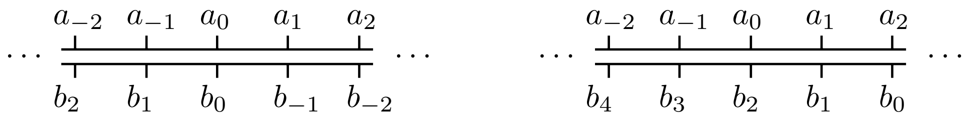

$$a * b_0 = \sum_{u=-\infty}^{\infty} a_u b_{-u} \qquad\qquad a * b_2 = \sum_{u=-\infty}^{\infty} a_u b_{2-u}$$

Figure 24. Graphical illustration of convolution of the infinite sequences $\{a_t\}$ and $\{b_t\}$. The left-hand plot shows two lines. The upper line is labeled at equal intervals with elements of the infinite sequence $\{a_t\}$. The lower line is likewise labeled, but now with the *reverse* of $\{b_t\}$, i.e., $\{b_{-t}\}$ The zeroth element $a * b_0$ of the convolution of $\{a_t\}$ and $\{b_t\}$ is obtained by multiplying the a_t's and b_t's facing each other and then summing. In general, the tth element $a * b_t$ is obtained in a similar fashion *after* the lower line has been shifted to the right by t divisions – for example, the right-hand plot shows the alignment of the lines that yields the second element $a * b_2$ of the convolution.

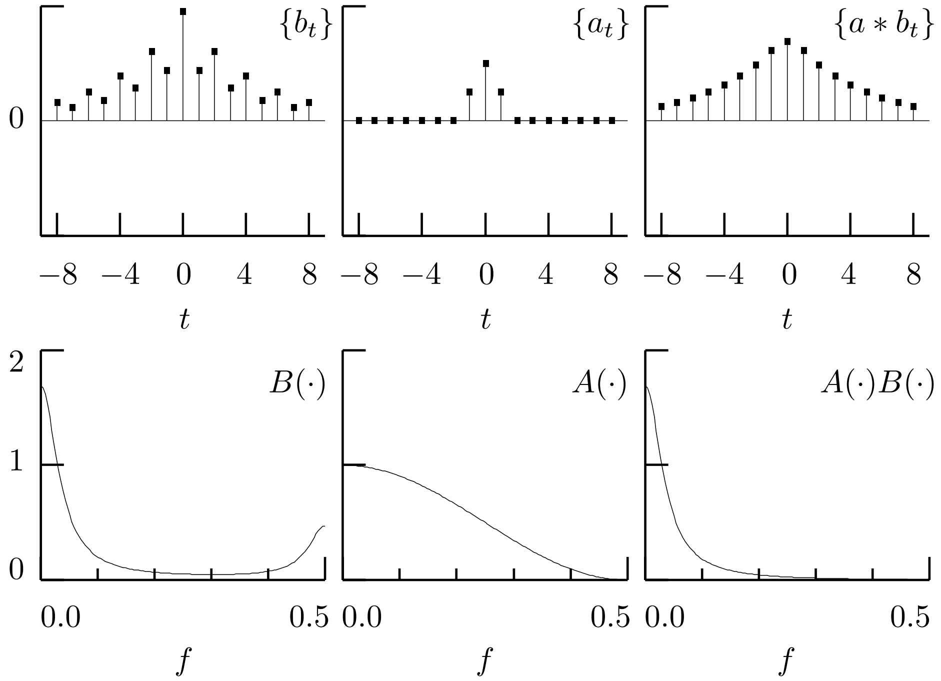

Figure 26. Example of filtering using a low-pass filter.

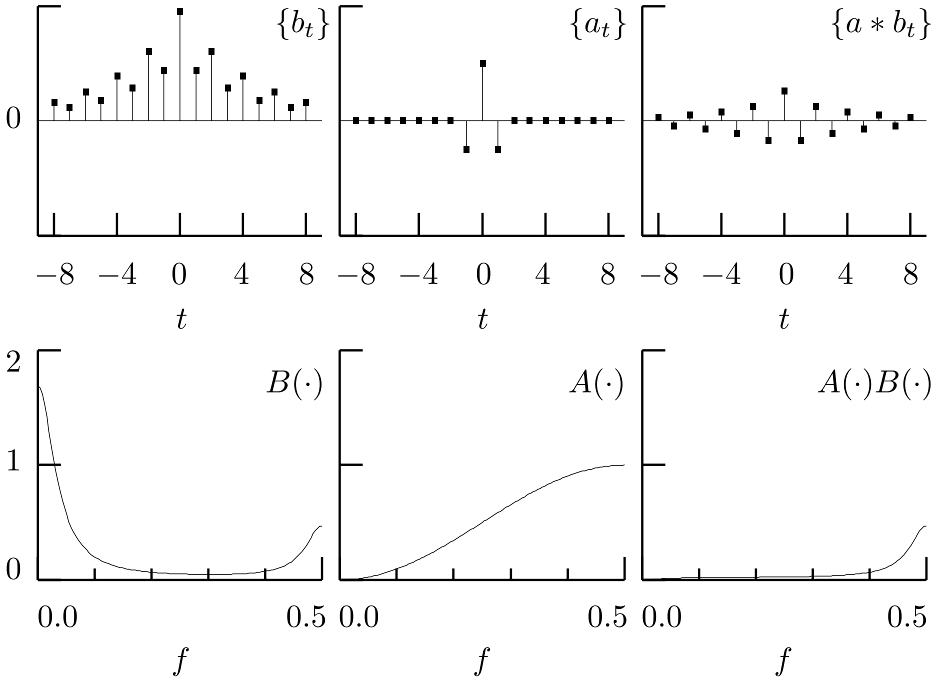

Figure 27. Example of filtering using a high-pass filter.

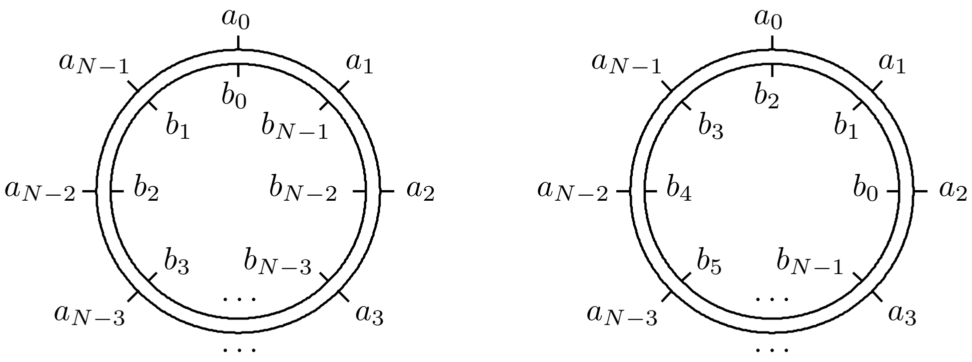

$$a * b_0 = \sum_{u=0}^{N-1} a_u b_{-u \bmod N} \qquad\qquad a * b_2 = \sum_{u=0}^{N-1} a_u b_{2-u \bmod N}$$

Figure 31a. Graphical illustration of circular convolution of the finite sequences $\{a_t\}$ and $\{b_t\}$. The left-hand plot shows two concentric circles. The outer circle is divided into N equal arcs, and the boundaries between the arcs are labeled clockwise from the top with $a_0, a_1, \ldots, a_{N-1}$. The inner circle is likewise divided, but now the boundaries are labeled counter-clockwise with $b_0, b_1, \ldots, b_{N-1}$. The zeroth element $a * b_0$ of the convolution of $\{a_t\}$ and $\{b_t\}$ is obtained by multiplying the a_t's and b_t's facing each other and then summing. In general, the tth element $a * b_t$ is obtained in a similar fashion *after* the inner circle has been rotated clockwise by t divisions – for example, the right-hand plot shows the alignment of the concentric circles that yields the second element $a * b_2$ of the convolution.

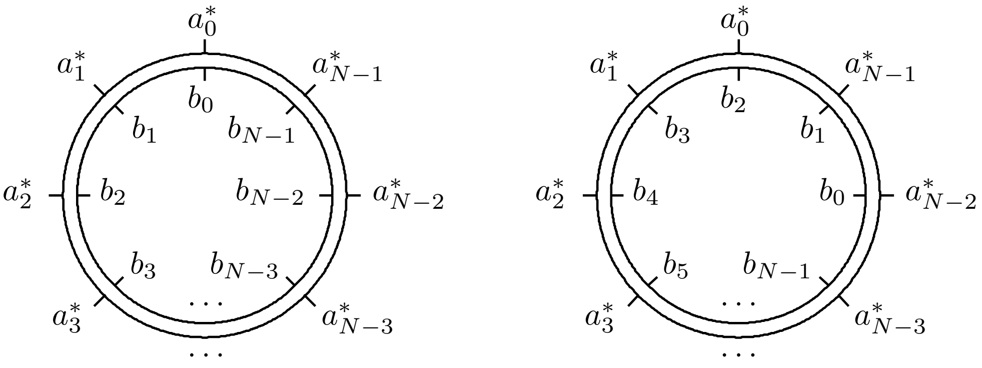

$$a^* \star b_0 = \sum_{u=0}^{N-1} a_u^* b_u \qquad\qquad a^* \star b_2 = \sum_{u=0}^{N-1} a_u^* b_{u+2 \bmod N}$$

Figure 31b. Graphical illustration of circular complex cross-correlation of $\{a_t\}$ and $\{b_t\}$. The layout is similar to Figure 31a.

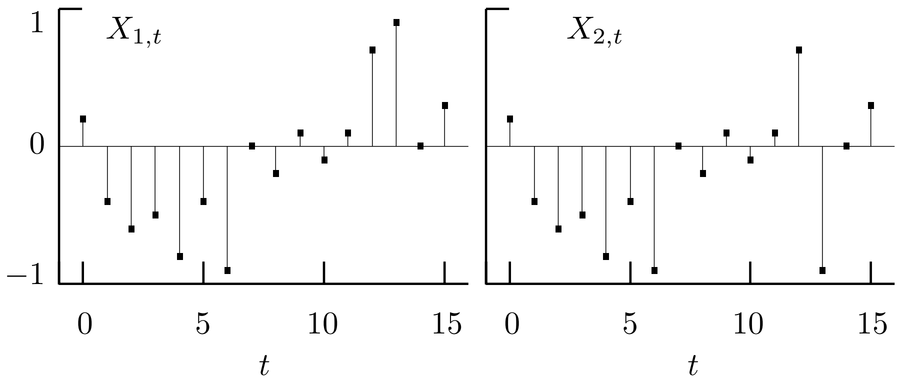

Figure 42. Two small time series $\{X_{1,t}\}$ and $\{X_{2,t}\}$, each with $N = 16$ values. The left-hand plot shows $X_{1,t}$ versus t for $t = 0, \ldots, 15$ as black dots, while the right-hand plot shows $X_{2,t}$. The two series differ only at the $t = 13$th value, for which $X_{2,13} = -X_{1,13}$. For the record, the 16 values for $\{X_{1,t}\}$ are 0.2, −0.4, −0.6, −0.5, −0.8, −0.4, −0.9, 0.0, −0.2, 0.1, −0.1, 0.1, 0.7, 0.9, 0.0 and 0.3.

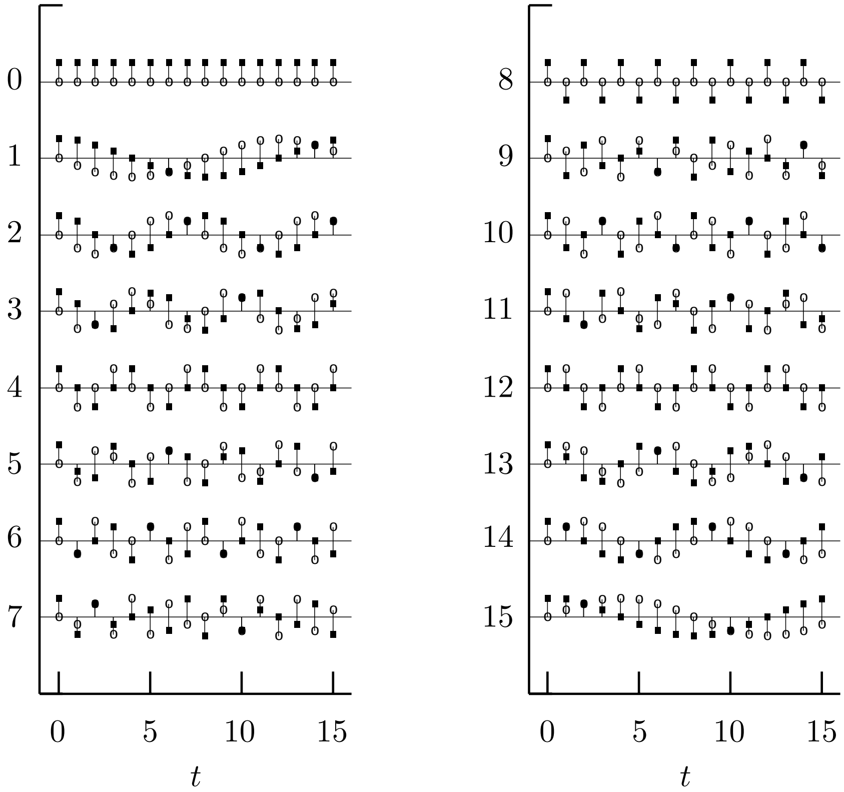

Figure 47. Row vectors $\mathcal{F}_{k\bullet}^{H}$ for the orthonormal discrete Fourier transform matrix $\mathcal{F}$ for $N = 16$ and $k = 0$ to 7 (top to bottom on left-hand plot) and $k = 8$ to 15 (right-hand plot). Most of the elements of $\mathcal{F}$ are complex-valued, so the real and imaginary components are represented, respectively, by solid squares and open circles. Note that the elements of $\mathcal{F}_{0\bullet}^{H}$ and $\mathcal{F}_{8\bullet}^{H}$ are real-valued and that, e.g., $\mathcal{F}_{15\bullet}^{H} = (\mathcal{F}_{1\bullet}^{H})^{*}$.

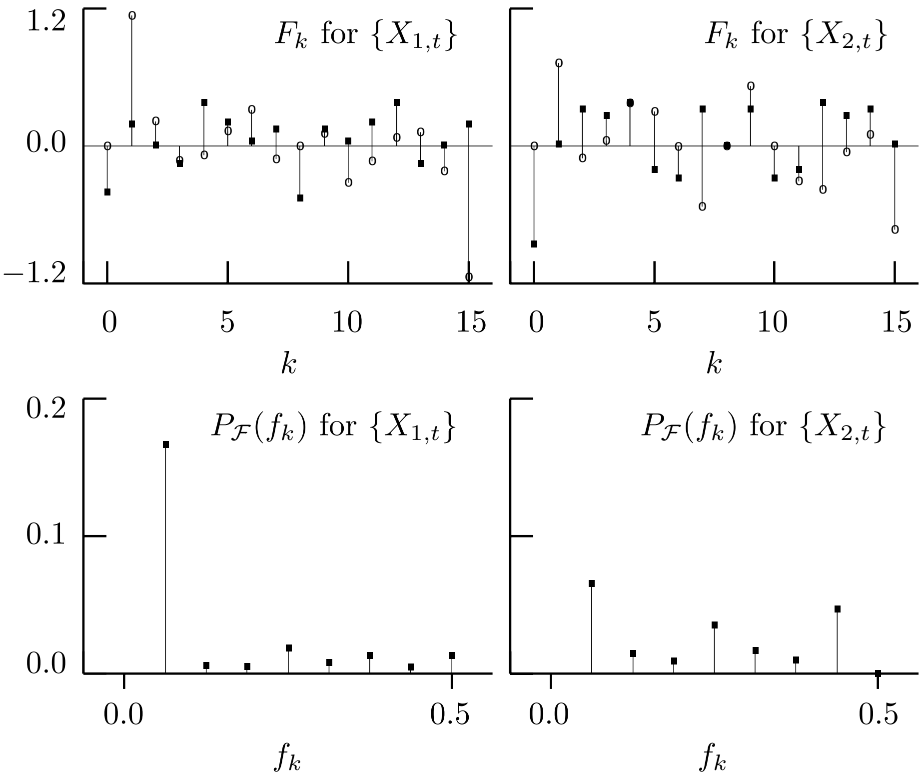

Figure 49. Orthonormal discrete Fourier transforms for the time series in Figure 42. The ODFTs $\mathbf{F}$ for $\{X_{1,t}\}$ and $\{X_{2,t}\}$ are plotted in the top row. The real and imaginary components of the ODFTs are represented by, respectively, solid squares and open circles. The discrete empirical power spectra corresponding to these ODFTs are shown in the bottom row.

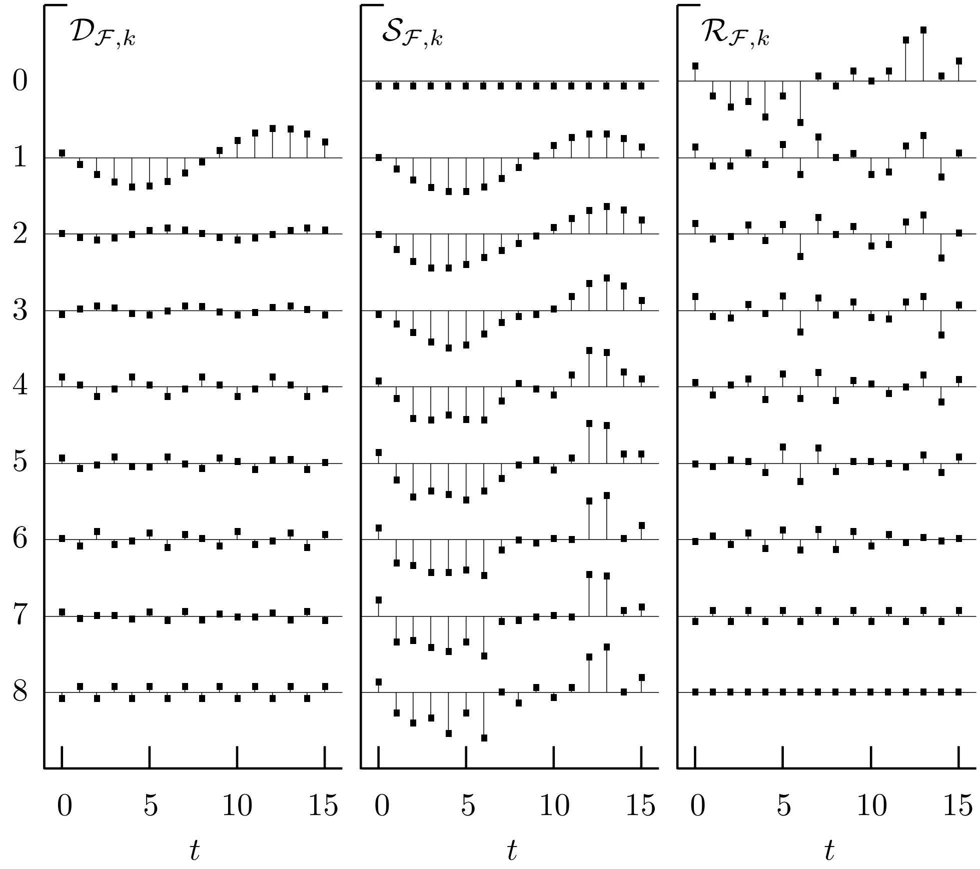

Figure 50. Fourier details $\mathcal{D}_{\mathcal{F},k}$, smooths $\mathcal{S}_{\mathcal{F},k}$ and roughs $\mathcal{R}_{\mathcal{F},k}$ for $\{X_{1,t}\}$ (left-hand plot of Figure 42) for $k = 0, \ldots, 8$ (top to bottom).

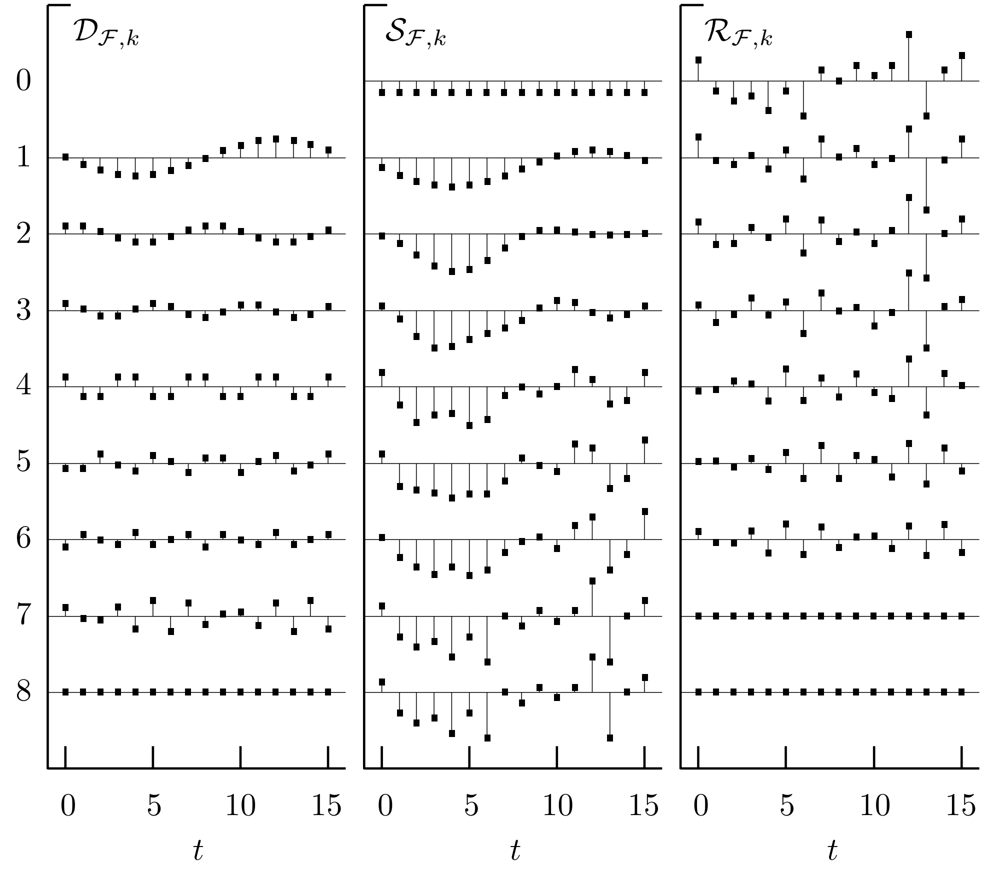

Figure 51. Fourier details $\mathcal{D}_{\mathcal{F},k}$, smooths $\mathcal{S}_{\mathcal{F},k}$ and roughs $\mathcal{R}_{\mathcal{F},k}$ for $\{X_{2,t}\}$ (right-hand plot of Figure 42) for $k = 0, \ldots, 8$ (top to bottom).

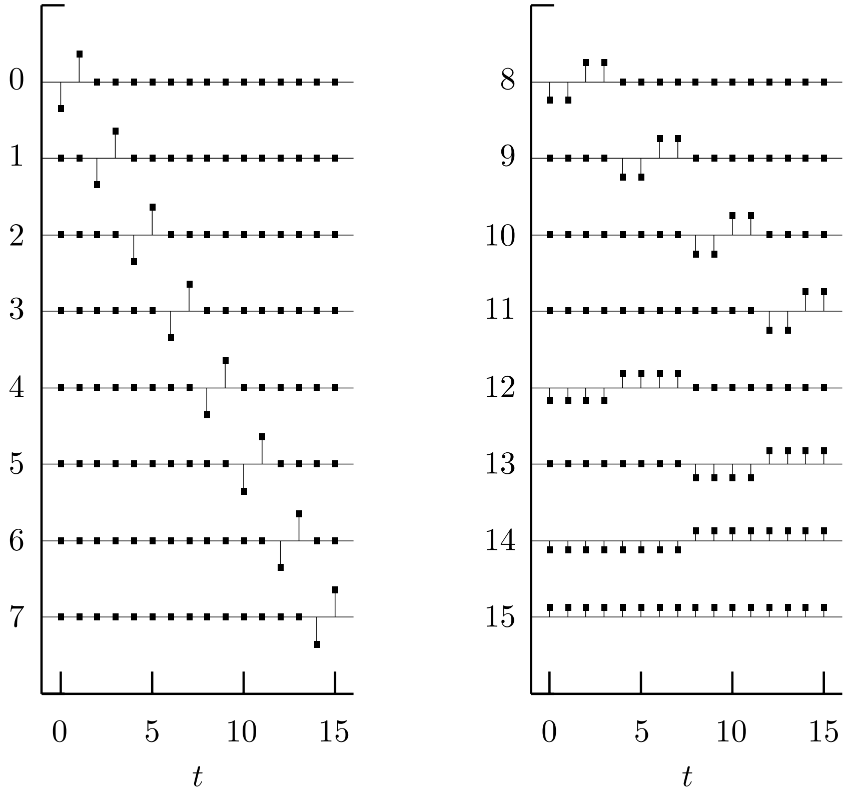

Figure 57. Row vectors $\mathcal{W}_{n\bullet}^{T}$ of the discrete wavelet transform matrix $\mathcal{W}$ based on the Haar wavelet for $N = 16$ and $n = 0$ to 7 (top to bottom on left plot) and $n = 8$ to 15 (right plot).

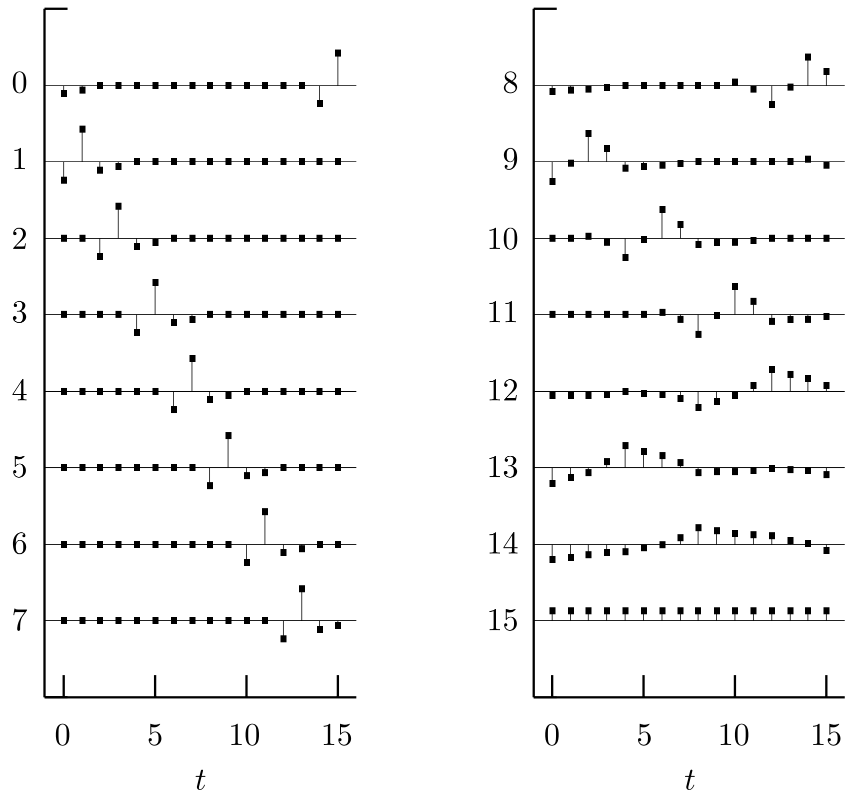

Figure 60. Row vectors $\mathcal{W}_{n\bullet}^T$ of the discrete wavelet transform matrix $\mathcal{W}$ based on the D(4) wavelet for $N = 16$ and $n = 0$ to 7 (top to bottom on left plot) and $n = 8$ to 15 (right plot).

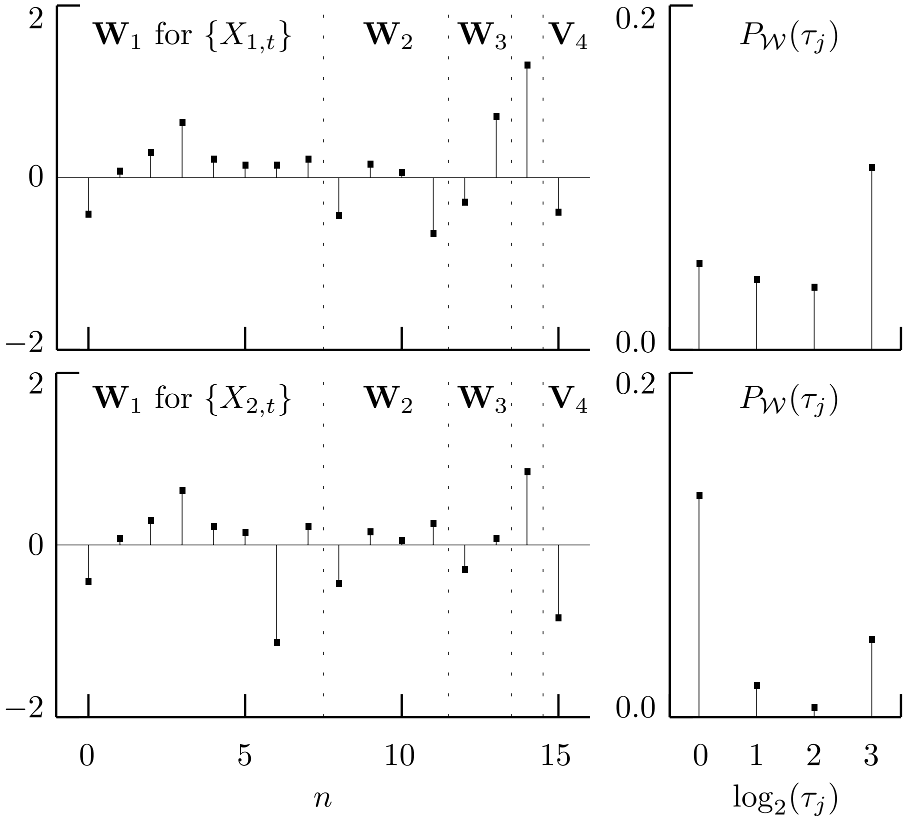

Figure 62. Haar DWTs for the two time series in Figure 42. The DWT coefficients $\mathbf{W}$ are shown in the left-hand plots (the corresponding discrete wavelet empirical power spectra are in the right-hand plots). The thin dotted lines delineate the subvectors $\mathbf{W}_1$, $\mathbf{W}_2$, $\mathbf{W}_3$, $\mathbf{W}_4$ and $\mathbf{V}_4$ (see Equation (61c); $\mathbf{W}_4$ is between $\mathbf{W}_3$ and $\mathbf{V}_4$ but is unlabeled due to lack of space).

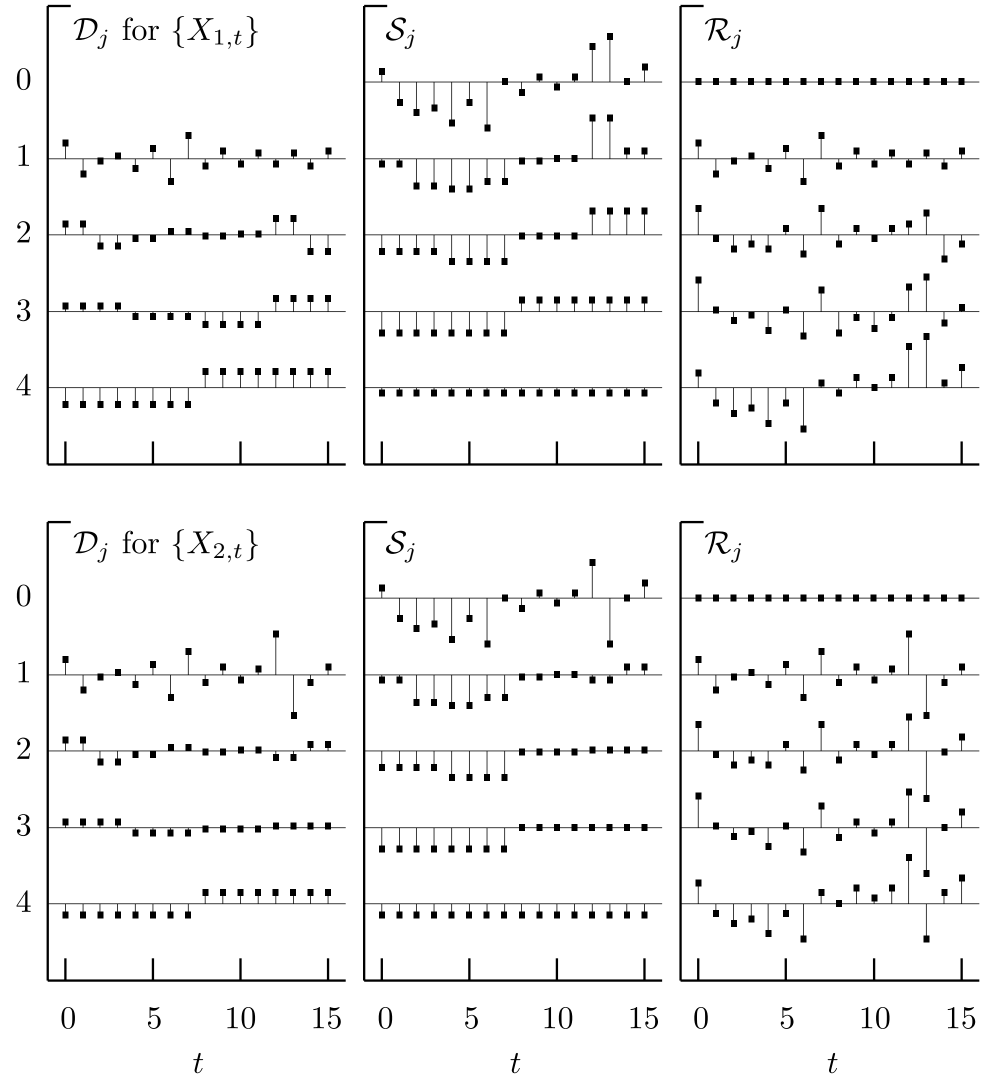

Figure 64. Haar wavelet details $\mathcal{D}_j$, smooths $\mathcal{S}_j$ and roughs $\mathcal{R}_j$ of levels $j = 0$ to 4 for $\{X_{1,t}\}$ (top plots) and $\{X_{2,t}\}$ (bottom). For any given j, we have $\mathcal{S}_j + \mathcal{R}_j = \mathbf{X}$. The jth detail can be interpreted as the difference between successive smooths or successive roughs: $\mathcal{D}_j = \mathcal{S}_{j-1} - \mathcal{S}_j$ and $\mathcal{D}_j = \mathcal{R}_j - \mathcal{R}_{j-1}$.

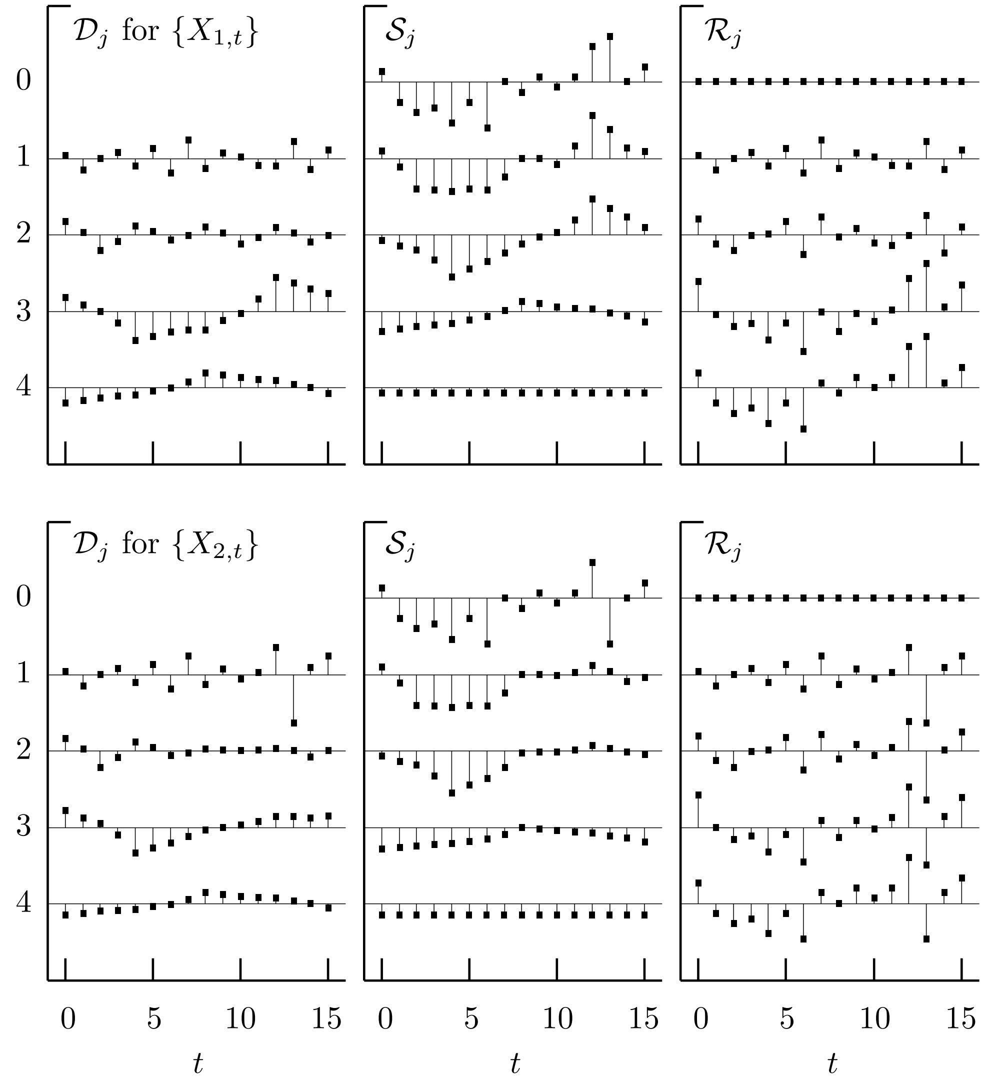

Figure 65. D(4) wavelet details $\mathcal{D}_j$, smooths $\mathcal{S}_j$ and roughs $\mathcal{R}_j$ for $\{X_{1,t}\}$ (top plots) and $\{X_{2,t}\}$ (bottom). Figure 64 has corresponding plots for the Haar wavelet. A comparison of these two figures shows that the Haar and D(4) smooths $\mathcal{S}_4$ agree perfectly for a given time series, which is a consequence of the fact that $\mathcal{V}_4$ is the same for both transforms (the roughs $\mathcal{R}_0$ also agree by definition).

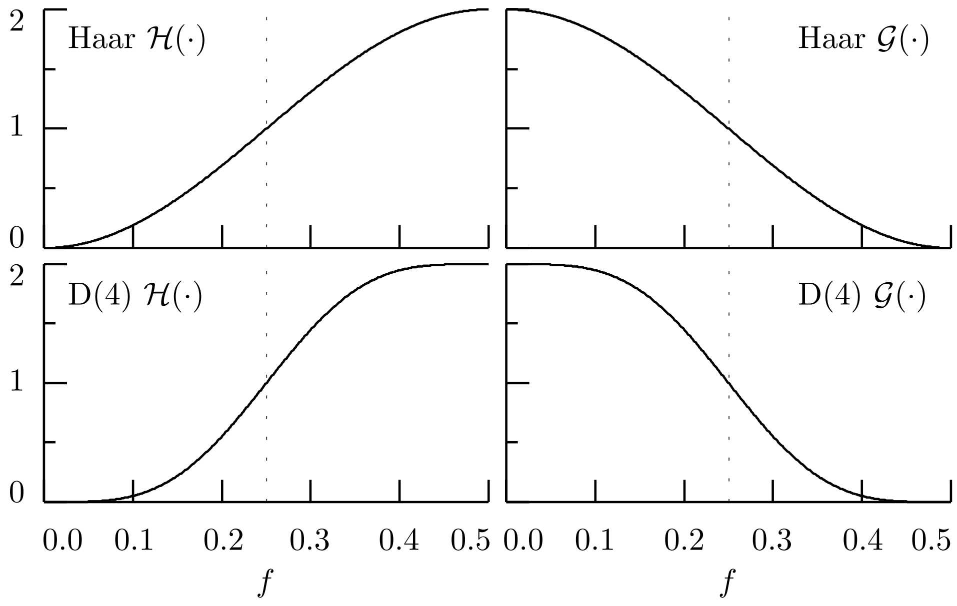

Figure 73. Squared gain functions for Haar wavelet filter (upper left-hand plot), Haar scaling filter (upper right), D(4) wavelet filter (lower left) and D(4) scaling filter (lower right). The dotted lines mark the frequency $f = 1/4$, which is the lower (upper) end of the nominal pass-band for the wavelet (scaling) filters.

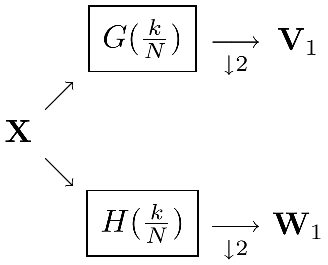

Figure 80. Flow diagram illustrating analysis of $\mathbf{X}$ into $\mathbf{W}_1$ and $\mathbf{V}_1$. The time series in the vector $\mathbf{X}$ of length N is circularly filtered using a wavelet filter $H(\cdot)$ periodized to length N (the frequency domain form of this filter is given by $\{H(\frac{k}{N}) : k = 0, \ldots, N-1\}$). All the odd indexed values of the filtered series are used to form the vector $\mathbf{W}_1$ of length $N/2$ containing the wavelet coefficients of level $j = 1$ ('$\downarrow 2$' indicates downsampling by two); in a similar manner, the vector $\mathbf{V}_1$ of length $N/2$ containing the scaling coefficients of level $j = 1$ is obtained by downsampling the output from filtering $\mathbf{X}$ with the scaling filter $G(\cdot)$ periodized to length N.

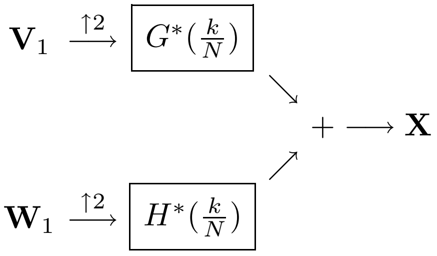

Figure 83. Flow diagram illustrating synthesis of $\mathbf{X}$ from $\mathbf{W}_1$ and $\mathbf{V}_1$. The vector $\mathbf{W}_1$ of length $N/2$ is upsampled by two to form a vector of length N, whose contents are then circularly filtered using the filter $\{H^*(\frac{k}{N})\}$ (here upsampling $\mathbf{W}_1$ by two means adding a zero before each element in that vector and is indicated on the flow diagram by '$\uparrow$ 2'). The vector $\mathbf{X}$ is formed by adding the output from this filter to a similar output obtained by filtering $\mathbf{V}_1$ (after upsampling) with the filter $\{G^*(\frac{k}{N})\}$.

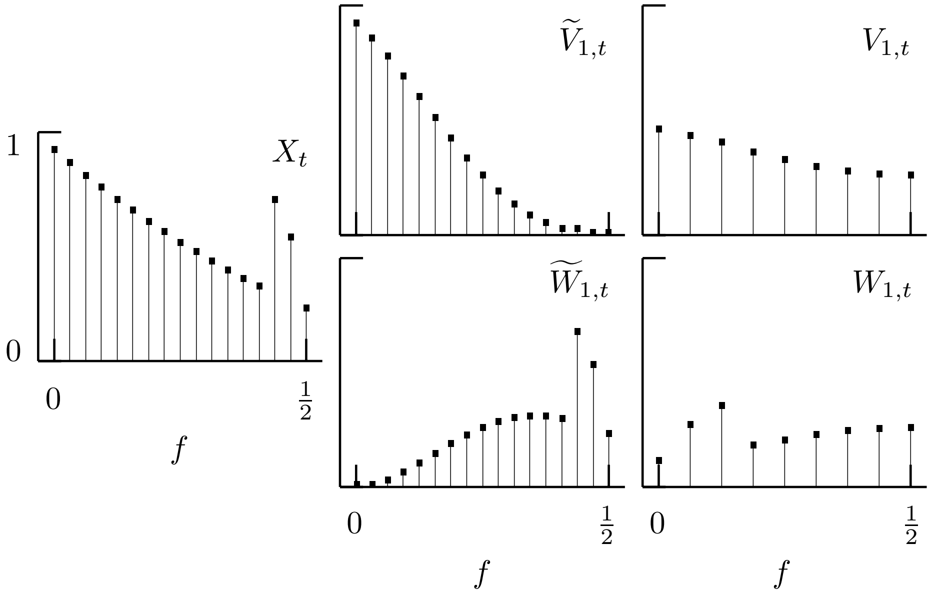

Figure 86. Magnitude squared DFT of the time series $\{X_t\}$ of Equation (85) (left-hand plot), along with the magnitude squared DFTs for the rescaled Haar scaling and wavelet filter outputs $\{\widetilde{V}_{1,t}\}$ and $\{\widetilde{W}_{1,t}\}$ (middle plots) and the Haar scaling and wavelet coefficients $\{V_{1,t}\}$ and $\{W_{1,t}\}$ (right-hand). Because $\{X_t\}$ and its filtered versions are real-valued, the squared magnitudes of all the DFTs are symmetric about zero, so just the values for the nonnegative Fourier frequencies are shown. The magnitude squared DFTs for $\{\widetilde{V}_{1,t}\}$ and $\{\widetilde{W}_{1,t}\}$ are obtained by multiplying the magnitude squared DFT for $\{X_t\}$ by values picked from the squared gain functions for $\{g_l/\sqrt{2}\}$ and $\{h_l/\sqrt{2}\}$ (these are defined by $\mathcal{G}(f)/2$ and $\mathcal{H}(f)/2$ – the shapes of these functions are shown in the top row of Figure 73). Note that $\{\widetilde{V}_{1,t}\}$ preserves the low frequency content of $\{X_t\}$ in its low frequencies, while $\{\widetilde{W}_{1,t}\}$ preserves the high frequency content of $\{X_t\}$ in its high frequencies. Whereas $\{\widetilde{V}_{1,t}\}$ and $\{\widetilde{W}_{1,t}\}$ are deficient in, respectively, high and low frequency content and hence are half-band series, the subsampled and rescaled series $\{V_{1,t}\}$ and $\{W_{1,t}\}$ are full-band series that preserve, respectively, the low and high frequency content of $\{X_t\}$. Whereas $\{V_{1,t}\}$ keeps the ordering of the frequencies in $\{X_t\}$, the ordering is reversed in $\{W_{1,t}\}$; e.g., the bulge at the high frequencies $f_{14} = \frac{14}{32}$ and $f_{15} = \frac{15}{32}$ in the DFT for $\{X_t\}$ appears in a reversed manner at the low frequencies $f'_1 = \frac{1}{16}$ and $f'_2 = \frac{2}{16}$ in the DFT for $\{W_{1,t}\}$.

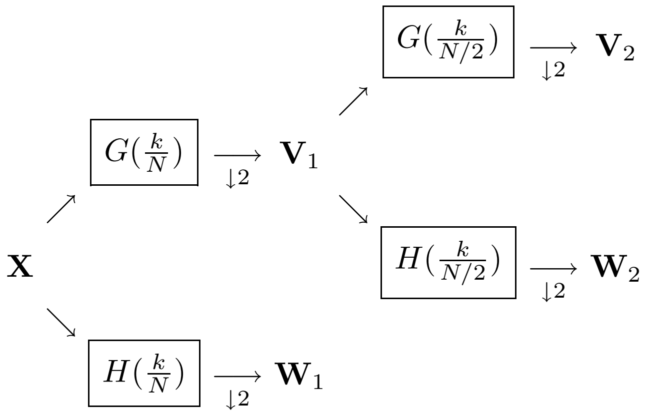

Figure 89. Flow diagram illustrating analysis of $\mathbf{X}$ into $\mathbf{W}_1$, $\mathbf{W}_2$ and $\mathbf{V}_2$.

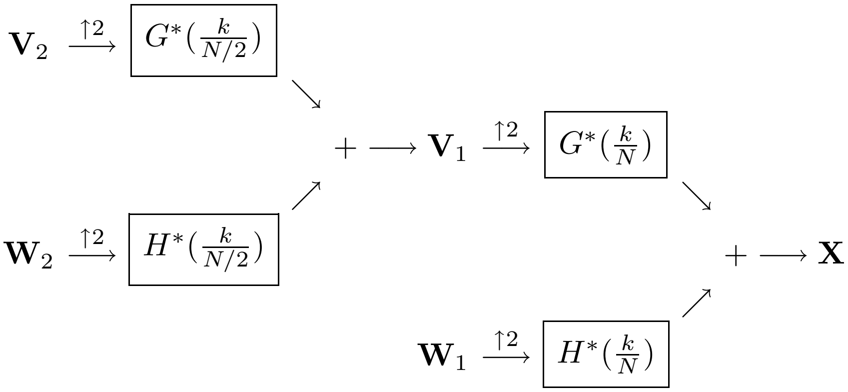

Figure 90. Flow diagram illustrating synthesis of $\mathbf{X}$ from $\mathbf{W}_1$, $\mathbf{W}_2$ and $\mathbf{V}_2$.

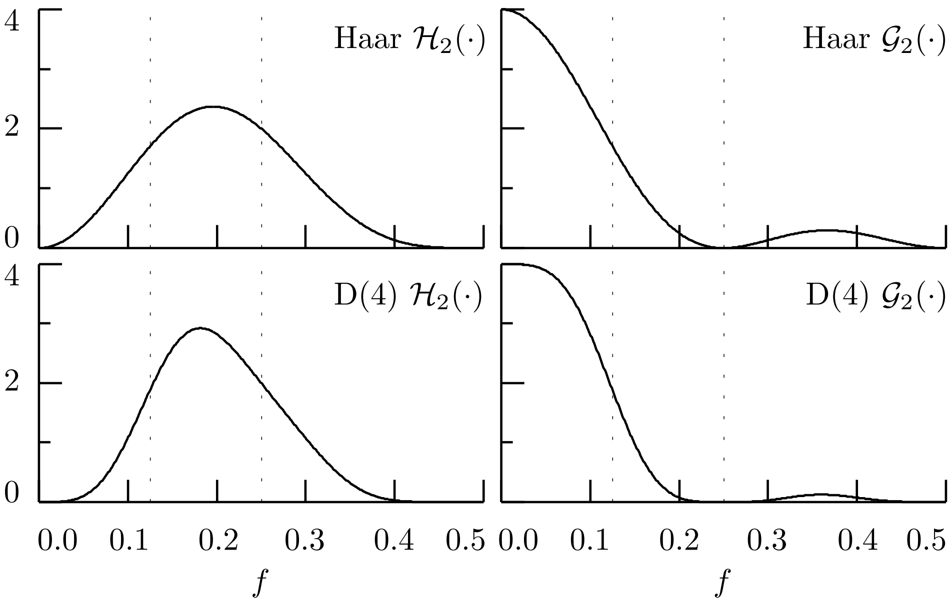

Figure 91. Squared gain functions for Haar $\{h_{2,l}\}$ and $\{g_{2,l}\}$ filters (upper left and right-hand plots, respectively) and D(4) $\{h_{2,l}\}$ and $\{g_{2,l}\}$ filters (lower left and right). The dotted lines mark the frequencies $f = 1/8$ and $f = 1/4$.

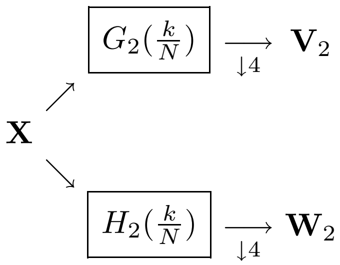

Figure 92. Flow diagram illustrating generation of $\mathbf{W}_2$ and $\mathbf{V}_2$ from $\mathbf{X}$. The time series in the vector $\mathbf{X}$ of length N is circularly filtered using the length N periodized version of the $j = 2$ level wavelet filter $\{h_{2,l}\}$ with transfer function $H_2(\cdot)$. All values of the filtered series with indices t such that $t + 1 \bmod 4 = 0$ are used to form the vector $\mathbf{W}_2$ ('$\downarrow$ 4' indicates downsampling every fourth value). The $N/4$ elements of $\mathbf{W}_2$ are the wavelet coefficients of level $j = 2$. Likewise, the vector $\mathbf{V}_2$ of length $N/4$ contains the scaling coefficients of level $j = 2$ and is obtained by downsampling (by four) the output from filtering $\mathbf{X}$ with the circular filter whose frequency domain representation is $\{G_2(\frac{k}{N})\}$.

$$\begin{tikzcd}
 & \boxed{G(\frac{k}{N/2^{j-1}})} \arrow[r, "\downarrow 2"'] & \mathbf{V}_j \arrow[r, "\uparrow 2"] & \boxed{G^*(\frac{k}{N/2^{j-1}})} \arrow[dr] & & \\
\mathbf{V}_{j-1} \arrow[ur] \arrow[dr] & & & & + \arrow[r] & \mathbf{V}_{j-1} \\
 & \boxed{H(\frac{k}{N/2^{j-1}})} \arrow[r, "\downarrow 2"'] & \mathbf{W}_j \arrow[r, "\uparrow 2"] & \boxed{H^*(\frac{k}{N/2^{j-1}})} \arrow[ur] & &
\end{tikzcd}$$

Figure 94. Flow diagram illustrating analysis of $\mathbf{V}_{j-1}$ into $\mathbf{W}_j$ and $\mathbf{V}_j$, followed by synthesis of $\mathbf{V}_{j-1}$ from $\mathbf{W}_j$ and $\mathbf{V}_j$.

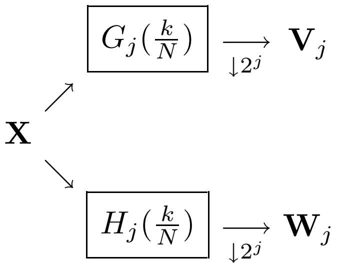

Figure 96. Flow diagram illustrating generation of $\mathbf{W}_j$ and $\mathbf{V}_j$ from $\mathbf{X}$. The time series in the vector $\mathbf{X}$ of length N is circularly filtered using a jth level wavelet filter $\{h_{j,l}\}$ with transfer function $H_j(\cdot)$, and all values of the filtered series with indices divisible by 2^j are used to form the vector $\mathbf{W}_j$ of length $N/2^j$ containing the wavelet coefficients of level j ('$\downarrow 2^j$' indicates downsampling every 2^jth value); in a similar manner, the vector $\mathbf{V}_j$ of length $N/2^j$ containing the scaling coefficients of level j is obtained by downsampling the output from filtering $\mathbf{X}$ using the jth level scaling filter with transfer function $G_j(\cdot)$.

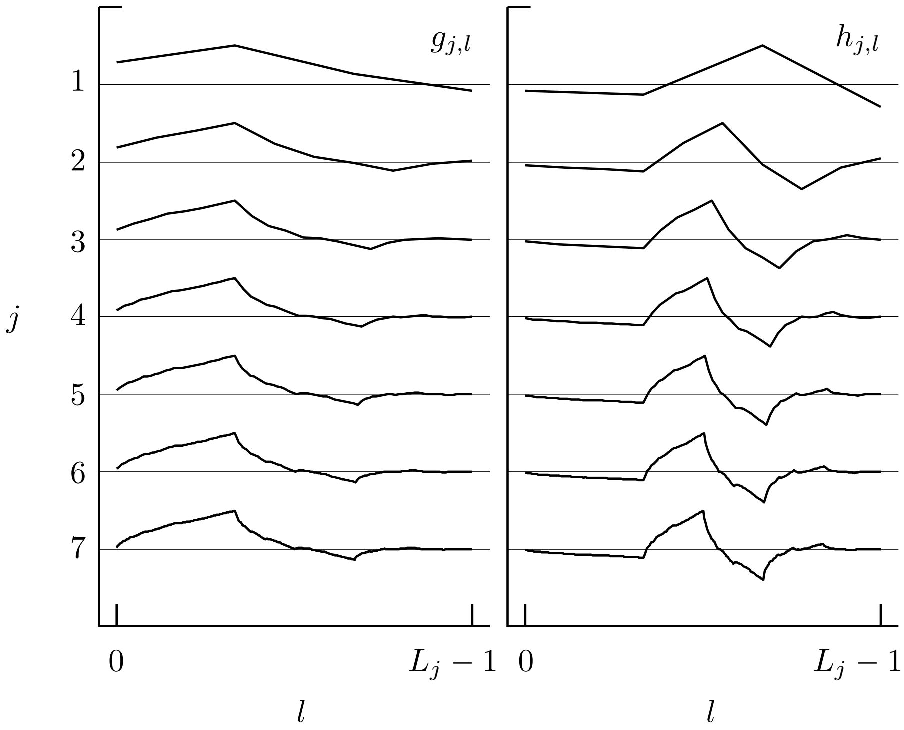

Figure 98a. D(4) scaling $\{g_{j,l}\}$ and wavelet $\{h_{j,l}\}$ filters for scales indexed by $j = 1, 2, \ldots, 7$ (here the individual values of the impulse response sequences are connected by lines).

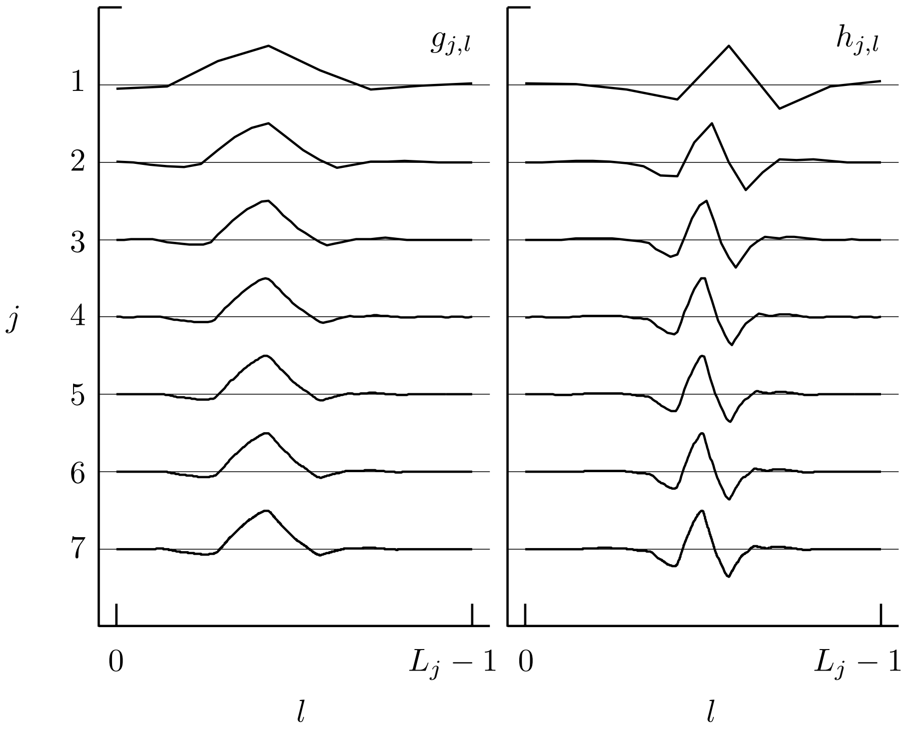

Figure 98b. LA(8) scaling $\{g_{j,l}\}$ and wavelet $\{h_{j,l}\}$ filters for scales indexed by $j = 1, 2, \ldots, 7$ (here the individual values of the impulse response sequences are connected by lines). These filters are defined in Section 4.8.

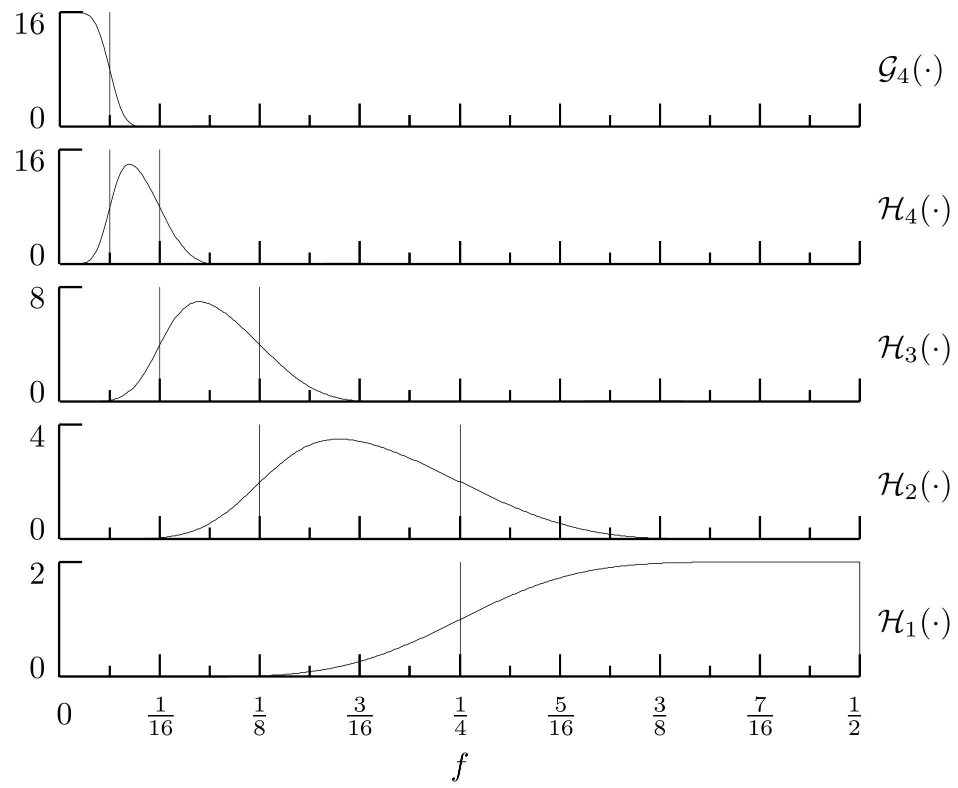

Figure 99. Squared gain functions for LA(8) filters $\{h_{j,l}\}, j = 1, \ldots, 4$, and $\{g_{4,l}\}$ (these filters are defined in Section 4.8).

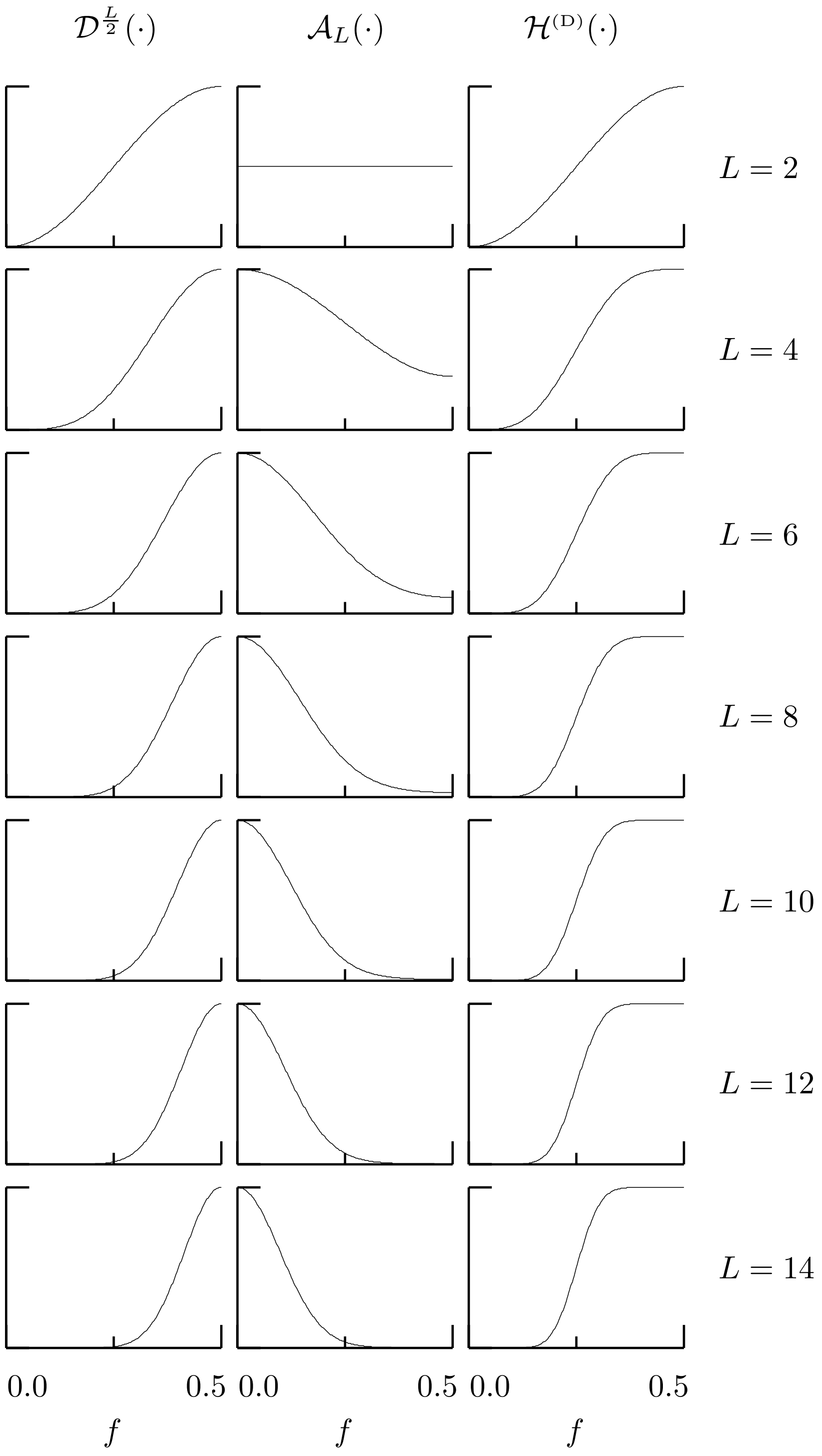

Figure 107. Squared gain functions $\mathcal{H}^{(\mathrm{D})}(\cdot)$ for Daubechies wavelet filters of widths $L = 2, 4, \ldots, 14$ (right-hand column). Each $\mathcal{H}^{(\mathrm{D})}(\cdot)$ is the product of two other squared gain functions, namely, $\mathcal{D}^{\frac{L}{2}}(\cdot)$ (left-hand column) and $\mathcal{A}_L(\cdot)$ (middle). The first corresponds to an $\frac{L}{2}$ order difference filter, while for $L \geq 4$ the second is associated with a weighted average (i.e., low-pass filter).

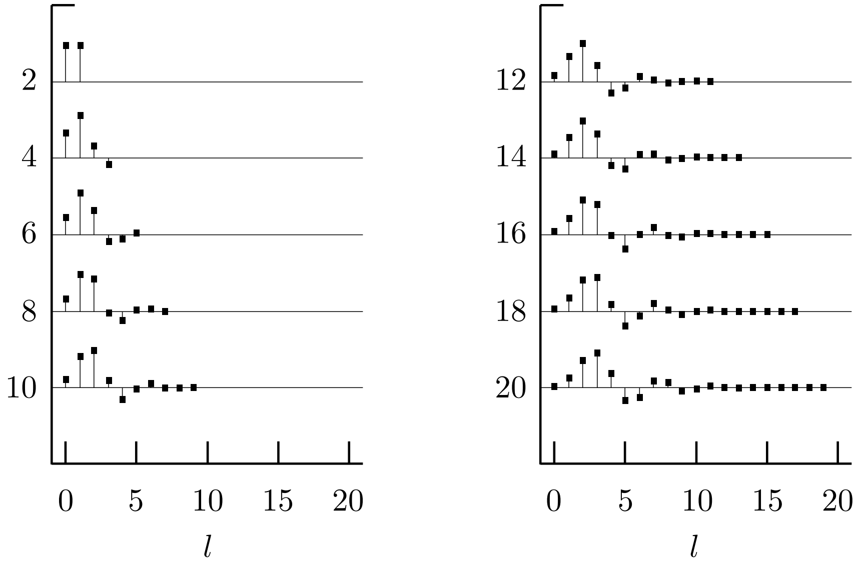

Figure 108a. Daubechies extremal phase scaling filters $\{g_l^{(\mathrm{ep})}\}$ for $L = 2, 4, \ldots, 20$ (values based on Daubechies, 1992, p. 195, Table 6.1).

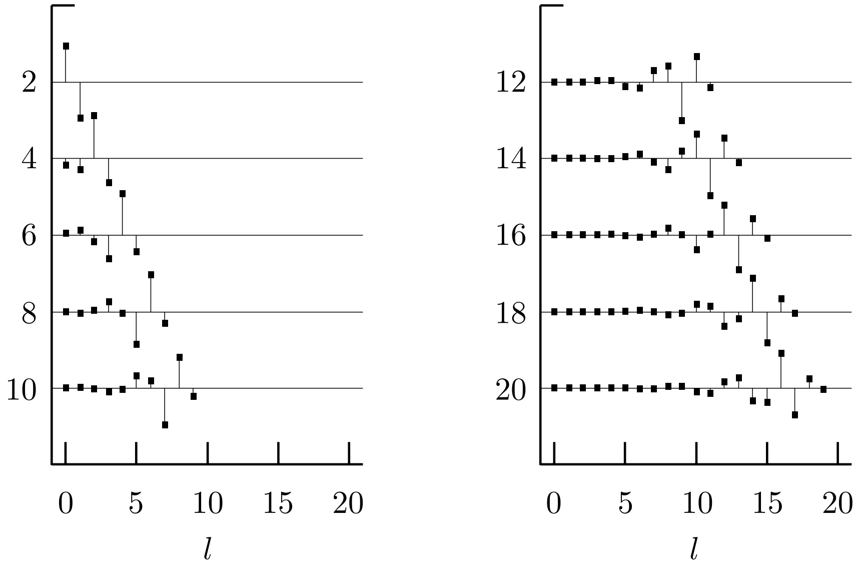

Figure 108b. Daubechies wavelet filters corresponding to the extremal phase scaling filters in Figure 108a.

l	g_l for D(6)	g_l for C(6)	g_l for D(8)
0	0.3326705529500827	−0.0156557285289848	0.2303778133074431
1	0.8068915093110928	−0.0727326213410511	0.7148465705484058
2	0.4598775021184915	0.3848648565381134	0.6308807679358788
3	−0.1350110200102546	0.8525720416423900	−0.0279837694166834
4	−0.0854412738820267	0.3378976709511590	−0.1870348117179132
5	0.0352262918857096	−0.0727322757411889	0.0308413818353661
6			0.0328830116666778
7			−0.0105974017850021

l	g_l for LA(8)	g_l for LA(12)	g_l for LA(16)
0	−0.0757657147893407	0.0154041093273377	−0.0033824159513594
1	−0.0296355276459541	0.0034907120843304	−0.0005421323316355
2	0.4976186676324578	−0.1179901111484105	0.0316950878103452
3	0.8037387518052163	−0.0483117425859981	0.0076074873252848
4	0.2978577956055422	0.4910559419276396	−0.1432942383510542
5	−0.0992195435769354	0.7876411410287941	−0.0612733590679088
6	−0.0126039672622612	0.3379294217282401	0.4813596512592012
7	0.0322231006040713	−0.0726375227866000	0.7771857516997478
8		−0.0210602925126954	0.3644418948359564
9		0.0447249017707482	−0.0519458381078751
10		0.0017677118643983	−0.0272190299168137
11		−0.0078007083247650	0.0491371796734768
12			0.0038087520140601
13			−0.0149522583367926
14			−0.0003029205145516
15			0.0018899503329007

Table 109. Coefficients for selected Daubechies scaling filters and for the coiflet scaling filter for $L = 6$ (the latter is discussed in Section 4.9). The coefficients in this table are derived from Daubechies (1992, 1993). These coefficients (and those for other $\{g_l\}$) are available on the Web site for this book (see page *xiv*).

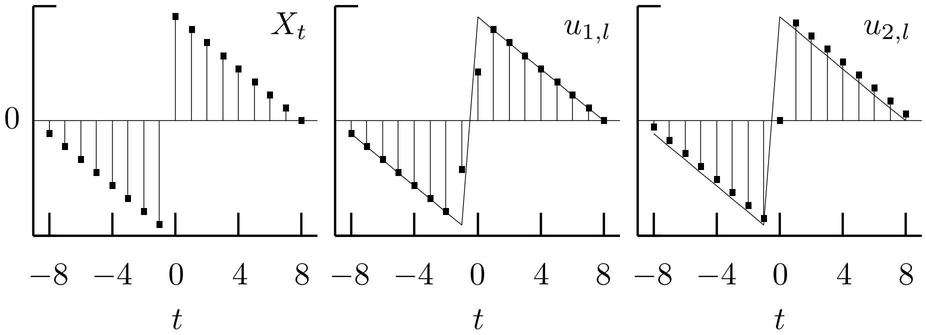

Figure 110. Example of filtering using a zero phase filter. The left-hand plot shows a time series $\{X_t\}$ with a discontinuity from $t = -1$ to $t = 0$. The solid points in the middle and right-hand plots show the results of filtering this series with, respectively, the filters $\{u_{1,l}\}$ (Equation (110a)) and $\{u_{2,l}\}$ (Equation (110b)), only the first of which has zero phase. The thin curves on these two plots show the original time series. Note that the discontinuity is spread out – but not shifted in location – using the zero phase filter $\{u_{1,l}\}$, whereas it is spread out and shifted forward in time using $\{u_{2,l}\}$.

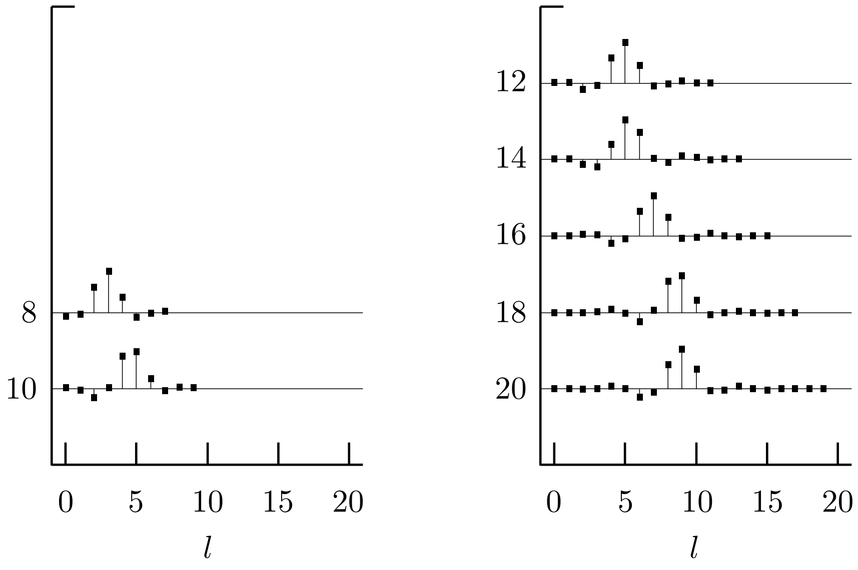

Figure 113a. Daubechies least asymmetric scaling filters $\{g_l^{(\mathrm{la})}\}$ for $L = 8, 10, \ldots, 20$ (values based on Daubechies, 1992, p. 198, Table 6.3, with modifications as noted in item [1] of the Comments and Extensions to this section).

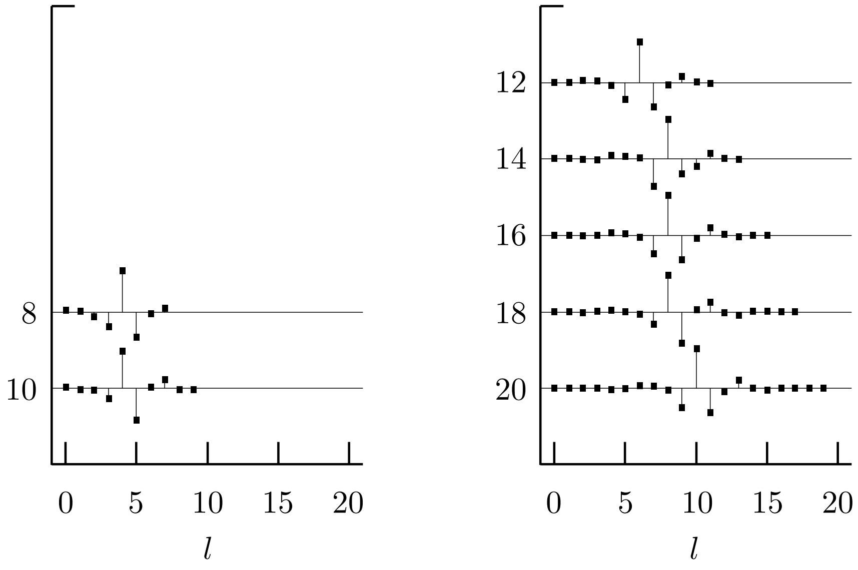

Figure 113b. Daubechies wavelet filters corresponding to the least asymmetric scaling filters shown in Figure 113a.

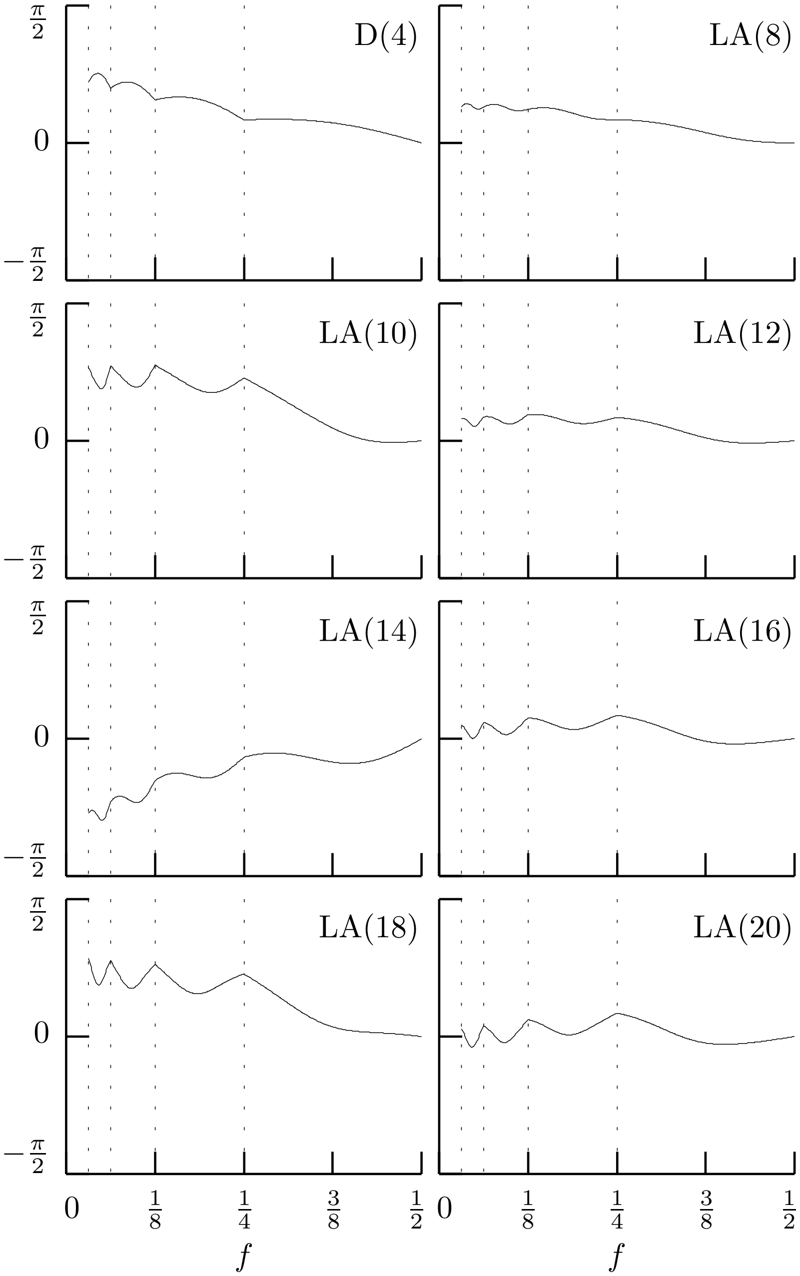

Figure 115. Exact phase functions of shifted LA wavelet filters $\{h_{j,l}\}$, $j = 1, 2, 3$ and 4 (the D(4) case is also shown, with shifts governed by setting $\nu = -1$). The phase functions for $\{h_{j,l}\}$ are plotted just over frequencies in the interval $[1/2^{j+1}, 1/2^j]$ – these intervals are indicated by the vertical dotted lines.

L	$\lvert\nu\rvert - e\{g_l\}$	L	$\lvert\nu\rvert - e\{g_l\}$
8	0.1536	14	−0.1615
10	0.4500	16	0.1546
12	0.1543	18	0.4471
		20	0.1547

Table 118. Comparison between advances $|p_j^{(H)}|$ and $|\nu_j^{(H)}|$ for Daubechies least asymmetric wavelet filters. Since $|p_j^{(H)}| - |\nu_j^{(H)}| = |\nu| - e\{g_l\}$ for all scale indices j, the above indicates that the two advances are the same when rounded to the nearest integer. To compare the advances for the corresponding scaling filters, the tabulated values must be multiplied by $2^j - 1$, so the advances diverge as j increases.

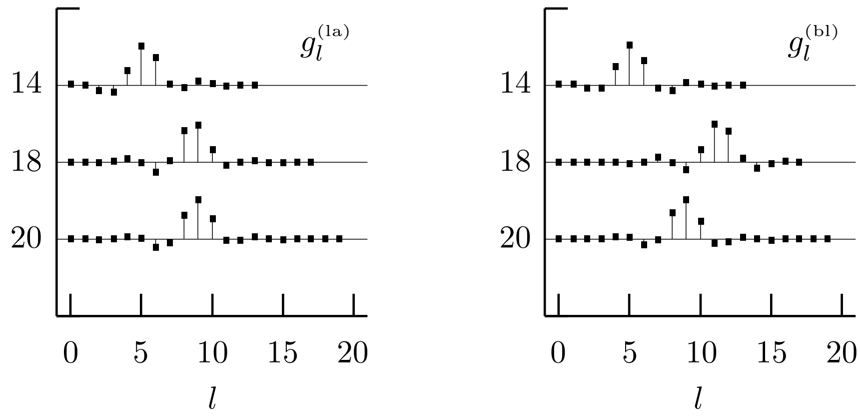

Figure 119. Least asymmetric scaling filters $\{g_l^{(\mathrm{la})}\}$ (left-hand column) and best localized scaling filters $\{g_l^{(\mathrm{bl})}\}$ (right) for $L = 14$, 18 and 20.

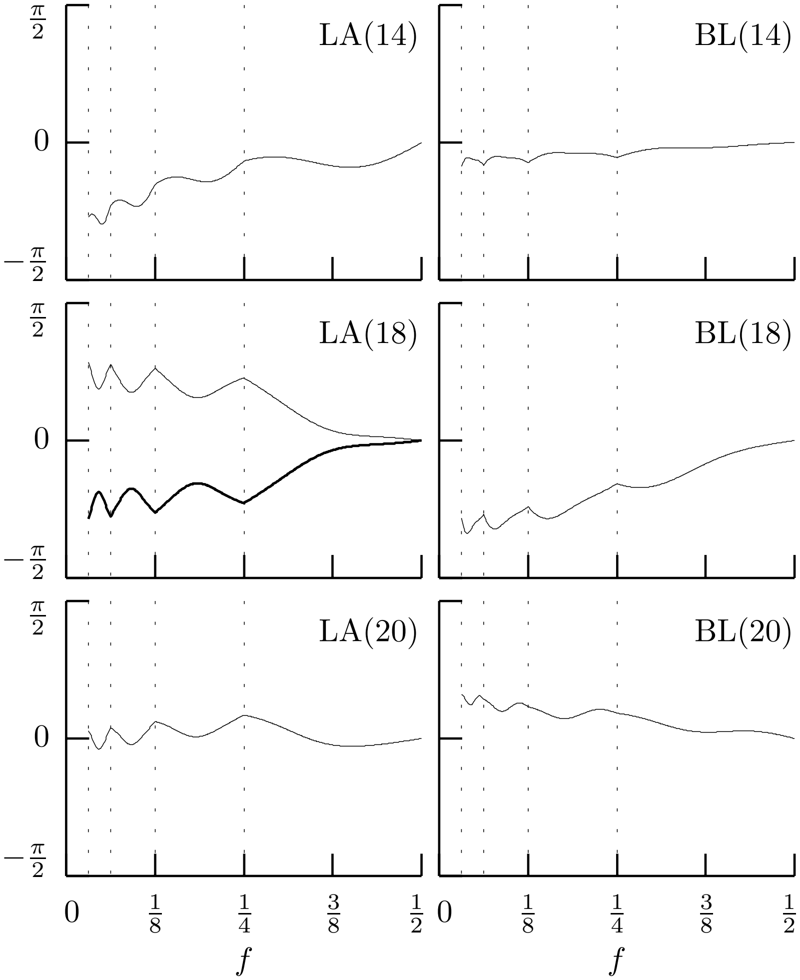

Figure 120. Exact phase functions of shifted least asymmetric and best localized wavelet filters (see the caption to Figure 115 and the text for details).

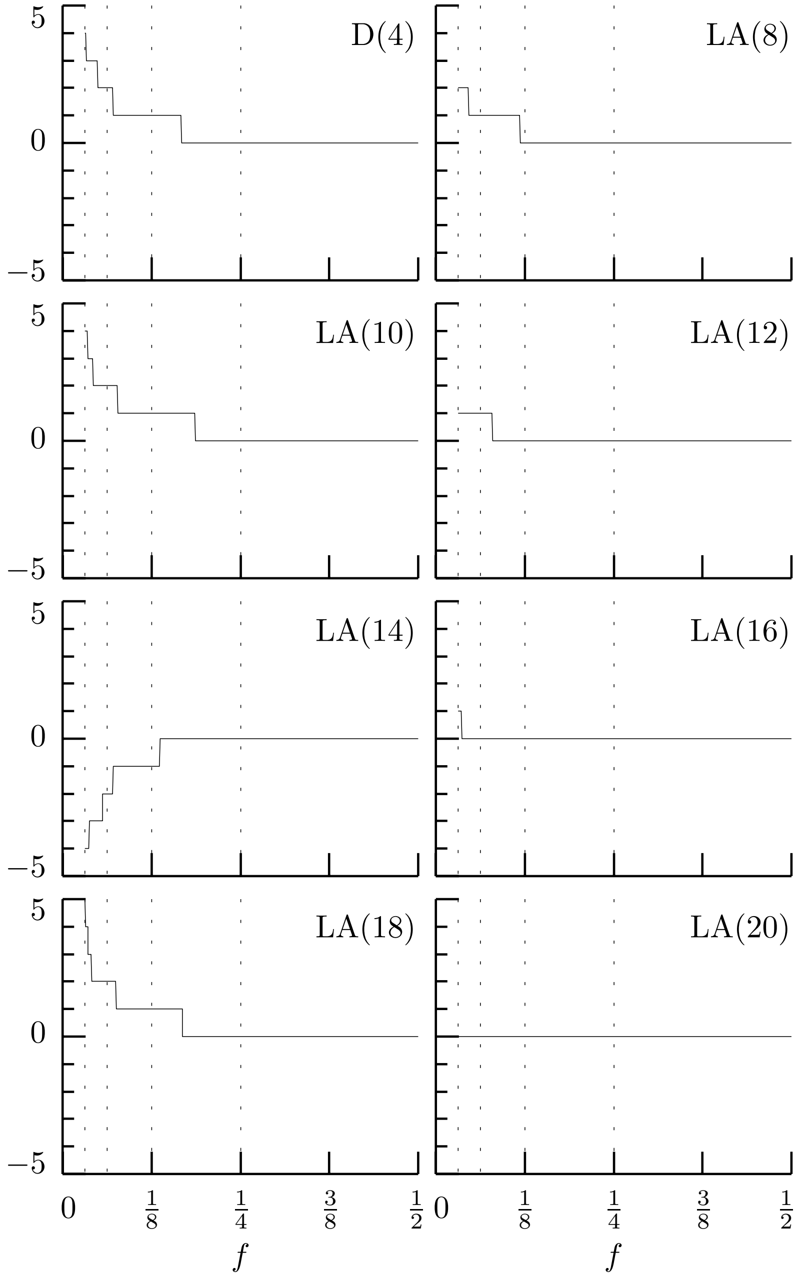

Figure 121. Time shift functions (rounded to the nearest integer) corresponding to the phase functions shown in Figure 115.

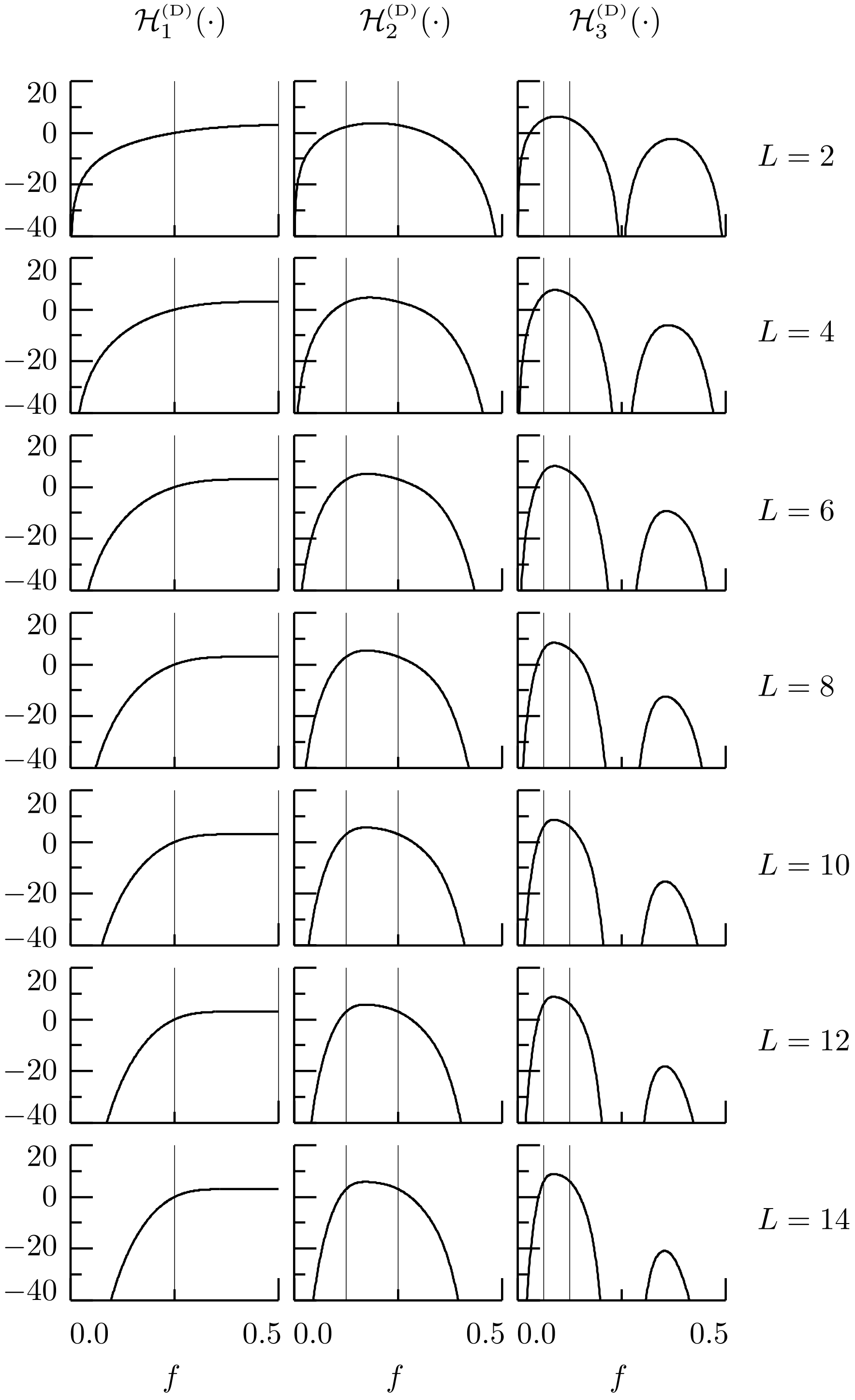

Figure 122. Squared gain functions $\mathcal{H}_j^{(D)}(\cdot)$, $j = 1, 2$ and 3 (left, middle and right columns, respectively), for Daubechies wavelet filters of widths $L = 2, 4, \ldots, 14$ (top to bottom rows, respectively). The two thin vertical lines in each plot delineate the nominal pass-band for the filter. The vertical axis is in decibels (i.e., we plot $10 \cdot \log_{10}(\mathcal{H}_j^{(D)}(f))$ versus f).

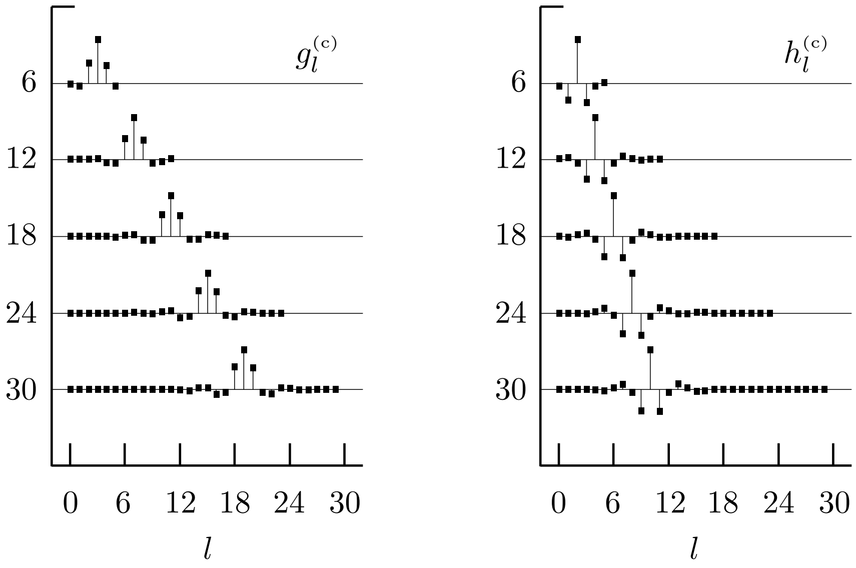

Figure 123. Coiflet scaling filters $\{g_l^{(c)}\}$ (left-hand column) and corresponding wavelet filters $\{h_l^{(c)}\}$ (right) of widths $L = 6$, 12, 18, 24 and 30 (Daubechies, 1992, p. 261, Table 8.1).

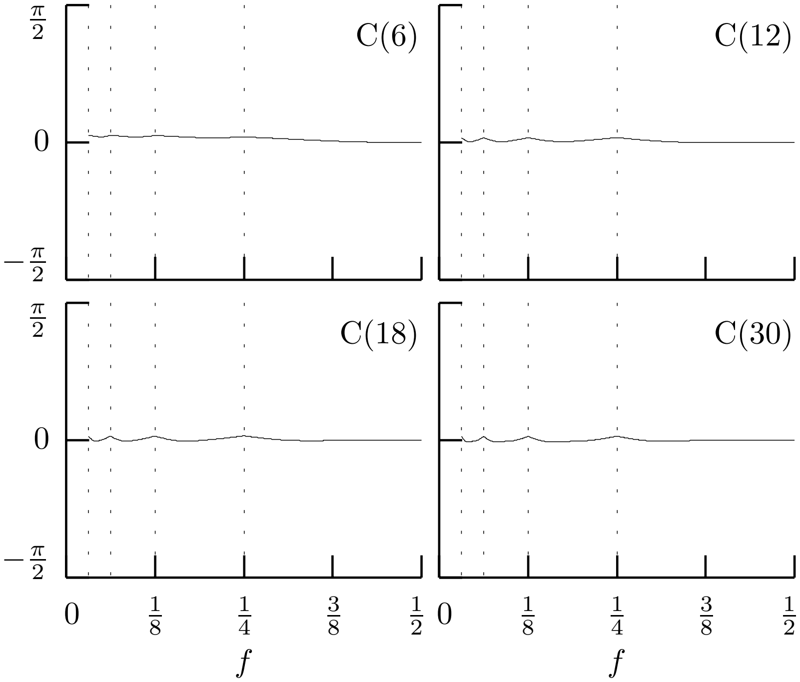

Figure 124. Exact phase functions of shifted coiflet wavelet filters (see the caption to Figure 115 and the text for details).

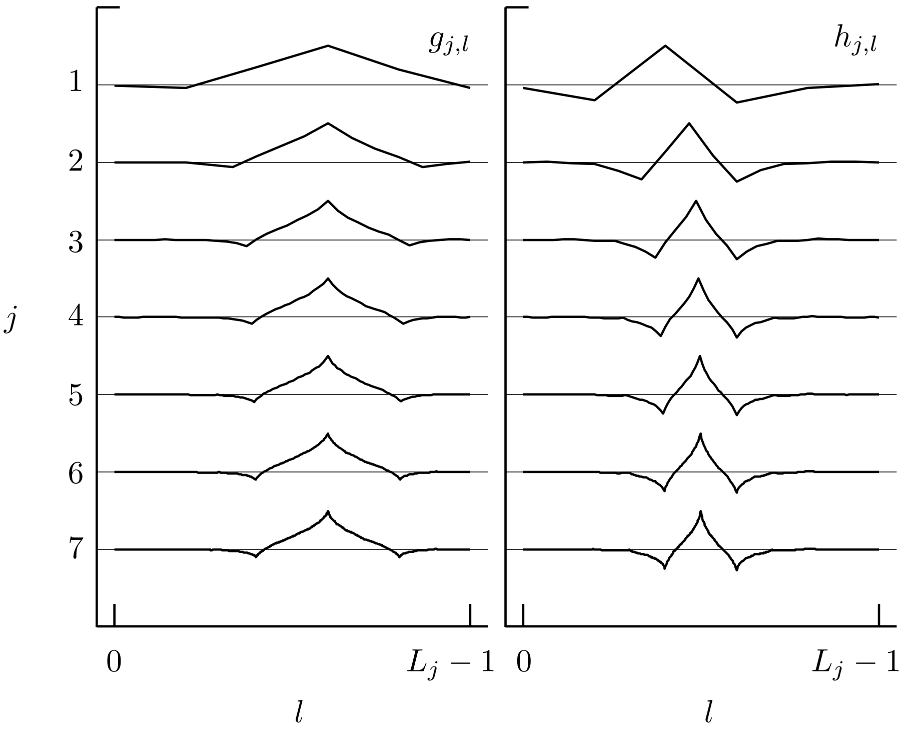

Figure 125. C(6) scaling $\{g_{j,l}\}$ and wavelet $\{h_{j,l}\}$ filters for scales indexed by $j = 1, 2, \ldots, 7$ (see Figures 98a and 98b for similar plots of the D(4) and LA(8) filters).

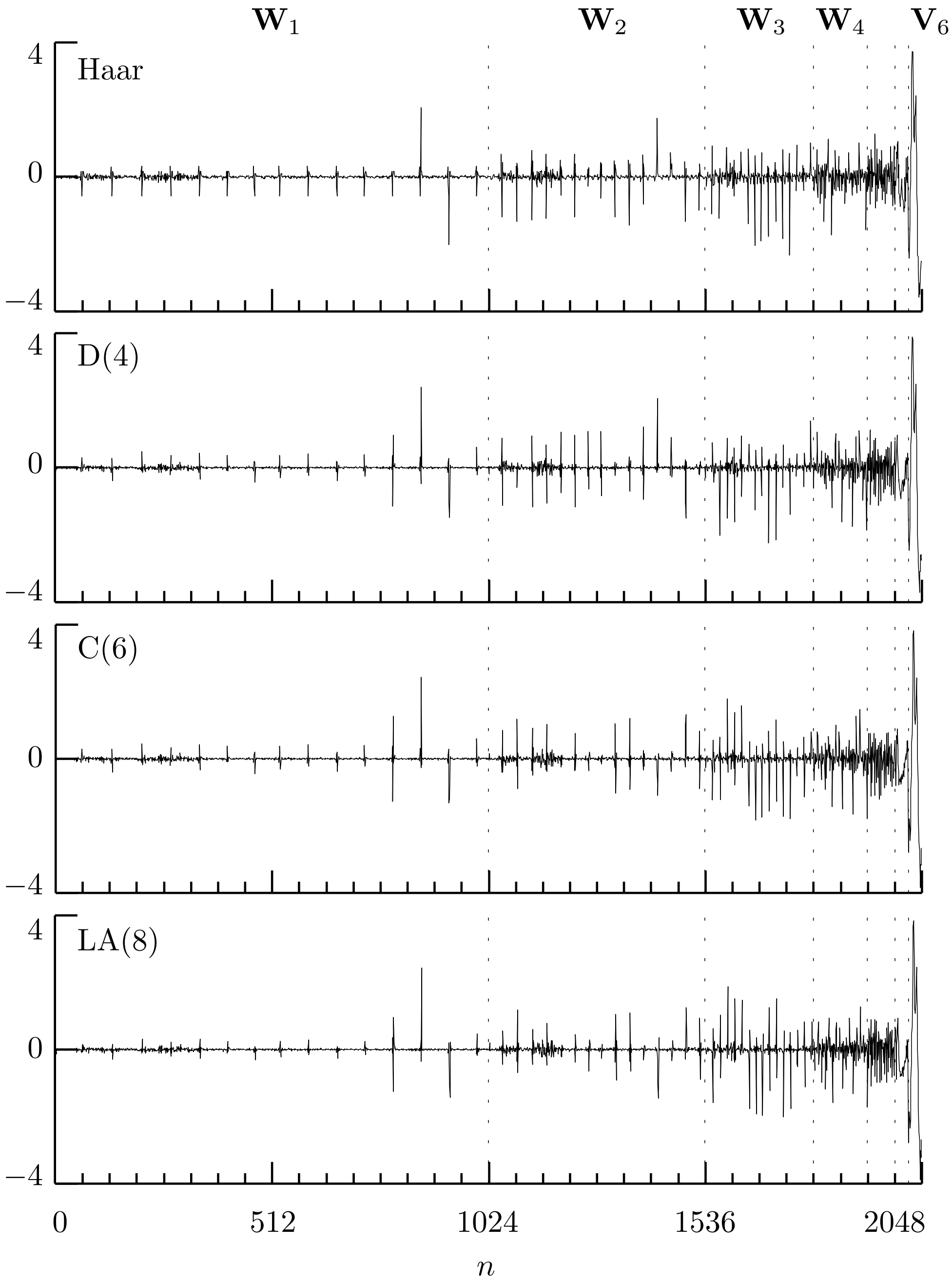

Figure 126. Partial DWT coefficients $\mathbf{W}$ of level $J_0 = 6$ for ECG time series using the Haar, D(4), C(6) and LA(8) wavelets. The elements W_n of $\mathbf{W}$ are plotted versus $n = 0, \ldots, N-1 = 2047$. The six vertical dotted lines delineate the seven subvectors of $\mathbf{W}$, namely, $\mathbf{W}_1, \ldots, \mathbf{W}_6$ and $\mathbf{V}_6$ ($\mathbf{W}_5$ and $\mathbf{W}_6$ are not labeled at the top of the figure due to lack of space).

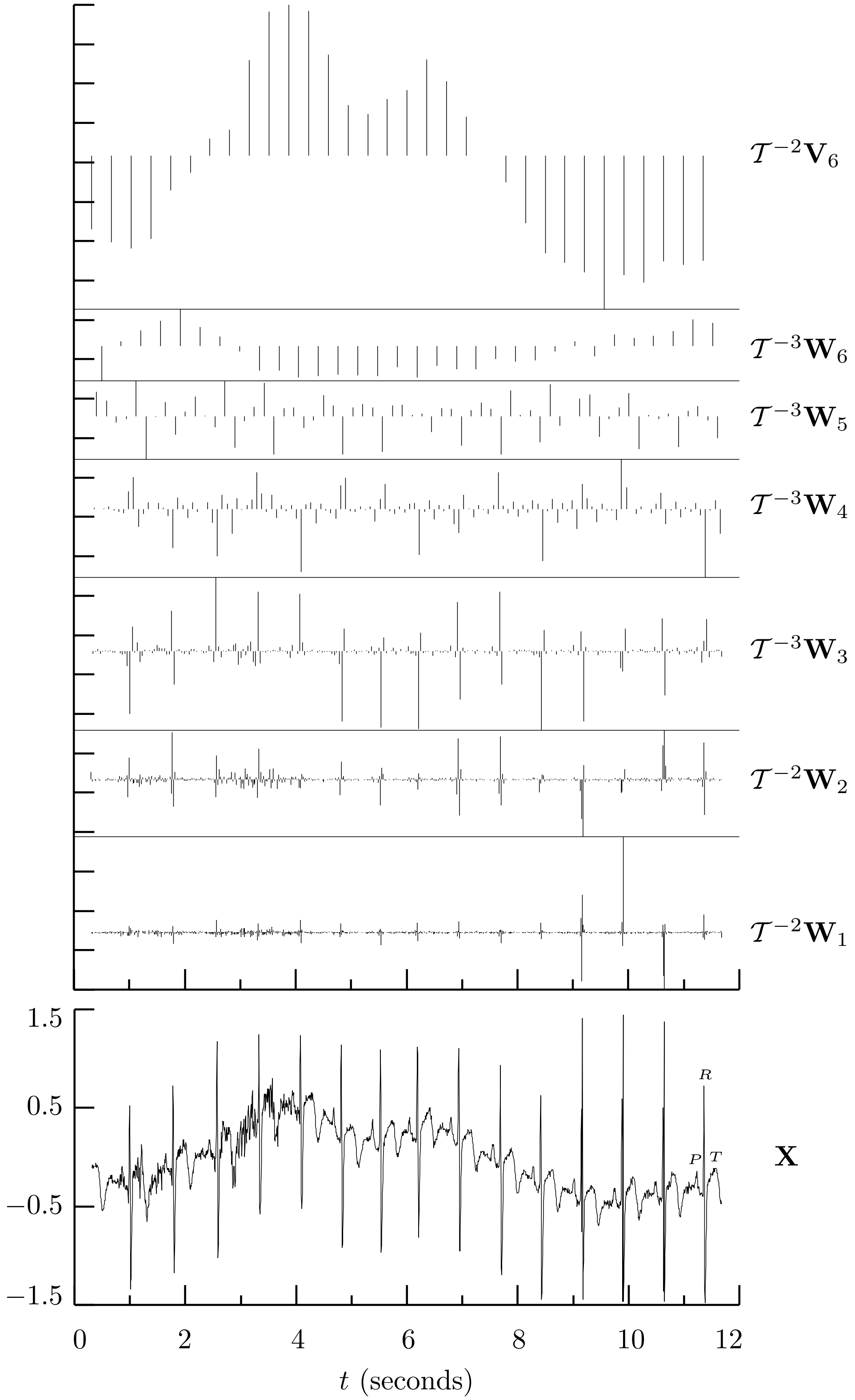

Figure 127. LA(8) DWT coefficients for ECG time series (data courtesy of Gust Bardy and Per Reinhall, University of Washington).

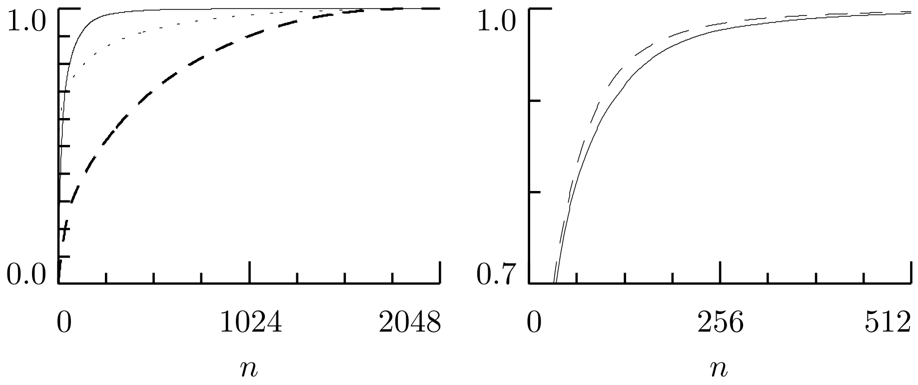

Figure 128. Normalized partial energy sequences. The left-hand plot has the NPESs for the original time series (thick dashed curve), the ODFT (dotted) and the Haar DWT (solid). The right-hand plot shows portions of the NPESs for the Haar DWT (solid curve again) and the D(4) DWT (thin dashed). The NPESs for the C(6) and LA(8) DWTs are virtually identical to the D(4) NPES.

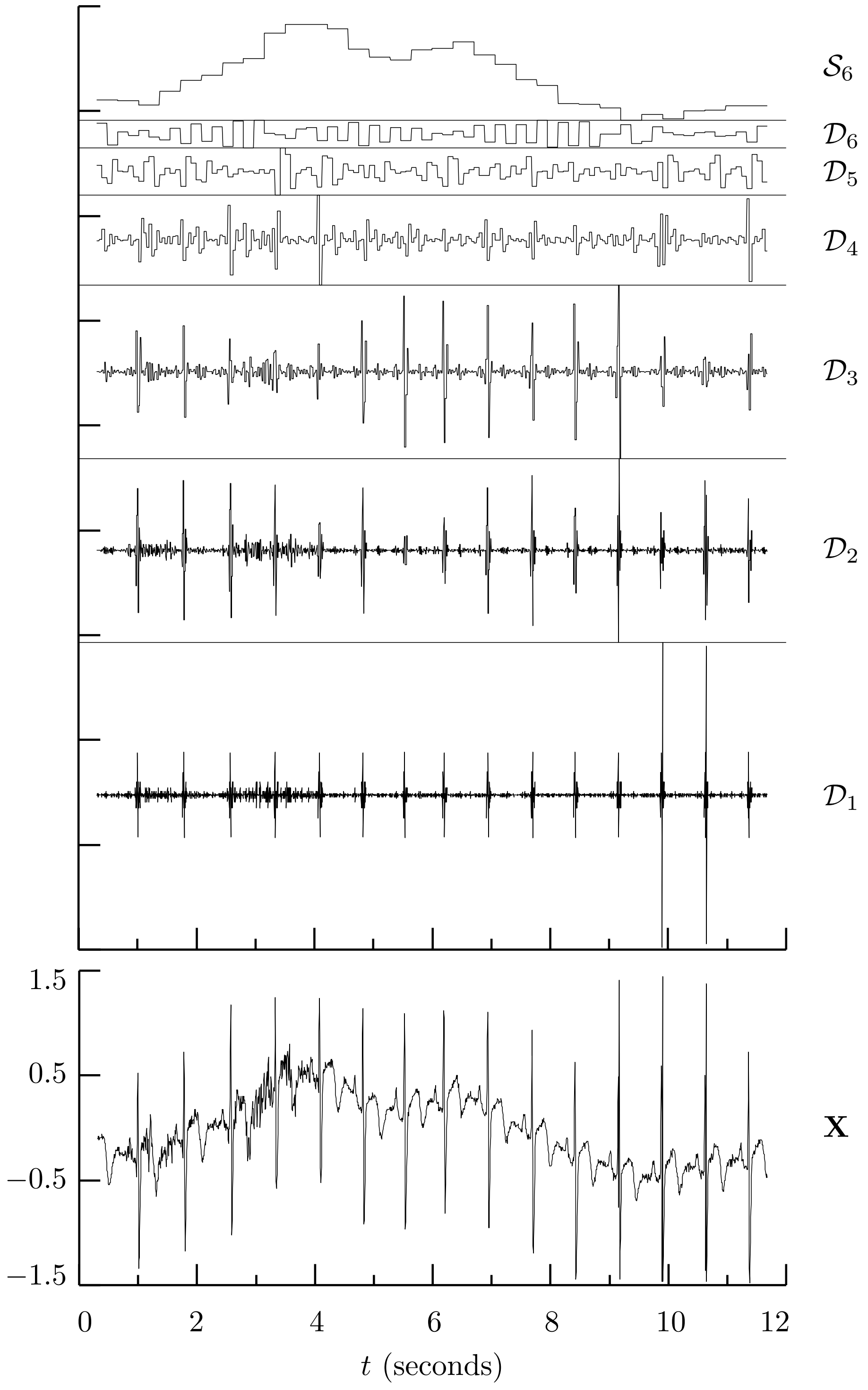

Figure 130. Haar DWT multiresolution analysis of ECG time series (see text for details).

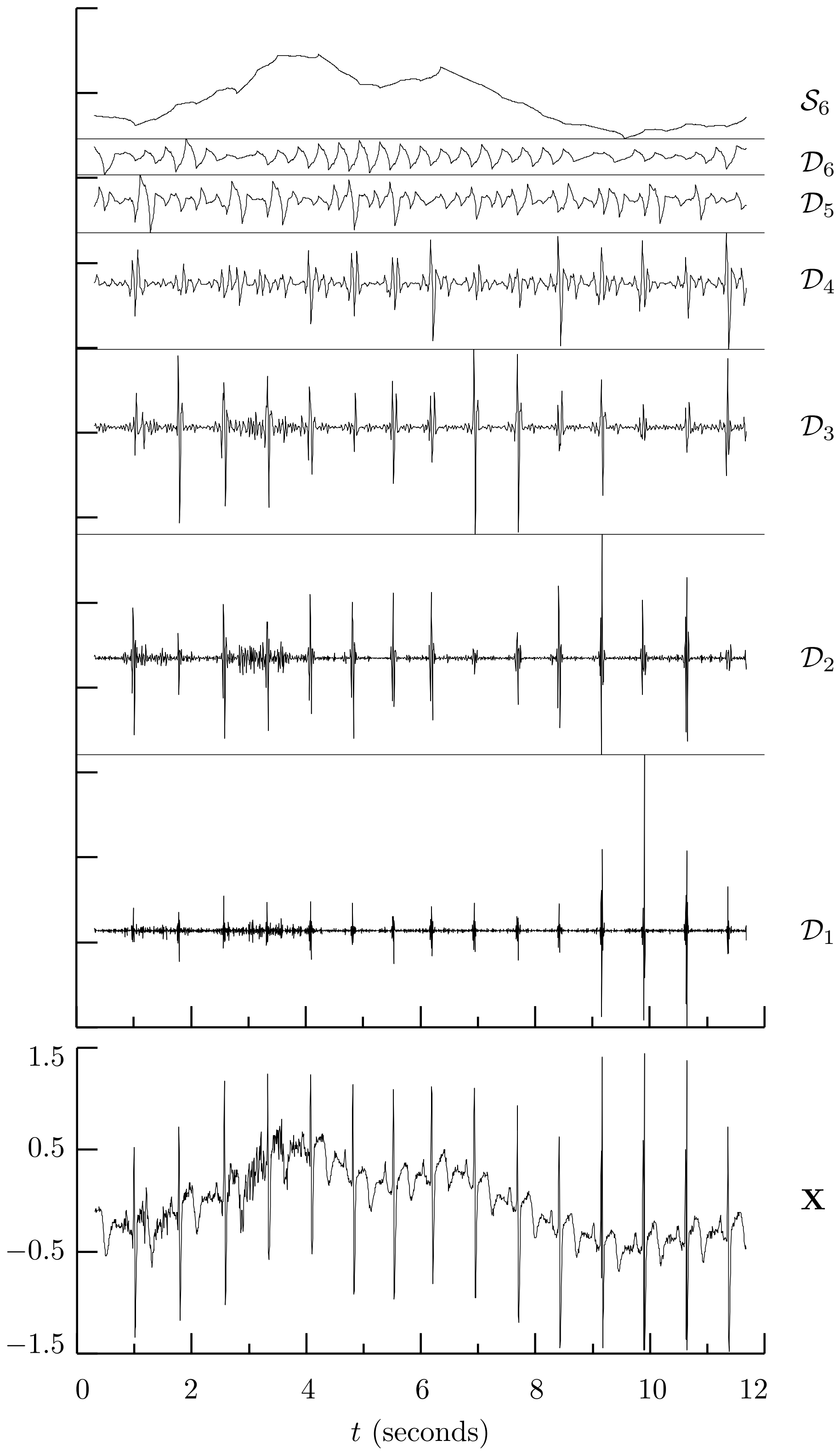

Figure 131. D(4) DWT multiresolution analysis of ECG time series (see text for details).

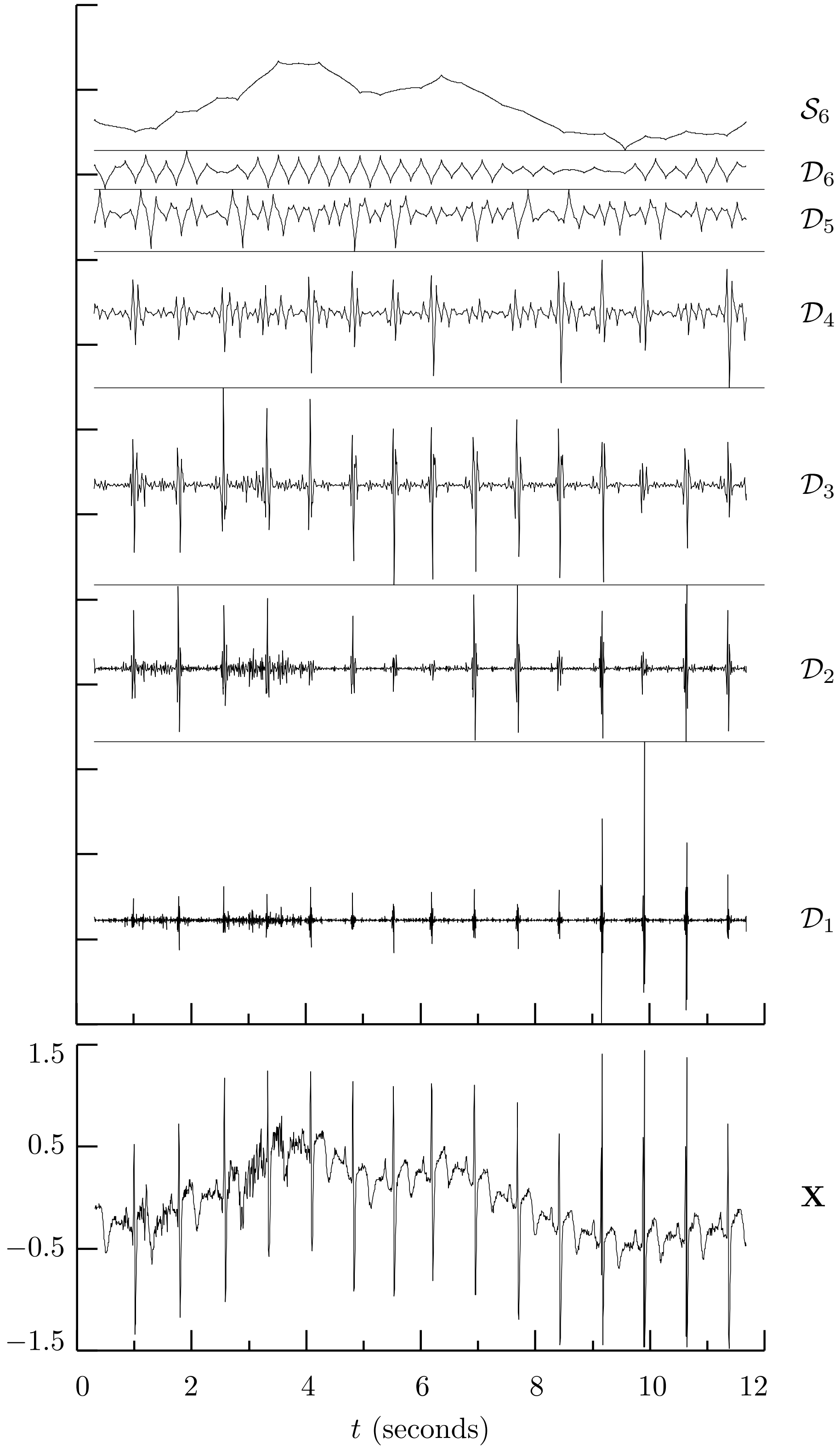

Figure 132. C(6) DWT multiresolution analysis of ECG time series (see text for details).

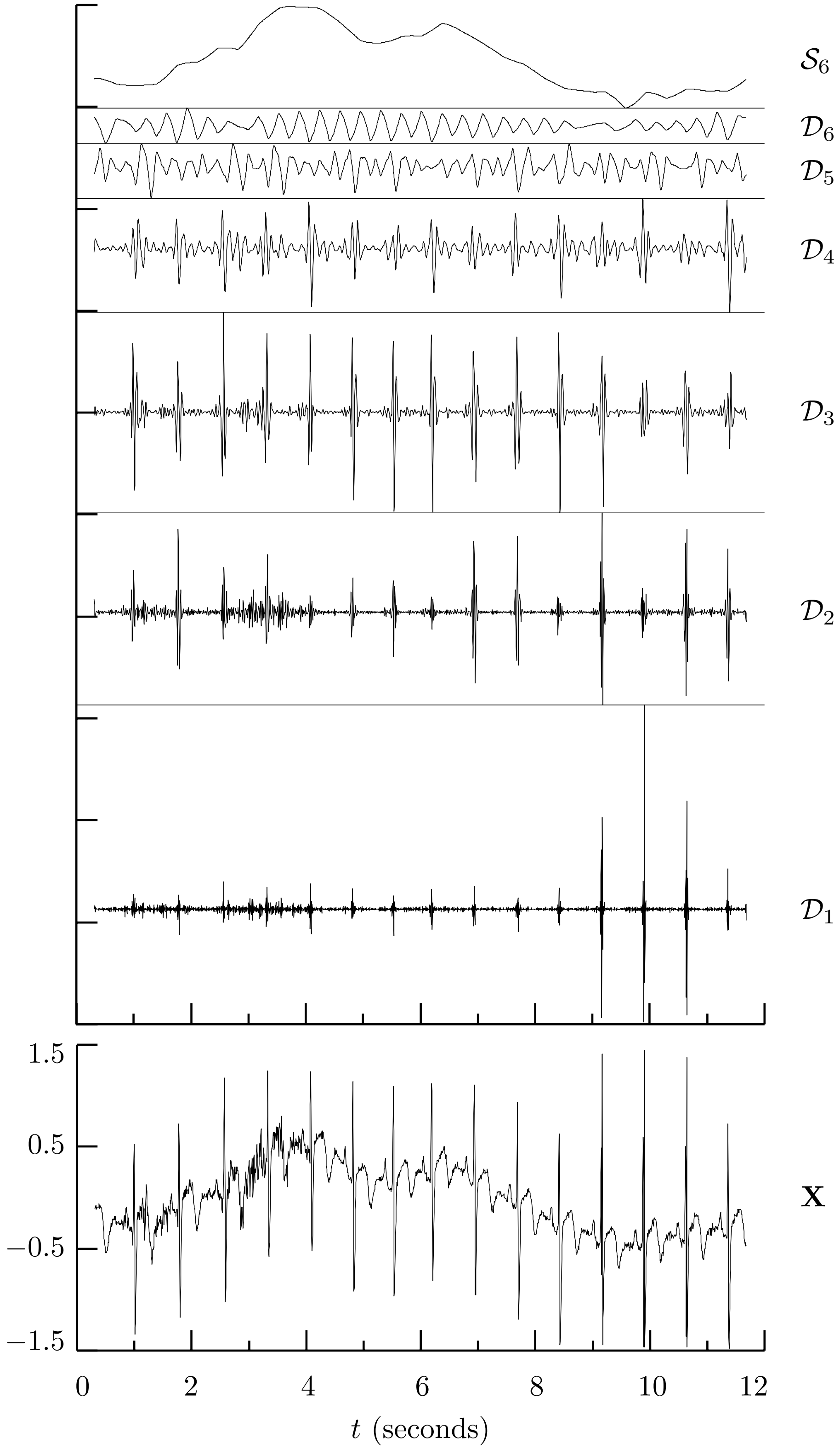

Figure 133. LA(8) DWT multiresolution analysis of ECG time series (see text for details).

L	L'_1	L'_2	L'_3	L'_4	$L'_{j\geq 5}$
2	0	0	0	0	0
4	1	2	2	2	2
6	2	3	4	4	4
8	3	5	6	6	6
10	4	6	7	8	8
12	5	8	9	10	10
14	6	9	11	12	12
16	7	11	13	14	14
18	8	12	14	15	16
20	9	14	16	17	18

Table 136. Number L'_j of boundary coefficients in $\mathbf{W}_j$ or $\mathbf{V}_j$ based on a wavelet filter of width L (here we assume $L'_j \leq N_j$, where $N_j = N/2^j$ is length of $\mathbf{W}_j$ or $\mathbf{V}_j$). The boundary coefficients are those that are influenced by boundary conditions at least to some degree.

L	$\bar{\gamma}_1^{(H)}, \gamma_1^{(H)}$	$\bar{\gamma}_2^{(H)}, \gamma_2^{(H)}$	$\bar{\gamma}_3^{(H)}, \gamma_3^{(H)}$	$\bar{\gamma}_4^{(H)}, \gamma_4^{(H)}$	$\bar{\gamma}_{j\geq 5}^{(H)}, \gamma_{j\geq 5}^{(H)}$
8	1,2	3,2	3,3	3,3	3,3
10	2,2	3,3	4,3	4,4	4,4
12	2,3	4,4	5,4	5,5	5,5
14	2,4	4,5	6,5	6,6	6,6
16	3,4	6,5	7,6	7,7	7,7
18	4,4	6,6	7,7	8,7	8,8
20	4,5	7,7	8,8	9,8	9,9

Table 137a. Number of LA boundary wavelet coefficients at the beginning and the end of $\mathcal{T}^{-\gamma_j^{(H)}}\mathbf{W}_j$ (assuming $L'_j \leq N_j$). The number at the beginning is given by $\bar{\gamma}_j^{(H)}$, and the number at the end, by $\gamma_j^{(H)}$. Note that $\bar{\gamma}_j^{(H)} + \gamma_j^{(H)} = L'_j$, which is the total number of boundary coefficients (see Table 136).

L	$\bar{\gamma}_1^{(G)}, \gamma_1^{(G)}$	$\bar{\gamma}_2^{(G)}, \gamma_2^{(G)}$	$\bar{\gamma}_3^{(G)}, \gamma_3^{(G)}$	$\bar{\gamma}_4^{(G)}, \gamma_4^{(G)}$	$\bar{\gamma}_{J_0\geq 5}^{(G)}, \gamma_{J_0\geq 5}^{(G)}$
8	2,1	3,2	4,2	4,2	4,2
10	2,2	3,3	3,4	4,4	4,4
12	3,2	5,3	5,4	6,4	6,4
14	4,2	6,3	7,4	8,4	8,4
16	4,3	6,5	7,6	8,6	8,6
18	4,4	6,6	7,7	7,8	8,8
20	5,4	8,6	9,7	9,8	10,8

Table 137b. As in Table 137a, but now for the LA scaling coefficients. Again we have $\bar{\gamma}_{J_0}^{(G)} + \gamma_{J_0}^{(G)} = L'_{J_0}$, where L'_{J_0} is given in Table 136.

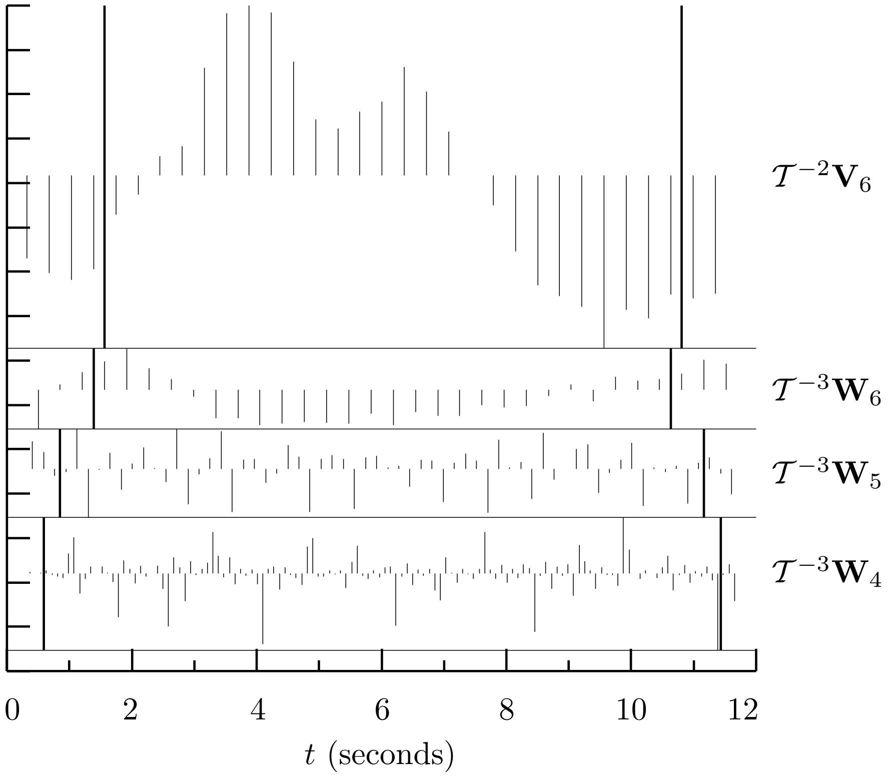

Figure 138. Four circularly advanced subvectors of the LA(8) DWT for the ECG time series (cf. Figure 127). The DWT coefficients plotted between the two thick vertical lines for a given subvector are unaffected by circularity, while those outside of the lines are the boundary coefficients. The number of plotted boundary coefficients agrees with the first rows of Tables 137a and 137b.

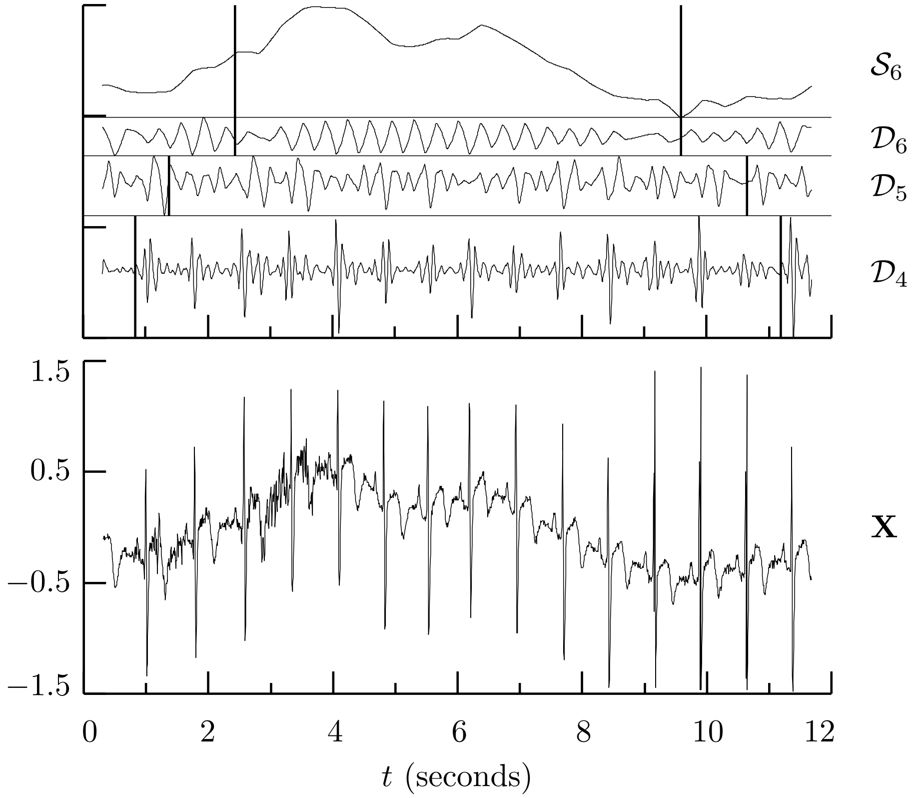

Figure 140. Portion of the LA(8) DWT multiresolution analysis for the ECG time series (the full analysis is shown in Figure 133). The thick vertical lines delineate the boundary regions in the details $\mathcal{D}_j$ and smooth $\mathcal{S}_6$ (i.e., those parts influenced to some degree by circularity).

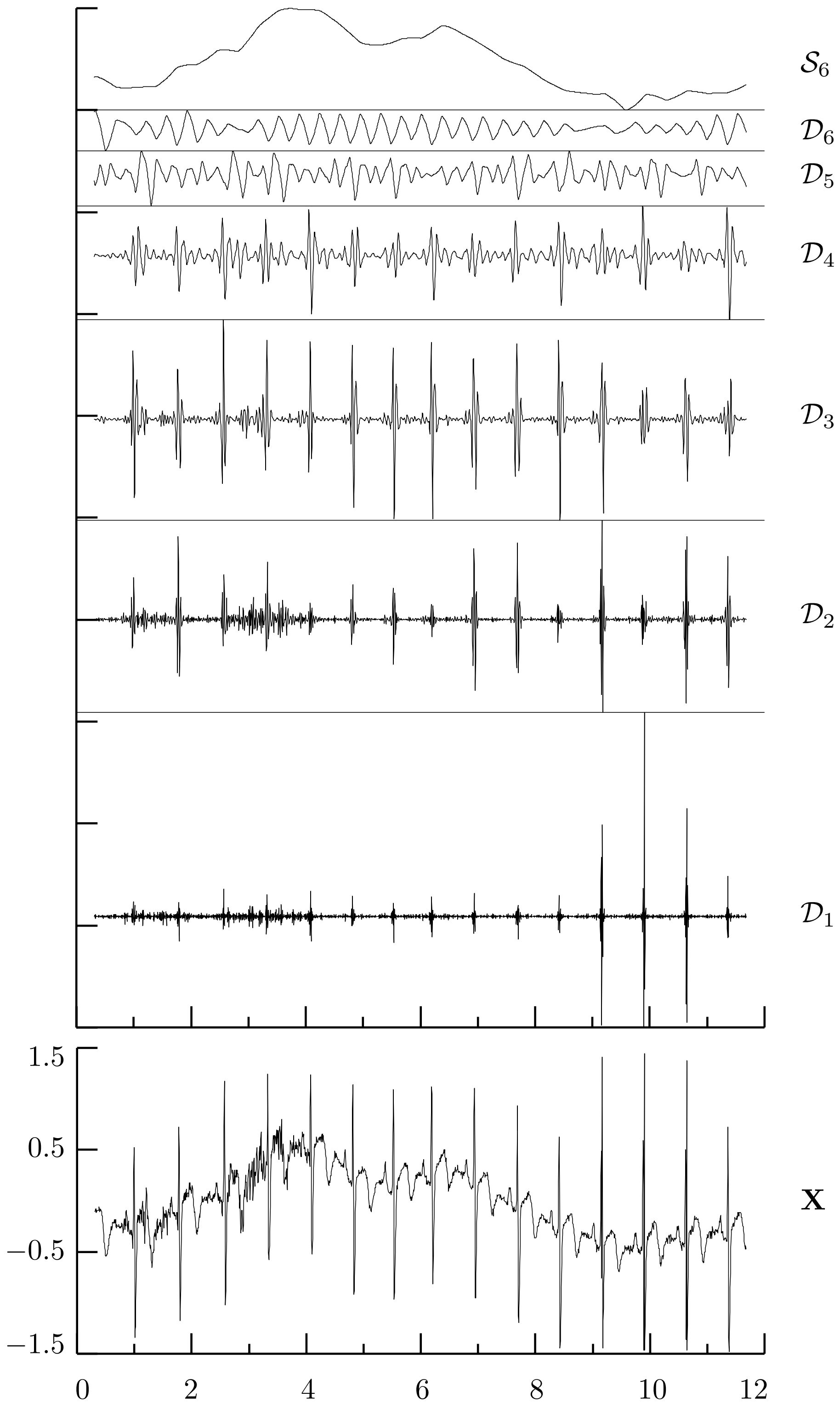

Figure 142. LA(8) DWT multiresolution analysis of ECG time series using reflection boundary conditions (cf. Figure 133).

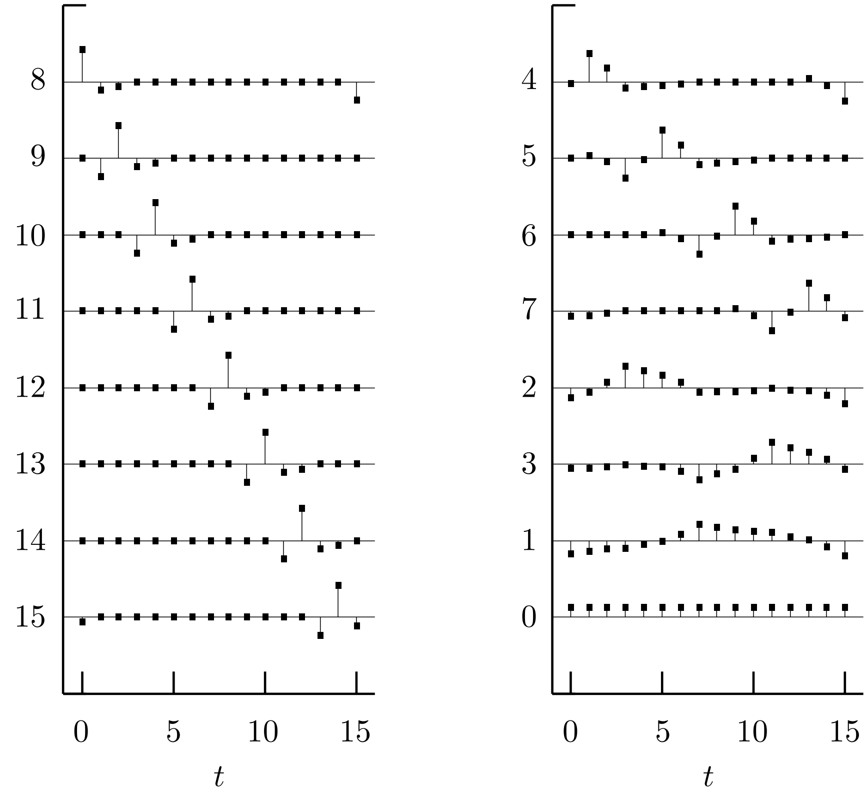

Figure 150. Row vectors of the discrete wavelet transform matrix based on the D(4) wavelet as defined in Bruce and Gao (1996a) – cf. Figure 60.

$\{h_l\} \longleftrightarrow H(\cdot)$	$\{g_l\} \longleftrightarrow G(\cdot)$
$h_l = (-1)^l g_{L-1-l}$	$g_l \equiv (-1)^{l+1} h_{L-1-l}$
$H(f) = -e^{-i2\pi f(L-1)} G(\frac{1}{2} - f)$	$G(f) = e^{-i2\pi f(L-1)} H(\frac{1}{2} - f)$
$\sum_l h_l = H(0) \equiv 0$	$\sum_l g_l = G(0) = \sqrt{2}$
$\sum_l h_l^2 \equiv 1$	$\sum_l g_l^2 = 1$
$\sum_l h_l h_{l+2n} \equiv 0, n \neq 0$	$\sum_l g_l g_{l+2n} = 0, n \neq 0$
$\sum_l g_l h_{l+2n} = 0$	
$\mathcal{H}(f) \equiv \lvert H(f) \rvert^2$	$\mathcal{G}(f) \equiv \lvert G(f) \rvert^2$
$\mathcal{H}(f) + \mathcal{H}(f + \frac{1}{2}) = 2$	$\mathcal{G}(f) + \mathcal{G}(f + \frac{1}{2}) = 2$
$\mathcal{G}(f) + \mathcal{H}(f) = 2$	
$W_{1,t} \equiv \sum_l h_l X_{2t+1-l \bmod N}$	$V_{1,t} \equiv \sum_l g_l X_{2t+1-l \bmod N}$
$W_{j,t} \equiv \sum_l h_l V_{j-1,2t+1-l \bmod N_{j-1}}$	$V_{j,t} \equiv \sum_l g_l V_{j-1,2t+1-l \bmod N_{j-1}}$
$h_{1,l} \equiv h_l, \;\; H_1(f) \equiv H(f)$	$g_{1,l} \equiv g_l, \;\; G_1(f) \equiv G(f)$
$H_j(f) \equiv H(2^{j-1} f) \prod_{l=0}^{j-2} G(2^l f)$	$G_j(f) \equiv \prod_{l=0}^{j-1} G(2^l f)$
$H_j(f) = H(2^{j-1} f) G_{j-1}(f)$	$G_j(f) = G(2^{j-1} f) G_{j-1}(f)$
$\{h_{j,l}\} \longleftrightarrow H_j(\cdot)$	$\{g_{j,l}\} \longleftrightarrow G_j(\cdot)$
$\sum_l h_{j,l} = H_j(0) = 0$	$\sum_l g_{j,l} = G_j(0) = 2^{j/2}$
$\sum_l h_{j,l}^2 = 1$	$\sum_l g_{j,l}^2 = 1$
$\sum_l h_{j,l} h_{j,l+2^j n} = 0, n \neq 0$	$\sum_l g_{j,l} g_{j,l+2^j n} = 0, n \neq 0$
$\sum_l g_{j,l} h_{j,l+2^j n} = 0$	
$\mathcal{H}_j(f) \equiv \lvert H_j(f) \rvert^2$	$\mathcal{G}_j(f) \equiv \lvert G_j(f) \rvert^2$
$W_{j,t} = \sum_l h_{j,l} X_{2^j(t+1)-1-l \bmod N}$	$V_{j,t} = \sum_l g_{j,l} X_{2^j(t+1)-1-l \bmod N}$

Table 154. Key relationships involving wavelet and scaling filters. Because $h_l = g_l = 0$ for all $l < 0$ and $l \geq L$, summations involving h_l or g_l can be taken to range from either $l = 0$ to $l = L - 1$ or over all integers; likewise, summations involving $h_{j,l}$ or $g_{j,l}$ can range either from $l = 0$ to $l = L_j - 1$ or over all integers (recall that $L_j \equiv (2^j - 1)(L - 1) + 1$ and that $N_j \equiv N/2^j$).

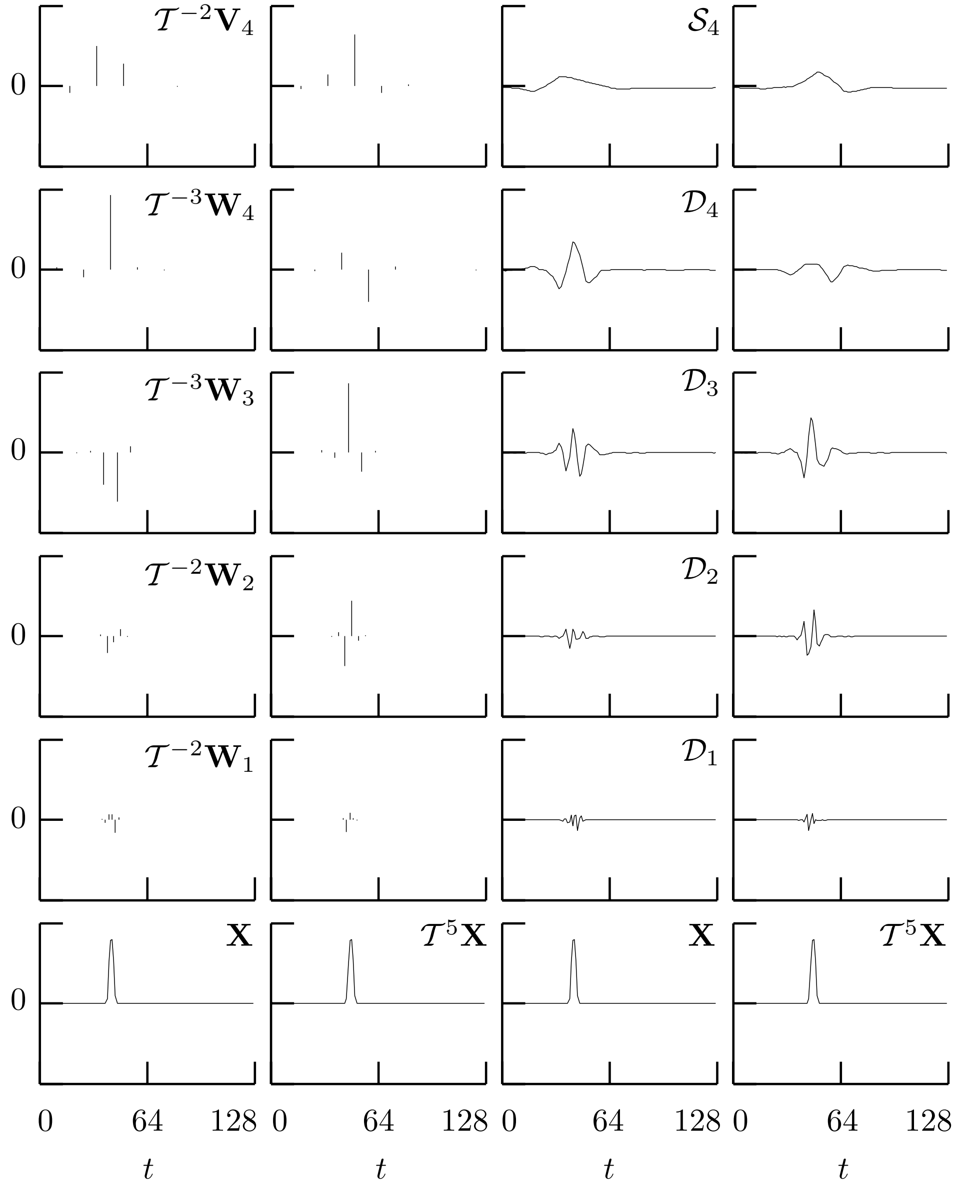

Figure 161. LA(8) DWTs of level $J_0 = 4$ (top five rows, first two columns) and corresponding multiresolution analyses (last two columns) for a time series $\mathbf{X}$ and its circularly shift $\mathcal{T}^5\mathbf{X}$ (bottom row of plots). A comparison of the first and second columns shows that circularly shifting a time series can yield substantial changes in its DWT; likewise, the third and fourth columns indicate the same is true for the corresponding MRAs. This figure should be compared with Figure 181, which uses the MODWT in place of the DWT.

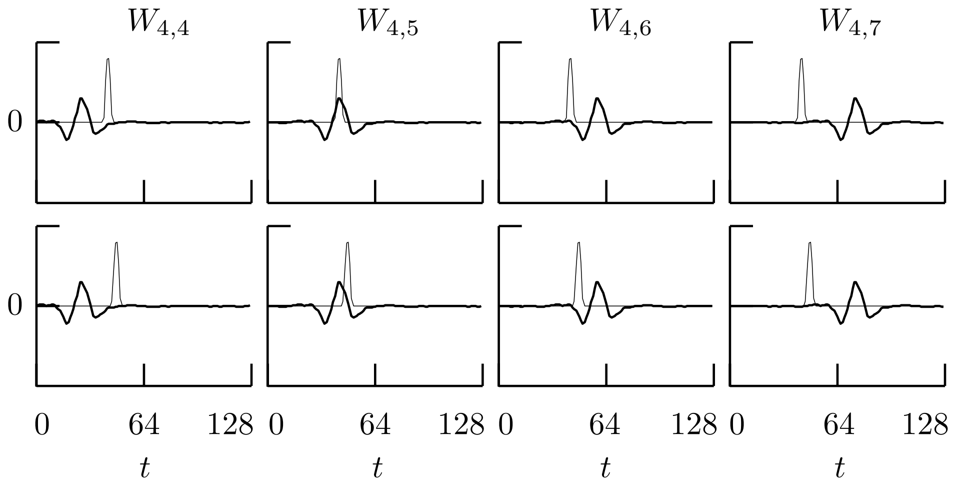

Figure 162. Level $J_0 = 4$ basis vectors used in the LA(8) DWT to produce the wavelet coefficients $W_{4,j}$, $j = 4, \ldots, 7$ (thick curves, respectively, from left to right in both rows of plots), along with a 'bump' time series $\mathbf{X}$ (thin curves in top row of plots) and $\mathcal{T}^5\mathbf{X}$ (thin curves, bottom row). The inner product between a plotted basis vector and a time series yields the wavelet coefficient labeled at the top of the figure.

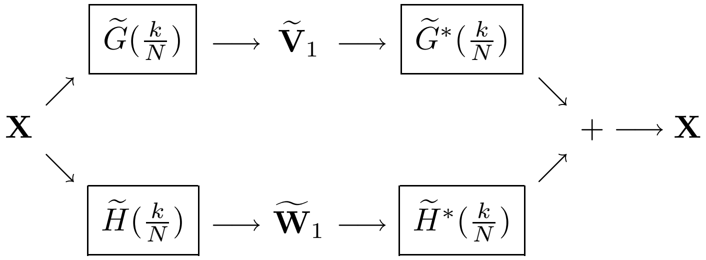

Figure 169. Flow diagram illustrating analysis of $\mathbf{X}$ into the MODWT wavelet and scaling coefficients $\widetilde{\mathbf{W}}_1$ and $\widetilde{\mathbf{V}}_1$ of first level, followed by the synthesis of $\mathbf{X}$ from $\widetilde{\mathbf{W}}_1$ and $\widetilde{\mathbf{V}}_1$.

$$\begin{tikzcd}
 & \boxed{\widetilde{G}(2^{j-1}\frac{k}{N})} \arrow[r] & \widetilde{\mathbf{V}}_j \arrow[r] & \boxed{\widetilde{G}^*(2^{j-1}\frac{k}{N})} \arrow[dr] & & \\
\widetilde{\mathbf{V}}_{j-1} \arrow[ur] \arrow[dr] & & & & + \arrow[r] & \widetilde{\mathbf{V}}_{j-1} \\
 & \boxed{\widetilde{H}(2^{j-1}\frac{k}{N})} \arrow[r] & \widetilde{\mathbf{W}}_j \arrow[r] & \boxed{\widetilde{H}^*(2^{j-1}\frac{k}{N})} \arrow[ur] & &
\end{tikzcd}$$

Figure 175. Flow diagram illustrating analysis of $\widetilde{\mathbf{V}}_{j-1}$ into $\widetilde{\mathbf{W}}_j$ and $\widetilde{\mathbf{V}}_j$, followed by the synthesis of $\widetilde{\mathbf{V}}_{j-1}$ from $\widetilde{\mathbf{W}}_j$ and $\widetilde{\mathbf{V}}_j$.

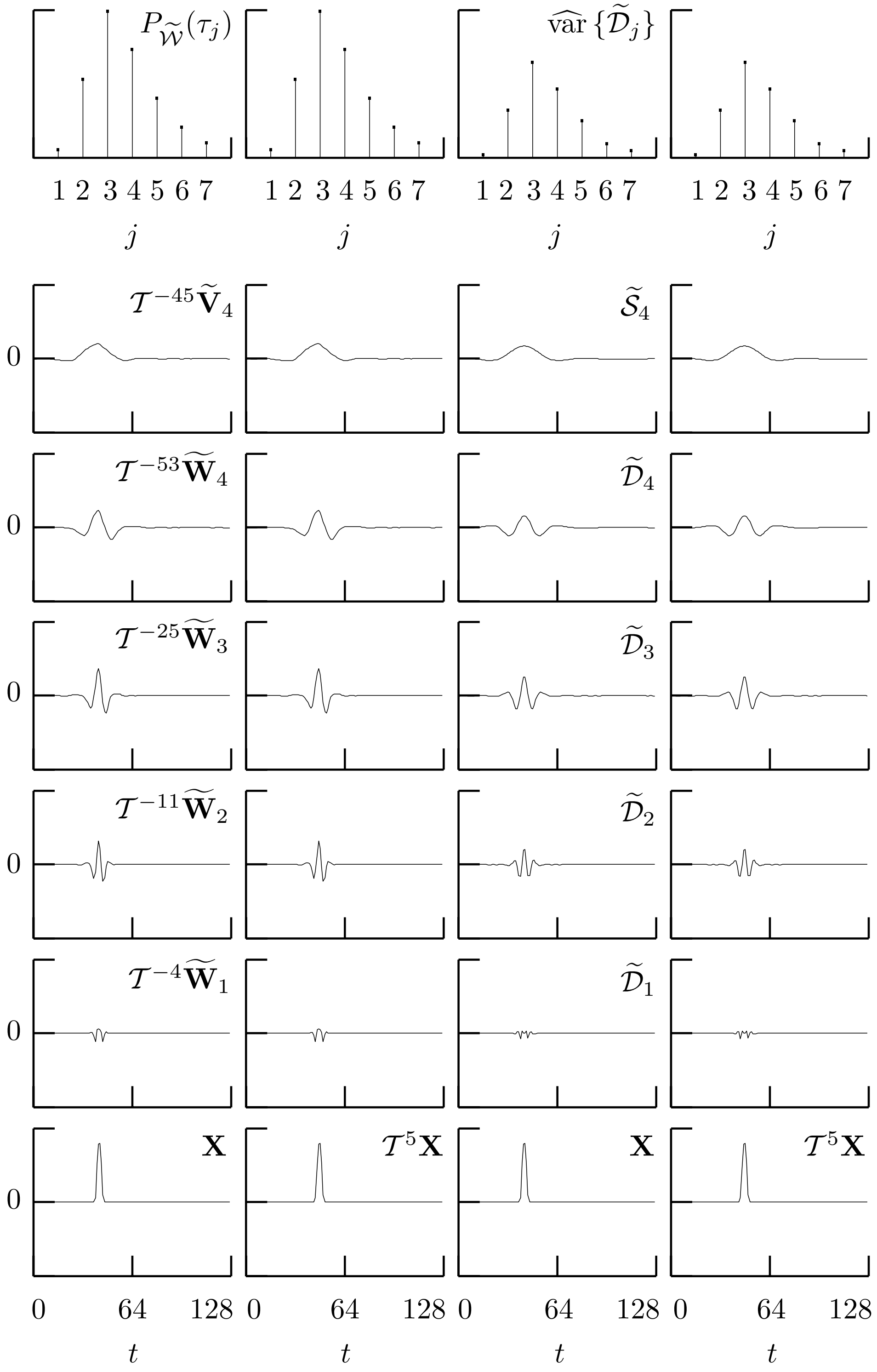

Figure 181. Bottom six rows as in Figure 161, with MODWT replacing DWT. The top row shows the discrete wavelet empirical power spectra (first two columns) and a corresponding quantity based upon level $j = 1, \ldots, 7$ MODWT details (last two columns) – see text for details.

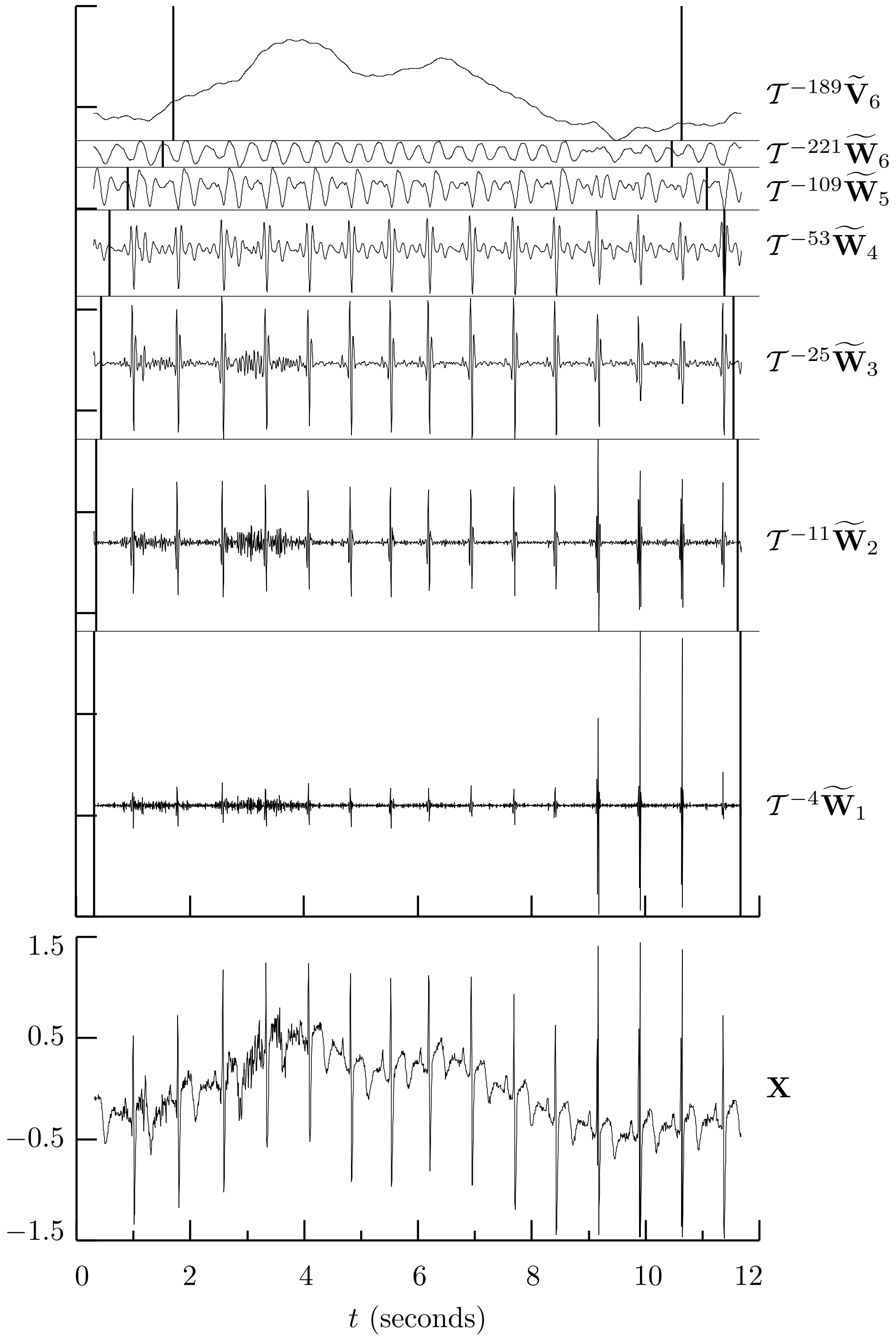

Figure 183. MODWT wavelet analysis of ECG time series using LA(8) wavelet. The above should be compared to Figure 127 for the corresponding DWT analysis (see text for details).

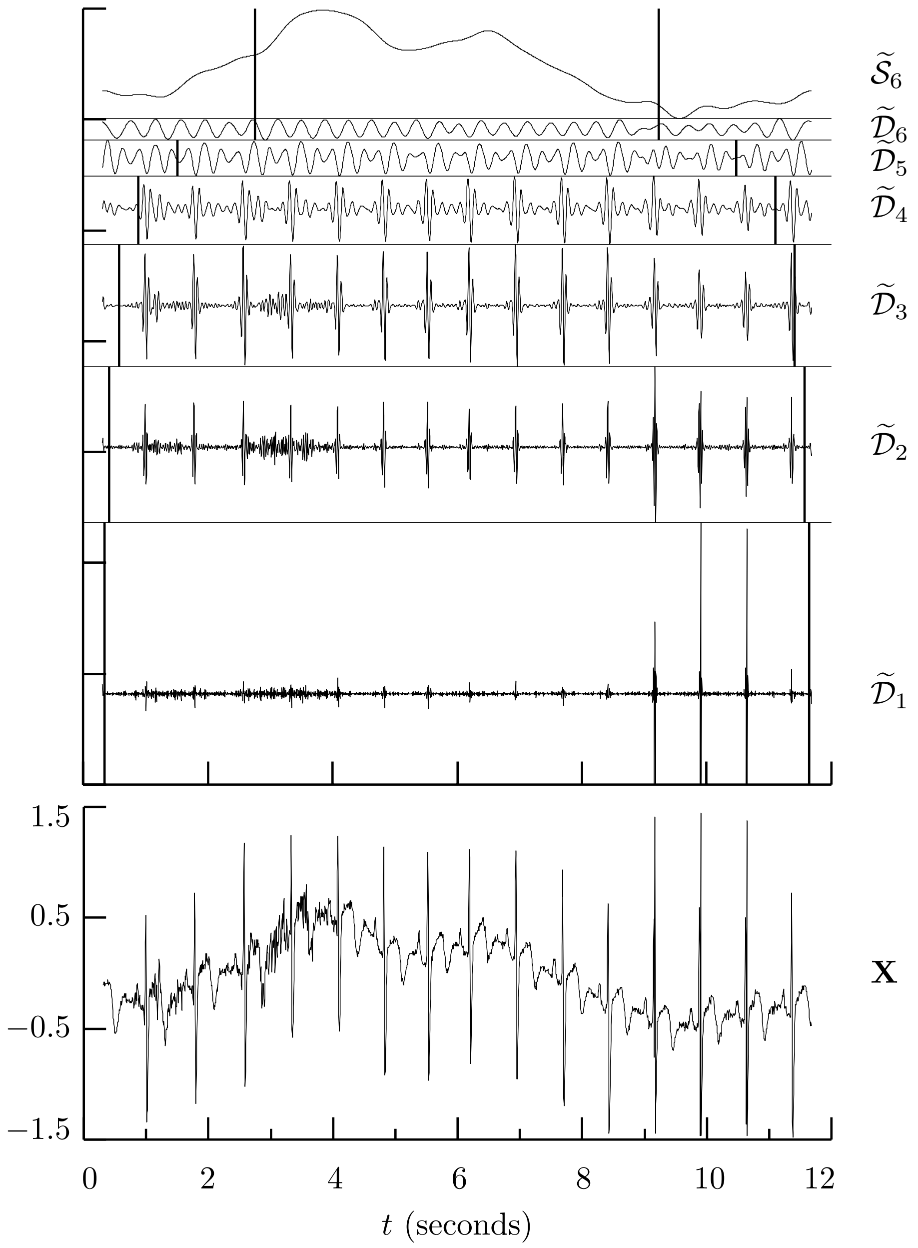

Figure 184. MODWT multiresolution analysis of ECG time series using LA(8) wavelet (see text for details). Figure 133 shows the corresponding DWT analysis.

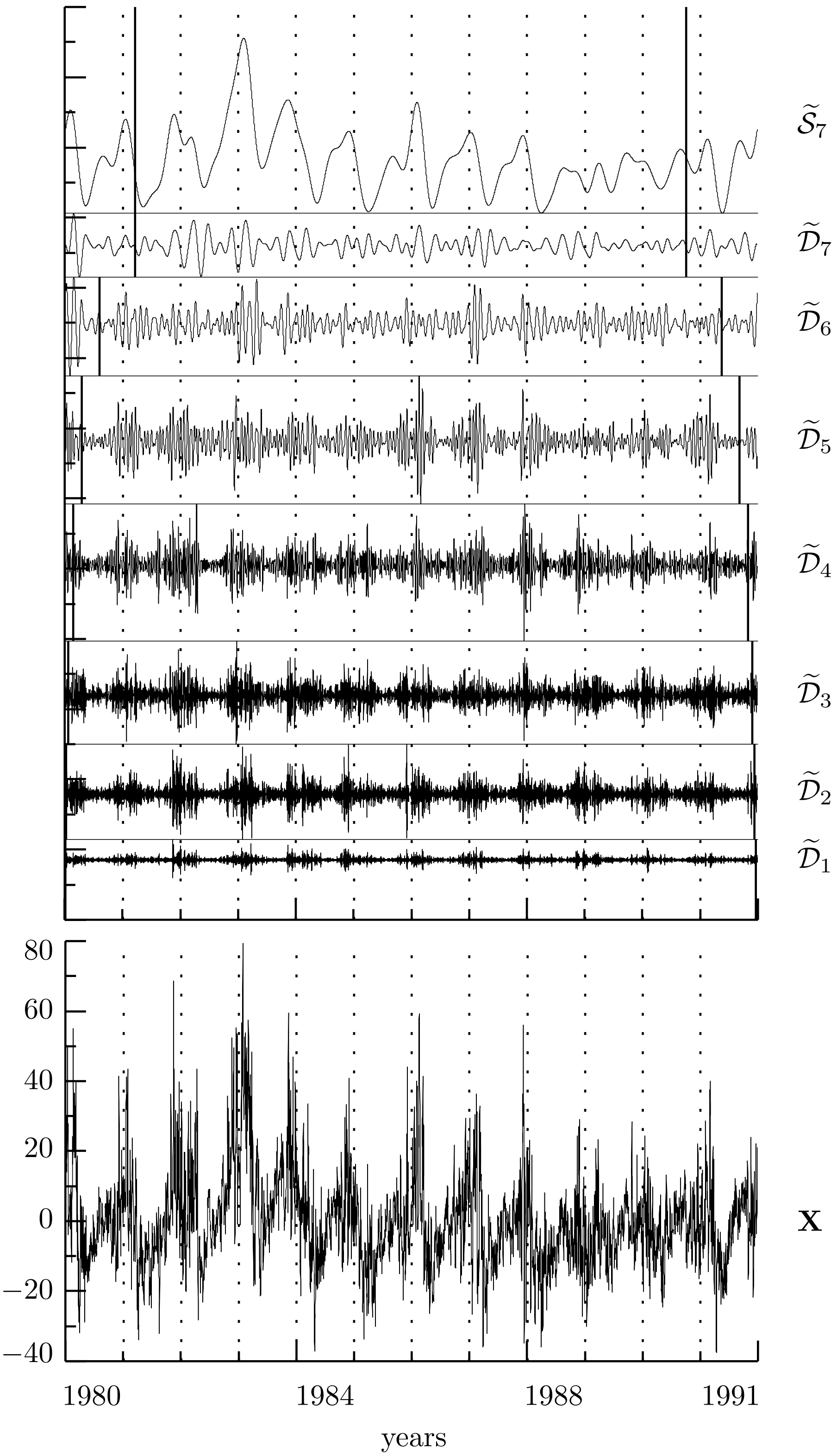

Figure 186. LA(8) MODWT multiresolution analysis for Crescent City subtidal variations (see text for details). This series is measured in centimeters.

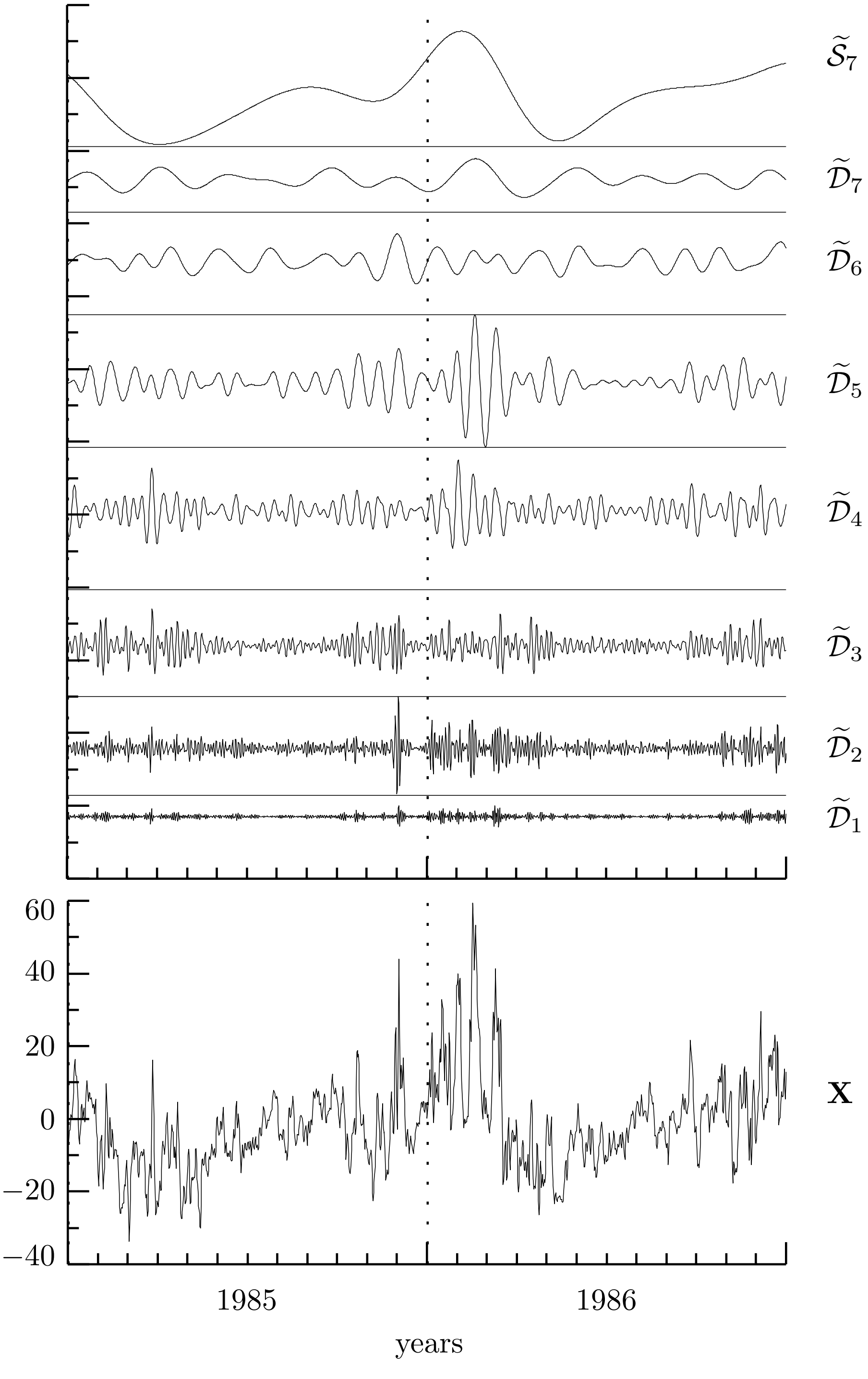

Figure 187. Expanded view of 1985 and 1986 portion of Figure 186.

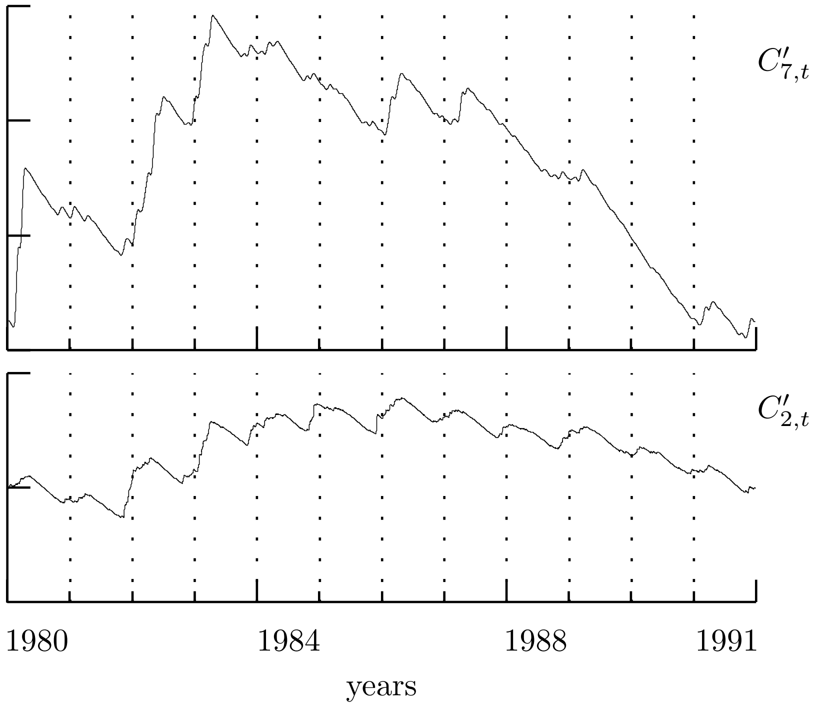

Figure 190. Rotated cumulative variance plots for subtidal sea level variations at physical scales $\tau_2\,\Delta t = 1$ day (bottom plot) and $\tau_7\,\Delta t = 32$ days (top).

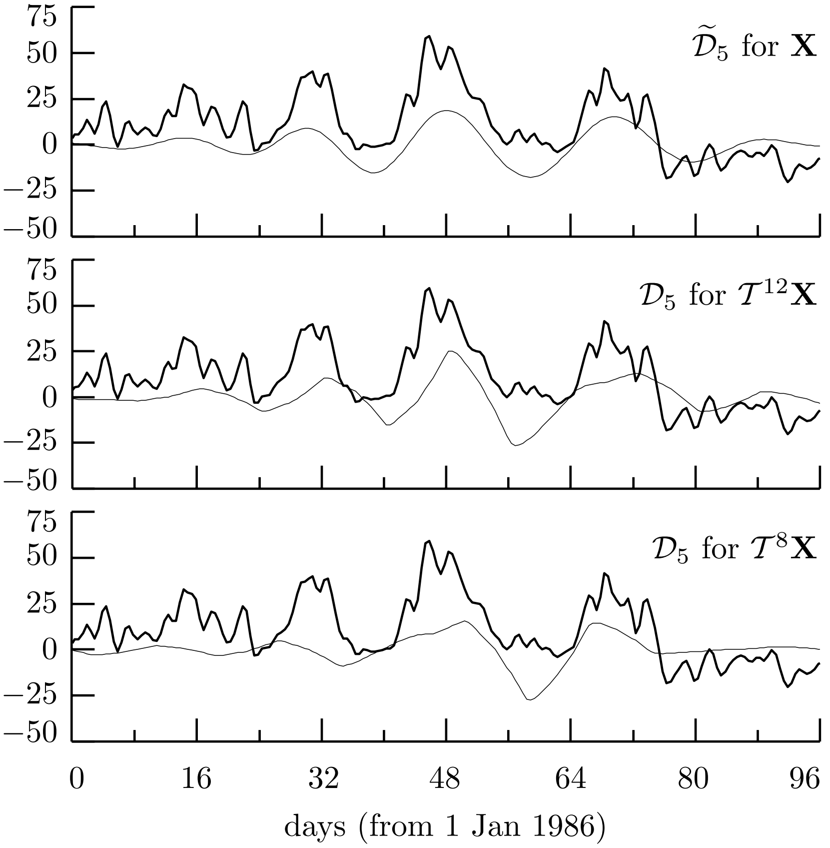

Figure 191. Demonstration of zero phase property of MODWT details. The thick curve in each plot is a 96 day portion of the Crescent City series starting at the beginning of 1986. The thin curves (from top to bottom) are the LA(8) MODWT detail $\widetilde{\mathcal{D}}_5$ for the original time series $\mathbf{X}$, the LA(8) DWT detail $\mathcal{D}_5$ for $\mathcal{T}^{12}\mathbf{X}$ (the time series delayed 12 data values) and the LA(8) DWT detail $\mathcal{D}_5$ for $\mathcal{T}^{8}\mathbf{X}$ (the time series delayed 8 data values). The physical scale associated with these details is $\tau_5\,\Delta t = 8$ days; i.e., the details should be associated with changes of averages on a scale of 8 days (this is the distance between minor tick marks on the horizontal axis).

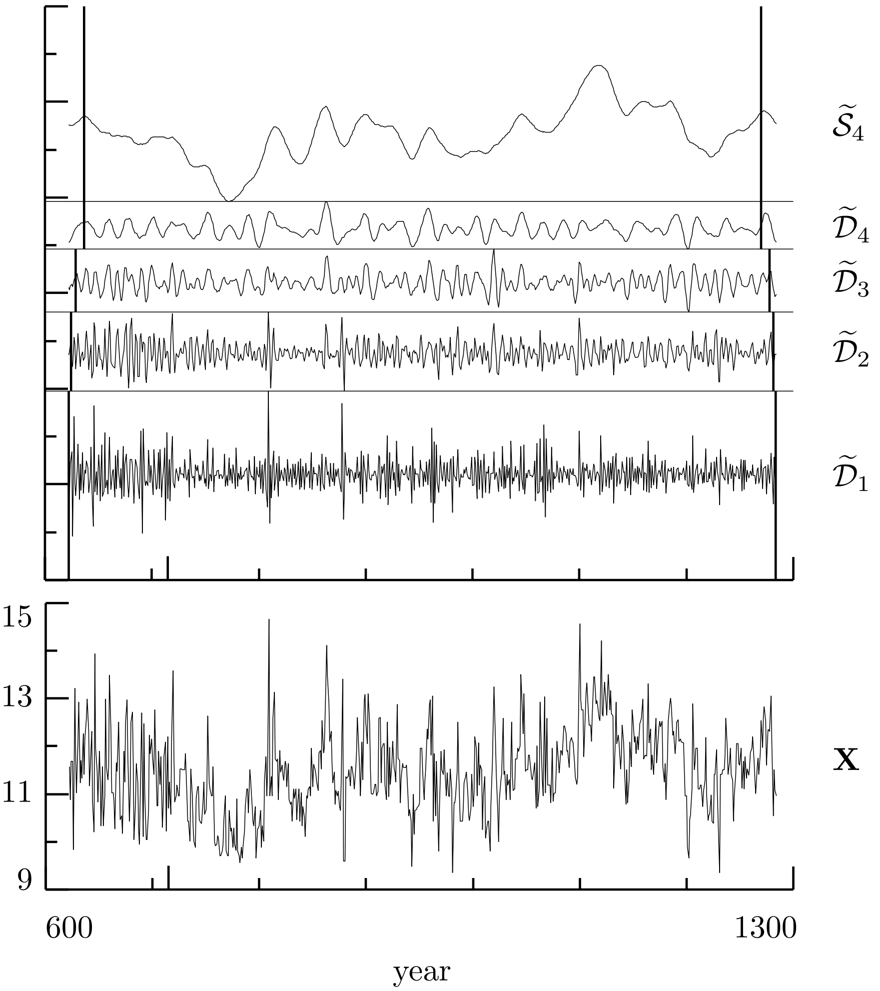

Figure 192. Level $J_0 = 4$ MODWT multiresolution analysis of Nile River minima (in meters) using the Haar wavelet filter.

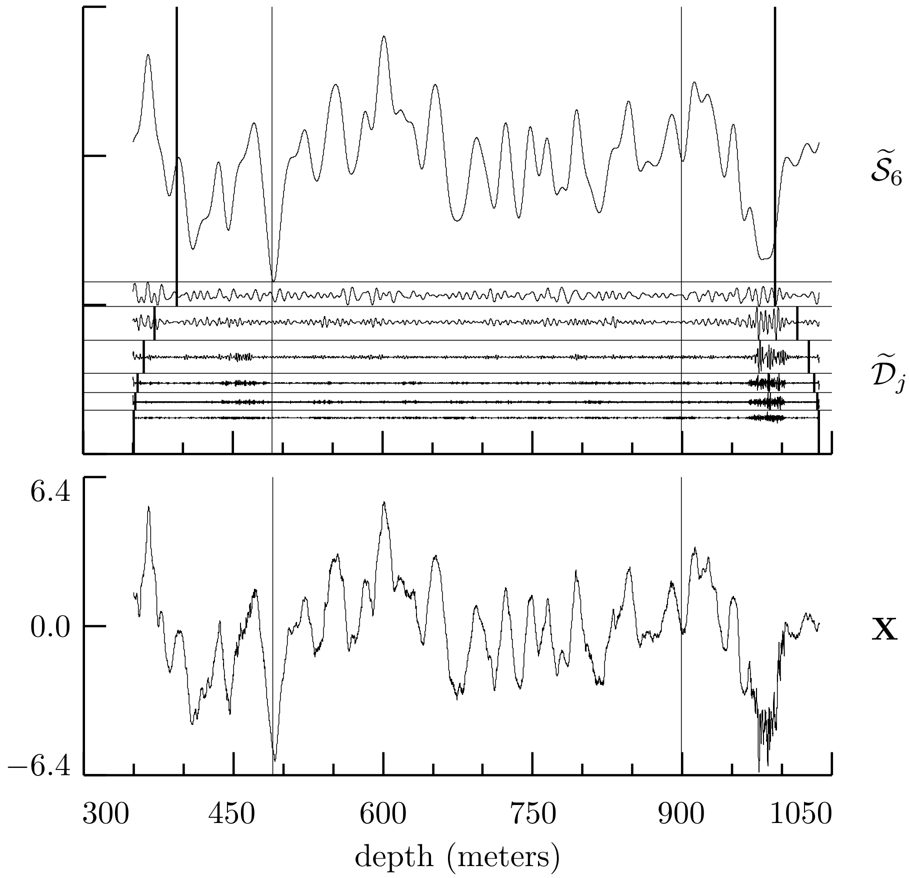

Figure 194. Level $J_0 = 6$ MODWT multiresolution analysis using LA(8) wavelet of vertical shear measurements (in inverse seconds) versus depth (in meters). This series was collected and supplied by Mike Gregg, Applied Physics Laboratory, University of Washington.

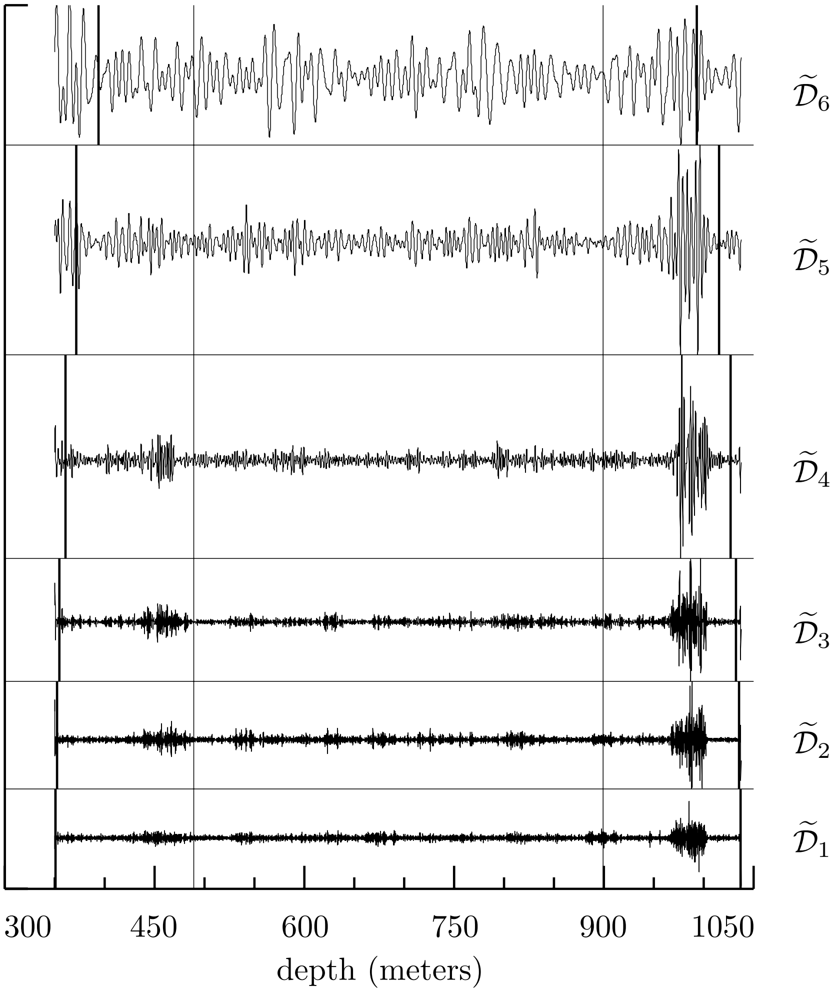

Figure 195. Expanded view of details series in MRA shown in Figure 194.

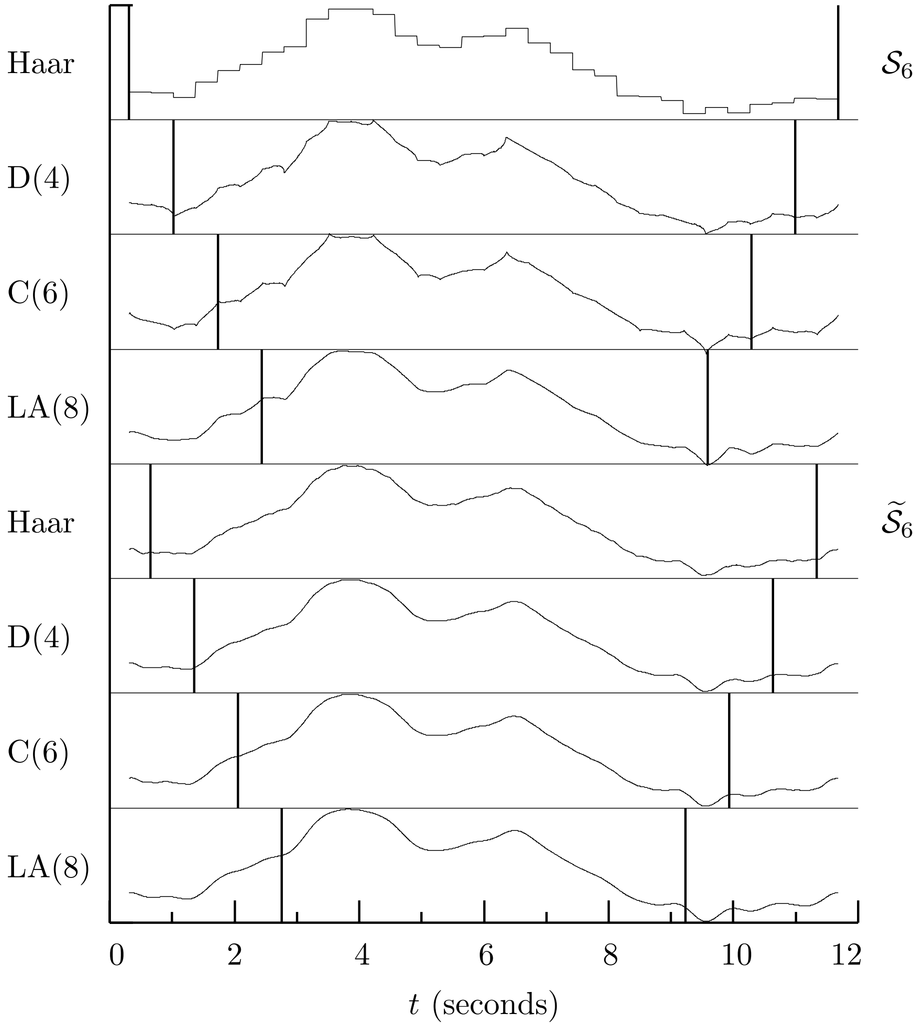

Figure 196. Comparison of DWT smooths $\mathcal{S}_6$ (top four series) and MODWT smooths $\widetilde{\mathcal{S}}_6$ (bottom four) for the ECG time series using, from top to bottom within each group, the Haar, D(4), C(6) and LA(8) wavelet filters. The thick vertical lines mark the boundary regions of the smooths, i.e., the parts of the smooths that are influenced (at least to some degree) by the assumption of circularity.

$\tilde{h}_l \equiv h_l/\sqrt{2}$	$\tilde{g}_l \equiv g_l/\sqrt{2}$
$\{\tilde{h}_l\} \longleftrightarrow \widetilde{H}(\cdot) = \frac{1}{\sqrt{2}}H(\cdot)$	$\{\tilde{g}_l\} \longleftrightarrow \widetilde{G}(\cdot) = \frac{1}{\sqrt{2}}G(\cdot)$
$\tilde{h}_l = (-1)^l \tilde{g}_{L-1-l}$	$\tilde{g}_l \equiv (-1)^{l+1}\tilde{h}_{L-1-l}$
$\widetilde{H}(f) = -e^{-i2\pi f(L-1)}\widetilde{G}(\frac{1}{2}-f)$	$\widetilde{G}(f) = e^{-i2\pi f(L-1)}\widetilde{H}(\frac{1}{2}-f)$
$\sum_l \tilde{h}_l = \widetilde{H}(0) \equiv 0$	$\sum_l \tilde{g}_l = \widetilde{G}(0) = 1$
$\sum_l \tilde{h}_l^2 \equiv \frac{1}{2}$	$\sum_l \tilde{g}_l^2 = \frac{1}{2}$
$\sum_l \tilde{h}_l\tilde{h}_{l+2n} \equiv 0, n \neq 0$	$\sum_l \tilde{g}_l\tilde{g}_{l+2n} = 0, n \neq 0$
$\sum_l \tilde{g}_l\tilde{h}_{l+2n} = 0$	
$\widetilde{\mathcal{H}}(f) \equiv \lvert\widetilde{H}(f)\rvert^2 = \frac{1}{2}\mathcal{H}(f)$	$\widetilde{\mathcal{G}}(f) \equiv \lvert\widetilde{G}(f)\rvert^2 = \frac{1}{2}\mathcal{G}(f)$
$\widetilde{\mathcal{H}}(f) + \widetilde{\mathcal{H}}(f+\frac{1}{2}) = 1$	$\widetilde{\mathcal{G}}(f) + \widetilde{\mathcal{G}}(f+\frac{1}{2}) = 1$
$\widetilde{\mathcal{G}}(f) + \widetilde{\mathcal{H}}(f) = 1$	
$\widetilde{W}_{1,t} \equiv \sum_l \tilde{h}_l X_{t-l \bmod N}$	$\widetilde{V}_{1,t} \equiv \sum_l \tilde{g}_l X_{t-l \bmod N}$
$\widetilde{W}_{j,t} = \sum_l \tilde{h}_l \widetilde{V}_{j-1,t-2^{j-1}l \bmod N}$	$\widetilde{V}_{j,t} = \sum_l \tilde{g}_l \widetilde{V}_{j-1,t-2^{j-1}l \bmod N}$
$\tilde{h}_{1,l} \equiv \tilde{h}_l,\ \ \widetilde{H}_1(f) \equiv \widetilde{H}(f)$	$\tilde{g}_{1,l} \equiv \tilde{g}_l,\ \ \widetilde{G}_1(f) \equiv \widetilde{G}(f)$
$\widetilde{H}_j(f) \equiv \widetilde{H}(2^{j-1}f)\prod_{l=0}^{j-2}\widetilde{G}(2^l f)$	$\widetilde{G}_j(f) \equiv \prod_{l=0}^{j-1}\widetilde{G}(2^l f)$
$\widetilde{H}_j(f) = \frac{1}{2^{j/2}}H_j(f)$	$\widetilde{G}_j(f) = \frac{1}{2^{j/2}}G_j(f)$
$\widetilde{H}_j(f) = \widetilde{H}(2^{j-1}f)\widetilde{G}_{j-1}(f)$	$\widetilde{G}_j(f) = \widetilde{G}(2^{j-1}f)\widetilde{G}_{j-1}(f)$
$\{\tilde{h}_{j,l}\} \longleftrightarrow \widetilde{H}_j(\cdot)$	$\{\tilde{g}_{j,l}\} \longleftrightarrow \widetilde{G}_j(\cdot)$
$\sum_l \tilde{h}_{j,l} = \widetilde{H}_j(0) = 0$	$\sum_l \tilde{g}_{j,l} = \widetilde{G}_j(0) = 1$
$\sum_l \tilde{h}_{j,l}^2 = \frac{1}{2^j}$	$\sum_l \tilde{g}_{j,l}^2 = \frac{1}{2^j}$
$\sum_l \tilde{h}_{j,l}\tilde{h}_{j,l+2^j n} = 0, n \neq 0$	$\sum_l \tilde{g}_{j,l}\tilde{g}_{j,l+2^j n} = 0, n \neq 0$
$\sum_l \tilde{g}_{j,l}\tilde{h}_{j,l+2^j n} = 0$	
$\widetilde{\mathcal{H}}_j(f) \equiv \lvert\widetilde{H}_j(f)\rvert^2 = \frac{1}{2^j}\mathcal{H}_j(f)$	$\widetilde{\mathcal{G}}_j(f) \equiv \lvert\widetilde{G}_j(f)\rvert^2 = \frac{1}{2^j}\mathcal{G}_j(f)$
$\widetilde{W}_{j,t} \equiv \sum_l \tilde{h}_{j,l} X_{t-l \bmod N}$	$\widetilde{V}_{j,t} \equiv \sum_l \tilde{g}_{j,l} X_{t-l \bmod N}$

Table 202. Key relationships involving MODWT wavelet and scaling filters (the conventions in Table 154 for limits on sums over l apply here too).

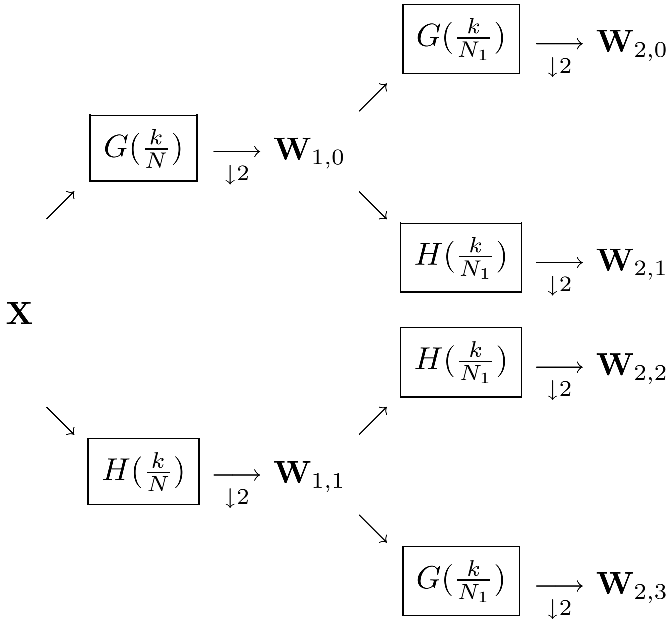

Figure 210a. Flow diagram illustrating the analysis of $\mathbf{X}$ into $\mathbf{W}_{2,0}$, $\mathbf{W}_{2,1}$, $\mathbf{W}_{2,2}$ and $\mathbf{W}_{2,3}$ (sequency ordering). In the above recall that $N_1 \equiv N/2$.

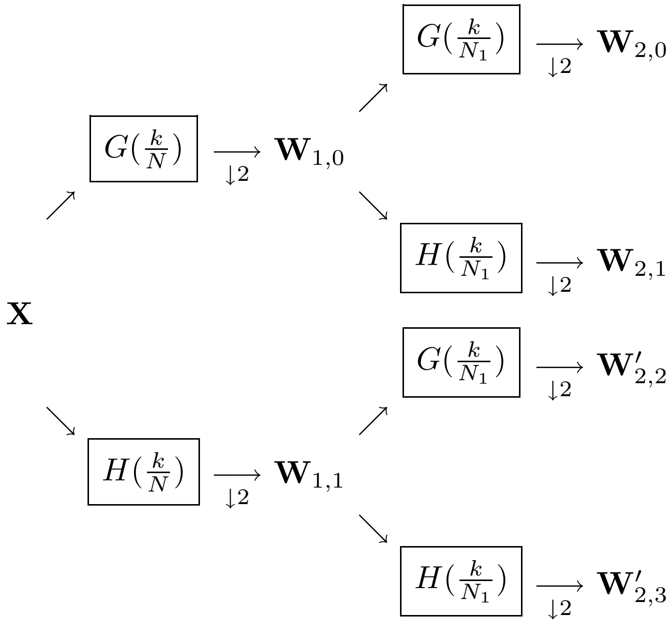

Figure 210b. Flow diagram illustrating the analysis of $\mathbf{X}$ into $\mathbf{W}_{2,0}, \mathbf{W}_{2,1}, \mathbf{W}'_{2,2}$ and $\mathbf{W}'_{2,3}$ (natural ordering).

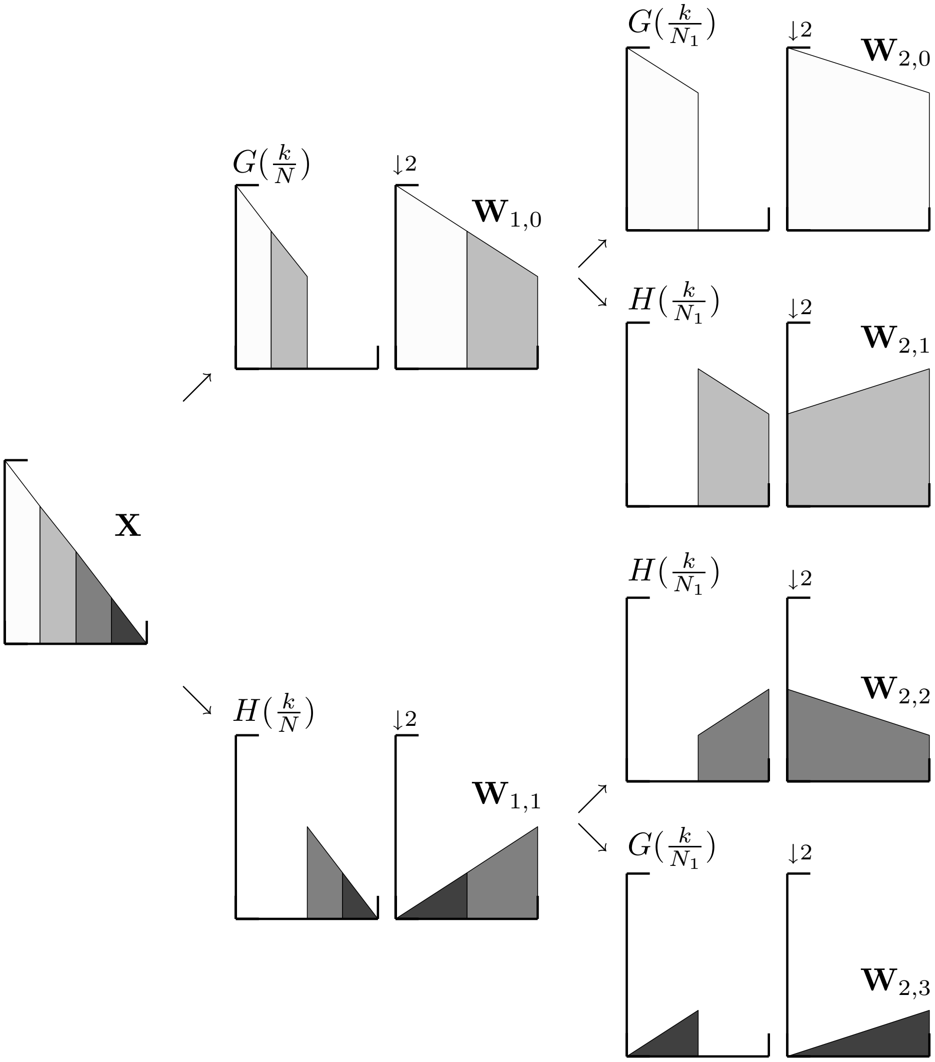

Figure 211. Illustration of effect in the frequency domain of filtering with ideal low- and high-pass filters $G(\cdot)$ and $H(\cdot)$, followed by downsampling (this figure parallels the flow diagram in Figure 210a). The magnitude squared DFT for the input $\mathbf{X}$ of length N is assumed to roll off linearly as f sweeps from 0 up to the Nyquist frequency. Filtering $\mathbf{X}$ with either $G(\cdot)$ or $H(\cdot)$ yields a half-band series that, after downsampling, becomes a full-band series (either $\mathbf{W}_{1,0}$ or $\mathbf{W}_{1,1}$, each with $N/2$ points). A second round of filtering and downsampling yields four new full-band series, namely, $\mathbf{W}_{2,n}$, $n = 0, 1, 2$ and 3. Each $\mathbf{W}_{2,n}$ is of length $N/4$ and is related to a single quarter-band in $\mathbf{X}$. Note that, each time that we create a half-band series by filtering with $H(\cdot)$, the subsequent downsampling creates a full-band series whose frequency content is reversed with respect to that of the half-band series; on the other hand, filtering with $G(\cdot)$ causes no such reversal (for an explanation of the reversal induced by $H(\cdot)$, see Section 4.4).

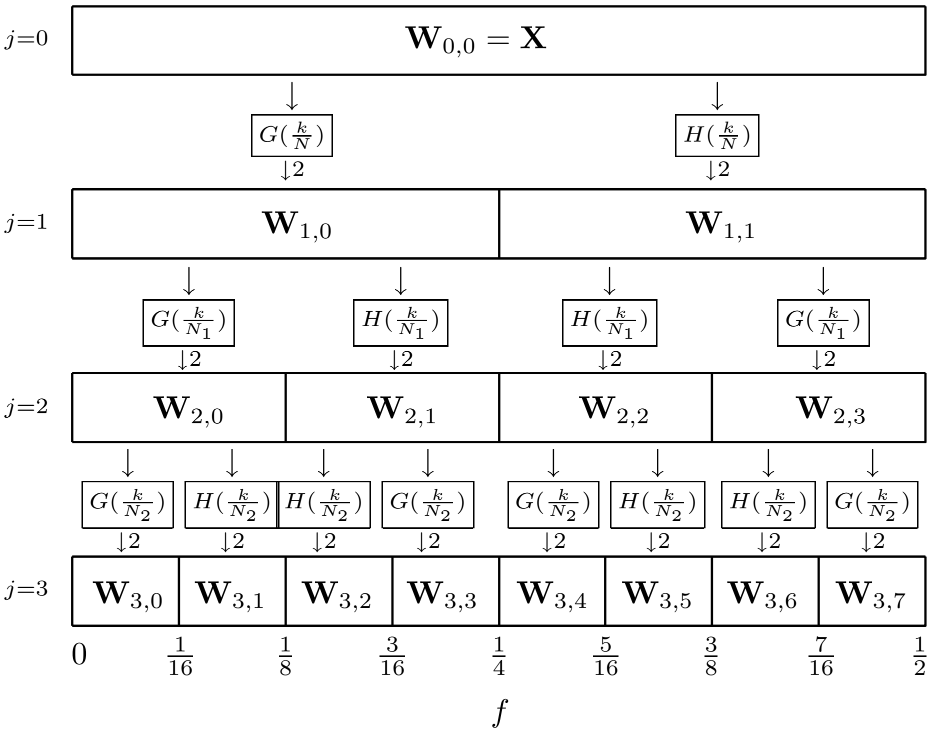

Figure 212a. Flow diagram illustrating the analysis of $\mathbf{X}$ into $\mathbf{W}_{3,0}, \ldots, \mathbf{W}_{3,7}$ (recall that $N_j \equiv N/2^j$).

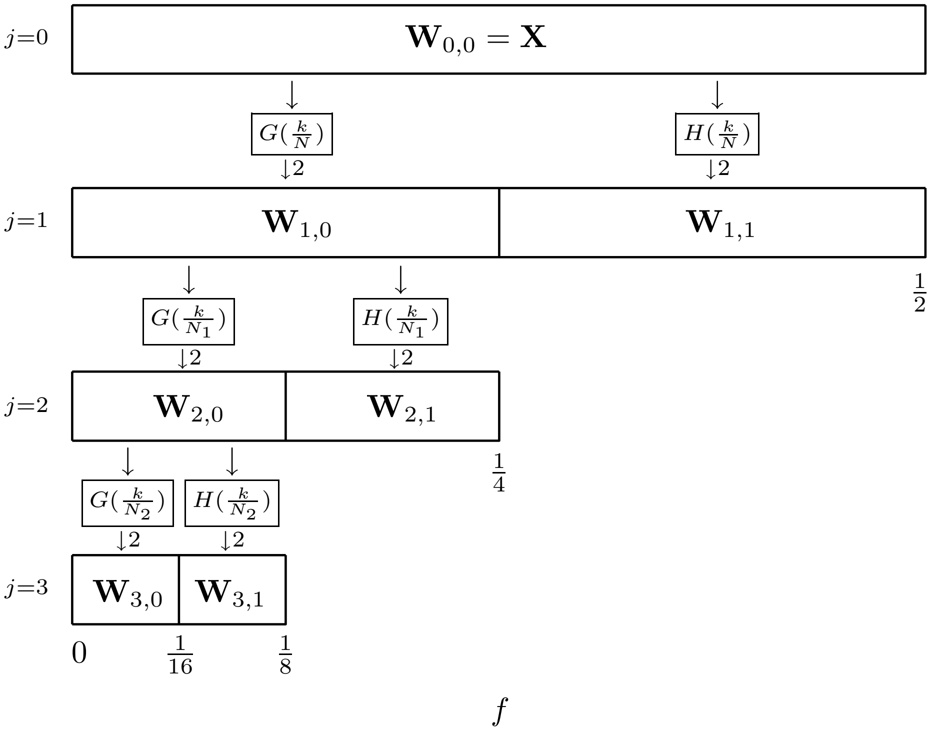

Figure 212b. Flow diagram illustrating the analysis of $\mathbf{X}$ into $\mathbf{W}_{3,0}$, $\mathbf{W}_{3,1}$, $\mathbf{W}_{2,1}$ and $\mathbf{W}_{1,1}$, which is identical to a partial DWT of level $J_0 = 3$.

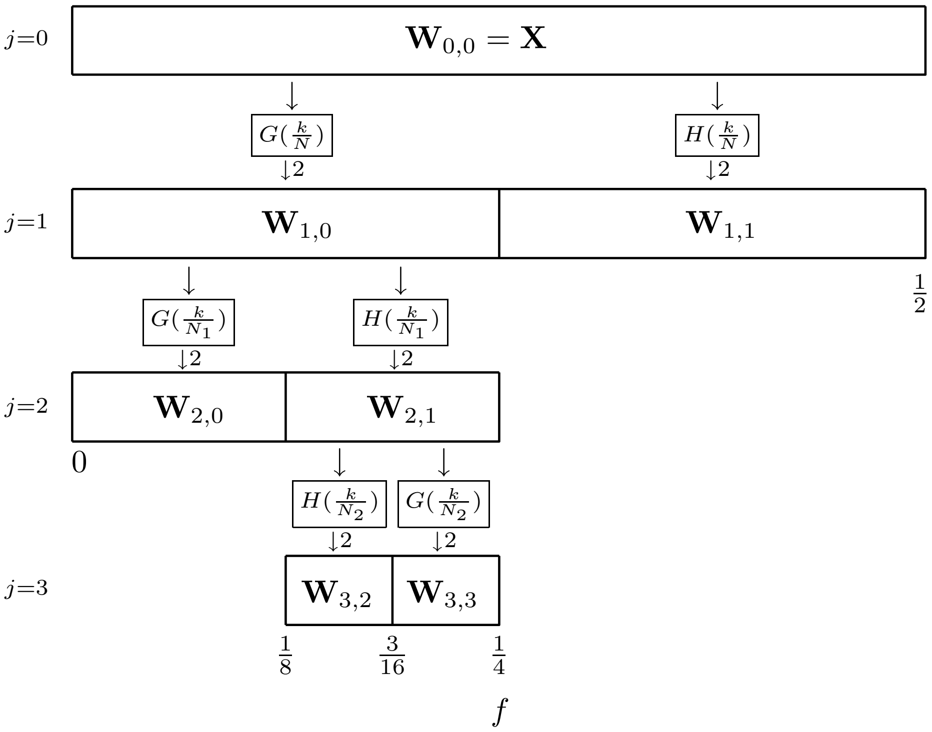

Figure 213. Flow diagram illustrating the analysis of $\mathbf{X}$ into $\mathbf{W}_{2,0}$, $\mathbf{W}_{3,2}$, $\mathbf{W}_{3,3}$ and $\mathbf{W}_{1,1}$, an arbitrary disjoint dyadic decomposition.

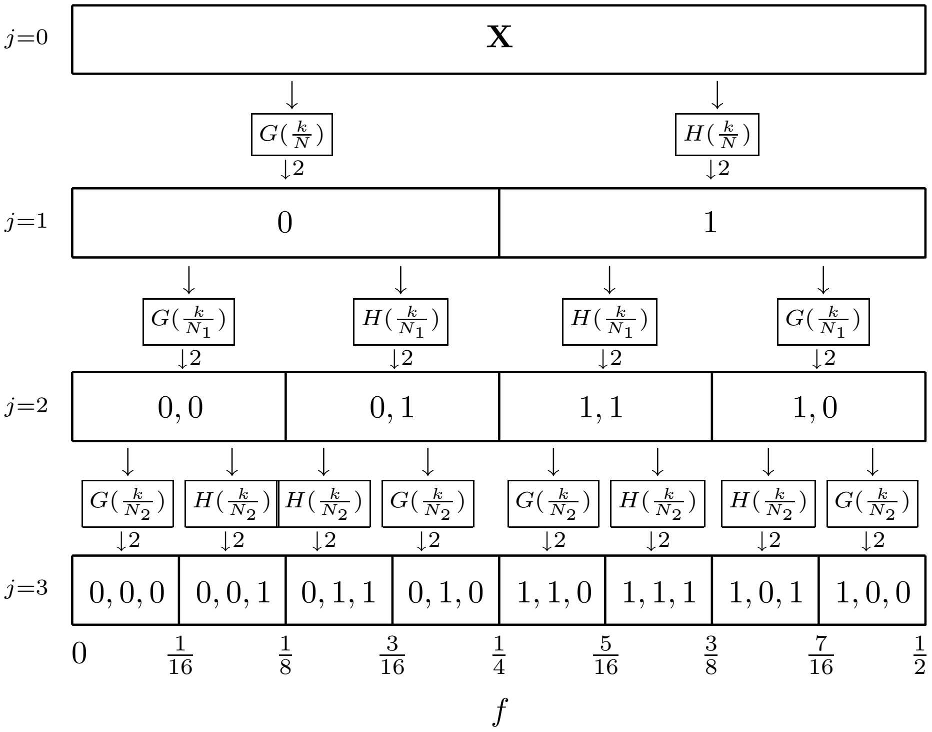

Figure 216. Illustration of the vectors $\mathbf{c}_{j,n}$ for the sequency ordered WP table for levels $j = 1, 2$ and 3 (0 or 1 indicate use of, respectively, a scaling (low-pass) or wavelet (high-pass) filter). Note that, if, in going from a parent node at level $j - 1$ to a child at level j, we require use of $G(\cdot)$, then we append a zero to the parent's $\mathbf{c}_{j-1,\lfloor \frac{n}{2} \rfloor}$ to obtain the child's $\mathbf{c}_{j,n}$; on the other hand, if we use $H(\cdot)$, then we append a one. Note also that, as we sweep from left to right across either row $j = 2$ or 3 and pick out the last element of each $\mathbf{c}_{j,n}$, we obtain the pattern '0, 1, 1, 0' or this pattern followed by a replicate (for general $j \geq 2$, collecting the last elements of $\mathbf{c}_{j,n}$, $n = 0, \ldots, 2^j - 1$, will yield 2^{j-2} replications of '0, 1, 1, 0').

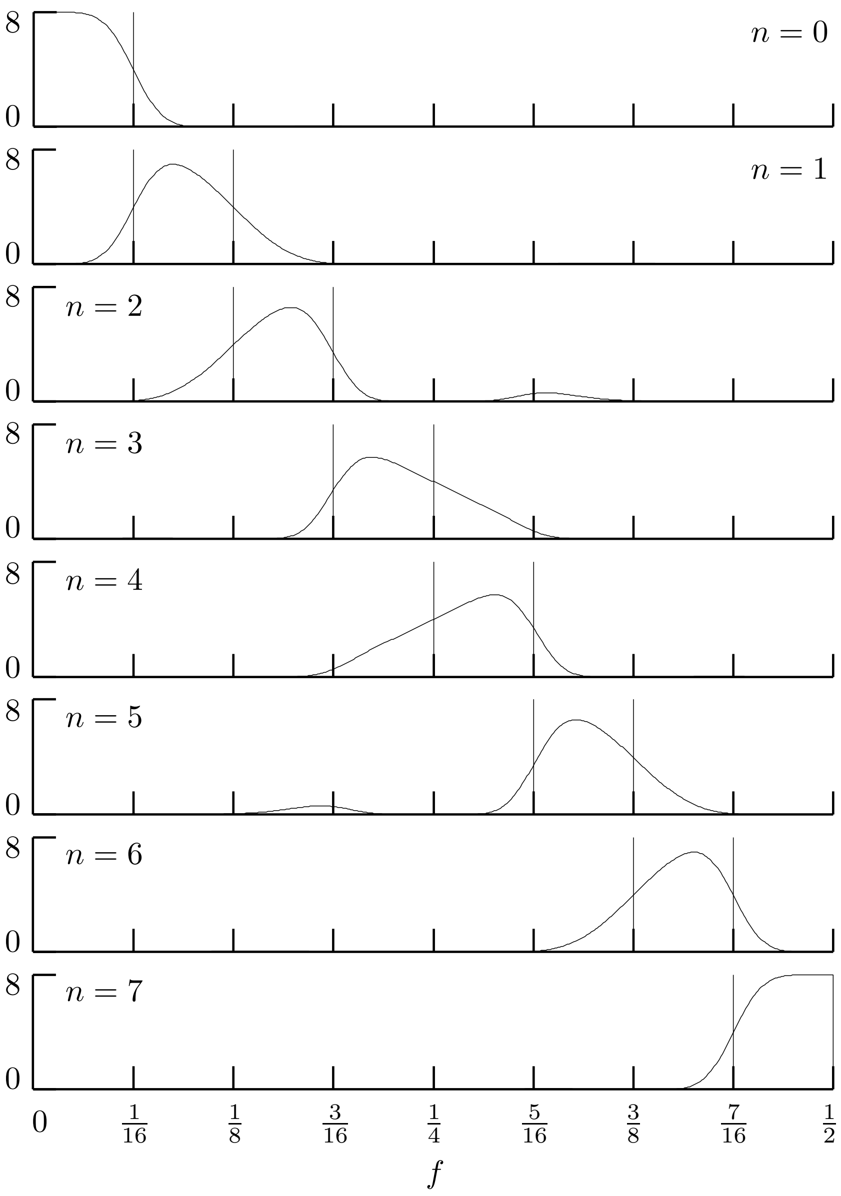

Figure 217. Squared gain functions $|U_{j,n}(\cdot)|^2$ for $j = 3$ and $n = 0, \ldots, 7$ based upon the LA(8) wavelet and scaling filters. The nominal 'ideal' pass-bands are marked by vertical lines.

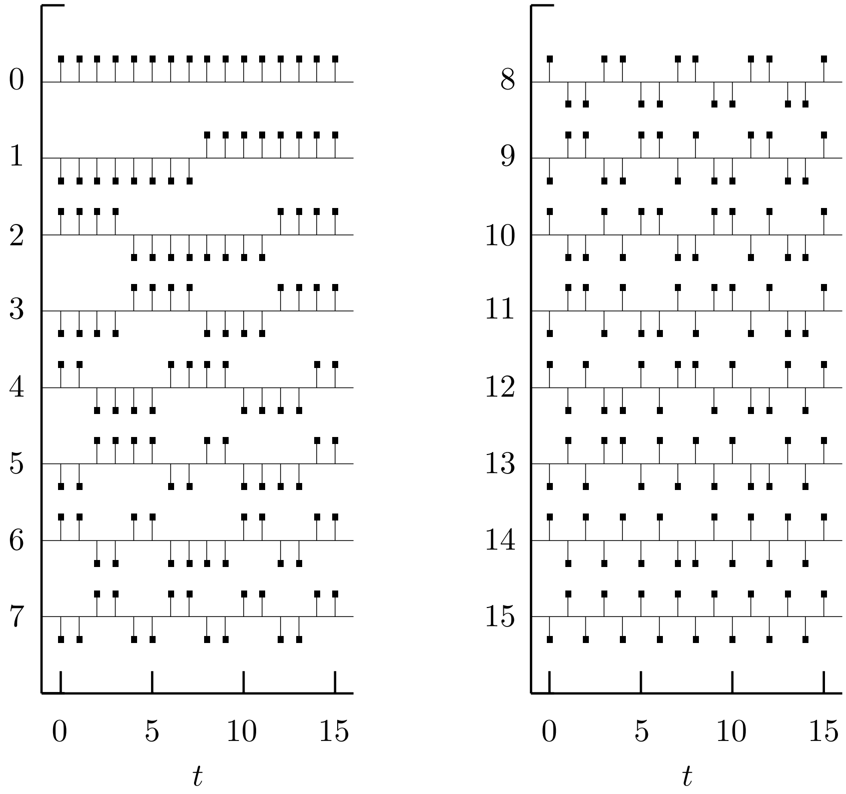

Figure 218. Row vectors for an $N = 16$ DWPT of level $J = 4$ constructed using the Haar wavelet filter. This transform is identical to what is known as the Walsh transform. The basis vectors are displayed in sequency ordering so that the inner product of (the transpose of) the nth row and a time series $\mathbf{X}$ would yield the single element in the coefficient vector $\mathbf{W}_{4,n}$.

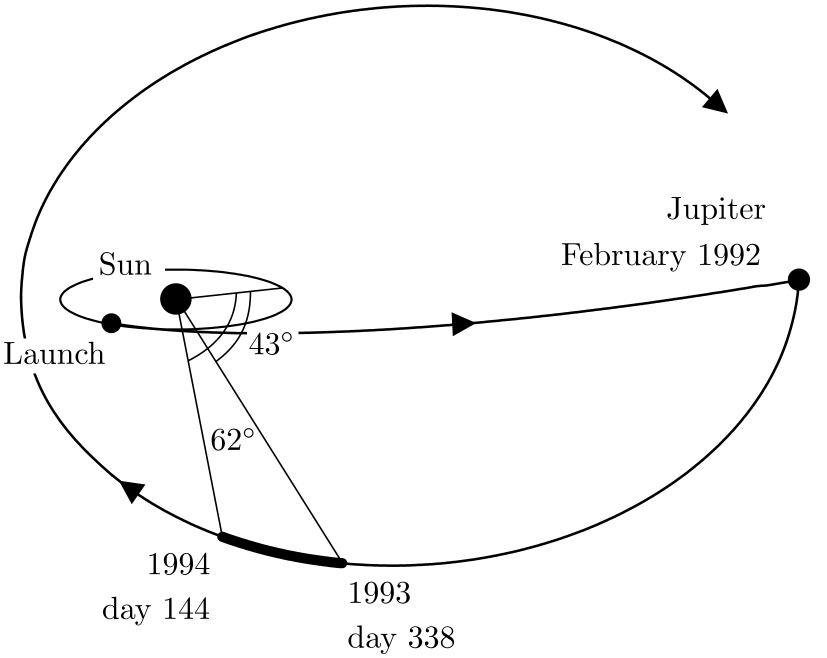

Figure 219. Path of the Ulysses spacecraft. After its launch, the spacecraft traveled in the plane of the Earth's orbit to near Jupiter, whose gravitational field then flung it into polar orbit about the Sun. The segment of data plotted at the bottom of Figure 222 was collected as the spacecraft traveled from heliographic latitude 43° S to 62° S south of the Sun – in changing latitudes, the spacecraft also decreased its distance from the Sun. After collecting the data of interest here, the spacecraft continued on its solar polar orbit, but now travelling north of the Sun. (Illustration courtesy of T. Horbury, Queen Mary and Westfield College, London.)

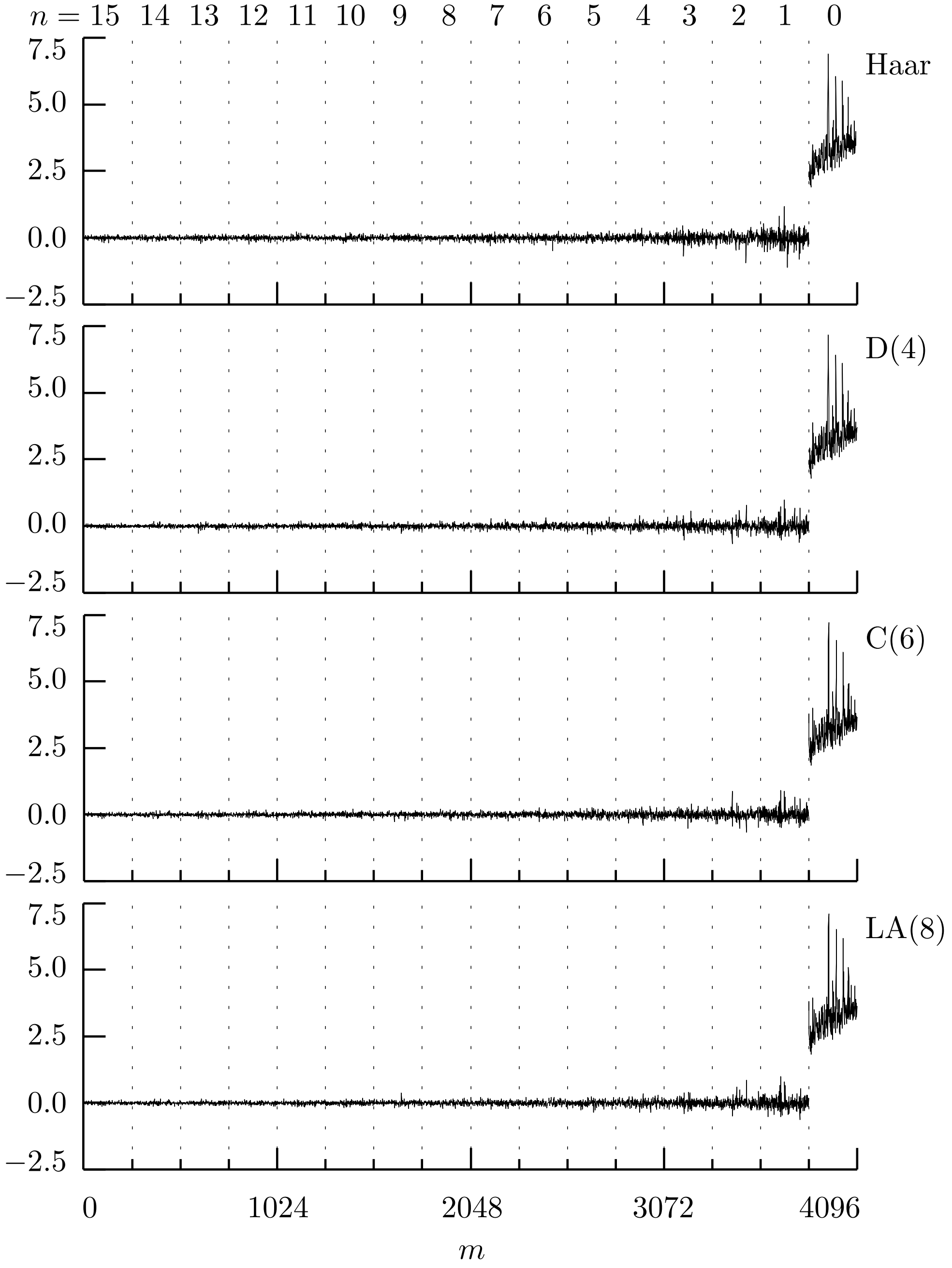

Figure 220. DWPT coefficients **W** of level $j = 4$ for solar physics time series using the Haar, D(4), C(6) and LA(8) wavelets. The elements W_m of **W** are plotted versus $m = 0, \ldots, N-1 = 4095$. The 15 vertical dotted lines delineate the 16 subvectors of **W**, namely, from left to right, $\mathbf{W}_{4,n}$, $n = 15, 14, \ldots, 0$.

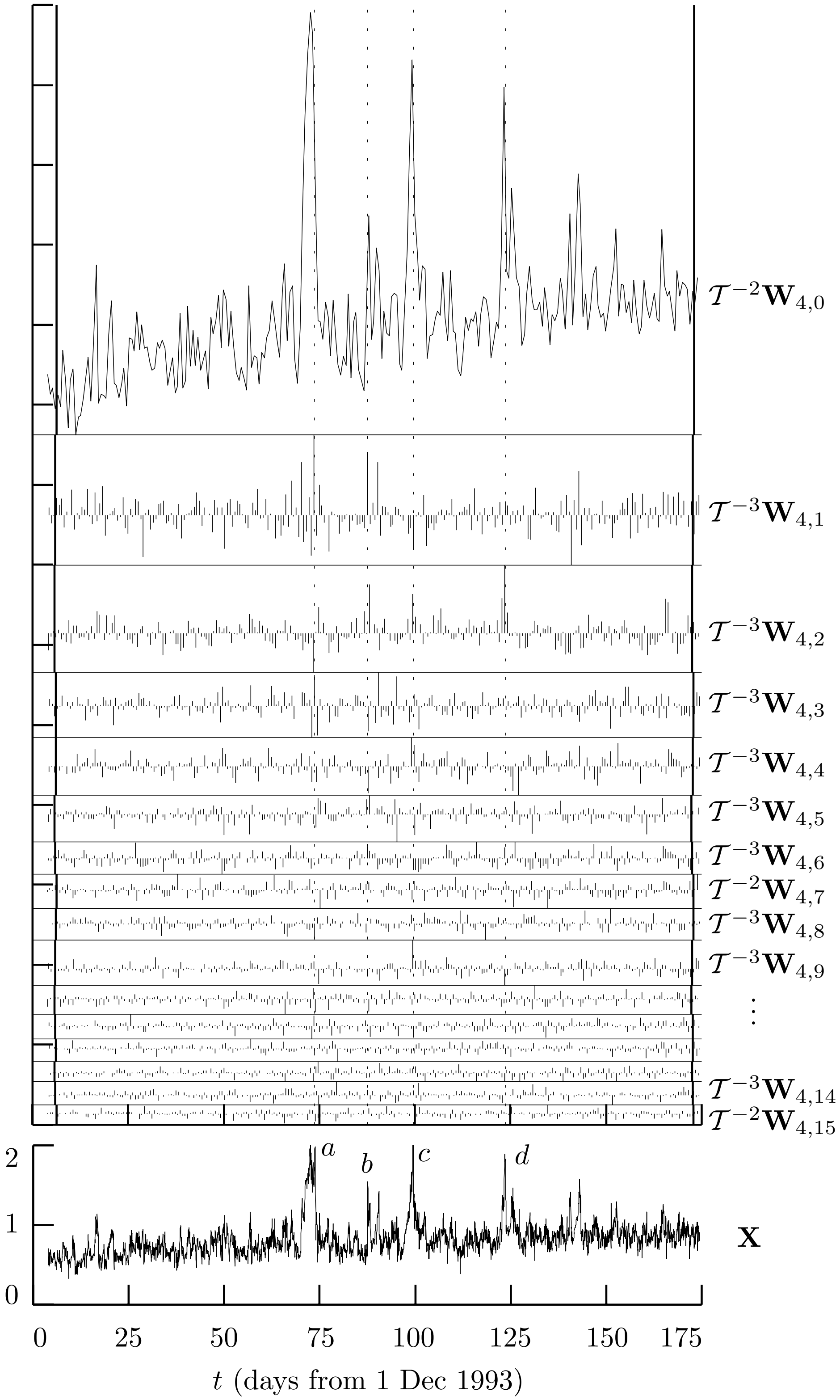

Figure 222. Level $j = 4$ LA(8) DWPT coefficients for solar physics time series (see text for details).

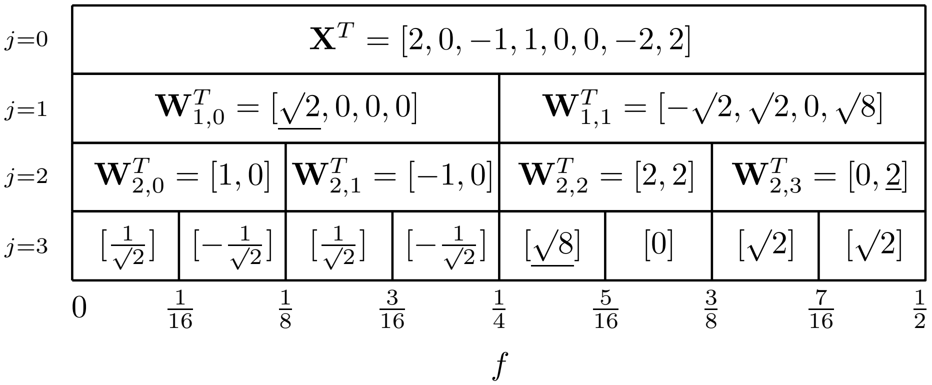

Figure 224. Haar DWPT coefficients $\mathbf{W}_{j,n}$ of levels $j = 1, 2$ and 3 for a time series $\mathbf{X}$ of length $N = 8$. The series $\mathbf{X}$ was constructed from a linear combination of three basis vectors, one from each of the three levels (see Equation (224)). In the above, the DWPT coefficients corresponding to the vectors used in formation of $\mathbf{X}$ are underlined (one each in $\mathbf{W}_{1,0}$, $\mathbf{W}_{2,3}$ and $\mathbf{W}_{3,4}$).

<table>
<tr><td>$j=0$</td><td colspan="8">1.45</td></tr>
<tr><td>$j=1$</td><td colspan="4">0.28</td><td colspan="4">0.88</td></tr>
<tr><td>$j=2$</td><td colspan="2">0.19</td><td colspan="2">0.19</td><td colspan="2">0.72</td><td colspan="2">0.36</td></tr>
<tr><td>$j=3$</td><td>**0.12**</td><td>**0.12**</td><td>**0.12**</td><td>**0.12**</td><td>**0.32**</td><td>**0.00**</td><td>**0.28**</td><td>**0.28**</td></tr>
</table>

$0 \quad \frac{1}{16} \quad \frac{1}{8} \quad \frac{3}{16} \quad \frac{1}{4} \quad \frac{5}{16} \quad \frac{3}{8} \quad \frac{7}{16} \quad \frac{1}{2}$

f

Figure 225. Cost table for the WP table shown in Figure 224. The entries in the above are the values of $M(\mathbf{W}_{j,n})$ computed using the $-\ell^2 \log(\ell^2)$ norm as a cost functional. The initial step of the best basis algorithm dictates that we mark the values in the bottom row in some manner – here we have done so by underlining and also by using a bold font.

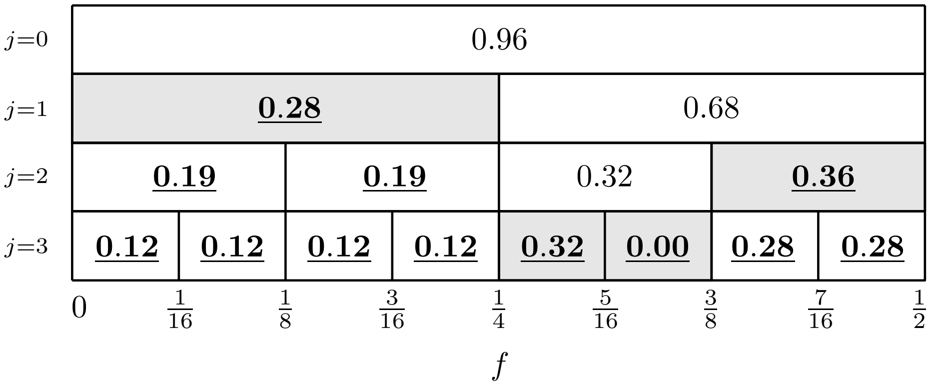

Figure 226. Final step of the best basis algorithm. The best basis transform is indicated by the shaded boxes. As is intuitively reasonable, the selected transform includes the three basis vectors used to form **X**.

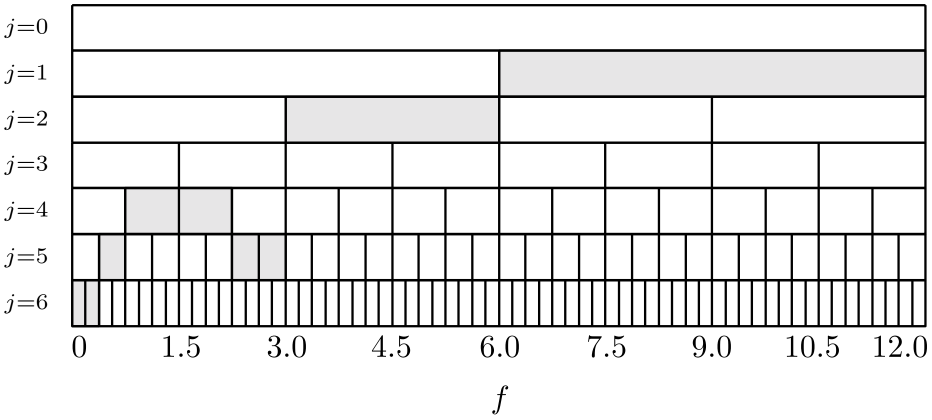

Figure 227. The best basis transform for the solar magnetic field magnitude data of Figure 222. This transform is based on the LA(8) wavelet filter and a cost functional based upon the $-\ell^2 \log(\ell^2)$ norm.

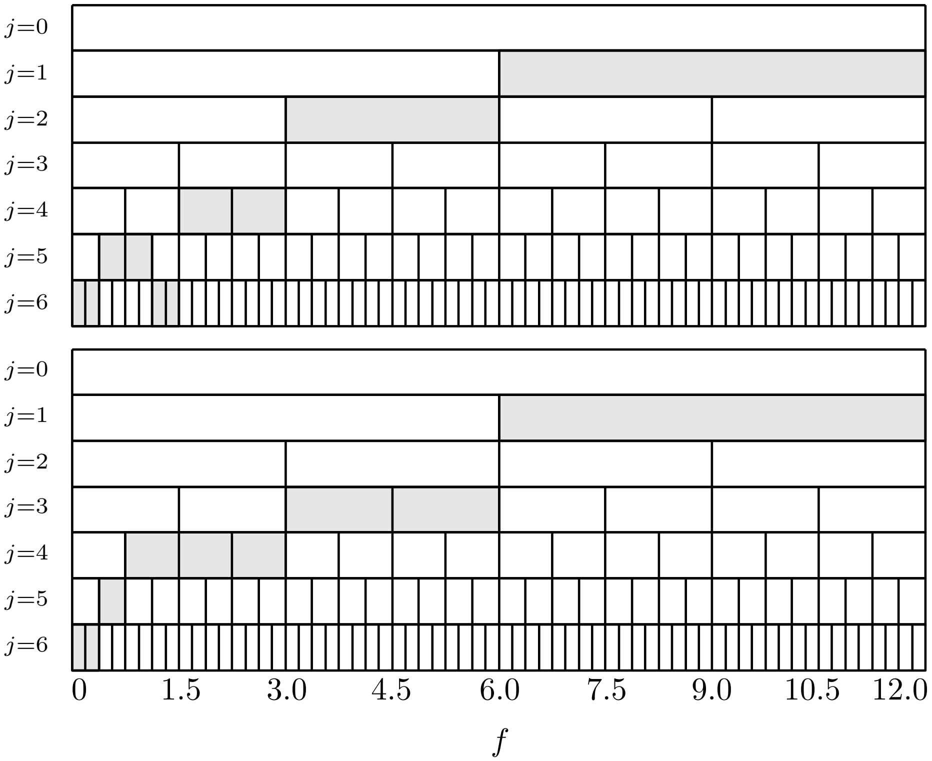

Figure 228. Best basis transform for the solar magnetic field magnitude data based upon reflection boundary conditions (top), and the best shift basis transform for the same data (bottom), again using reflection boundary conditions. Both transforms are based on the same wavelet filter and cost functional as used in Figure 227. The best shift basis algorithm selected the shift $m = 52$ (i.e., $\mathcal{T}^{52}$) as the best shift.

j	n	$\mathbf{c}_{j,n}$	$S_{j,n,0}$	$S_{j,n,1}$	$\lvert\nu_{j,n}\rvert$	LA(8)	$\lvert p_{j,n}\rvert$	LA(8)
1	0	0	1	0	$\frac{L_1}{2}-1$	3	$e\{g_l\}$	2.8
	1	1	0	1	$\frac{L_1}{2}+0$	4	$e\{h_l\}$	4.2
2	0	0,0	3	0	$\frac{L_2}{2}-2$	9	$3e\{g_l\}$	8.5
	1	0,1	1	2	$\frac{L_2}{2}+0$	11	$e\{g_l\}+2e\{h_l\}$	11.2
	2	1,1	0	3	$\frac{L_2}{2}+1$	12	$3e\{h_l\}$	12.5
	3	1,0	2	1	$\frac{L_2}{2}-1$	10	$2e\{g_l\} + e\{h_l\}$	9.8
3	0	0,0,0	7	0	$\frac{L_3}{2}-4$	21	$7e\{g_l\}$	19.9
	1	0,0,1	3	4	$\frac{L_3}{2}+0$	25	$3e\{g_l\}+4e\{h_l\}$	25.2
	2	0,1,1	1	6	$\frac{L_3}{2}+2$	27	$e\{g_l\}+6e\{h_l\}$	27.8
	3	0,1,0	5	2	$\frac{L_3}{2}-2$	23	$5e\{g_l\}+2e\{h_l\}$	22.5
	4	1,1,0	4	3	$\frac{L_3}{2}-1$	24	$4e\{g_l\}+3e\{h_l\}$	23.8
	5	1,1,1	0	7	$\frac{L_3}{2}+3$	28	$7e\{h_l\}$	29.1
	6	1,0,1	2	5	$\frac{L_3}{2}+1$	26	$2e\{g_l\}+5e\{h_l\}$	26.5
	7	1,0,0	6	1	$\frac{L_3}{2}-3$	22	$6e\{g_l\} + e\{h_l\}$	21.2

Table 230. Form of the advances $|\nu_{j,n}|$ required to achieve approximate zero phase output using a filter $\{u_{j,n,l}\}$ based upon an LA filter with $L/2$ even. Here we let $j = 1, 2$ and 3 and $n = 0, \ldots, 2^j - 1$. The seventh column gives specific values for the LA(8) filter (see Comments and Extensions to Section 6.5 for a discussion on the last two columns).

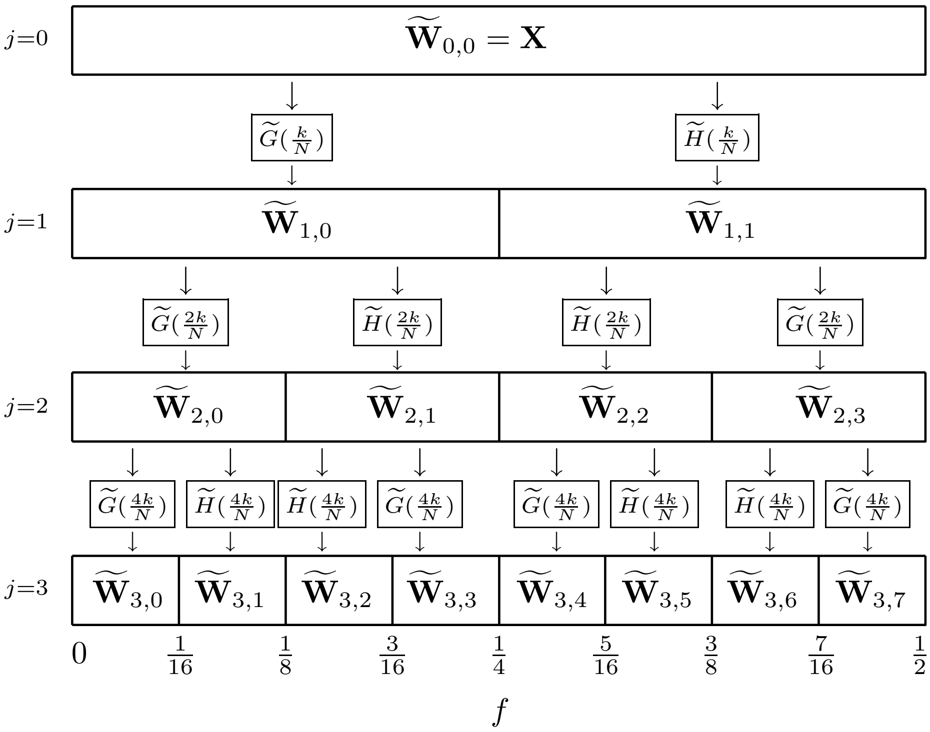

Figure 232. Flow diagram illustrating the analysis of $\mathbf{X}$ into MODWPT coefficients $\widetilde{\mathbf{W}}_{j,n}$ of levels $j = 1, 2$ and 3. Collectively, all the coefficients in the jth row constitute the level j MODWPT of $\mathbf{X}$. Note that, within the jth level, the frequency index n ranges from 0 to $2^j - 1$ and that each $\widetilde{\mathbf{W}}_{j,n}$ has length N (by contrast, in Figure 212a for the DWPT, each $\mathbf{W}_{j,n}$ has length $N/2^j$).

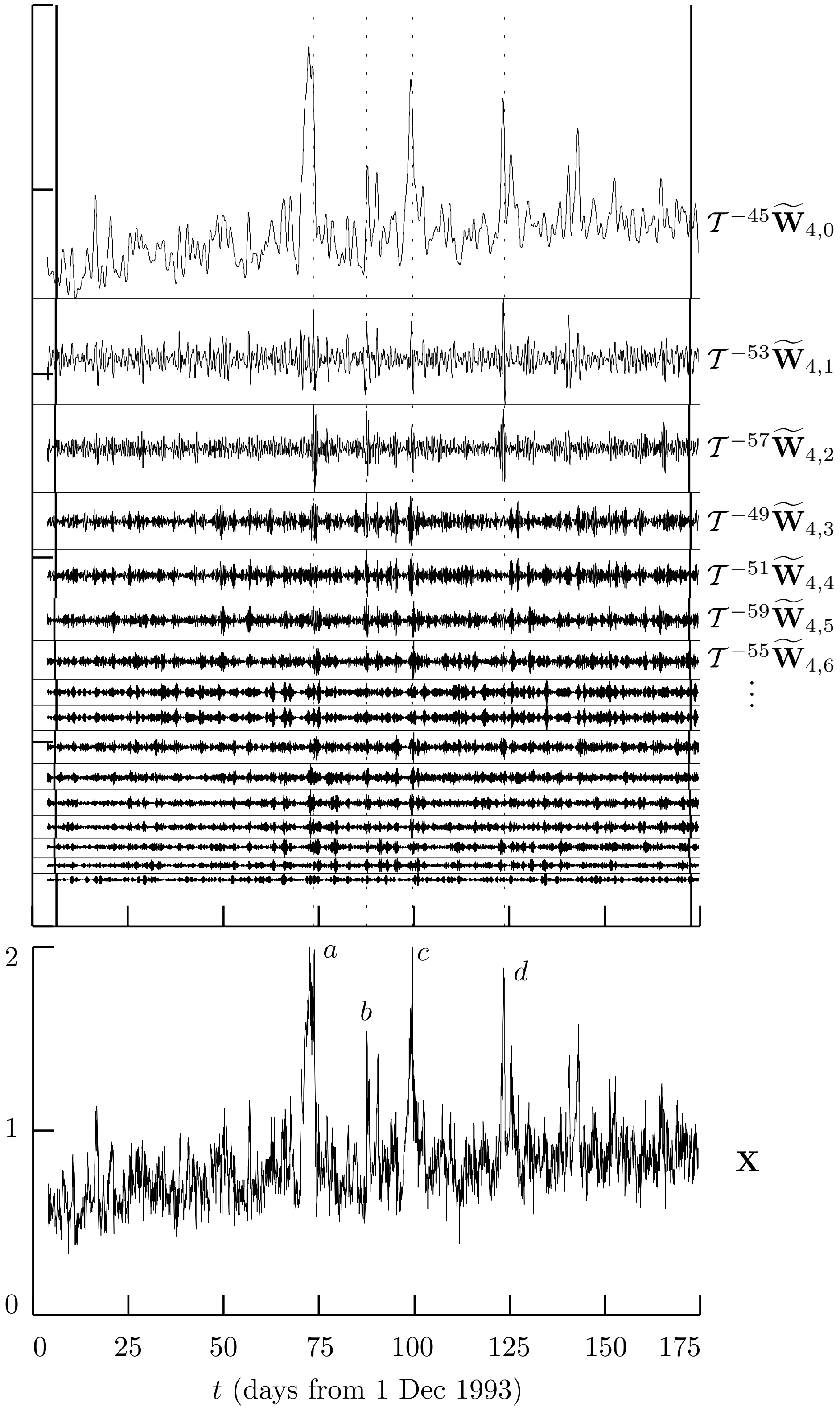

Figure 235. Level $j = 4$ LA(8) MODWPT coefficients for solar physics time series (see text for details).

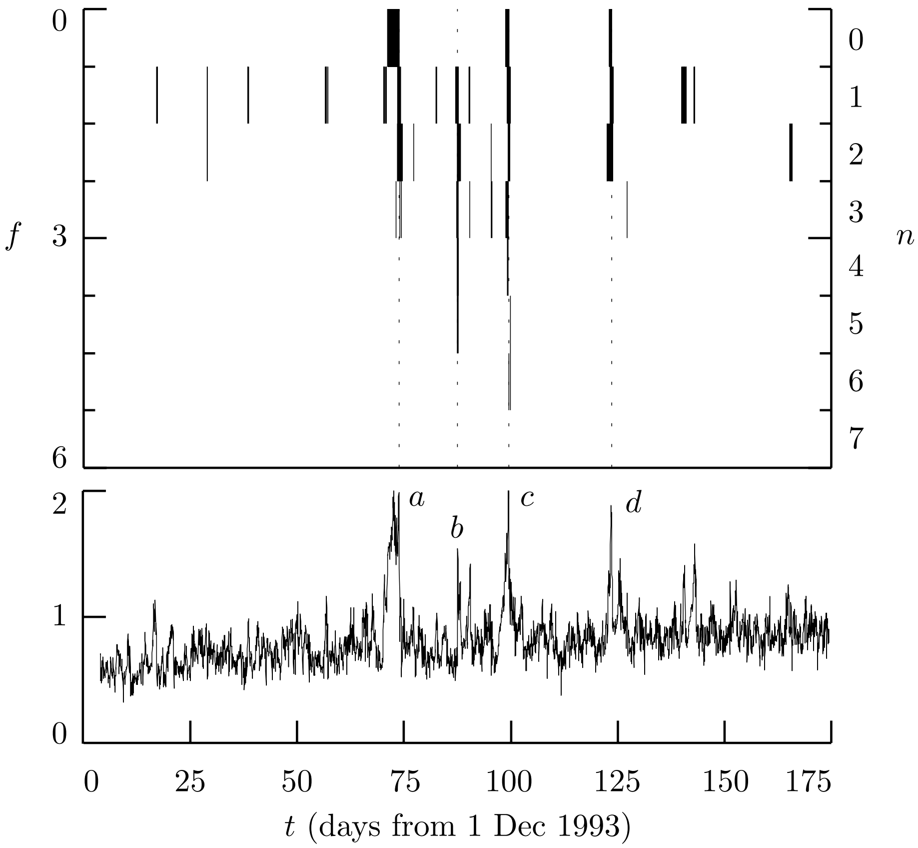

Figure 236. Southern hemisphere solar magnetic field magnitude data (lower plot) and corresponding modified time/frequency plot (upper). The data are measured in nanoteslas and were recorded by the Ulysses space craft from 21 hours Universal Time (UT) on day 338 of 1993 (4 December) until 12 hours UT on day 144 of 1994 (24 May). The frequency f is measured in cycles per day. The four shock wave structures are labeled a to d on the lower plot, while vertical dotted in the upper plot mark their locations as determined by Balogh *et al.* (1995).

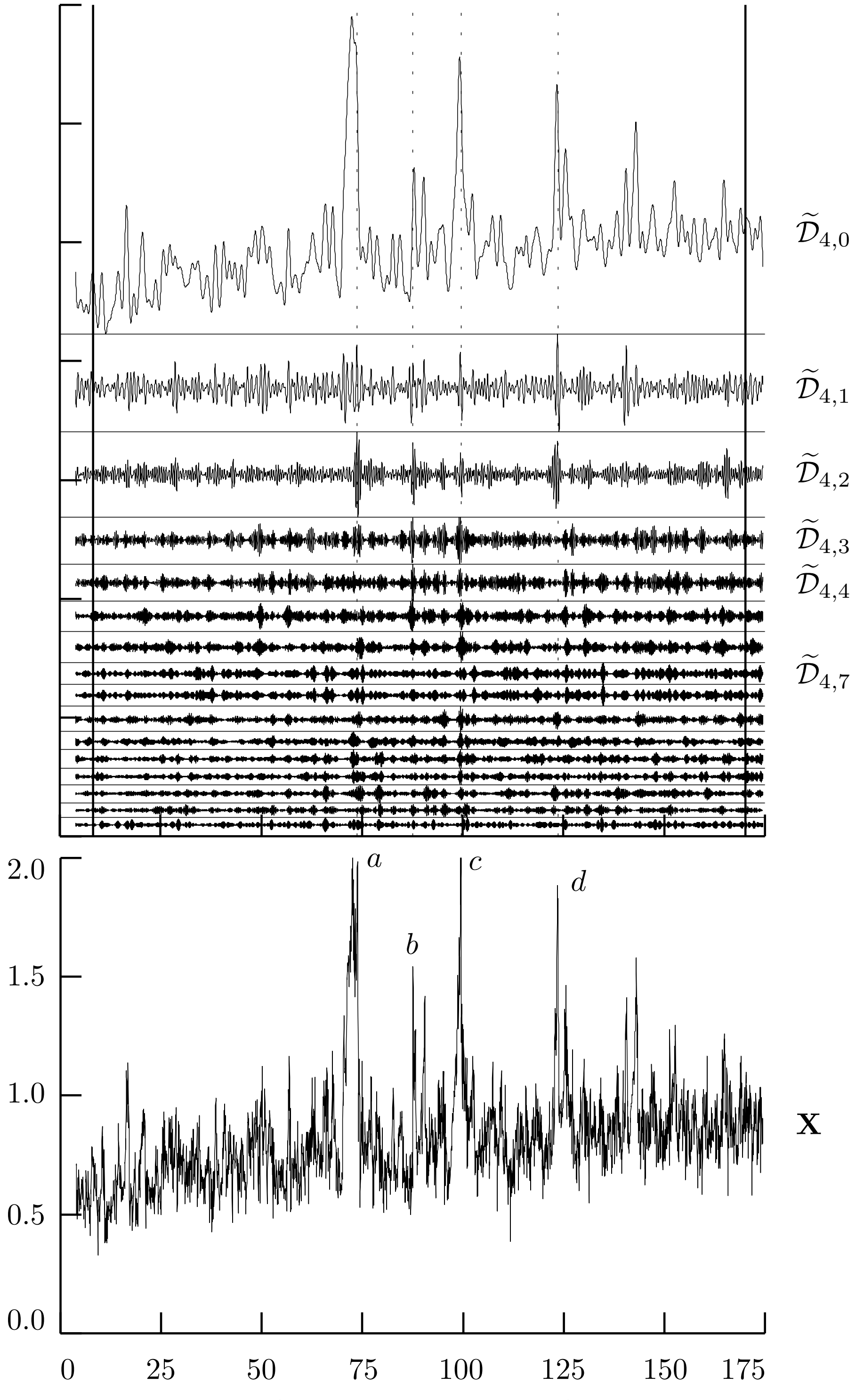

Figure 238. Solar magnetic field magnitude data (lower plot) and corresponding plot of the MODWPT details $\widetilde{\mathcal{D}}_{4,n}$, $n = 0, \ldots, 15$ (upper). The nth detail corresponds to the frequency band from $0.75n$ cycles per hour to $0.75(n + 1)$ cycles per hour.

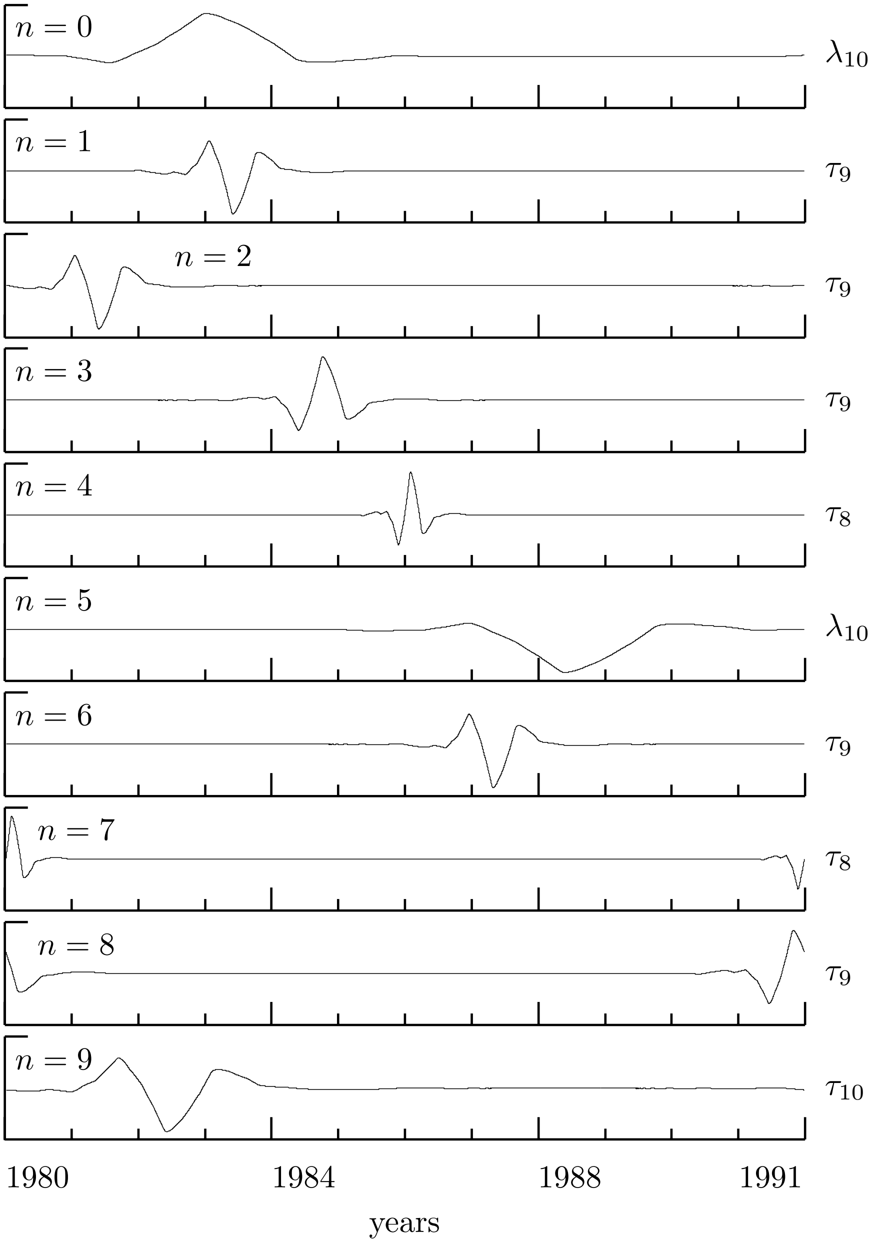

Figure 244. First ten MODWT vectors selected using the matching pursuit algorithm applied to the subtidal sea level fluctuations. The dictionary is $\mathbb{D}^{(\text{modwt})}$ constructed using the LA(8) wavelet filter. Each vector has been multiplied by $+1$ or -1 according to the sign of its inner product with $\mathbf{R}^{(n)}$, thus enabling visual correlation with the original series. The standardized scale for each vector is written to the right of its plot (τ_j for a vector from $\widetilde{\mathcal{W}}_j$ and λ_{10} for one from $\widetilde{\mathcal{V}}_{10}$).

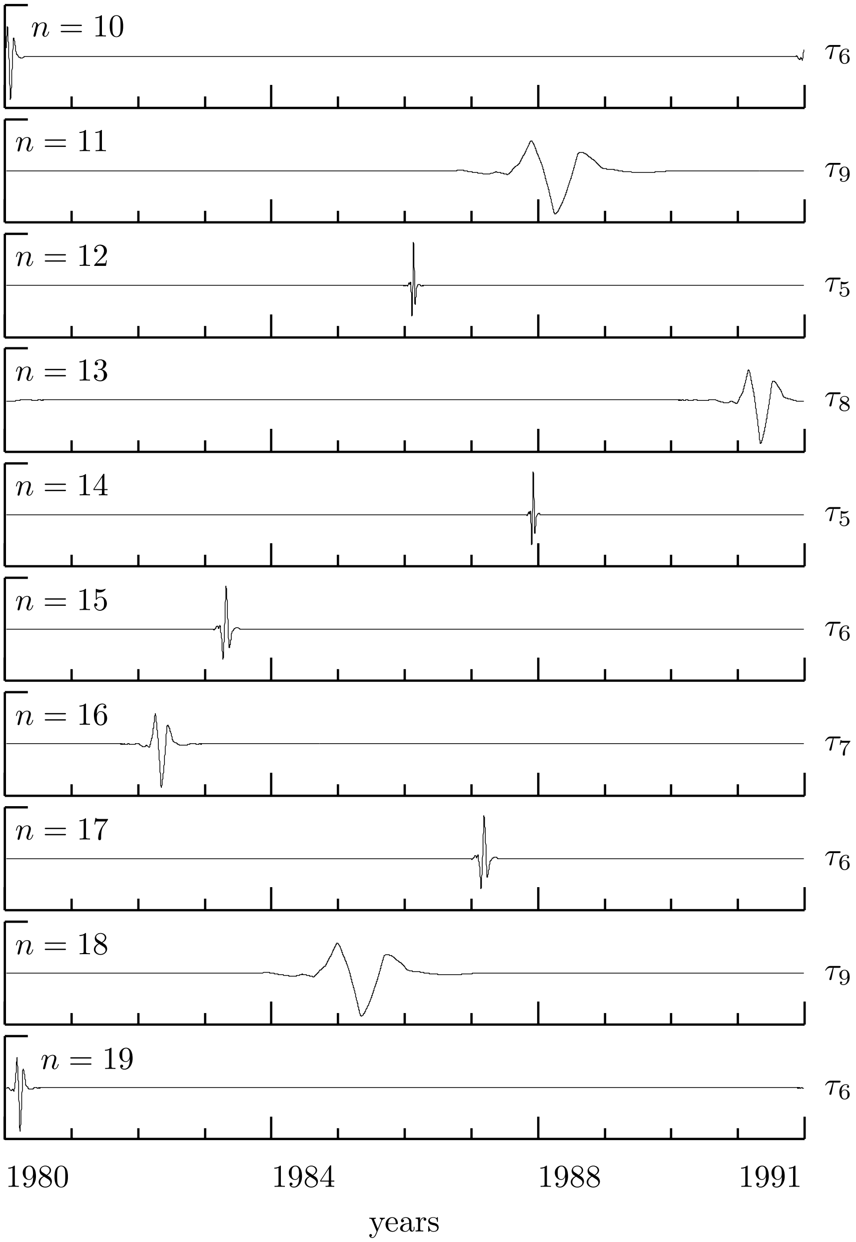

Figure 245. MODWT vectors selected eleventh to twentieth using the matching pursuit algorithm (see Figure 244 for details).

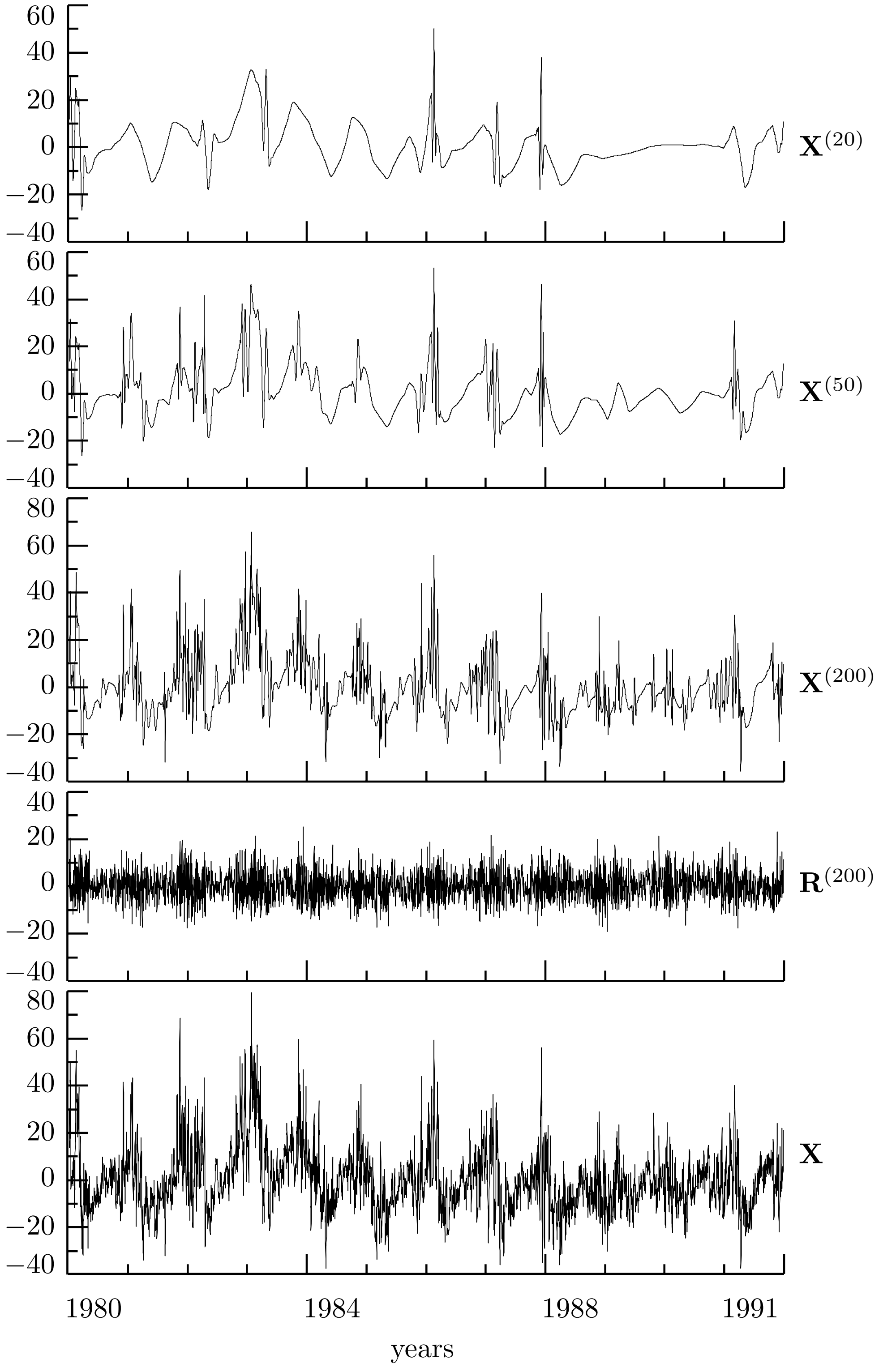

Figure 246. Matching pursuit approximations $\mathbf{X}^{(m)}$ of the subtidal sea level fluctuations $\mathbf{X}$ using $m = 20$, 50 and 200 vectors from a MODWT dictionary. The residuals $\mathbf{R}^{(200)}$ corresponding to $\mathbf{X}^{(200)}$ are shown above the plot of $\mathbf{X}$.

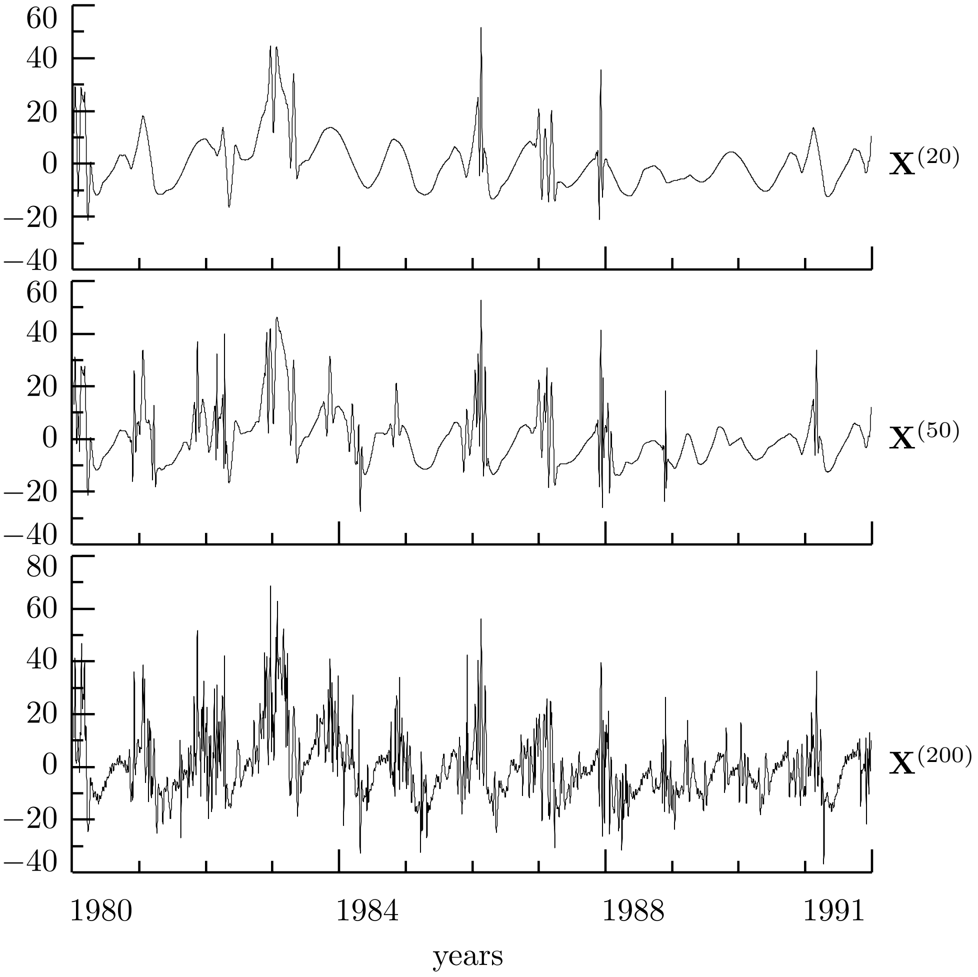

Figure 248a. Matching pursuit approximations $\mathbf{X}^{(m)}$ of the subtidal sea level fluctuations $\mathbf{X}$ using $m = 20$, 50 and 200 vectors, but now from a dictionary composed of both MODWT and ODFT vectors.

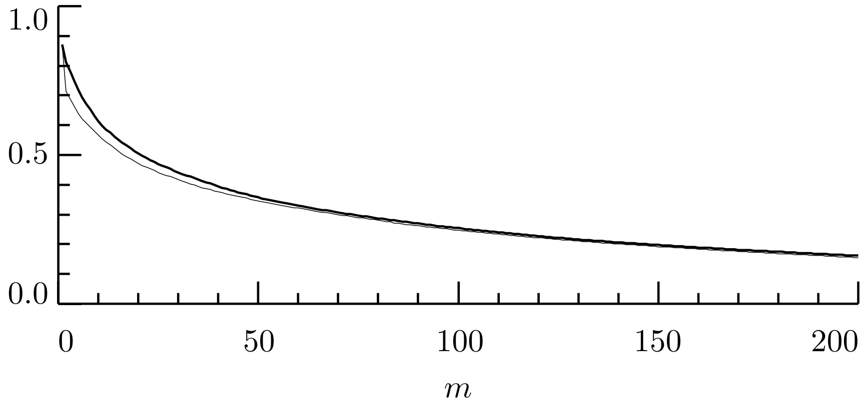

Figure 248b. Normalized residual sum of squares $\|\mathbf{R}^{(m)}\|^2/\|\mathbf{X}\|^2$ versus the number of terms m in the matching pursuit approximation using the MODWT dictionary $\mathbb{D}^{(\text{modwt})}$ (thick curve) and this dictionary combined with vectors from the ODFT (thin curve).

	p					
η	0.005	0.025	0.05	0.95	0.975	0.995
1	0.00004	0.0010	0.0039	3.8415	5.0239	7.8794
1.5	0.0015	0.0131	0.0332	4.9802	6.2758	9.3310
2	0.0100	0.0506	0.1026	5.9915	7.3778	10.5966
2.5	0.0321	0.1186	0.2108	6.9281	8.3923	11.7538
3	0.0717	0.2158	0.3518	7.8147	9.3484	12.8382
3.5	0.1301	0.3389	0.5201	8.6651	10.2621	13.8696
4	0.2070	0.4844	0.7107	9.4877	11.1433	14.8603
4.5	0.3013	0.6494	0.9201	10.2882	11.9985	15.8183
5	0.4117	0.8312	1.1455	11.0705	12.8325	16.7496
5.5	0.5370	1.0278	1.3845	11.8376	13.6486	17.6583
6	0.6757	1.2373	1.6354	12.5916	14.4494	18.5476
6.5	0.8268	1.4584	1.8967	13.3343	15.2369	19.4201
7	0.9893	1.6899	2.1673	14.0671	16.0128	20.2777
7.5	1.1621	1.9306	2.4463	14.7912	16.7783	21.1222
$\Phi^{-1}(p)$	-2.5758	-1.9600	-1.6449	1.6449	1.9600	2.5758

Table 263. Percentage points $Q_\eta(p)$ for χ^2_η distribution for $\eta = 1$ to 7.5 in steps of 0.5. The bottom row gives percentage points $\Phi^{-1}(p)$ for the standard Gaussian distribution.

	$c = 1$	$c = 2$	$c = 3$	$c = 4$
$r = 0$	2.5216281	−4.7715359	7.9199915	−11.9769211
$r = 1$	16.0778828	−20.6343346	25.0531521	−28.8738136
$r = 2$	31.8046265	−34.0071373	34.7700272	−34.3151321
$r = 3$	32.7861099	−30.2861233	26.7109356	−22.8838310
$r = 4$	18.7432098	−14.5717688	10.7177744	−7.5322194
$r = 5$	4.7226319	−2.6807923	1.3391306	−0.5167125

Table 272. Coefficients $\{\phi_{24,n} : n = 1, \ldots, 24\}$ for AR(24) process (Gao, 1997). The coefficient in row r and column c is $\phi_{24,4r+c}$. These coefficients are available on the Web site for this book (see page *xiv*).

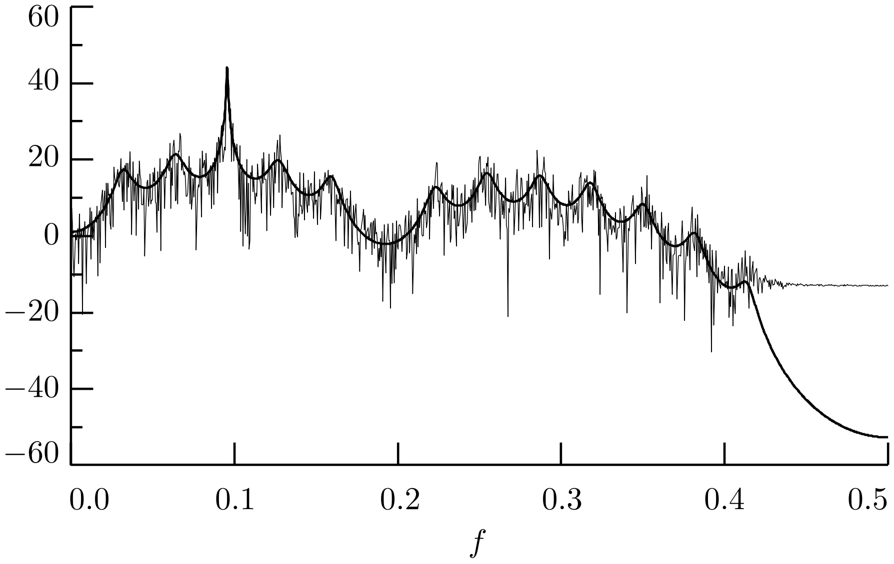

Figure 273. Periodogram (thin jagged curve) and true SDF (thick smooth) for a time series of length $N = 2048$ that is a realization of an AR(24) process (see Table 272 for the coefficients defining this process). Both the periodogram and true SDF are plotted on a decibel (dB) scale. Leakage is evident here in the periodogram at high frequencies, where the bias becomes as large as 40 dB (i.e., four orders of magnitude).

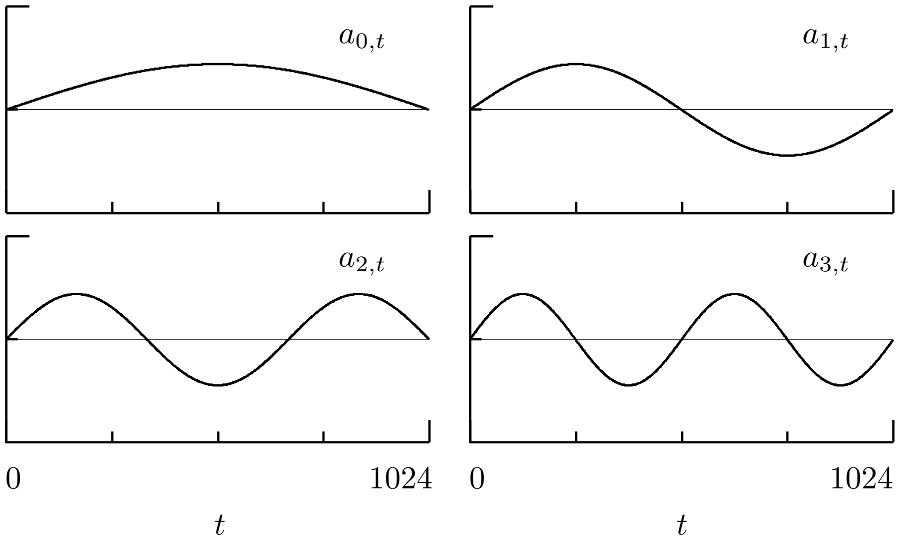

Figure 274. Sine tapers $\{a_{n,t}\}$ of orders $n = 0, 1, 2$ and 3 for $N = 1024$.

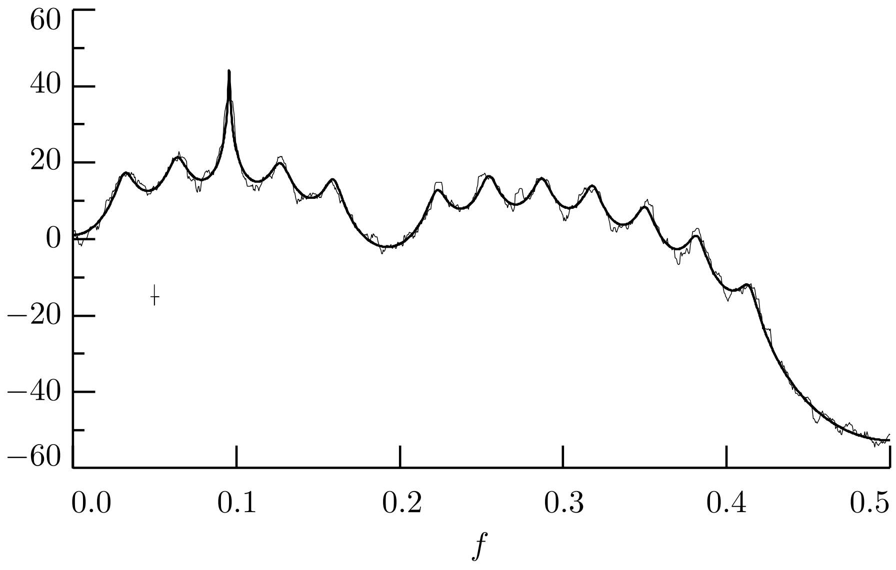

Figure 275. Multitaper SDF estimate $\hat{S}_X^{(\mathrm{mt})}(\cdot)$ (thin jagged curve) and true SDF (thick smooth) for a simulated AR(24) time series of length $N = 2048$ (the corresponding periodogram is shown in Figure 273). The multitaper estimate is based on $K = 10$ sine tapers. Both $\hat{S}_X^{(\mathrm{mt})}(\cdot)$ and the true SDF are plotted on a decibel scale. The width of the crisscross in the left-hand portion of the plot gives the bandwidth of $\hat{S}_X^{(\mathrm{mt})}(\cdot)$ (i.e., $\frac{K+1}{(N+1)} \doteq 0.0054$), while its height gives the length of a 95% confidence interval for a given $10 \cdot \log_{10}(S_X(f))$.

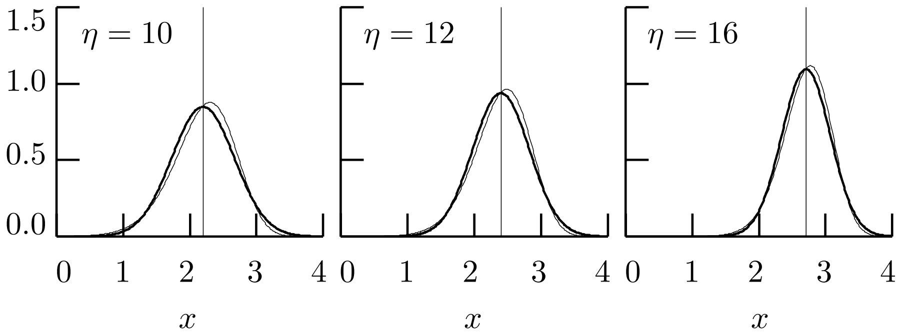

Figure 276. PDFs for $\log(\chi^2_\eta)$ RVs (thin curves) compared to Gaussian PDFs (thick curves) having the same means and variances. The degrees of freedom η are, from left to right, 10, 12 and 16 (these would be the degrees of freedom associated with a multitaper SDF estimator $\hat{S}^{(\mathrm{mt})}_X(\cdot)$ formed from, respectively, $K = 5$, 6 and 8 data tapers). The vertical lines indicate the means for the $\log(\chi^2_\eta)$ RVs – from left to right, these are $\psi(5) + \log(2) \doteq 2.199$, $\psi(6) + \log(2) \doteq 2.399$ and $\psi(8) + \log(2) \doteq 2.709$. The square roots of the corresponding variances are, respectively, $\sqrt{\psi'(5)} \doteq 0.470$, $\sqrt{\psi'(6)} \doteq 0.426$ and $\sqrt{\psi'(8)} \doteq 0.365$. (Exercise [7.1] concerns the derivation of the $\log(\chi^2_\eta)$ PDF.)

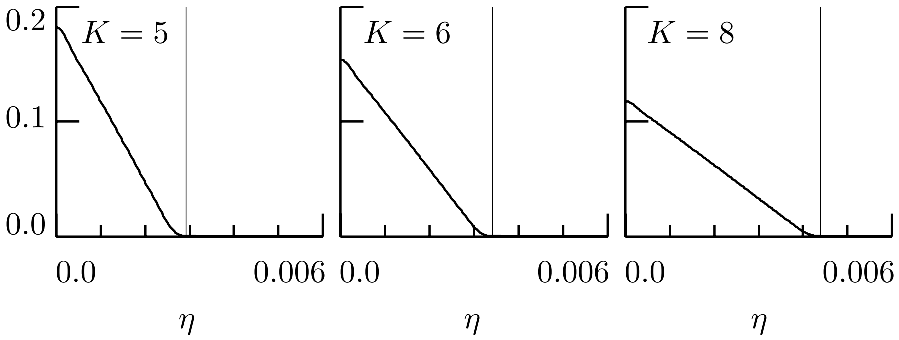

Figure 277. The autocovariance $\tilde{s}_\eta(\nu)$ versus ν for $N = 2048$ and $K = 5, 6$ and 8 sine tapers. Each vertical line shows the bandwidth $\frac{K+1}{N+1}$ of the associated multitaper SDF estimator.

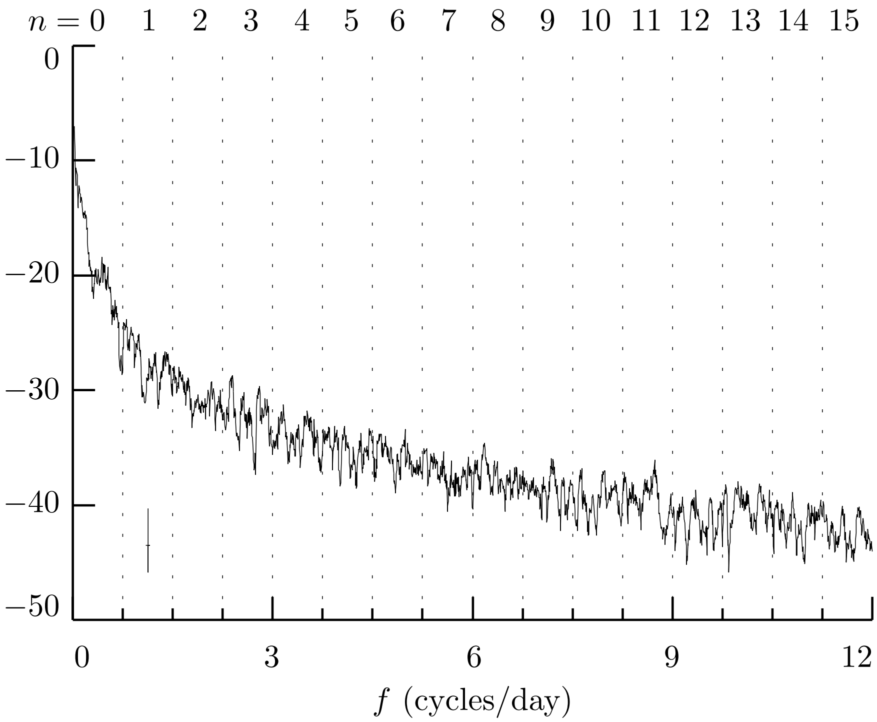

Figure 278. Multitaper SDF estimate $\hat{S}_X^{(\mathrm{mt})}(\cdot)$ (in decibels) of the solar physics time series using $K = 10$ sine tapers (this series of $N = 4096$ values is plotted in Figures 222 and 235). The vertical dotted lines partition the frequency interval $[0, 12$ cycles/day$]$ into 16 subintervals, the same as would be achieved by a level $j = 4$ DWPT (see Figures 220) or MODWPT (Figure 236). The width of the crisscross in the lower left-hand corner of the plot gives the physical bandwidth of $\hat{S}_X^{(\mathrm{mt})}(\cdot)$ (i.e., $\frac{K+1}{(N+1)\,\Delta t} \doteq 0.0644$ cycles/day – here $\Delta t = 1/24$ days), while its height gives the length of a 95% confidence interval for a given $10 \cdot \log_{10}(S_X(f))$.

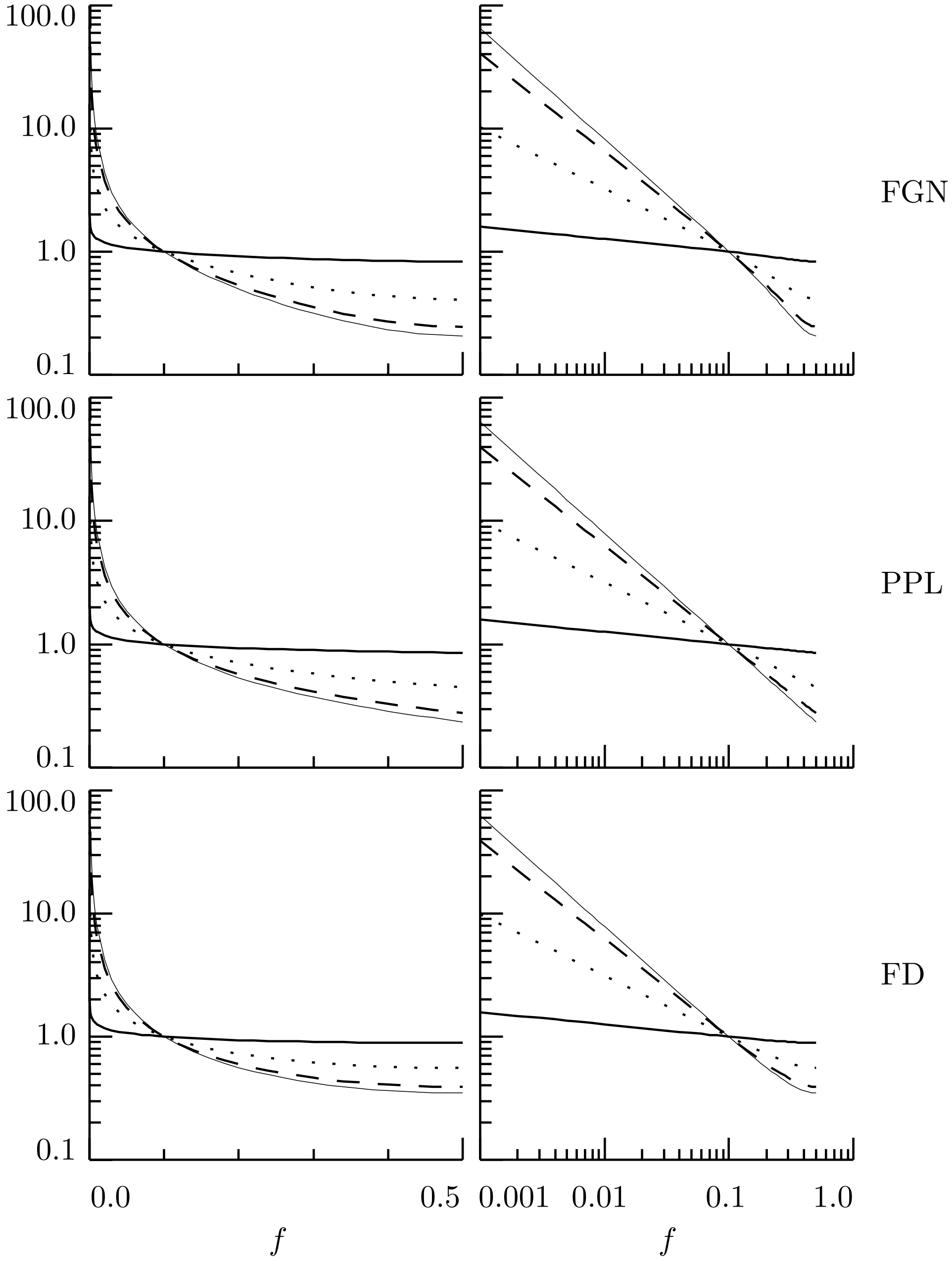

Figure 282. SDFs for FGN, PPL and FD processes (top to bottom rows, respectively) on both linear/log and log/log axes (left- and right-hand columns, respectively). Each SDF $S_X(\cdot)$ is normalized such that $S_X(0.1) = 1$. The table below gives the parameter values for the various plotted curves.

process	thick solid	dotted	dashed	thin solid
FGN	$H = 0.55$	$H = 0.75$	$H = 0.90$	$H = 0.95$
PPL	$\alpha = -0.1$	$\alpha = -0.5$	$\alpha = -0.8$	$\alpha = -0.9$
FD	$\delta = 0.05$	$\delta = 0.25$	$\delta = 0.40$	$\delta = 0.45$

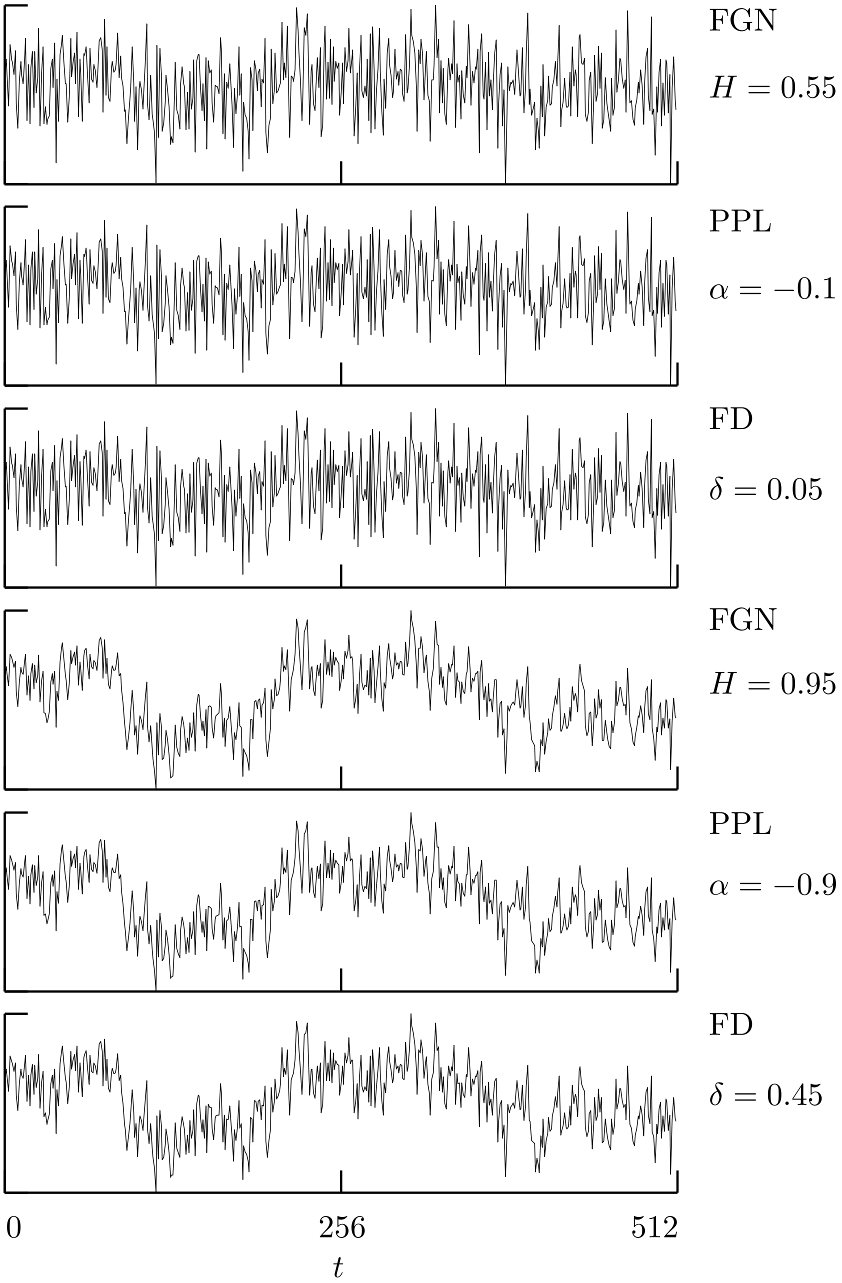

Figure 283. Simulated realizations of FGN, PPL and FD processes. The thick (thin) solid curves in Figure 282 show the SDFs for the top (bottom) three series – these SDFs differ markedly only at high frequencies. We formed each simulated $X_0, \ldots, X_{511}$ using the Davies–Harte method (see Section 7.8), which does so by transforming a realization of a portion $Z_0, \ldots, Z_{1023}$ of a white noise process (the Z_t values are on the Web site for this book – see page *xiv*). To illustrate the similarity of FGN, PPL and FD processes with comparable H, α and δ, we used the same Z_t to create all six series. Although the top (bottom) three series appear to be identical, estimates of their SDFs show high frequency differences consistent with their theoretical SDFs.

process	nonstationary LMP	stationary LMP	white noise	stationary not LMP
FGN	—	$\frac{1}{2} < H < 1$	$H = \frac{1}{2}$	$0 < H \leq \frac{1}{2}$
PPL	$\alpha \leq -1$	$-1 < \alpha < 0$	$\alpha = 0$	$\alpha \geq 0$
FD	$\delta \geq \frac{1}{2}$	$0 < \delta < \frac{1}{2}$	$\delta = 0$	$\delta \leq 0$

Table 286. Parameter ranges for each named stochastic process for which the form of the process is (a) nonstationary long memory, (b) stationary long memory, (c) white noise or (d) stationary but not long memory.

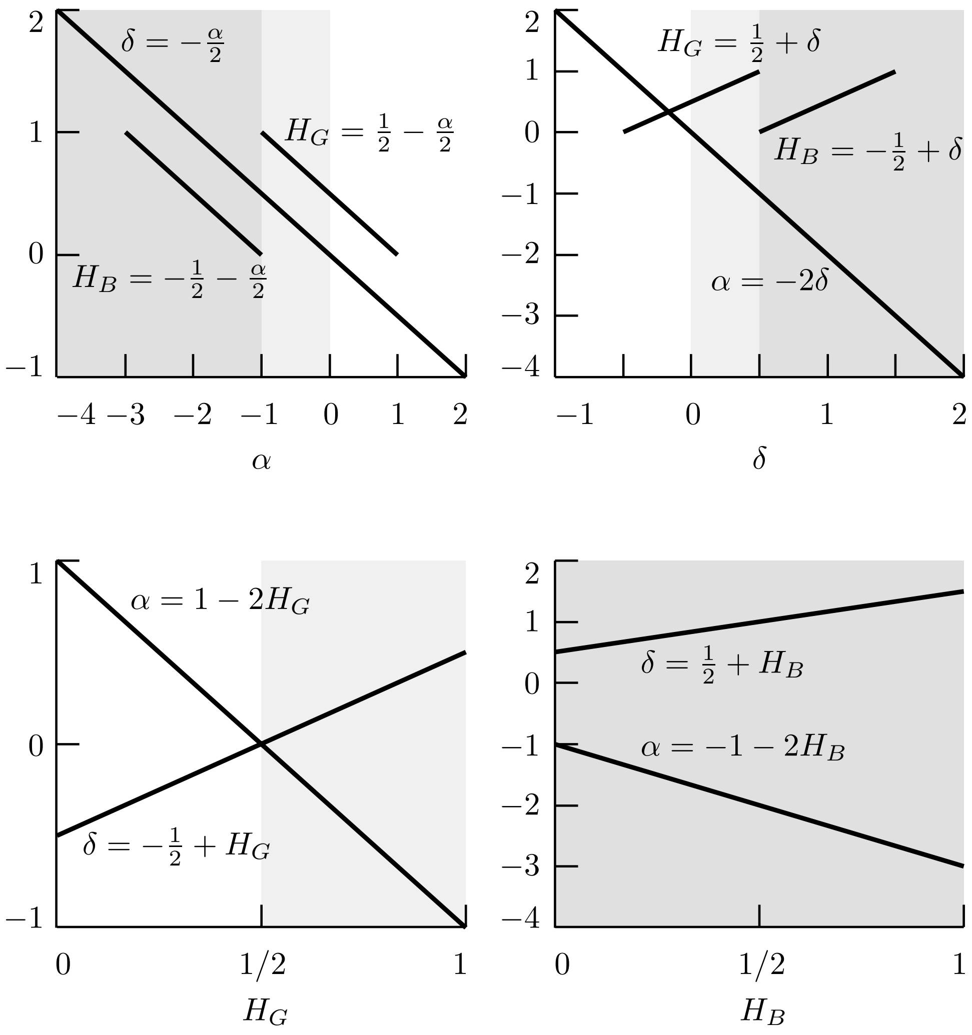

Figure 286. Relationships amongst the spectral slope α, the fractional difference parameter δ and the Hurst coefficient H (both for FGN and DFBM). The unshaded, lightly shaded and heavily shaded regions represent parameter values corresponding to, respectively, stationary processes without long memory, stationary long memory processes and nonstationary long memory processes (white noise processes occur when the boundary between the unshaded and lightly shaded regions crosses a thick line). For this plot only, we distinguish between H as a parameter for DFBM and for FGN by using H_B in the former case and H_G in the latter. Note that, while α and δ range over the entire real axis, we must have $0 < H < 1$ for both DFBM and FGN.

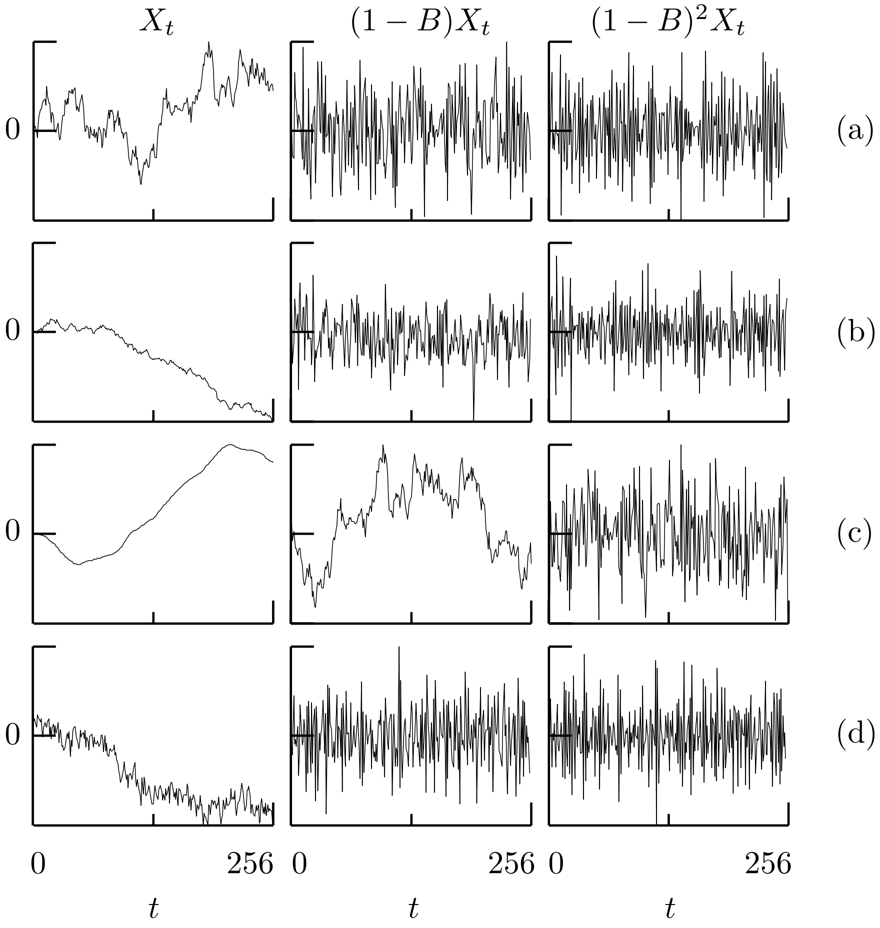

Figure 289. Simulated realizations of nonstationary processes $\{X_t\}$ with stationary backward differences of various orders (first column) along with their first backward differences $\{(1-B)X_t\}$ (second column) and second backward differences $\{(1-B)^2X_t\}$ (final column). From top to bottom, the processes are (a) a random walk; (b) a modified random walk, formed using a white noise sequence with mean $\mu_\varepsilon = -0.2$; (c) a random run; and (d) a process formed by summing the line given by $-0.05t$ and a simulation of a stationary FD process with $\delta = 0.45$.

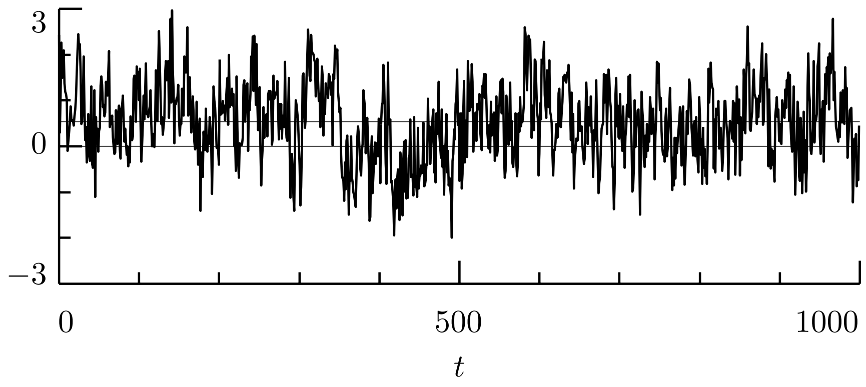

Figure 300. Realization of a fractional Gaussian noise (FGN) process with self-similarity parameter $H = 0.9$. The sample mean of approximately 0.53 and the true mean of zero are indicated by the thin horizontal lines.

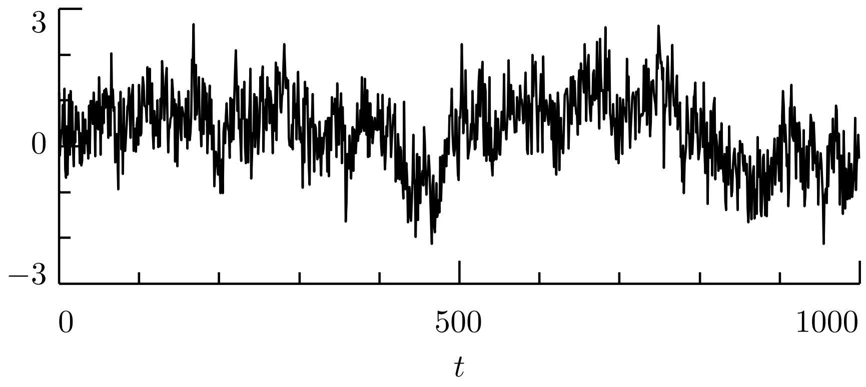

Figure 301. Realization of a stochastic process whose first order backward difference is an FGN process with self-similarity parameter $H = 0.1$. Depending upon its precise definition, the variance for this process is either infinite for all t or is time dependent and increases to infinity as $|t|$ goes to infinity.

$$X_t \longrightarrow \boxed{\mathcal{D}^d(\cdot)} \longrightarrow Y_t \longrightarrow \boxed{\mathcal{D}^{\frac{L}{2}-d}(\cdot)} \longrightarrow O_t \longrightarrow \boxed{\widetilde{\mathcal{A}}_L(\cdot)} \longrightarrow \overline{W}_{1,t}$$

Figure 305. Flow diagram depicting filtering of $\{X_t\}$ using the Daubechies MODWT wavelet filter $\{\tilde{h}_l\}$ to obtain $\overline{W}_{1,t}$. The actual filter can be decomposed into a cascade involving three filters (indicated above by their squared gain functions $\mathcal{D}^d(\cdot)$, $\mathcal{D}^{\frac{L}{2}-d}(\cdot)$ and $\widetilde{\mathcal{A}}_L(\cdot)$). By assumption the dth order backward difference of $\{X_t\}$ is a stationary process $\{Y_t\}$, while the wavelet filter has a width $L \geq 2d$ and hence implicitly involves $L/2$ backward difference filters $\mathcal{D}(\cdot)$. When $L = 2d$, the processes $\{Y_t\}$ and $\{O_t\}$ are identical (the filter $\mathcal{D}^0(\cdot)$ is taken to be a 'do nothing' filter); when $L > 2d$, we obtain $\{O_t\}$ by taking $\frac{L}{2} - d$ successive backward differences of $\{Y_t\}$. In either case, the process $\{O_t\}$ is then subjected to the smoothing filter $\widetilde{\mathcal{A}}_L(\cdot)$, yielding the first level wavelet coefficient process $\{\overline{W}_{1,t}\}$.

δ	$L = 2$	$L = 4$	$L = 6$	$L = 8$
$-1/2$	0.85	0.89	0.91	0.92
$-1/4$	0.81	0.86	0.89	0.90
$-1/8$	0.78	0.84	0.87	0.89
0	0.75	0.82	0.85	0.87
$1/8$	0.72	0.80	0.83	0.86
$1/4$	0.68	0.77	0.81	0.84
$1/2$	0.61	0.72	0.77	0.80
1	0.50	0.61	0.67	0.71
$3/2$	—	0.52	0.58	0.62

Table 310. Asymptotic relative efficiencies (AREs) of the DWT-based estimator $\hat{\hat{\nu}}_X^2(\tau_1)$ with respect to the MODWT-based estimator $\hat{\nu}_X^2(\tau_1)$ for various combinations of FD processes and Daubechies wavelet filters. Note that an ARE of less than unity implies that $\hat{\nu}_X^2(\tau_1)$ has smaller large sample variance than $\hat{\hat{\nu}}_X^2(\tau_1)$.

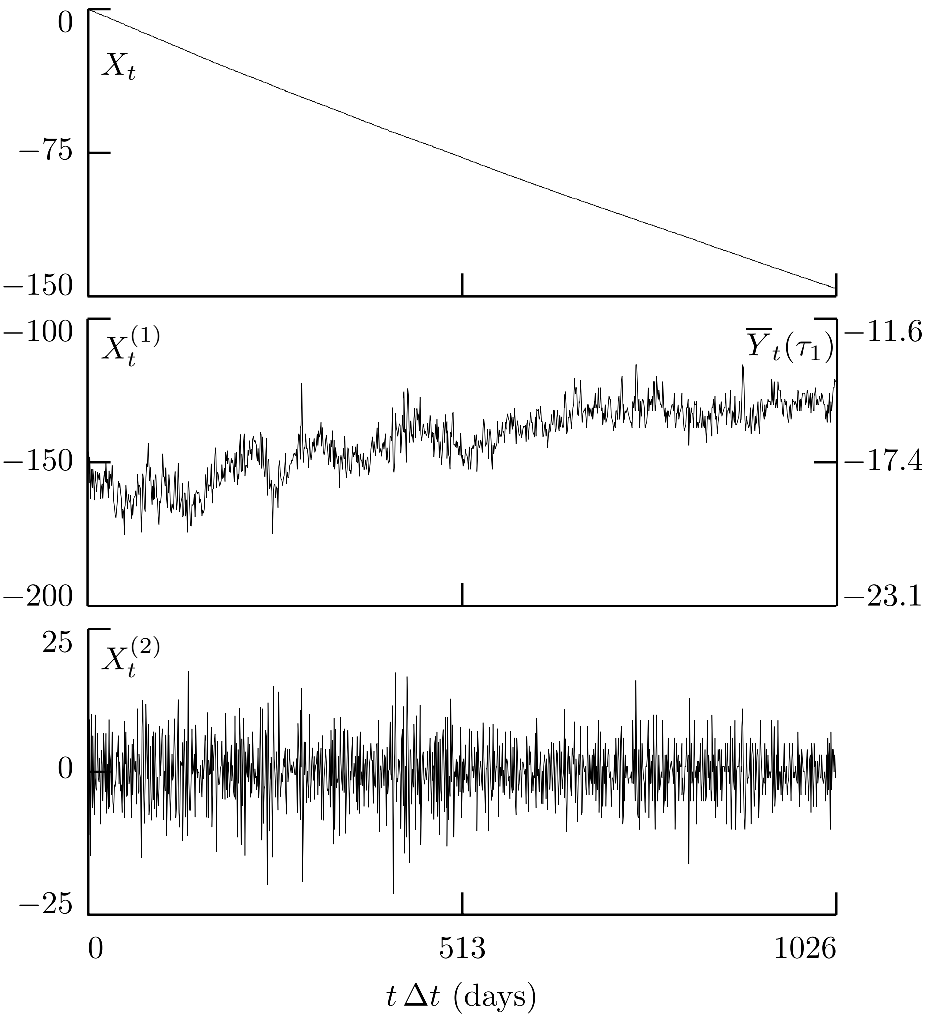

Figure 318. Plot of differences in time $\{X_t\}$ as kept by clock 571 (a cesium beam atomic clock) and as kept by the time scale UTC(USNO) maintained by the US Naval Observatory, Washington, DC (top plot); its first backward difference $\{X_t^{(1)}\}$ (middle); and its second backward difference $\{X_t^{(2)}\}$ (bottom). In the middle plot, $\overline{Y}_t(\tau_1)$ denotes the τ_1 average fractional frequency deviates (given in parts in 10^{13}) – these are defined by Equation (321c) and are proportional to $X_t^{(1)}$.

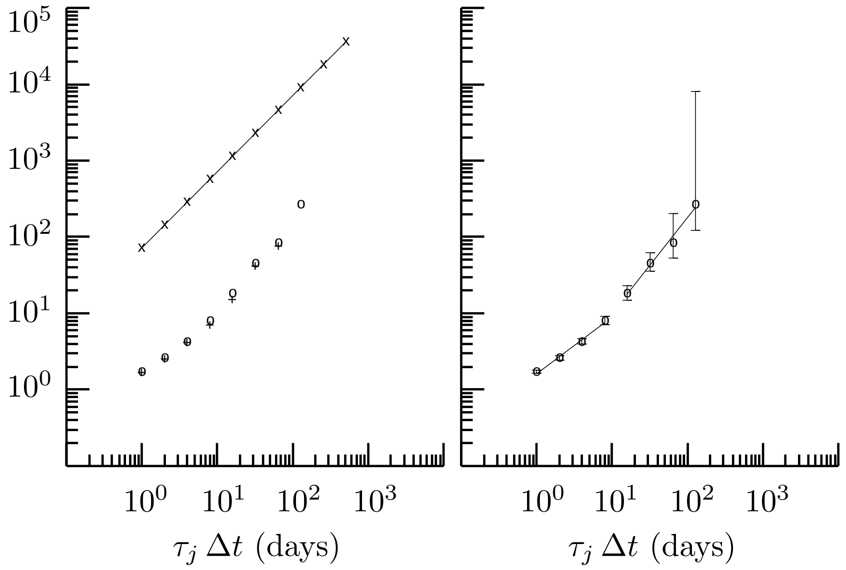

Figure 319. Square roots of wavelet variance estimates for atomic clock time differences $\{X_t\}$ based upon the unbiased MODWT estimator and the following wavelet filters: Haar (x's in left-hand plot, through which a least squares line has been fit), D(4) (circles in left- and right-hand plots) and D(6) (pluses in left-hand plot). The 95% confidence intervals in the second plot are the square roots of intervals computed using Equation (313c), with η given by $\hat{\eta}_1$ of Equation (313d) for $j = 1, \ldots, 6$ and by η_3 of Equation (314c) for $j = 7, 8$. The actual values for the various $\hat{\nu}_X(\tau_j)$ are listed on the Web site for this book – see page *xiv*.

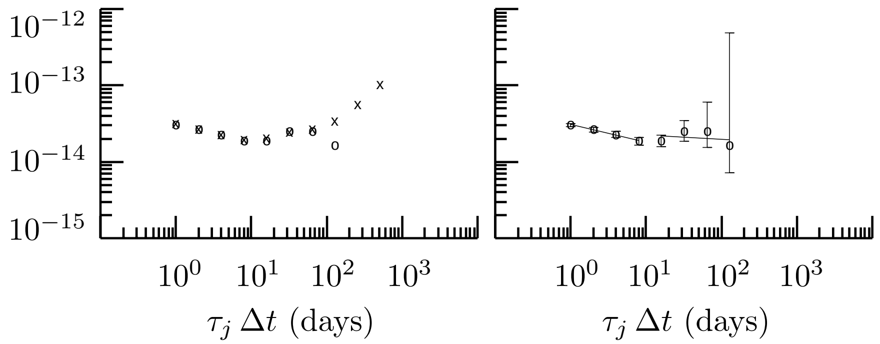

Figure 322. Square roots of wavelet variance estimates for atomic clock one day average fractional frequency deviates $\{\overline{Y}_t(\tau_1)\}$ based upon the unbiased MODWT estimator and the following wavelet filters: Haar (`x`'s in left-hand plot) and D(4) (circles in left and right-hand plots). The actual values for $\hat{\nu}_{\overline{Y}}(\tau_j)$ are listed on the Web site for this book – see page *xiv*.

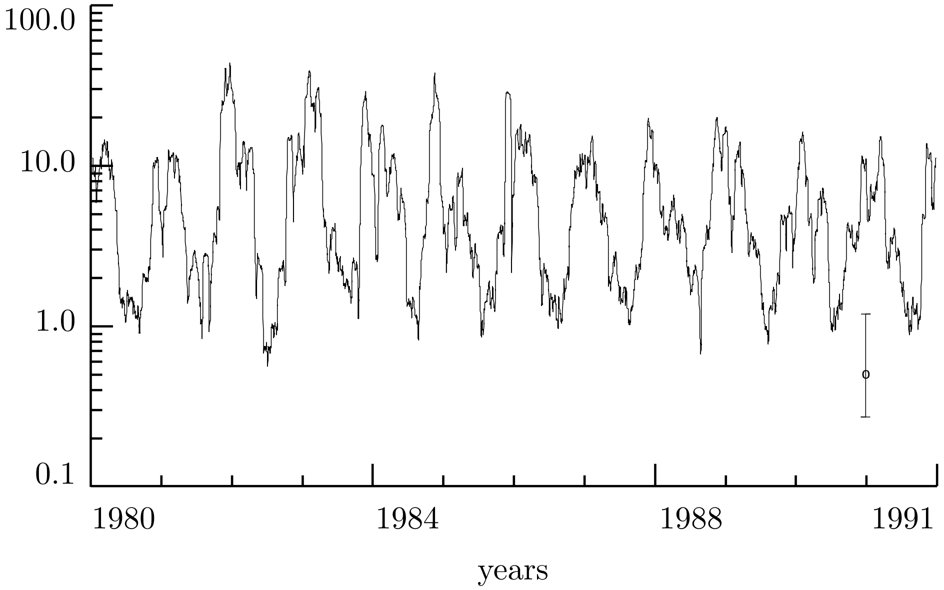

Figure 324. Estimated time-dependent LA(8) wavelet variances for physical scale $\tau_2 \, \Delta t =$ 1 day for the Crescent City subtidal sea level variations of Figure 186, along with a representative 95% confidence interval based upon a hypothetical wavelet variance estimate of 1/2 and a chi-square distribution with $\nu = 15.25$ (see text for details).

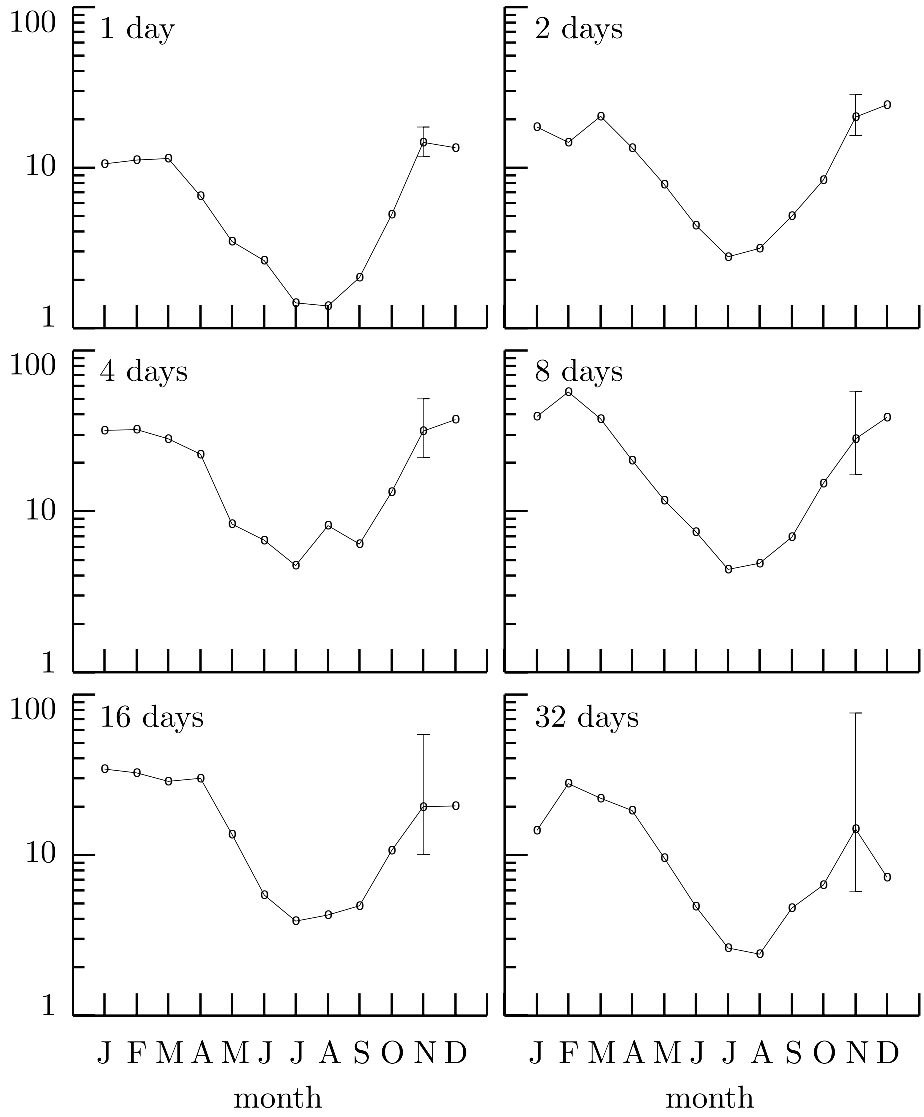

Figure 326. Estimated LA(8) wavelet variances for physical scales $\tau_j \, \Delta t = 2^{j-2}$ days, $j = 2, \ldots, 7$, grouped by calendar month for the subtidal sea level variations of Figure 186.

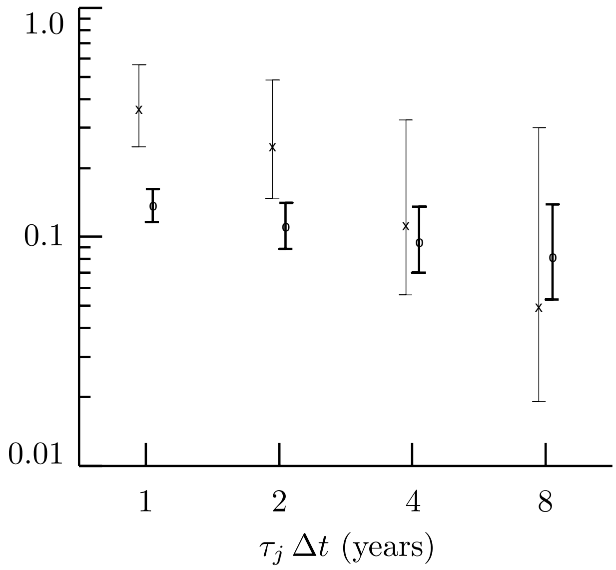

Figure 327. Estimated Haar wavelet variances for the Nile River minima time series before and after year 715.5 (`x`'s and `o`'s, respectively), along with 95% confidence intervals (thin and thick lines, respectively) based upon a chi-square approximation with EDOFs determined by η_3 of Equation (314c). The actual values for $\hat{\nu}_X^2(\tau_j)$ are listed on the Web site for this book – see page *xiv*.

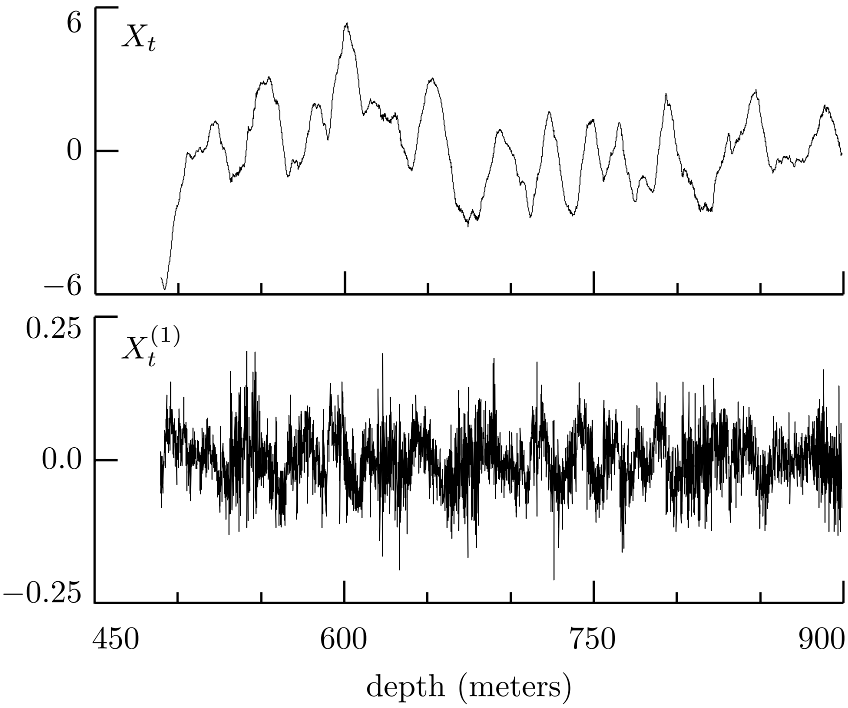

Figure 328. Selected portion $\{X_t\}$ of $N = 4096$ vertical shear measurements (top plot) and associated backward differences $\{X_t^{(1)}\}$ (bottom). The full series is plotted at the bottom of Figure 194, on which the subseries is delineated by two thin vertical lines.

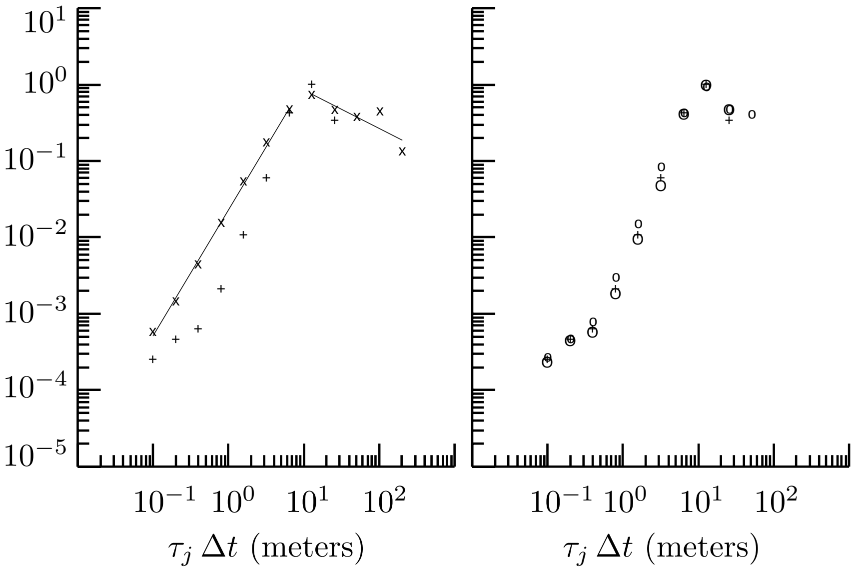

Figure 329. Wavelet variances estimated for vertical shear series using the unbiased MODWT estimator and the following wavelet filters: Haar (x's in left-hand plot, through which two regression lines have been fit), D(4) (small circles, right-hand plot), D(6) (+'s, both plots) and LA(8) (big circles, right-hand plot). The values for the various $\hat{\nu}_X^2(\tau_j)$ are listed on the Web site for this book – see page *xiv*.

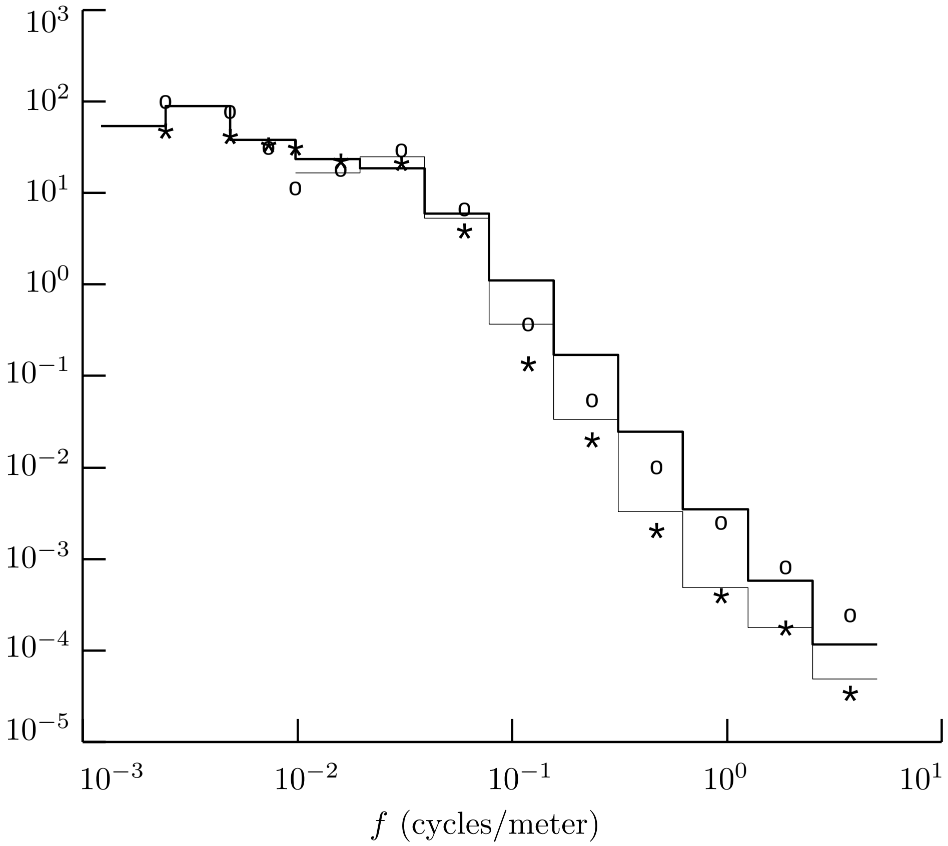

Figure 330. Comparison of 'octave band' SDF estimates for the vertical shear measurements based on the periodogram (o's), a multitaper SDF estimate formed using $K = 7$ sine tapers ($\star$'s) and Haar and D(6) wavelet variance estimates (thick and thin staircases, respectively). See text for details.

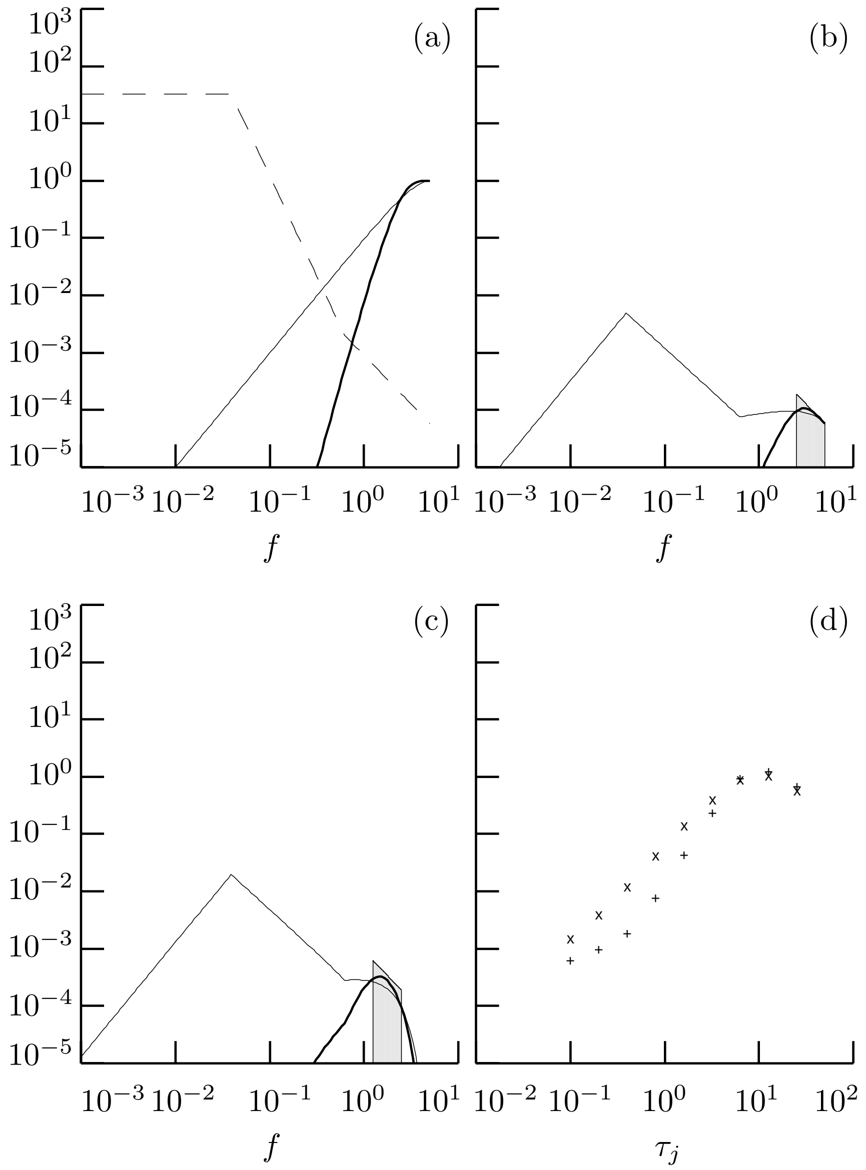

Figure 331. Leakage in Haar wavelet variance (see text for details).

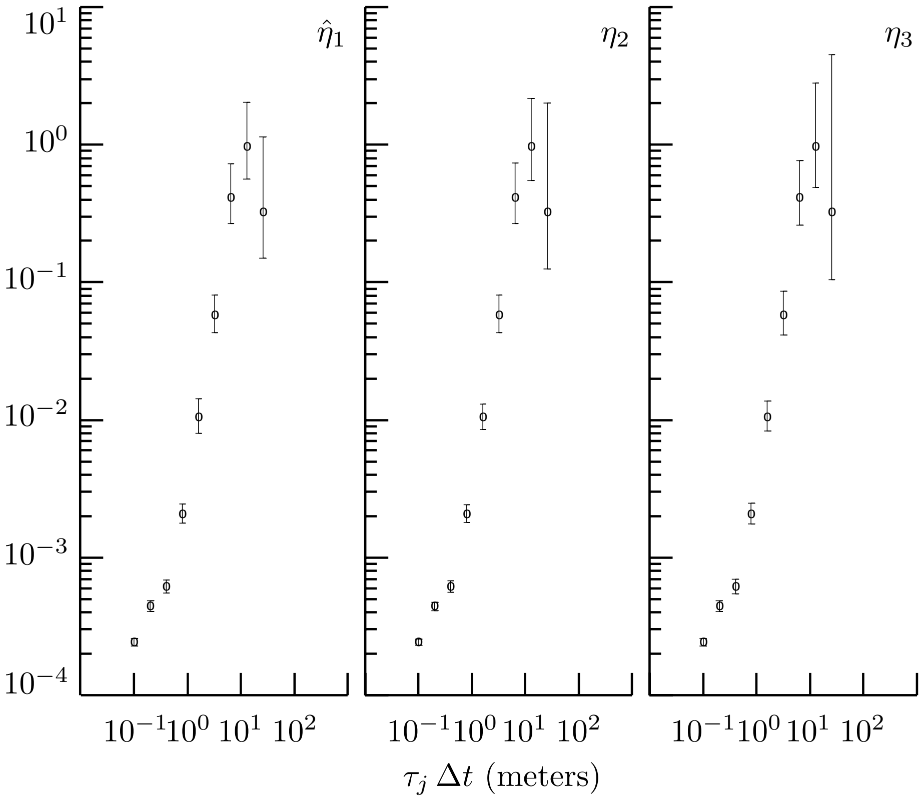

Figure 333. 95% confidence intervals for the D(6) wavelet variance for the vertical ocean shear series. The intervals are based upon the unbiased MODWT estimator (+'s in Figure 329 and o's above) and χ^2 approximations to its distribution with EDOFs determined by, from left to right, $\hat{\eta}_1$ of Equation (313d); η_2 of Equation (314b) using the nominal model for $S_X(\cdot)$ given by Equation (331); and η_3 of Equation (314c) (Table 333 lists the values for the EDOFs).

	j								
	1	2	3	4	5	6	7	8	9
$\hat{\eta}_1$	1890	1027	584	289	94	82	32	20	8
η_2	2850	1633	899	359	173	78	31	17	5
η_3	2046	1020	508	251	123	59	27	11	3
M_j	4091	4081	4061	4021	3941	3781	3461	2821	1541

Table 333. Equivalent degrees of freedom $\hat{\eta}_1$, η_2 and η_3 (rounded to the nearest integer) associated with the D(6) wavelet variance estimates $\hat{\nu}_X^2(\tau_j)$, $j = 1, \ldots, 9$, shown in Figure 333. The bottom row gives the number M_j of MODWT wavelet coefficients at each scale.

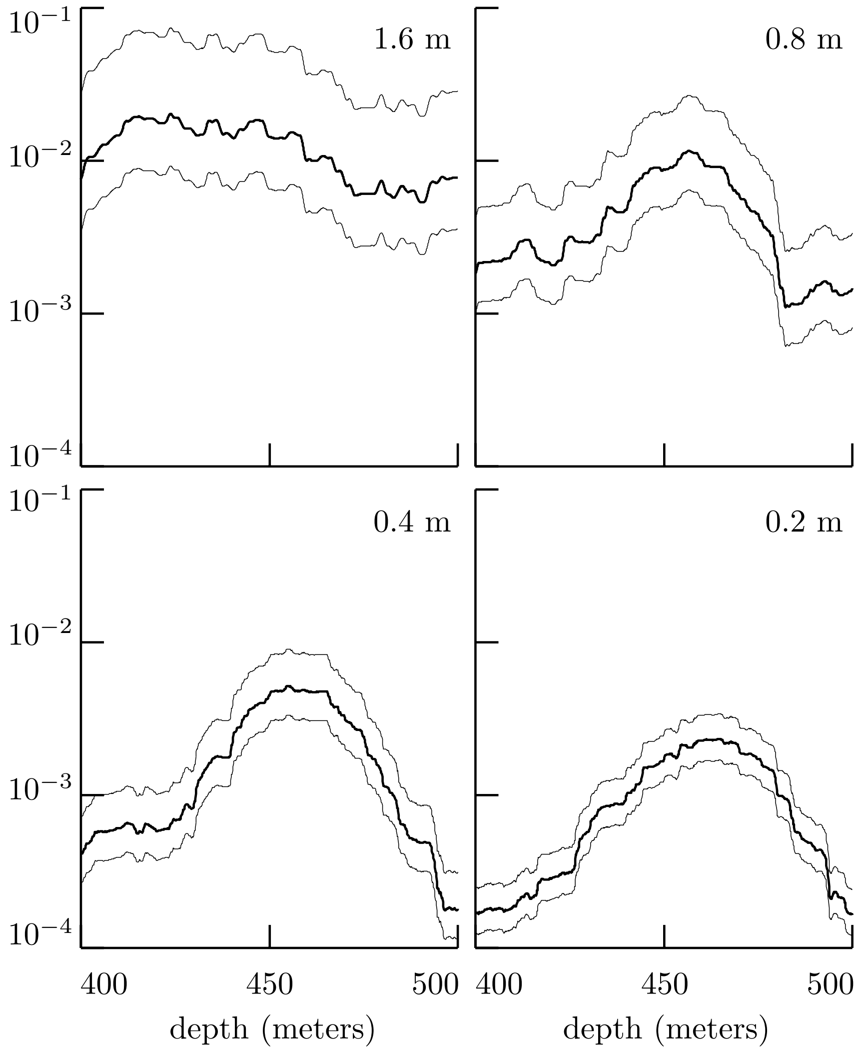

Figure 334. Estimated LA(8) wavelet variances (thick curves) for the shear data, computed using a running segment of 257 MODWT wavelet coefficients for depths surrounding 450 meters. As marked on the plots, the physical scales are 0.2, 0.4, 0.8 and 1.6 meters (i.e., $\tau_j\,\Delta t$, $j = 2, \ldots, 5$). The thin curves above and below the estimates are 95% confidence intervals as per Equation (313c) with $\eta = 257/2^j$ (this is in accordance with η_3 of Equation (314c)).

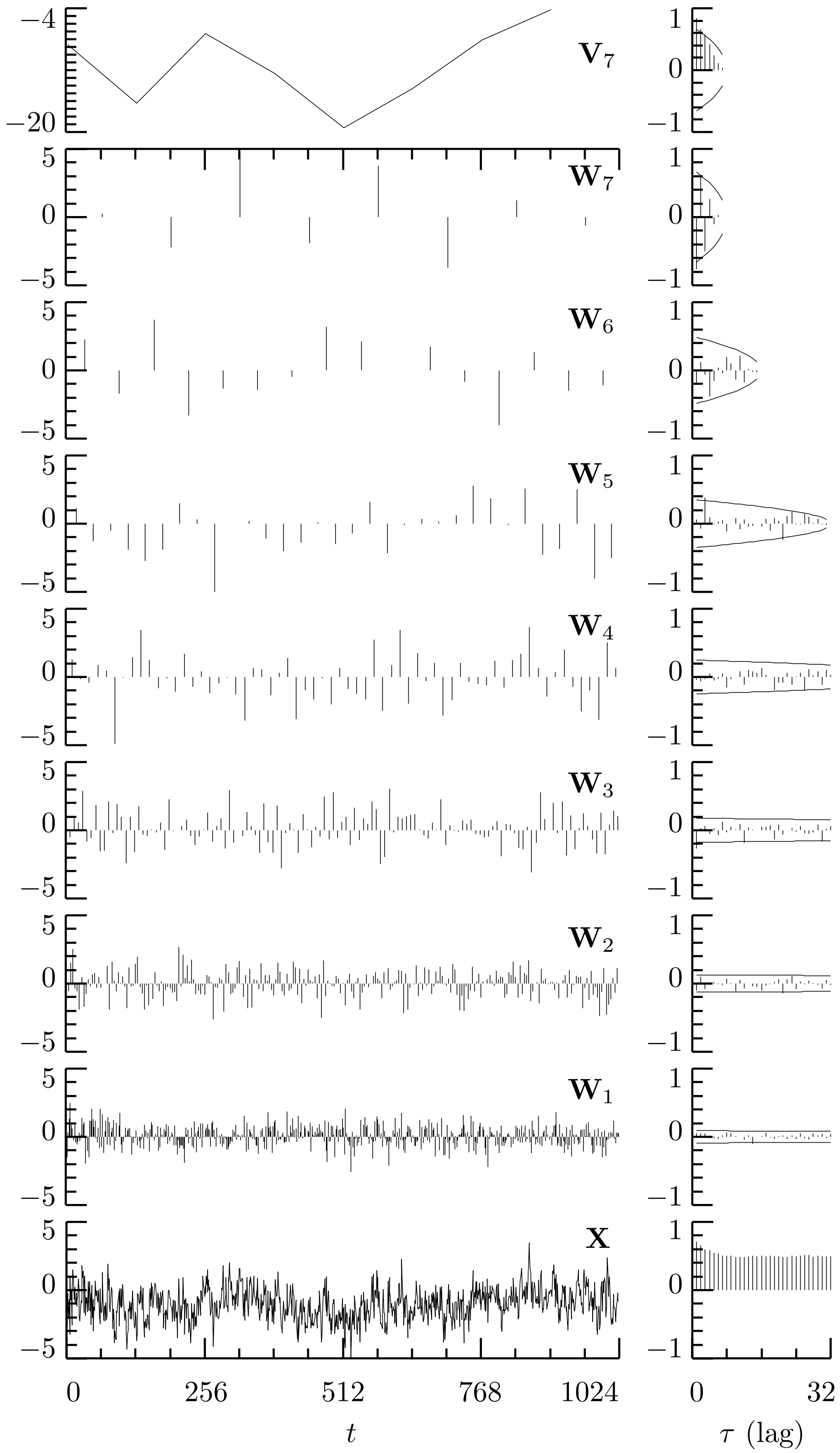

Figure 342. LA(8) DWT coefficients for simulated FD(0.4) time series and sample ACSs.

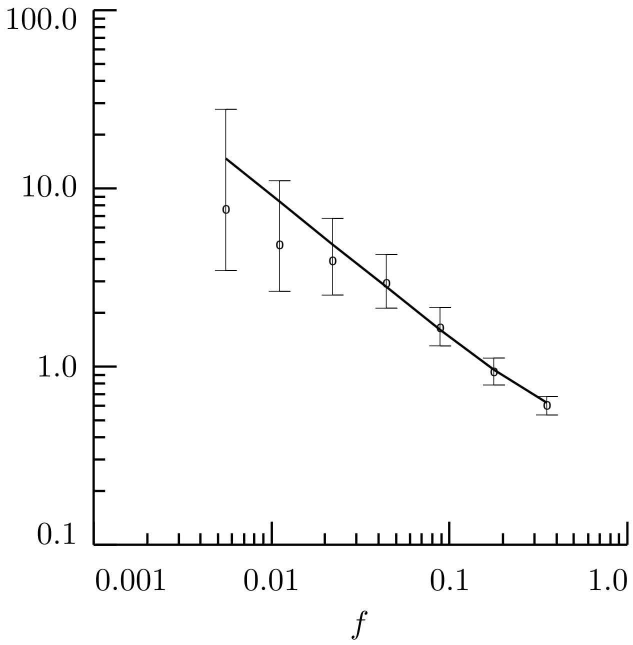

Figure 344. Sample variances of LA(8) wavelet coefficients from Figure 342 for – from right to left – levels $j = 1, \ldots, 7$ (circles) along with true FD(0.4) SDF evaluated at the center frequency $1/2^{j+\frac{1}{2}}$ of the octave bands $[\frac{1}{2^{j+1}}, \frac{1}{2^j}]$ (thick curve).

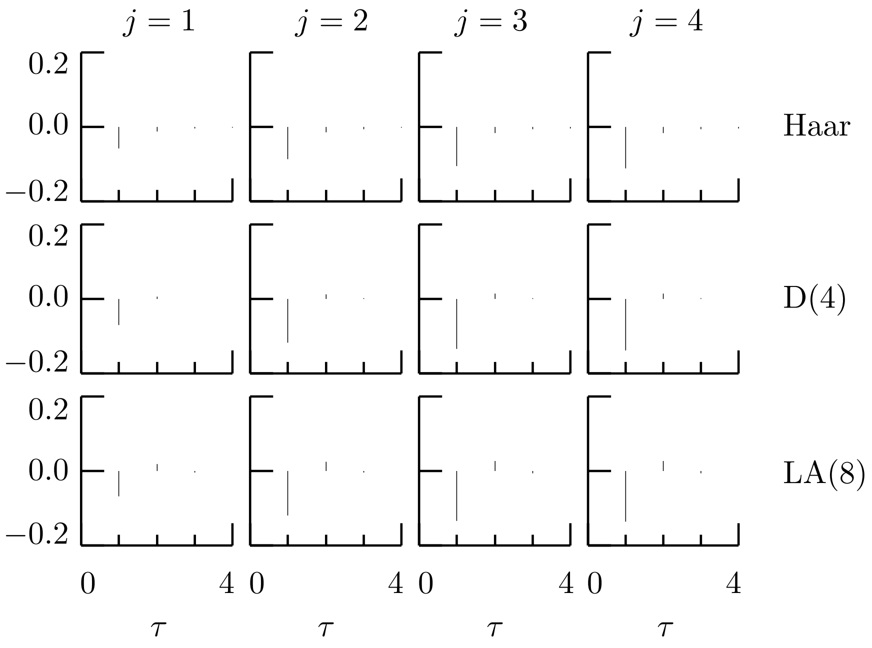

Figure 346a. ACSs at $\tau = 1, \ldots, 4$ for Haar, D(4) and LA(8) wavelet coefficients $W_{j,t}$, $j = 1, \ldots, 4$, of an FD(0.4) process. The ACS values are plotted as deviations from zero (some are not visible because they are so close to zero).

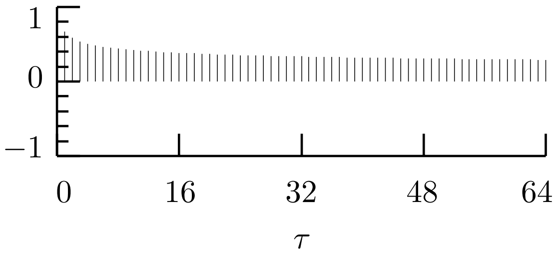

Figure 346b. ACS for FD process with $\delta = 0.4$ out to lag $\tau = 64$.

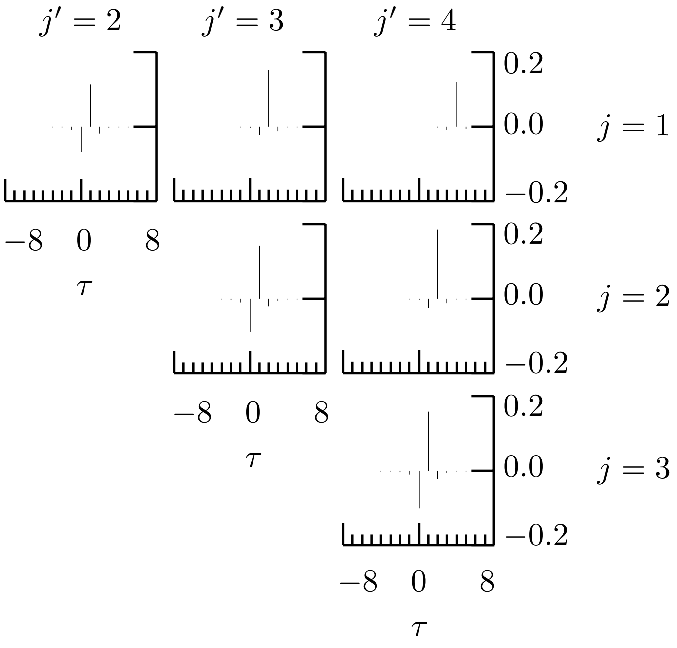

Figure 347a. Correlation between the Haar wavelet coefficients $W_{j,t}$ and $W_{j',t'}$ formed from an FD(0.4) process and for levels satisfying $1 \le j < j' \le 4$. By setting $t = 2^{|j'-j|-1}$ and $t' = t + \tau$ with $\tau = -8, \ldots, 8$, we capture two coefficients exhibiting the maximum absolute correlation over all possible combinations of t and t'.

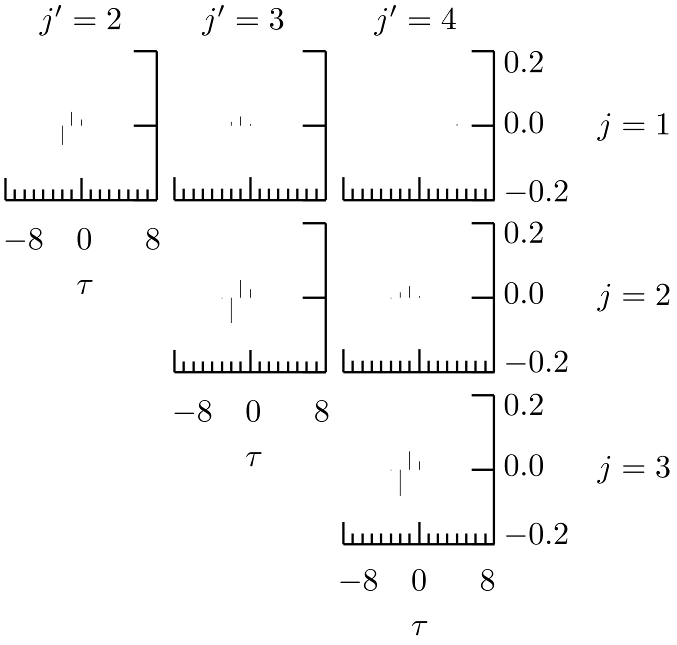

Figure 347b. As in Figure 347a, but now using the LA(8) DWT and with t set as per Equation (346).

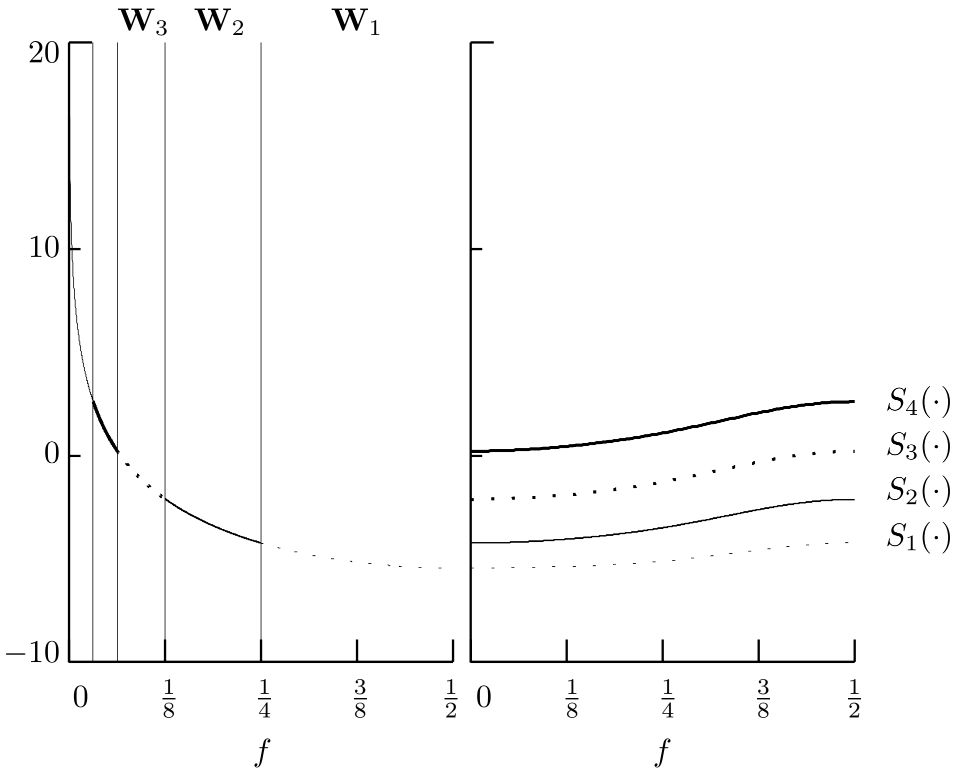

Figure 349. SDFs for an FD(0.4) process (left-hand plot) and for nonboundary LA(8) wavelet coefficients in $\mathbf{W}_1$, $\mathbf{W}_2$, $\mathbf{W}_3$ and $\mathbf{W}_4$ (right-hand). The vertical axis is in units of decibels (i.e., we plot $\log_{10}(S_X(f))$ versus f). The vertical lines in the left-hand plot denote the nominal pass-bands for the four $\mathbf{W}_j$.

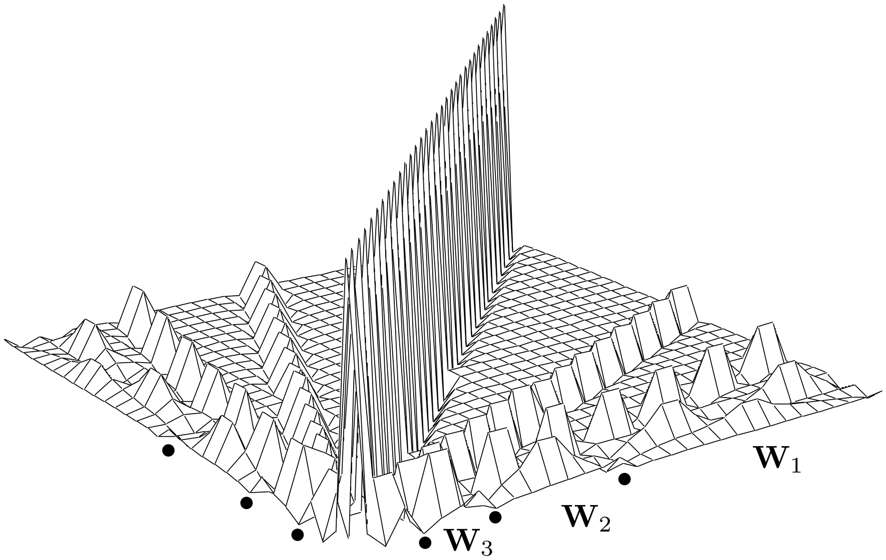

Figure 350. Correlation matrix of Haar wavelet coefficients for a portion of length $N = 32$ from an FD process with $\delta = 0.4$.

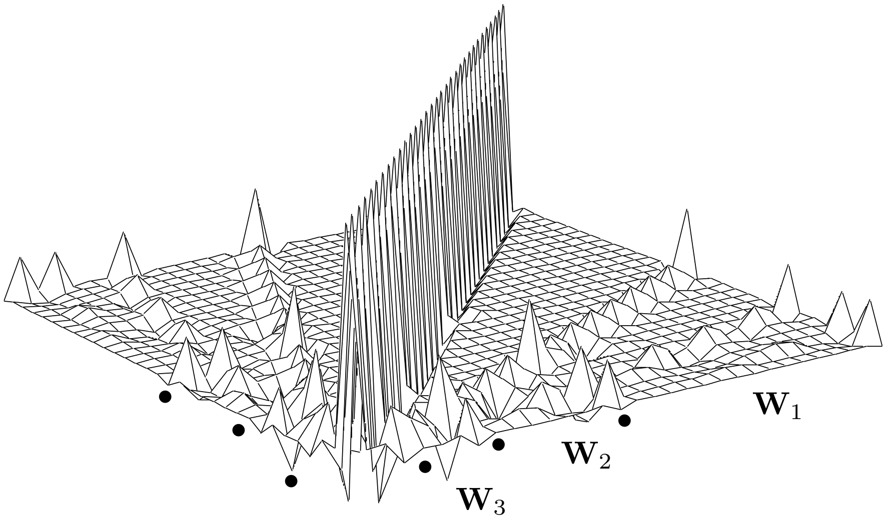

Figure 351a. As in Figure 350, but now using the D(4) DWT.

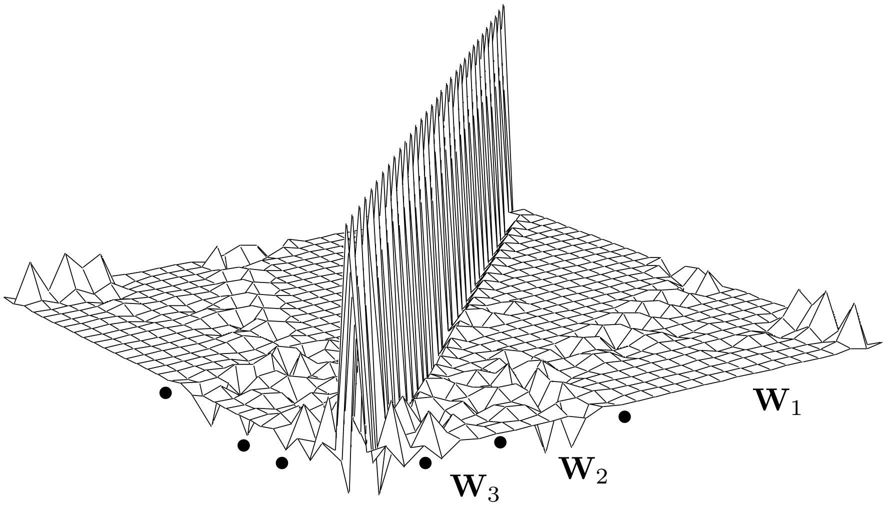

Figure 351b. As in Figure 350, but now using the LA(8) DWT.

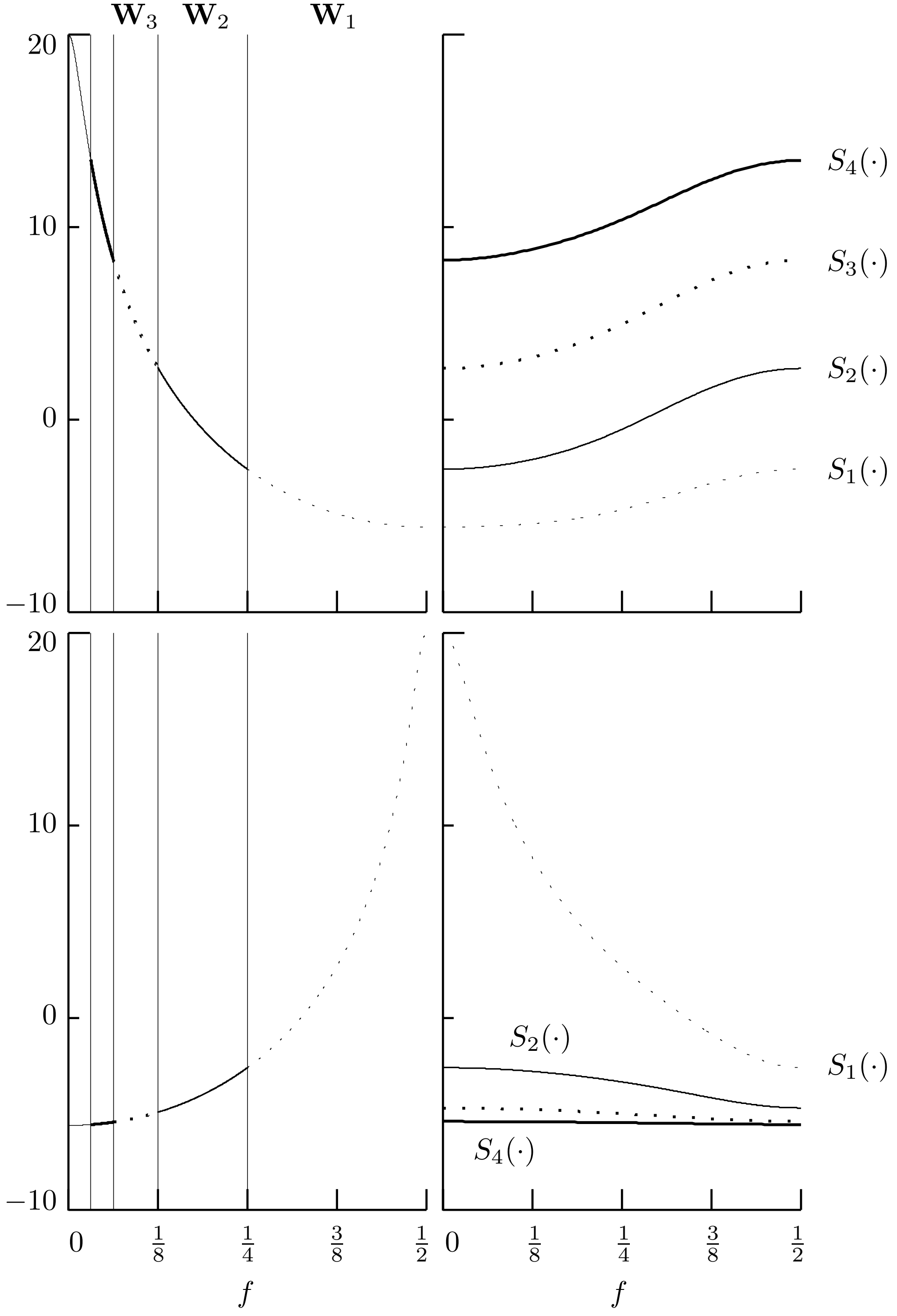

Figure 352. SDFs for AR(1) processes with $\phi = 0.9$ (top left-hand plot) and -0.9 (bottom left-hand) and for corresponding nonboundary LA(8) wavelet coefficients in $\mathbf{W}_1$ to $\mathbf{W}_4$ (right-hand plots). The vertical axes are in decibels, and the vertical lines in the left-hand plots delineate the nominal pass-bands for the four $\mathbf{W}_j$.

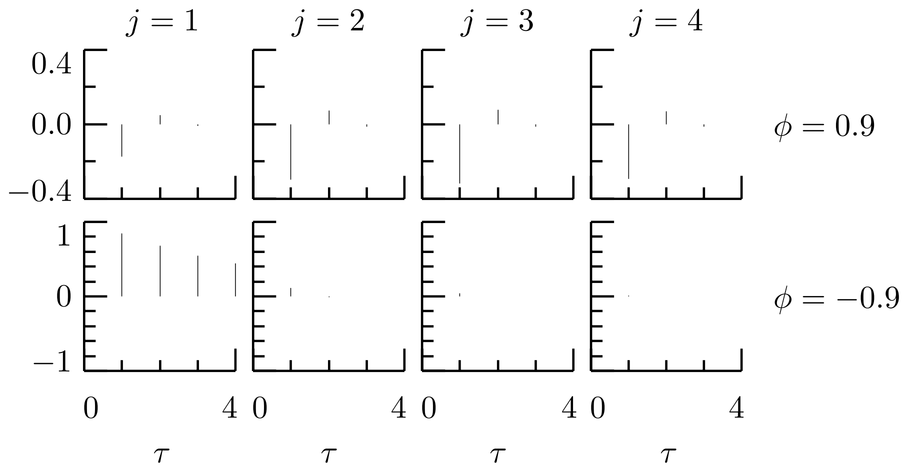

Figure 353. ACSs at $\tau = 1, \ldots, 4$ for LA(8) wavelet coefficients $W_{j,t}$, $j = 1, \ldots, 4$, of an AR(1) process with $\phi = 0.9$ and -0.9 (top and bottom rows, respectively).

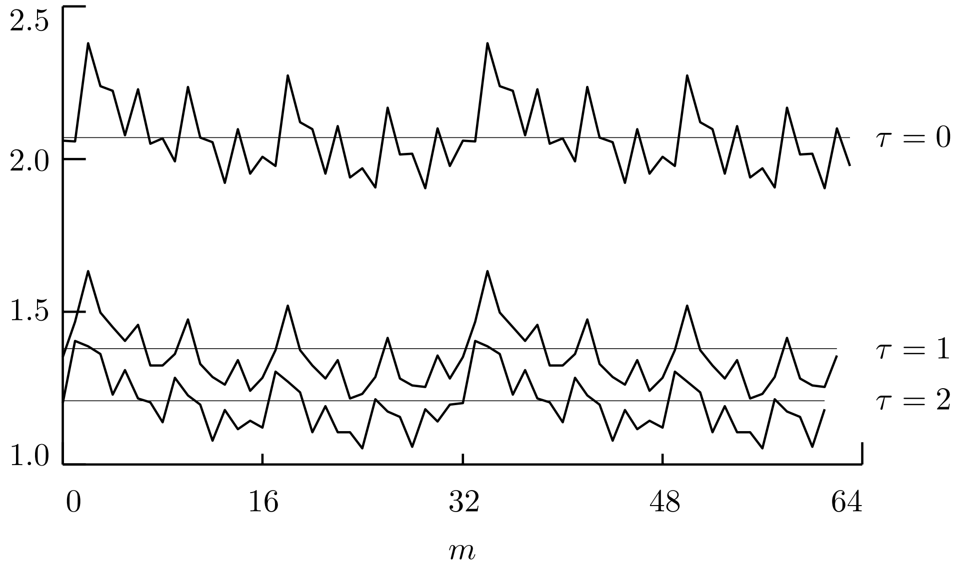

Figure 356. Diagonal elements $\Sigma_{\mathbf{Y},m,m+\tau}$ and $\Sigma_{\mathbf{X},m,m+\tau}$, $m = 0, \ldots, N-1-\tau$, of the covariance matrices $\Sigma_{\mathbf{Y}}$ and $\Sigma_{\mathbf{X}}$ (thick jagged curves and thin horizontal lines, respectively) for sample size $N = 64$ from an FD(0.4) process with $\sigma_{\varepsilon}^2 = 1$ and with $\Sigma_{\mathbf{Y}}$ constructed using an LA(8) DWT. Three diagonals are plotted for each covariance matrix, namely, the main diagonal ($\tau = 0$) and the first two off-diagonals ($\tau = 1$ and 2). Whereas $\Sigma_{\mathbf{X}}$ exhibits the Toeplitz structure required for a stationary process, its approximation $\Sigma_{\mathbf{Y}}$ does not.

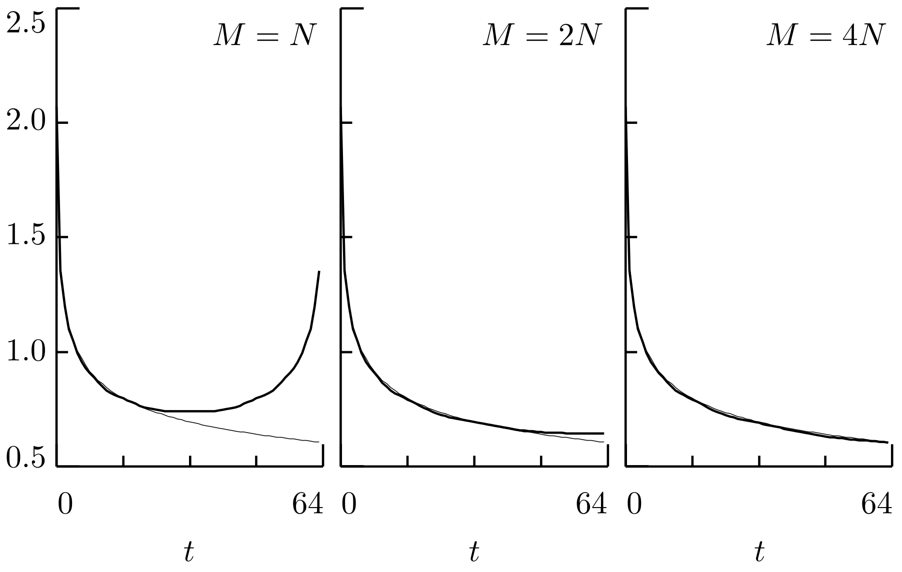

Figure 357. True ACVS (thin curves) and wavelet-based approximate ACVSs (thick) for an FD(0.4) process. The approximating ACVSs are based on an LA(8) DWT in which we generate a series of length M and then extract a series of length $N = 64$. As M goes from N to $4N$, the approximate ACVS gets closer to the true ACVS.

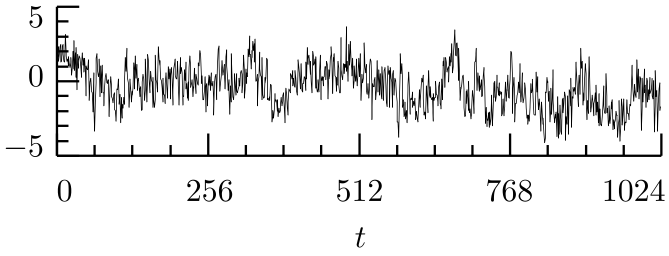

Figure 358. LA(8) wavelet-based simulation of a series of length $N = 1024$ from an FD process with zero mean and with parameters $\delta = 0.4$ and $\sigma_{\varepsilon}^2 = 1.0$.

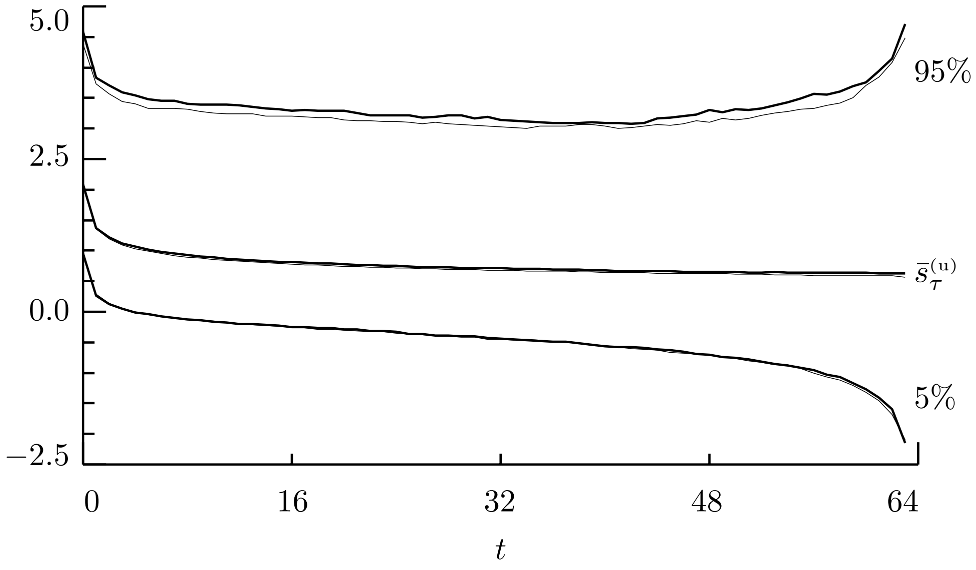

Figure 359. Estimated ACVSs averaged over 10 000 realizations generated via the Davies–Harte method (thin curve, middle of the plot) and the LA(8) wavelet-based method (thick curve) for an FD(0.4) process. The corresponding lower and upper pairs of curves indicate the 5% and 95% percentage points of the empirical distribution of the 10 000 simulations.

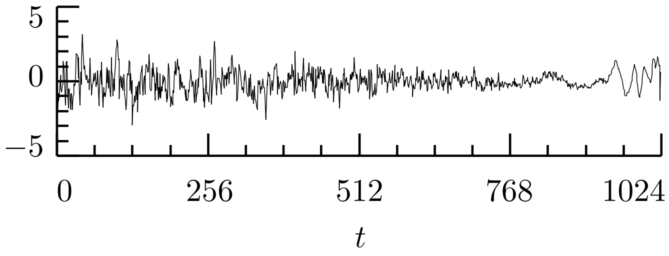

Figure 360. LA(8) wavelet-based simulation of a series of length $N = 1024$ from process with time varying statistical properties.

δ		MLE			
		Haar	D(4)	LA(8)	exact
0.25	mean	0.2184	0.2293	0.2328	0.2374
	bias	−0.0316	−0.0207	−0.0172	−0.0126
	SD	0.0713	0.0705	0.0710	0.0673
	RMSE	0.0780	0.0735	0.0731	0.0685
0.4	mean	0.3614	0.3727	0.3768	0.3797
	bias	−0.0386	−0.0273	−0.0232	−0.0203
	SD	0.0675	0.0652	0.0640	0.0604
	RMSE	0.0778	0.0707	0.0681	0.0637

Table 363. Sample mean, bias, standard deviation and root mean square error of 1024 wavelet-based approximate MLEs $\tilde{\delta}^{(\mathrm{s})}$ of the parameter δ based on the likelihood function of Equation (362a) using Haar, D(4) and LA(8) wavelet filters. All 1024 time series were of length $N = 128$ and were simulated using the Davies–Harte method. Corresponding statistics for exact MLEs $\hat{\delta}$ are given in the final column.

		MLE			
δ		Haar	D(4)	LA(8)	exact
0.25	mean	0.2256	0.2363	0.2402	0.2443
	bias	−0.0244	−0.0137	−0.0098	−0.0057
	SD	0.0505	0.0495	0.0502	0.0479
	RMSE	0.0561	0.0514	0.0511	0.0483
0.4	mean	0.3710	0.3832	0.3886	0.3900
	bias	−0.0290	−0.0168	−0.0114	−0.0100
	SD	0.0488	0.0478	0.0465	0.0437
	RMSE	0.0567	0.0506	0.0479	0.0448

Table 364. As in Table 363, but now with $N = 256$.

δ		MLE			
		Haar	D(4)	LA(8)	exact
0.25	mean	0.2058	0.2182	0.2227	0.2274
	bias	−0.0442	−0.0318	−0.0273	−0.0226
	SD	0.0559	0.0551	0.0557	0.0528
	RMSE	0.0712	0.0636	0.0620	0.0575
0.4	mean	0.3449	0.3602	0.3672	0.3687
	bias	−0.0551	−0.0398	−0.0328	−0.0313
	SD	0.0550	0.0538	0.0525	0.0494
	RMSE	0.0778	0.0669	0.0619	0.0585

Table 366. As in Table 364, but now with the process mean assumed unknown and hence estimated using the sample mean $\overline{X}$.

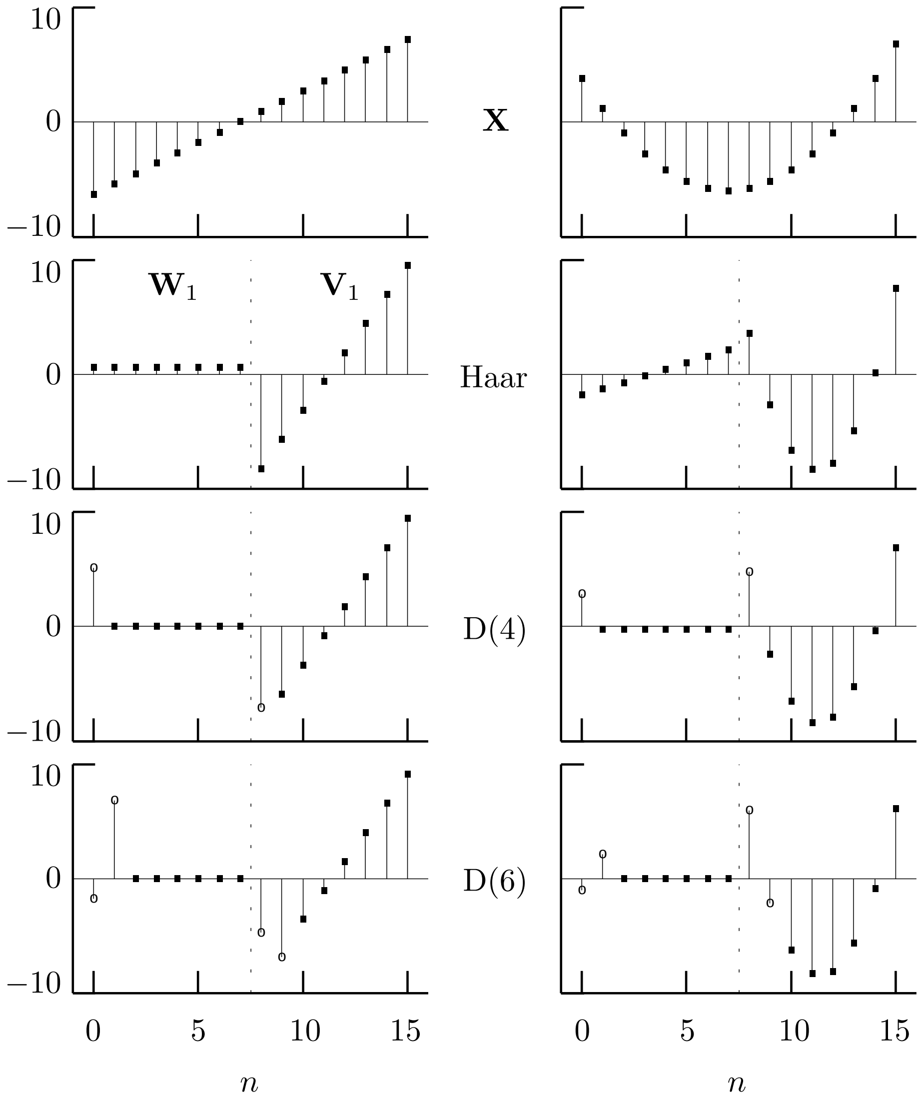

Figure 369. Linear and quadratic trends $\mathbf{T}$ (top plots), below which are shown their partial DWT coefficients $\mathbf{W} = [\mathbf{W}_1^T, \mathbf{V}_1^T]^T$ based on the Haar, D(4) and D(6) wavelet filters (second to fourth rows, respectively). The vertical dotted lines delineate the subvectors $\mathbf{W}_1$ and $\mathbf{V}_1$. Boundary wavelet and scaling coefficients are indicated by circles (there are none for the Haar; one each in $\mathbf{W}_1$ and $\mathbf{V}_1$ for the D(4); and two in each of the subvectors for the D(6)). Because the Haar wavelet does not reduce either linear or quadratic polynomials to zero, its wavelet coefficients are all nonzero; on the other hand, the D(6) wavelet reduces both polynomials to zero, so its six nonboundary wavelet coefficients are zero in both $\mathbf{W}_1$. The D(4) wavelet can handle a linear polynomial, but not a quadratic, which is why its seven nonboundary wavelet coefficients are zero for the former and nonzero for the latter. (For the record, the linear and quadratic trends are defined by $T_t = 0.9 \cdot (t - 7)$ and $T_t = 0.2 \cdot (t - 7)^2 - 6$. This illustration is due to W. Constantine, MathSoft, Seattle.)

δ		MLE Haar	D(4)	LA(8)	exact
0.4	mean	0.3670	0.3762	0.3792	0.3900
	bias	-0.0330	-0.0238	-0.0208	-0.0100
	SD	0.0588	0.0732	0.0943	0.0437
	RMSE	0.0674	0.0769	0.0966	0.0448
	σ_δ	0.0530	0.0673	0.0869	
0.75	mean	0.7230	0.7277	0.7346	0.7677
	bias	-0.0270	-0.0223	-0.0154	0.0177
	SD	0.0783	0.0878	0.0863	0.0272
	RMSE	0.0829	0.0906	0.0877	0.0325
	σ_δ	0.0526	0.0665	0.0857	

Table 372. As in Table 364, but now using the likelihood function of Equation (371a) to define the wavelet-based approximate MLE $\tilde{\delta}^{(\mathrm{s/ns})}$ for δ (the $\delta = 0.4$ results for the exact MLE in the final column are replicated from Table 364). The nature of the term σ_δ is explained in the text.

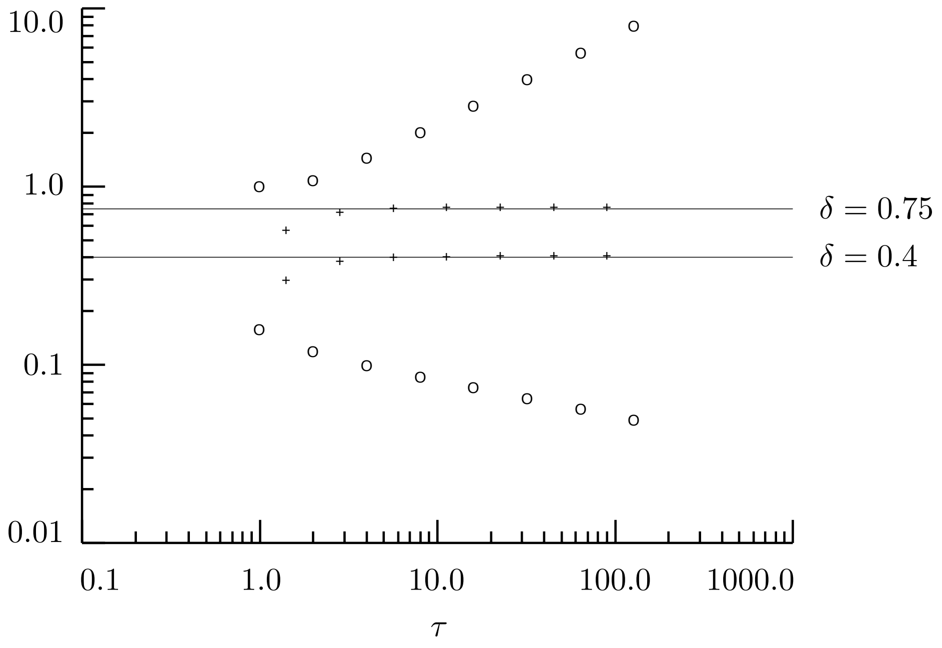

Figure 375. Approximations $C_j/2^j$ (computed from Equation (343b) via numerical integration) to wavelet variances $\nu_X^2(\tau_j)$ versus scales τ_j, $j = 1, \ldots, 8$, for FD processes with $\delta = 0.4$ (lower circles) and 0.75 (upper). See the text for an explanation of the portion of the plot between these sets of circles.

		WLSE			MLE
δ		Haar	D(4)	LA(8)	exact
0.4	mean	0.3925	0.4006	0.4044	0.3900
	bias	−0.0075	0.0006	0.0044	−0.0100
	SD	0.0715	0.0886	0.1185	0.0437
	RMSE	0.0719	0.0886	0.1186	0.0448
0.75	mean	0.7398	0.7443	0.7435	0.7677
	bias	−0.0102	−0.0057	−0.0065	0.0177
	SD	0.0779	0.0877	0.1196	0.0272
	RMSE	0.0786	0.0879	0.1198	0.0325
	$\sqrt{\mathrm{var}\,\{\hat{\beta}^{(\mathrm{wls})}\}}$	0.0891	0.1145	0.1552	

Table 377. As in Table 372, but now using the wavelet-based WLSE $\hat{\delta}^{(\mathrm{wls})}$ (the final column is replicated from Table 372). The WLSEs are based on the unbiased MODWT estimators $\hat{\nu}_X^2(\tau_j)$ of the wavelet variance, which are presumed to have EDOFs $\eta_j = \max\{M_j/2^j, 1\}$. We set $J_1 = 2$ for all three wavelets. The results reported in the table are based on 1024 simulated time series of sample size $N = 256$.

δ		WLSE Haar	WLSE D(4)	WLSE LA(8)	MLE exact
0.4	mean	0.3881	0.3994	0.4000	0.3900
	bias	−0.0119	−0.0006	−0.0000	−0.0100
	SD	0.0669	0.0700	0.0728	0.0437
	RMSE	0.0680	0.0700	0.0728	0.0448
0.75	mean	0.7278	0.7432	0.7442	0.7677
	bias	−0.0222	−0.0068	−0.0058	0.0177
	SD	0.0739	0.0718	0.0726	0.0272
	RMSE	0.0772	0.0721	0.0728	0.0325

Table 378. As in Table 377, but now using an WLSE $\tilde{\delta}^{(\mathrm{wls})}$ based upon a biased MODWT estimator of the wavelet variance along with reflection boundary conditions.

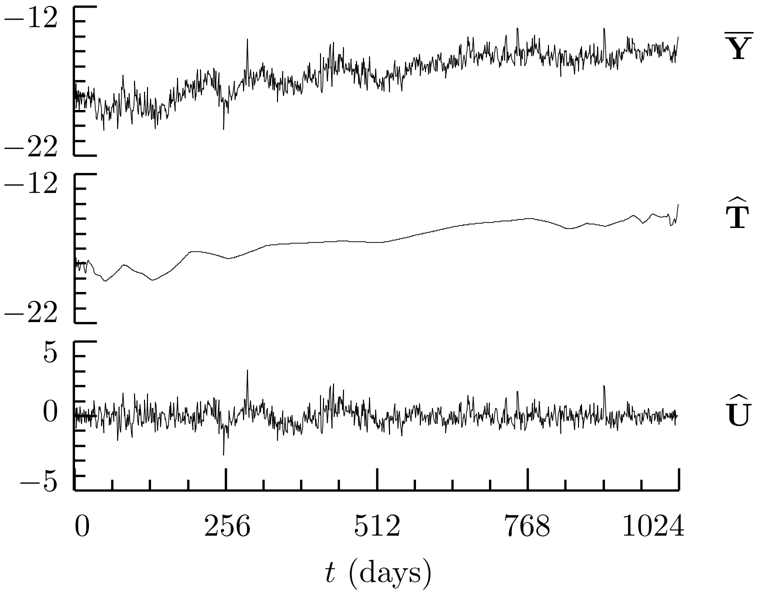

Figure 383. Wavelet-based decomposition of atomic clock fractional frequency deviates $\overline{\mathbf{Y}}$ into an estimated trend $\widehat{\mathbf{T}}$ and residuals $\widehat{\mathbf{U}}$ about the trend. Here we used an LA(8) partial DWT of level $J_0 = 7$. Note that $\widehat{\mathbf{T}}$ has much more structure than a low order polynomial and in fact resembles the output from a variable bandwidth smoother: it is quite smooth near the middle of the series, but then becomes rougher in appearance toward the end points.

	Haar	D(4)	LA(8)
$\tilde{\delta}^{(\mathrm{s/ns})}$	0.5031	0.3943	0.3921
$\sigma_{\tilde{\delta}^{(\mathrm{s/ns})}}$	0.0252	0.0282	0.0318
$\tilde{\sigma}_{\varepsilon}^{2}$	0.3057	0.2838	0.2740
$\hat{\delta}^{(\mathrm{wls})}$	0.4449	0.3812	0.3460
$\sqrt{\mathrm{var}\,\{\hat{\delta}^{(\mathrm{wls})}\}}$	0.0374	0.0418	0.0479
J_0	10	8	7

Table 384. Parameter estimation for the atomic fractional frequency deviates (see text for details).

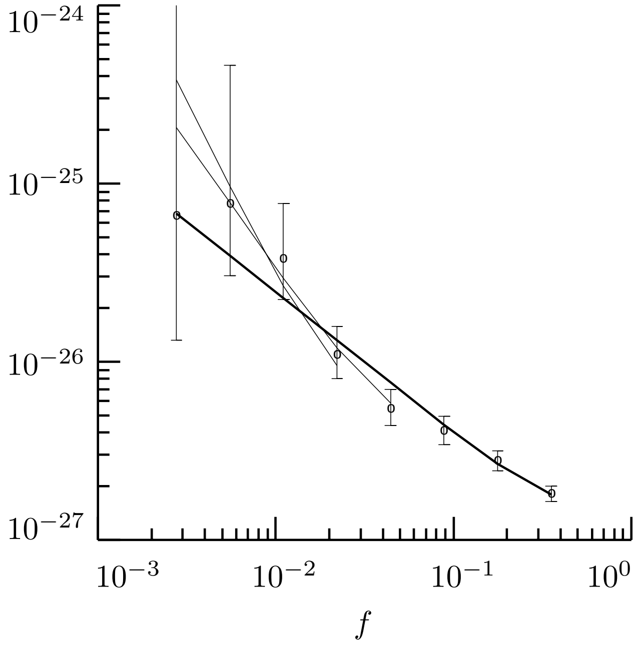

Figure 384. D(4) MODWT wavelet variance estimates for atomic clock fractional frequency deviates (re-expressed as spectral levels C_j), along with spectral levels deduced from MLEs of δ and σ_{ε}^{2} (thick curve). The two shorter thin curves are discussed in the text.

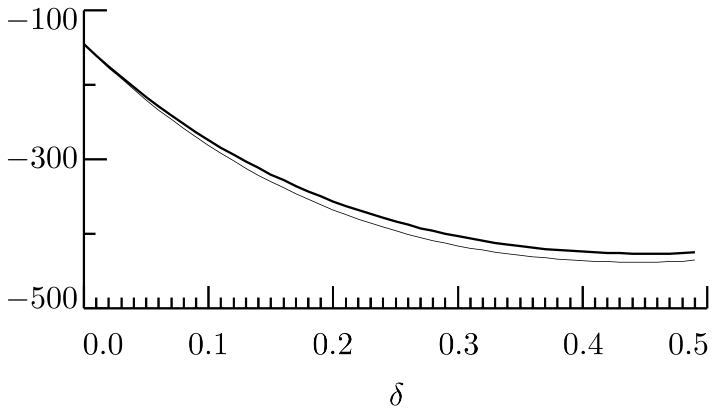

Figure 386. Reduced log likelihood functions for the FD parameter δ computed using the final 512 observations of the Nile River time series (see Figure 192). The thick curve is based on the LA(8) wavelet and attains its minimum at the estimate $\tilde{\delta}^{(s)} \doteq 0.4532$, while the thin curve is for the exact method and reaches its minimum at $\hat{\delta} \doteq 0.4452$.

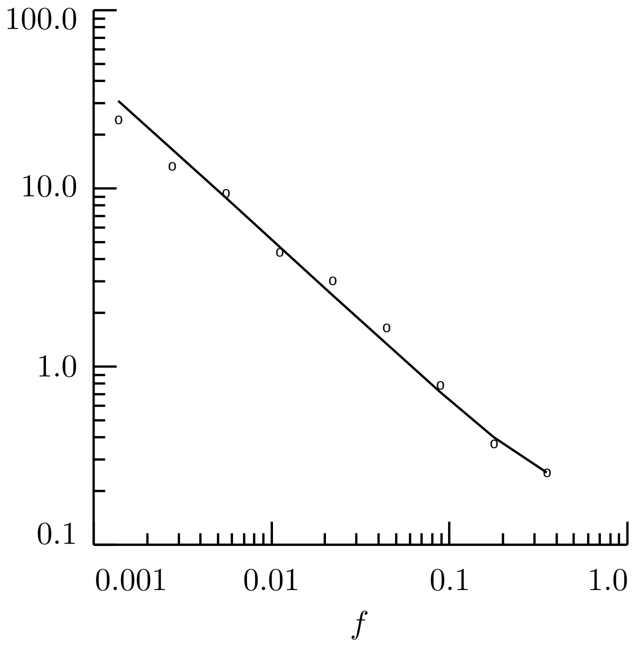

Figure 387. Variance of wavelet coefficients computed via LA(8) MLEs $\tilde{\delta}^{(\mathrm{s})}$ and $\tilde{\sigma}_{\varepsilon}^{2}(\tilde{\delta}^{(\mathrm{s})})$ (solid curve) as compared to sample variances of LA(8) wavelet coefficients (circles).

			critical levels		
τ_j	M'_j	D	10%	5%	1%
1 year	331	0.1559	0.0945	0.1051	0.1262
2 years	165	0.1754	0.1320	0.1469	0.1765
4 years	82	0.1000	0.1855	0.2068	0.2474
8 years	41	0.2313	0.2572	0.2864	0.3436

Table 387. Results of testing Nile River minima for homogeneity of variance using the Haar wavelet filter critical values determined by computer simulations (Whitcher *et al.*, 2000a).

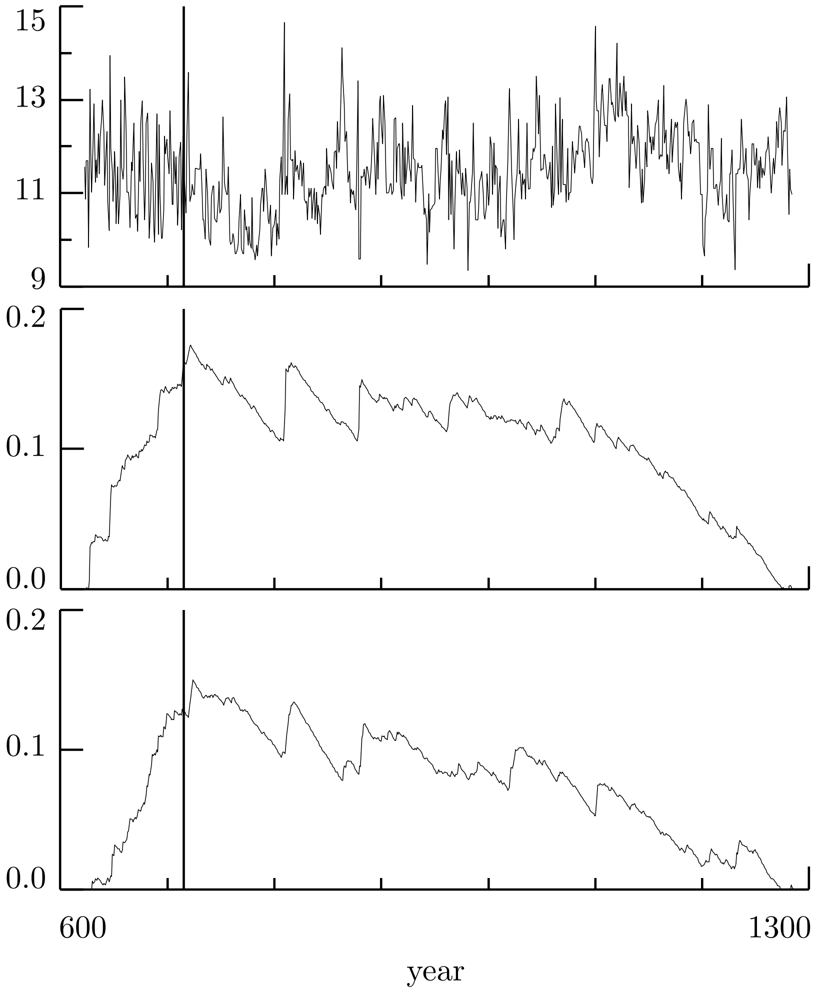

Figure 388. The Nile River minima (top plot) along with Δ_k^- versus k for scales τ_1 and τ_2 (middle and bottom plots, respectively). The thick vertical lines denote the year 715.

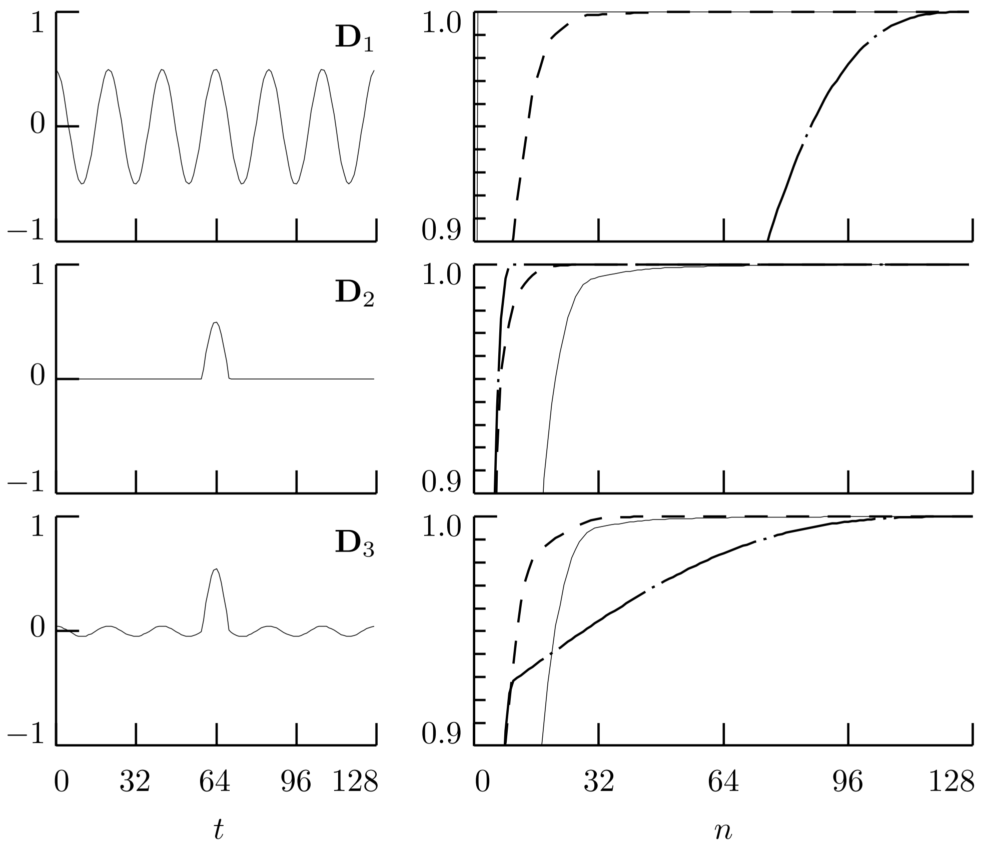

Figure 396. Three signals (left-hand column) and their corresponding normalized partial energy sequences (right-hand column) for the signals themselves (curves broken by intermittent dots), their ODFT coefficients (thin solid curves) and their LA(8) DWT coefficients (dashed curves).

	domain of signal		
	frequency	time	mixture
$\mathcal{F}$	2	29	28
I_N	105	9	75
$\mathcal{W}$	22	14	21

Table 396. Number of coefficients required to obtain no more than a 1% relative approximation error for three signals using an orthonormal discrete Fourier transform $\mathcal{F}$, an identity transform I_N and an LA(8) DWT transform $\mathcal{W}$ (see text for details).

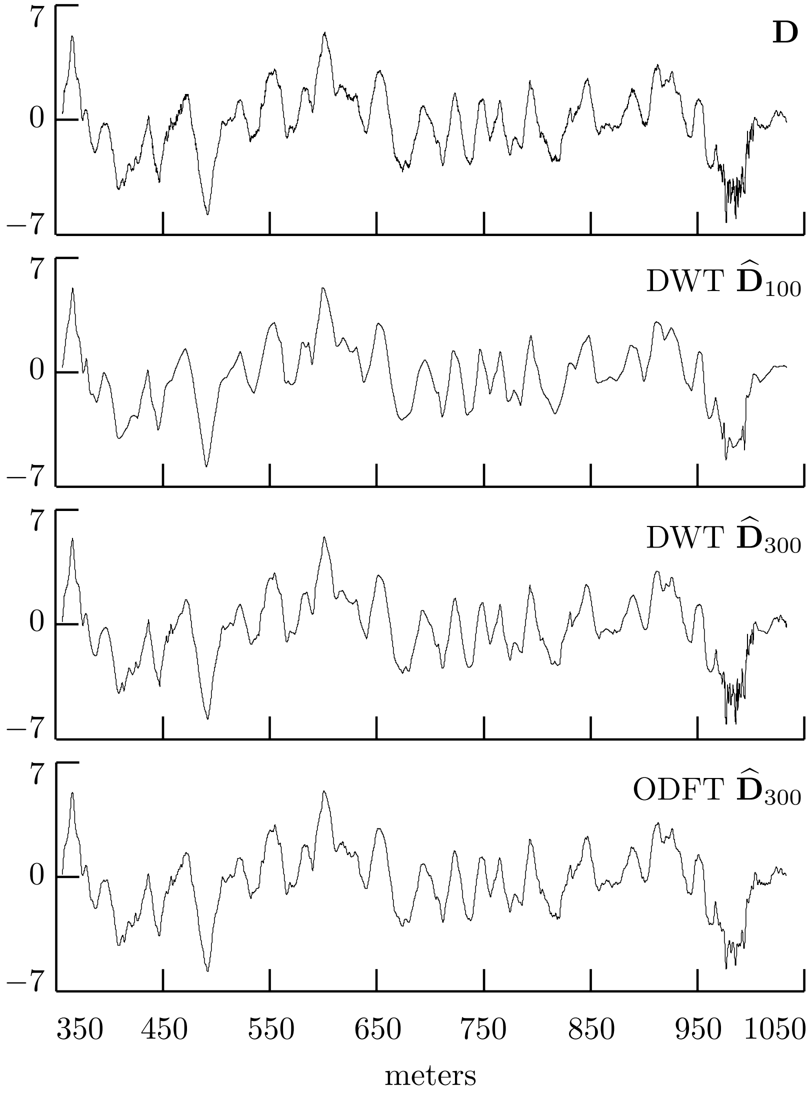

Figure 397. Plot of $N = 6784$ values of a hypothesized signal $\mathbf{D}$ related to vertical shear in the ocean versus depth in meters (top plot), along with reconstructions using 100 LA(8) DWT coefficients, 300 LA(8) DWT coefficients and 300 ODFT coefficients. See Section 5.10 for more discussion about these data.

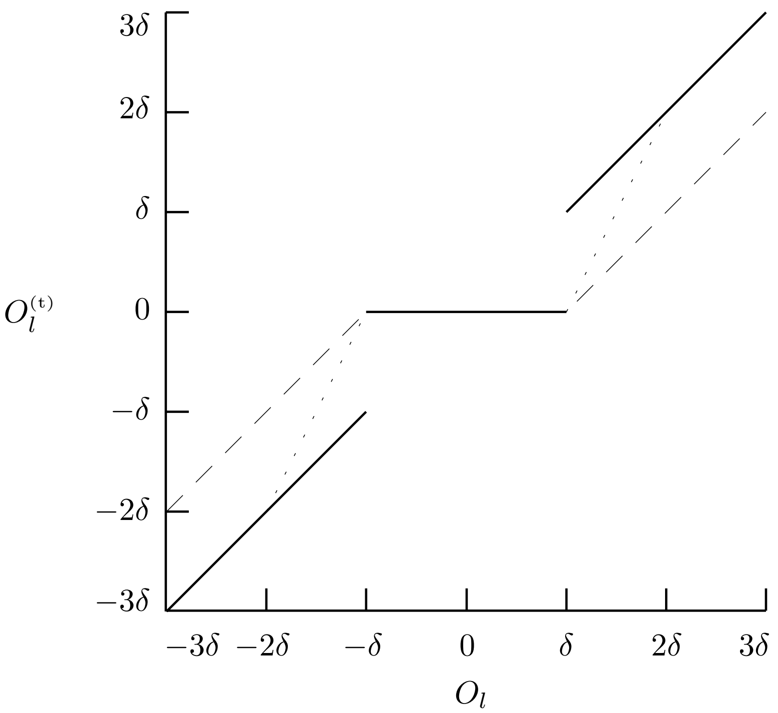

Figure 399. Mappings from O_l to $O_l^{(\mathrm{t})}$, where $O_l^{(\mathrm{t})}$ is either $O_l^{(\mathrm{ht})}$ for hard thresholding (solid lines), $O_l^{(\mathrm{st})}$ for soft thresholding (dashed lines), or $O_l^{(\mathrm{mt})}$ for mid thresholding (dotted lines). Note that the effect of all three thresholding schemes is the same when $-\delta \leq O_l \leq \delta$.

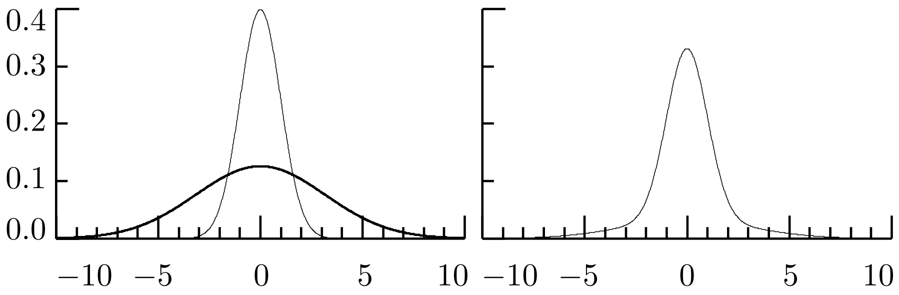

Figure 410. PDFs for $\mathcal{N}(0,1)$ and $\mathcal{N}(0,10)$ RVs (left-hand plot, thin and thick curves, respectively) and for an RV obeying a Gaussian mixture model (right-hand plot). The mixture PDF is non-Gaussian and is formed by adding the $\mathcal{N}(0,1)$ and $\mathcal{N}(0,10)$ PDFs, weighted by $p_l = 0.75$ and $1 - p_l = 0.25$, respectively (adapted from Figure 1 of Chipman *et al.*, 1997).

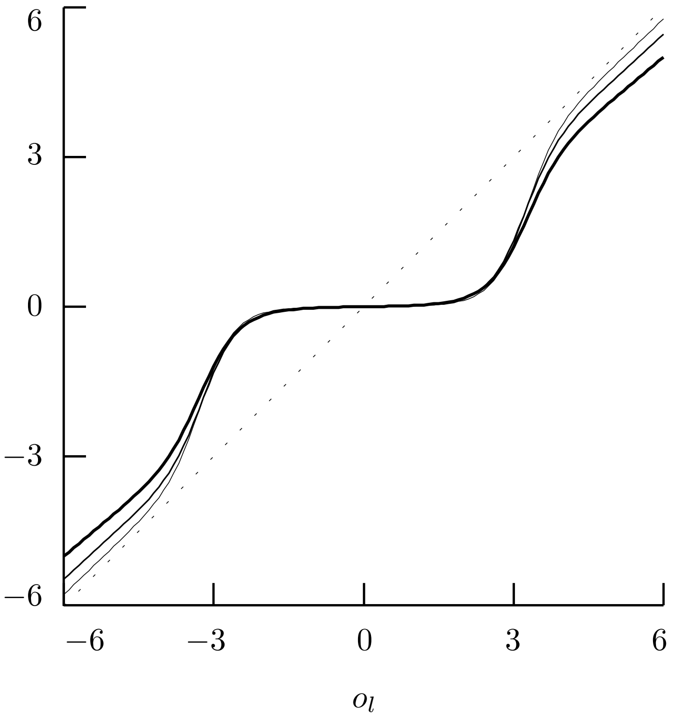

Figure 412. The conditional mean shrinkage rule of Equation (411c) for $p_l = 0.95, \sigma^2_{n_l} = 1$ and $\sigma^2_{G_l} = 5$ (thickest curve, furthest from dotted diagonal), 10 and 25 (thinnest curve, nearest to diagonal). Because of the correspondence between conditional mean shrinkage rules and the Bayes rule estimators of Chipman *et al.* (1997) with respect to squared error loss, the above also illustrates $B_2(\cdot)$ of Equation (414a).

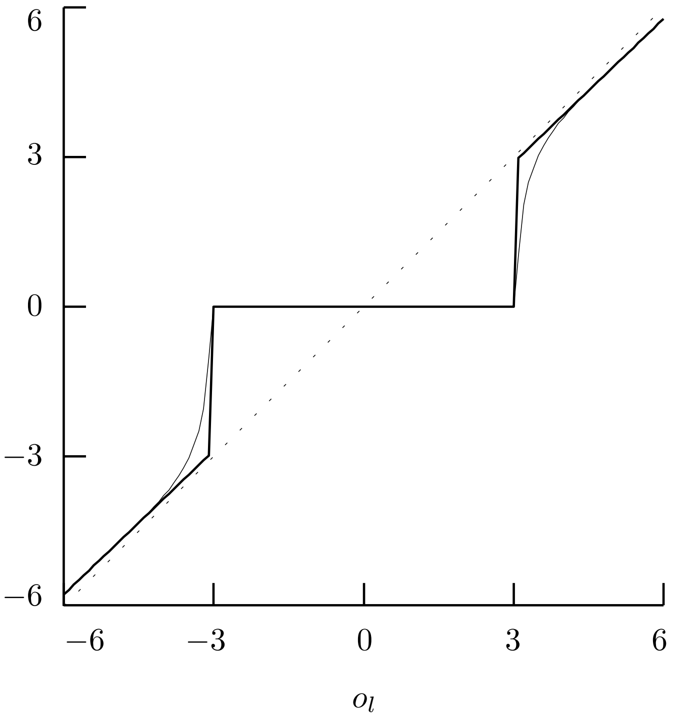

Figure 416. Comparison of the posterior median $B_1(o_l)$ (thin curve) to the *approximate* conditional median $U_1(o_l)$ (thick) when $\sigma^2_{G_l} = 25, p_l = 0.95$ and $\sigma^2_{n_l} = 1$. The dotted line marks the diagonal.

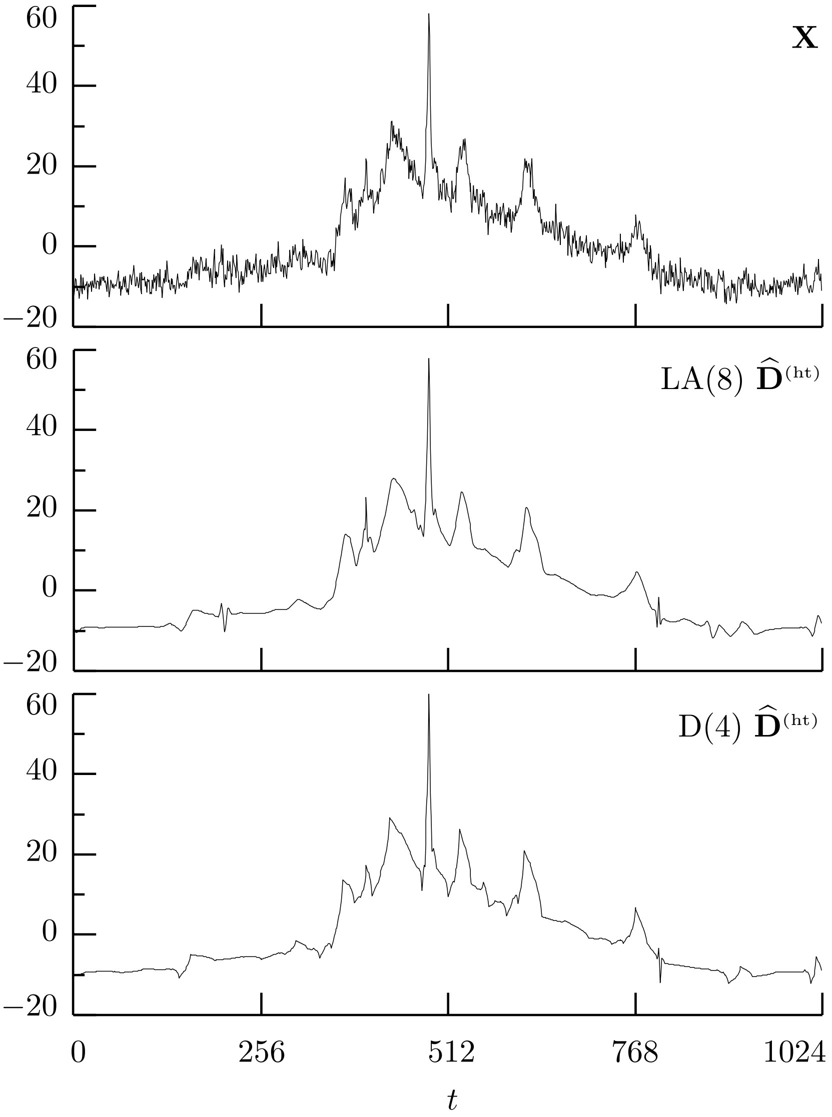

Figure 418. Nuclear magnetic resonance (NMR) spectrum (top plot), along with wavelet-based hard threshold signal estimates using the level $J_0 = 6$ partial LA(8) DWT (middle) and a similar D(4) DWT (bottom). In both cases, we determine the noise variance σ_ϵ^2 using the MAD standard deviation estimate $\hat{\sigma}_{(\mathrm{mad})}$, after which we set the universal threshold level $\hat{\delta}^{(\mathrm{u})} \equiv \sqrt{[2\hat{\sigma}^2_{(\mathrm{mad})} \log{(N)}]}$. This NMR spectrum was extracted from the public domain software package `WaveLab`, to which it was provided by Andrew Maudsley, Department of Radiology, University of California, San Francisco (the data can be accessed via the Web site for this book – see page *xiv*).

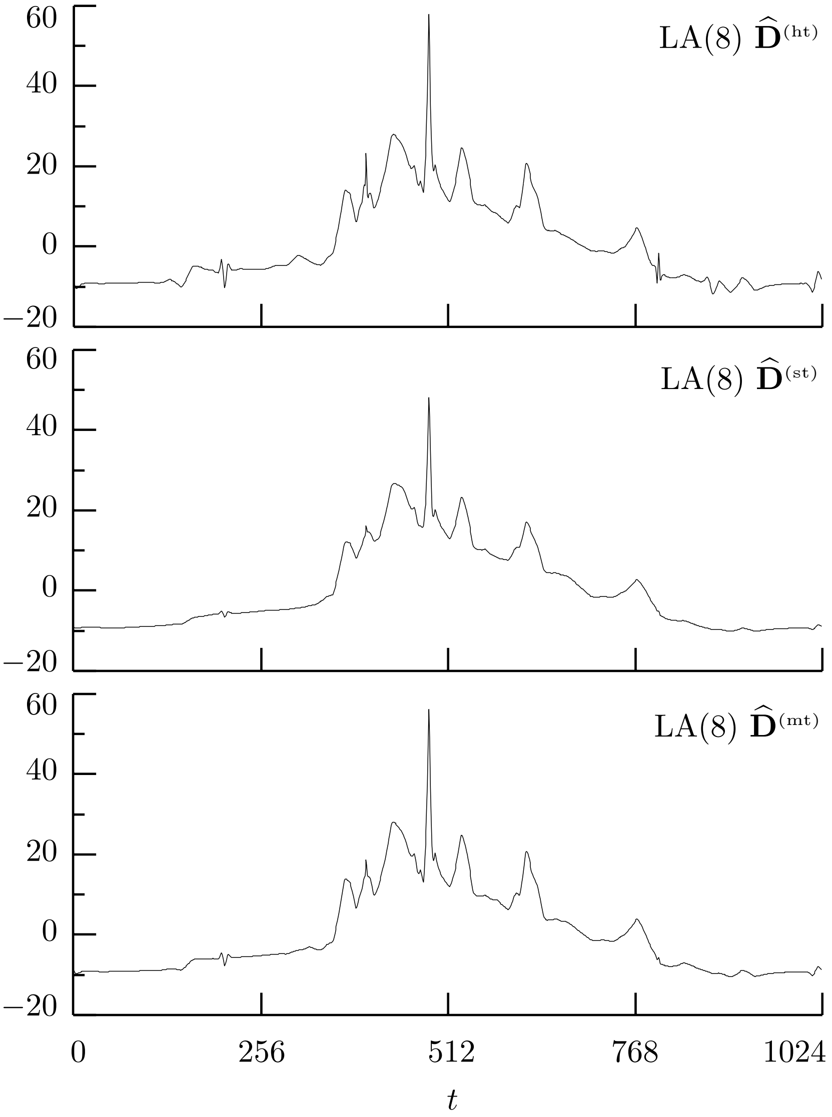

Figure 419. Thresholding signal estimates of the NMR spectrum based upon the level $J_0 = 6$ partial LA(8) DWT with – from top to bottom – hard, soft and mid thresholding (the top plot is a repeat of the middle of Figure 418). For all three estimates, we use the universal threshold level $\hat{\delta}^{(\mathrm{u})} \equiv \sqrt{[2\hat{\sigma}^2_{(\mathrm{mad})} \log(N)]} \doteq 6.12622$ based upon the MAD standard deviation estimate $\hat{\sigma}_{(\mathrm{mad})} \doteq 1.64538$.

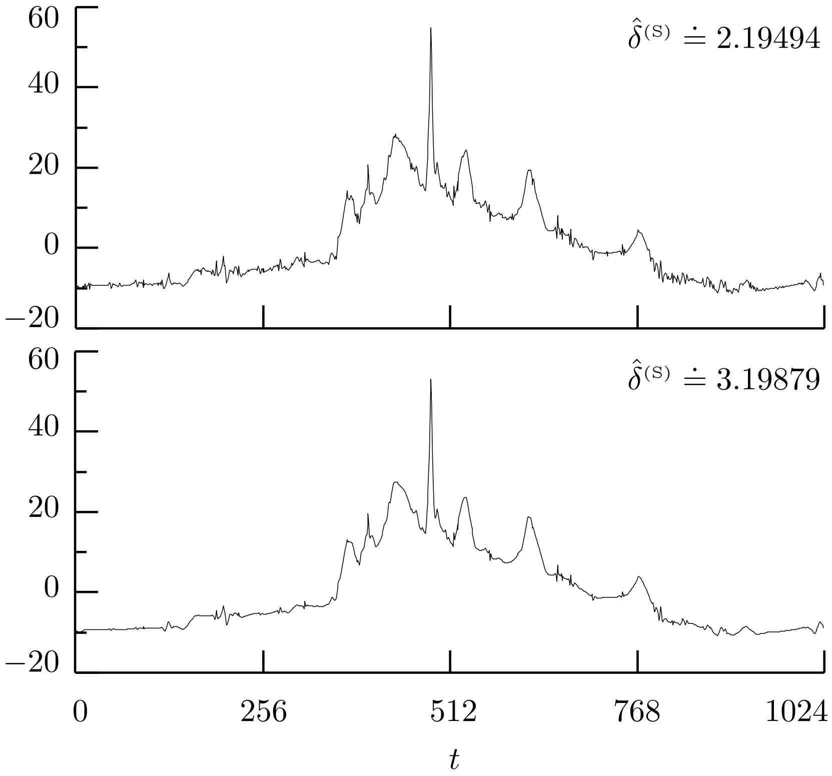

Figure 421. Thresholding signal estimates of the NMR spectrum based upon the level $J_0 = 6$ partial LA(8) DWT with soft thresholding and SURE threshold levels $\hat{\delta}^{(\mathrm{S})}$, which are computed using MAD scale estimates based on, respectively, just the unit scale wavelet coefficients (top plot) and wavelet coefficients from all six scales (bottom).

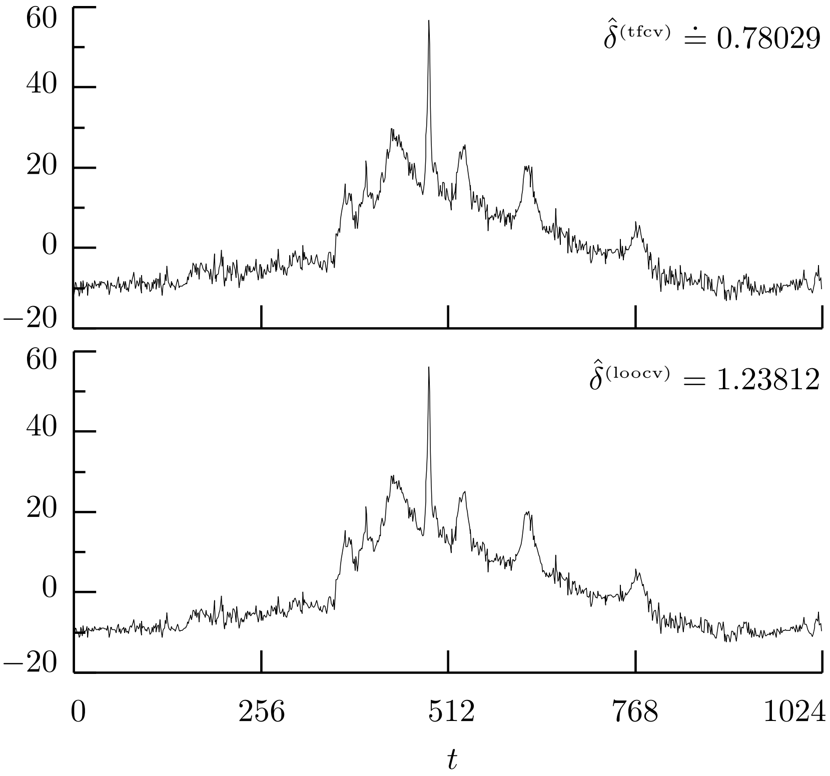

Figure 423. Thresholding signal estimates of the NMR spectrum based upon the level $J_0 = 6$ partial LA(8) DWT with soft thresholding and threshold levels determined by two-fold cross-validation (top plot) and leave-one-out cross-validation (bottom).

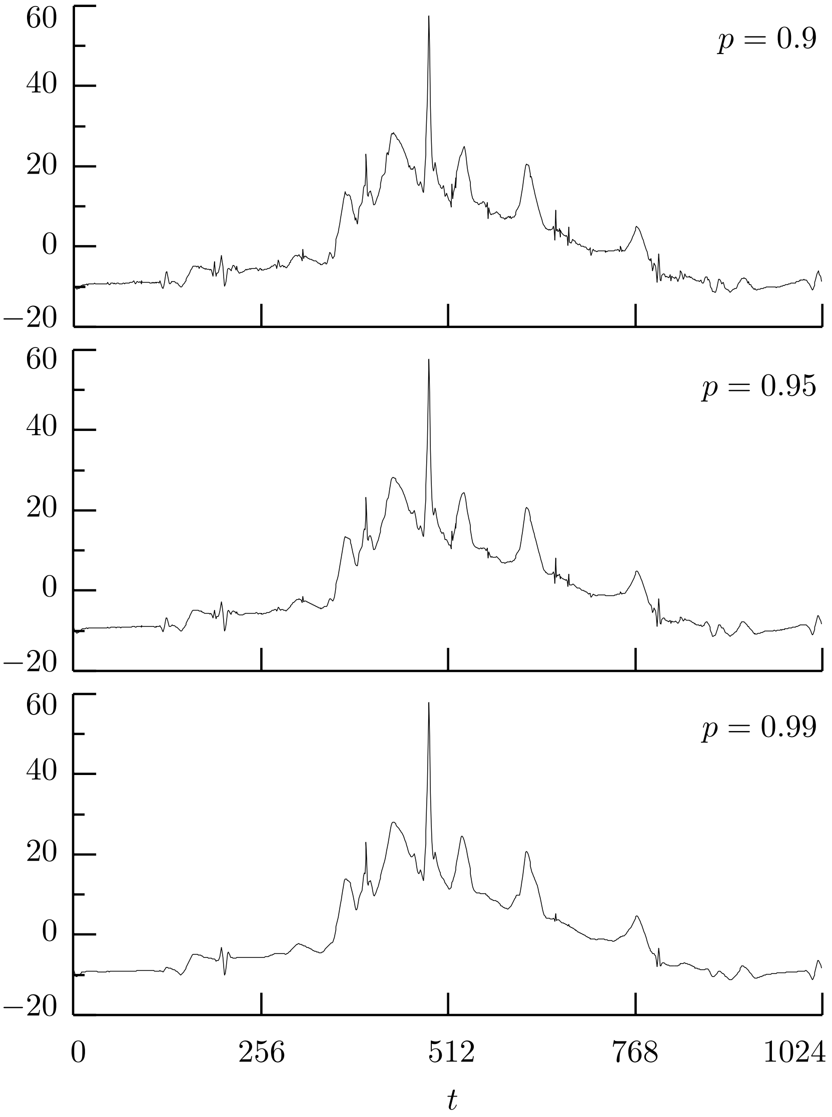

Figure 425. Shrinkage signal estimates of the NMR spectrum based upon the level $J_0 = 6$ partial LA(8) wavelet transform and the conditional mean with $p = 0.9$ (top plot), 0.95 (middle) and 0.99 (bottom). The remaining parameters (namely, σ_ϵ^2, σ_W^2 and σ_G^2) are estimated as explained in the text.

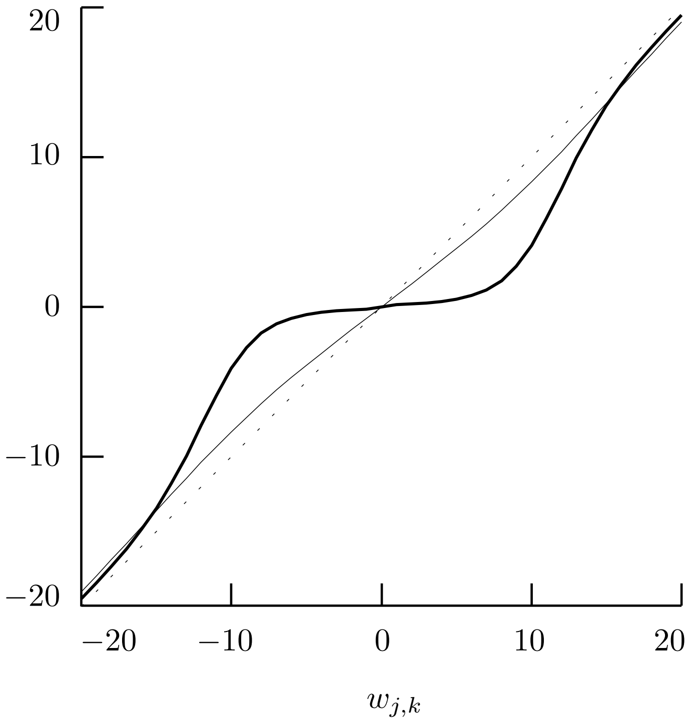

Figure 427. Bayes rules $B_2(w_{j,k})$ versus $w_{j,k}$ for the Vidakovic (1998) scheme as applied to the NMR spectrum. The thin and thick curves depict $B_2(\cdot)$ assuming degrees of freedom ϑ of, respectively, 5 and 2.01. The dotted line marks the diagonal. The corresponding signal estimates are shown in Figure 428.

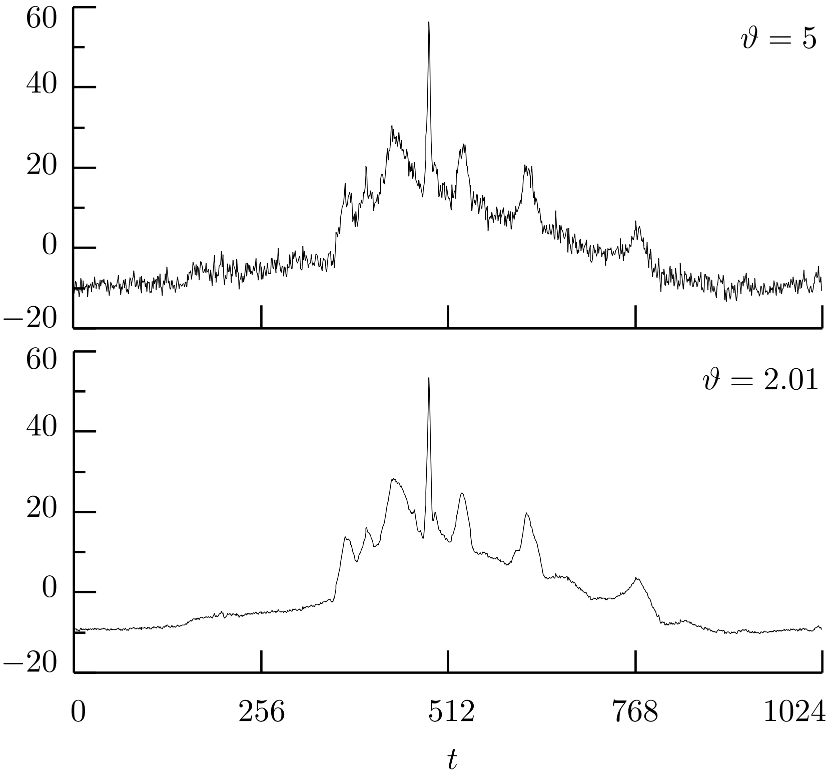

Figure 428. Shrinkage signal estimates of the NMR spectrum based upon the level $J_0 = 6$ partial LA(8) wavelet transform and the Bayes rule $B_2(\cdot)$ as formulated by Vidakovic (1998) and given in Equation (414b) (the specific rule for each estimate is plotted in Figure 427). The difference between the two estimates is solely due to the choice of the degrees of freedom ϑ for the signal PDF $f_R(\cdot)$, with the remaining two parameters (κ and υ) estimated as described in the text.

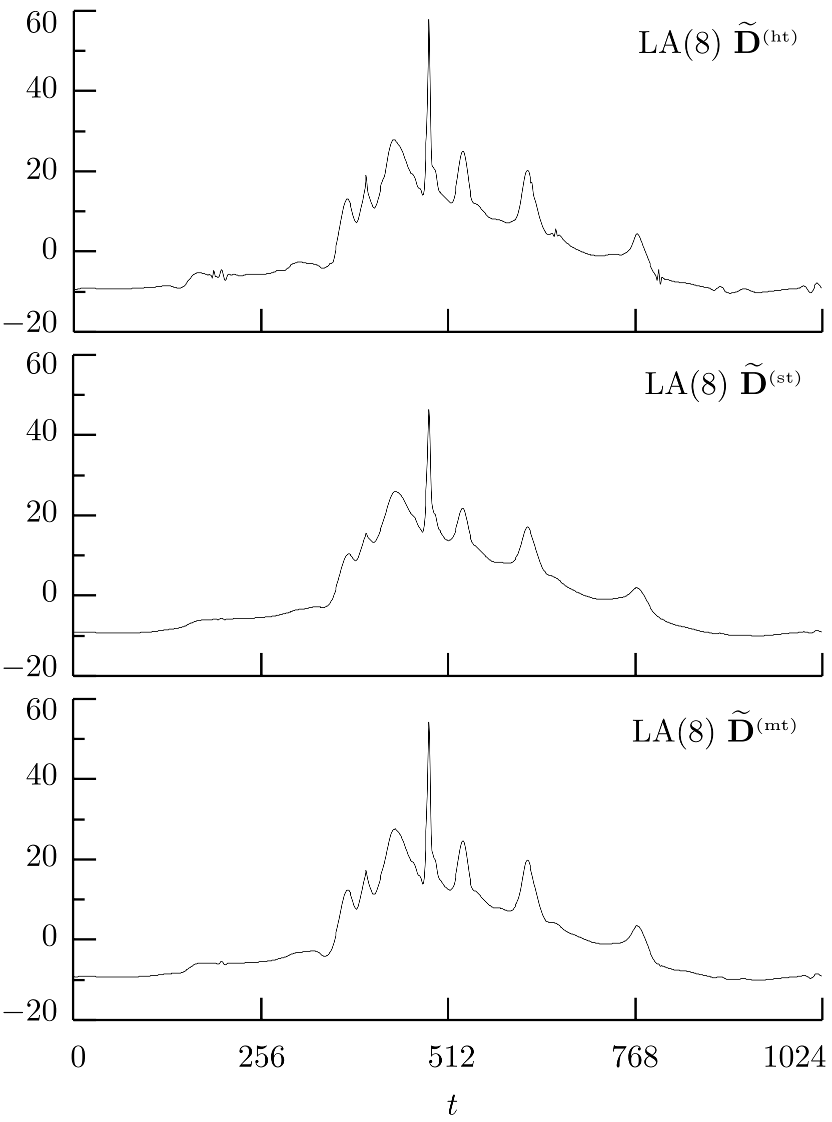

Figure 430. Thresholding signal estimates of the NMR spectrum based upon the level $J_0 = 6$ LA(8) MODWT with – from top to bottom – hard, soft and mid thresholding (Figure 419 has corresponding plots for the DWT). Each estimate uses the universal threshold levels $\tilde{\delta}_j^{(\mathrm{u})} \equiv \sqrt{[2\tilde{\sigma}^2_{(\mathrm{mad})} \log{(N)}/2^j]} \doteq 6.49673/2^{j/2}$ computed via the MODWT-based MAD standard deviation estimate $\tilde{\sigma}_{(\mathrm{mad})} \doteq 1.74489$.

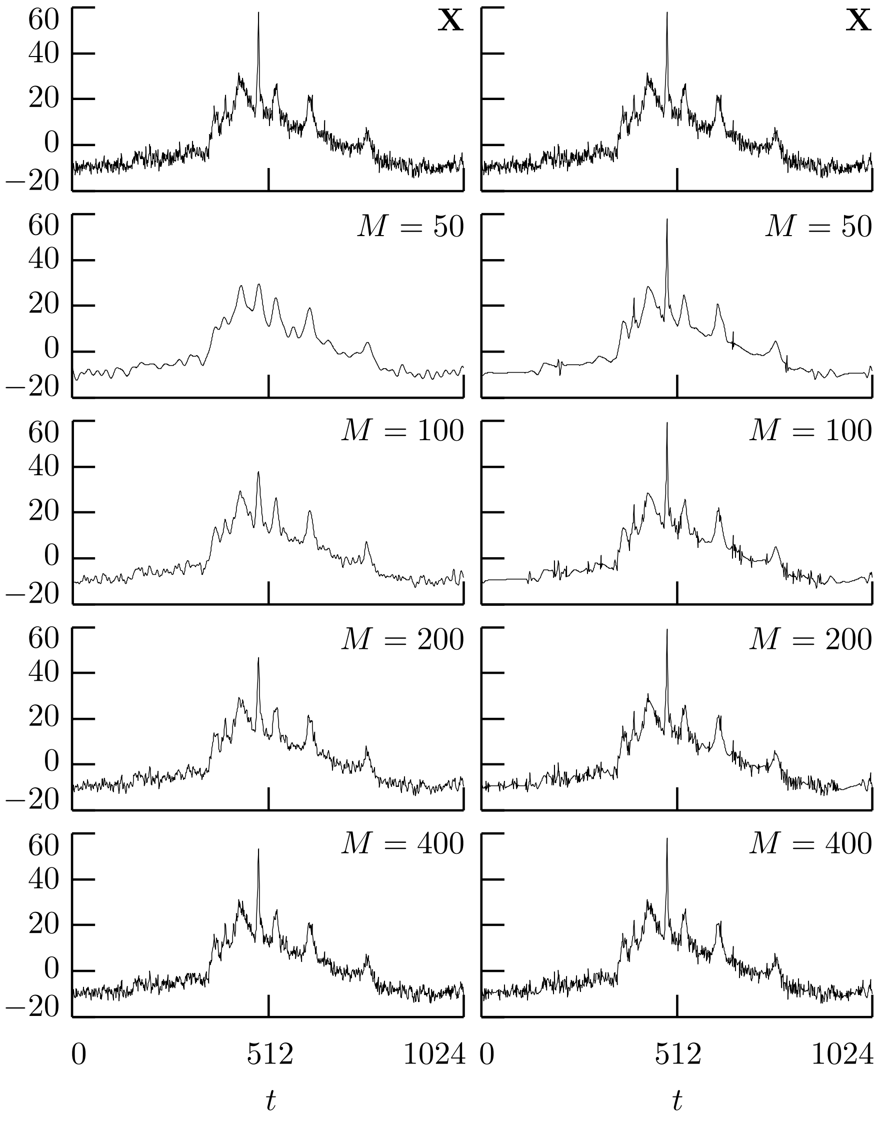

Figure 431. Denoising of NMR spectrum (top plot) using hard thresholding based upon keeping the M coefficients with the largest magnitudes in the ODFT (left-hand column) and the level $J_0 = 6$ partial LA(8) DWT (right-hand) for $M = 50$, 100, 200 and 400 (second to fifth rows, respectively).

	j							
	1	2	3	4	5	6	7	8
$-\delta^{(\mathrm{l})}_{j,\frac{\alpha}{2}}$	7.825	7.031	6.228	5.750	5.460	5.287	5.182	5.118
$\delta^{(\mathrm{u})}_{j,\frac{\alpha}{2}}$	5.556	5.601	5.142	4.976	4.913	4.901	4.910	4.925

Table 436. Lower and upper thresholds $\delta^{(\mathrm{l})}_{j,\frac{\alpha}{2}}$ and $\delta^{(\mathrm{u})}_{j,\frac{\alpha}{2}}$, $j = 1, \ldots, 8$, for wavelet-based thresholding of the log periodogram using the LA(8) DWT. Here we use the approximation $\alpha = P_F/M$ with $P_F = 0.1$ and $M = 1024$. For convenience, we have tabulated $-\delta^{(\mathrm{l})}_{j,\frac{\alpha}{2}}$ instead of $\delta^{(\mathrm{l})}_{j,\frac{\alpha}{2}}$. Note that, as j increases, the lower and upper thresholds come closer to each other in magnitude, as would be expected due to convergence to Gaussianity.

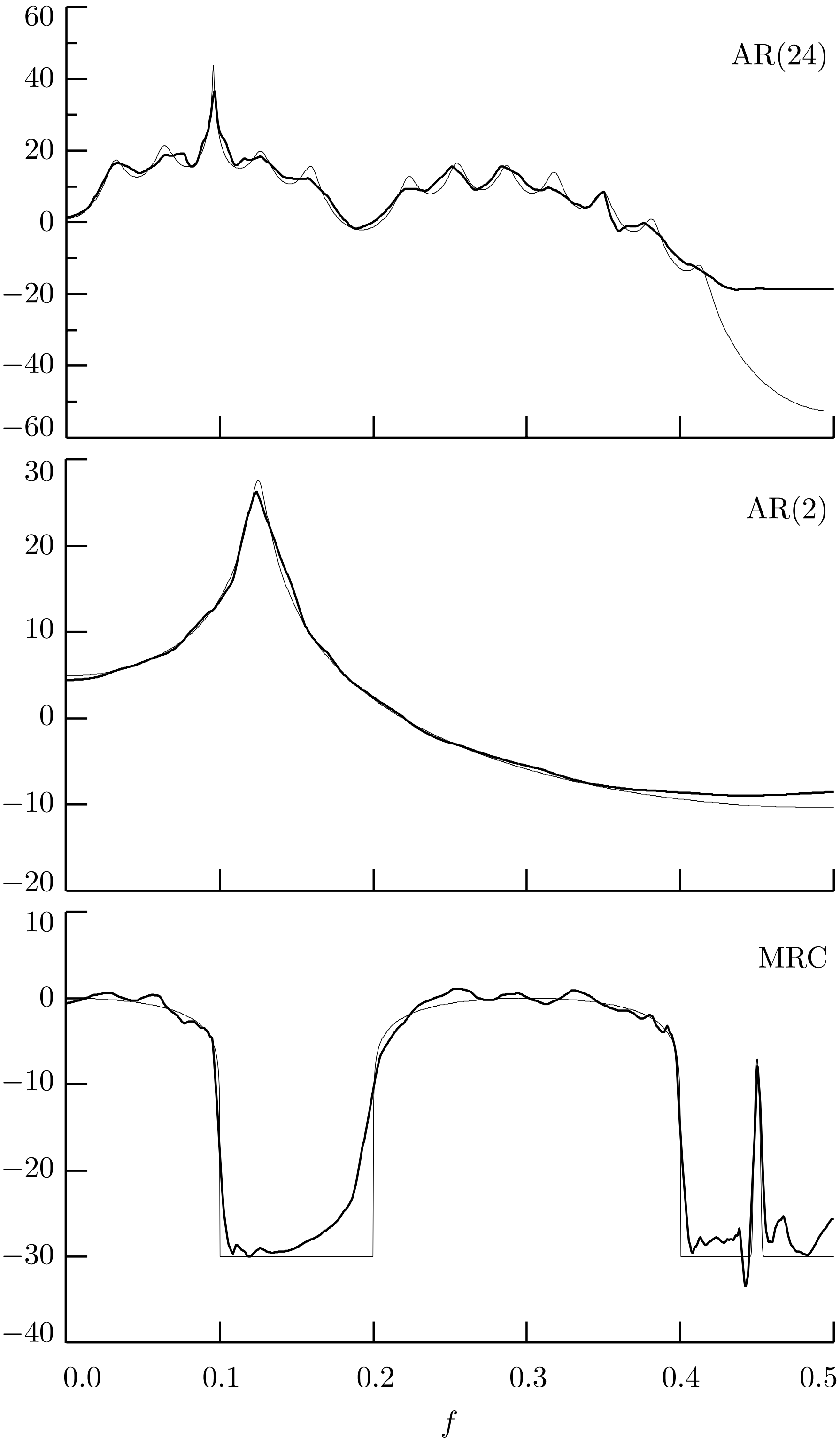

Figure 438. Periodogram-based estimated SDFs (thick curves) and true SDFs (thin) for the AR(24), AR(2) and MRC processes (see the text for details).

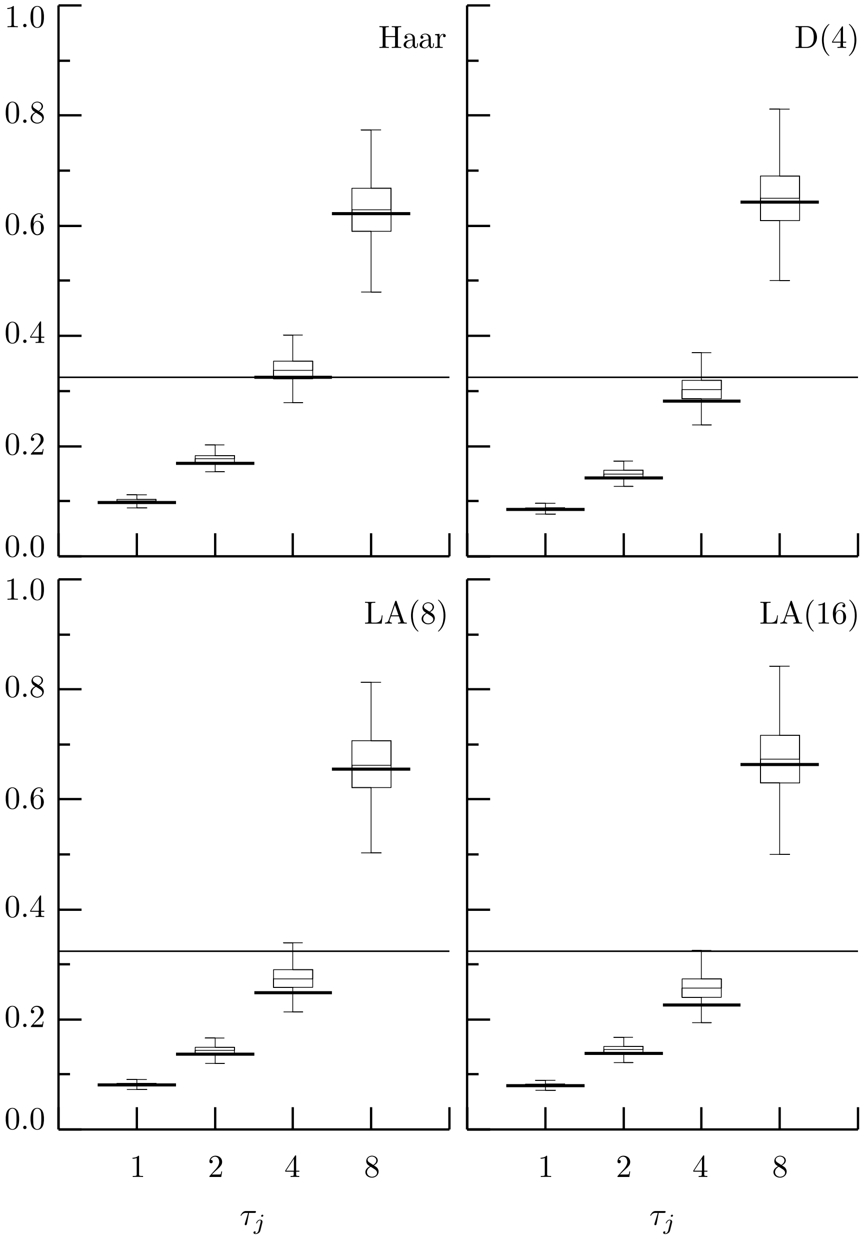

Figure 443. Box plots of the estimated standard deviations $\hat{\sigma}_j$ of wavelet coefficients $n_{j,t}$ at levels $j = 1, 2, 3$ and 4 derived from the AR(2) process using different wavelet filters, for $N = 2048$ and $K = 10$. The horizontal solid lines extending beyond each box plot indicate the value of σ_j derived from Equation (441b). The 'nominal' standard deviation $\sigma_\eta = \sqrt{[\psi'(10)]} \doteq 0.32$ is marked as a solid horizontal line right across each of the plots.

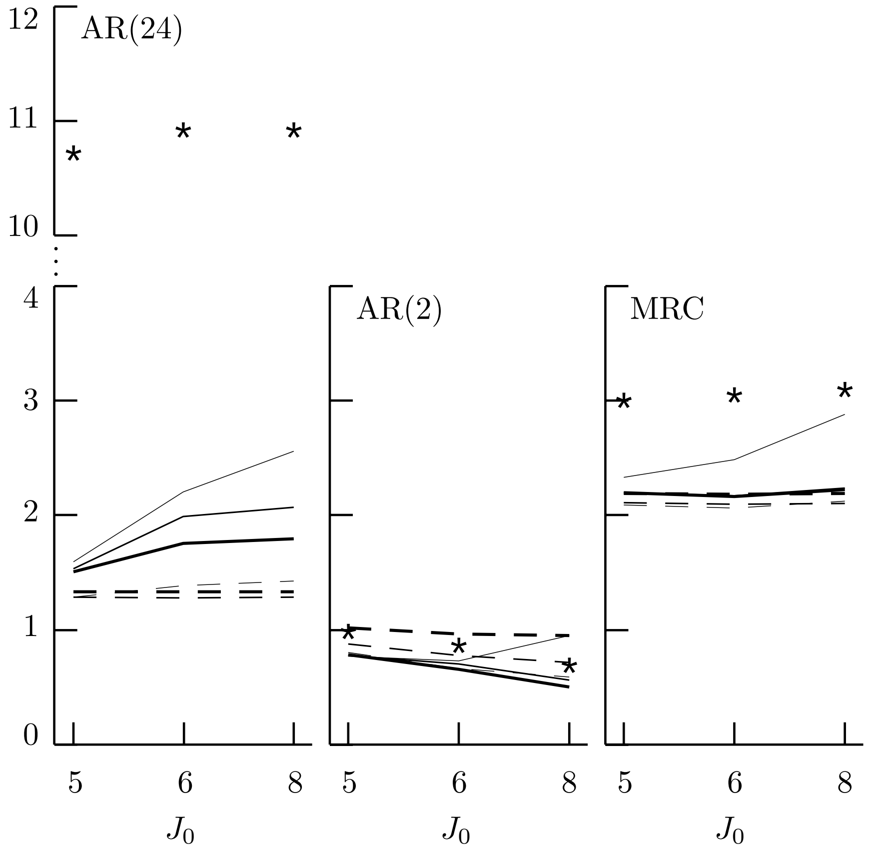

Figure 446. Average value over a thousand simulations of the RMSEs for the AR(24) (left-hand plot), AR(2) (center) and MRC models (right-hand). In each plot, the average RMSE (in dBs) is plotted for the level-dependent multitaper-based method with hard (solid thick curve), mid (solid medium) and soft (solid thin) thresholding and also for the level-independent method with hard (dashed thick curve), mid (dashed medium) and soft (dashed thin) thresholding. Three values of level J_0 are considered, namely 5, 6 and 8, corresponding to 64, 32 and 8 scaling coefficients left untouched by the thresholding. The asterisks show average RMSEs for the periodogram-based method. In all cases, the series length is $N = 2048$, and we use the LA(8) wavelet to compute the DWT.

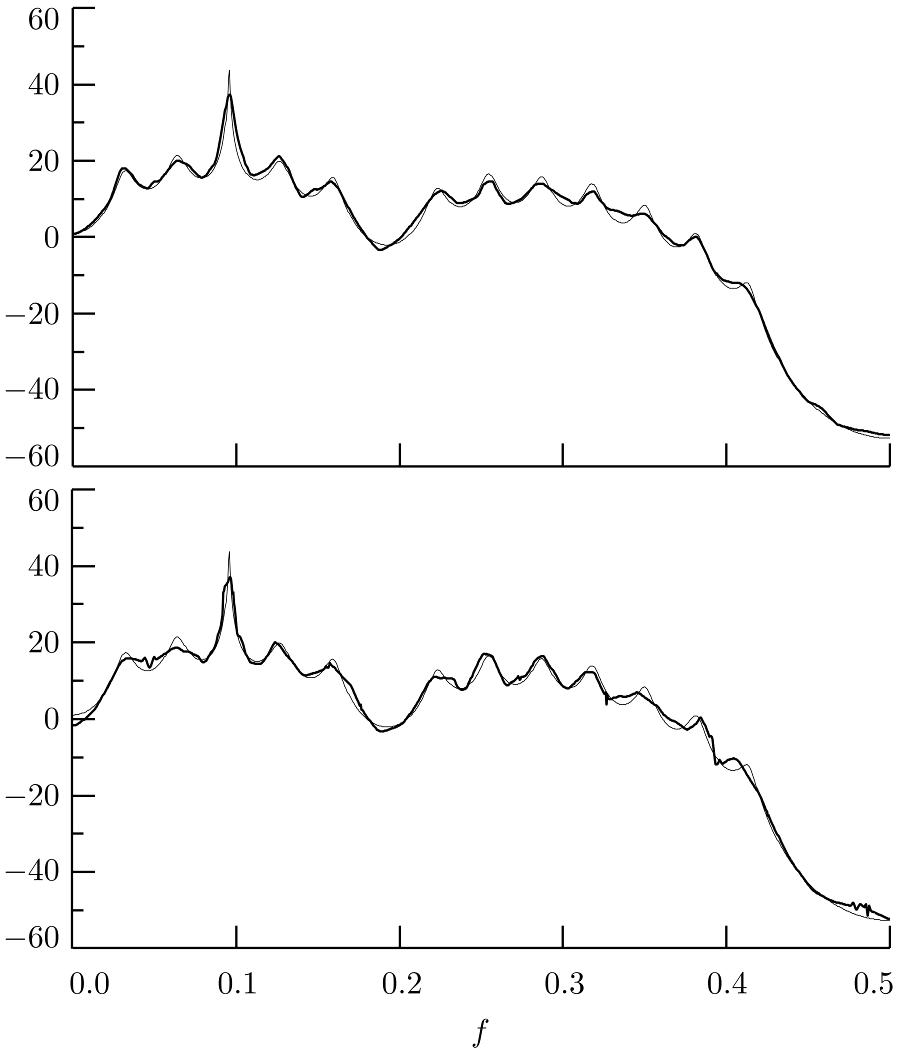

Figure 447. Estimated SDFs (thick curves) and true SDF (thin) for the AR(24) process. The SDF estimates are representative in that they have RMSEs closest to the average RMSE over a thousand simulations. The upper plot is for level-independent soft thresholding, and the lower plot, level-dependent hard thresholding, with $J_0 = 5$ in both cases. The simulated series are of length $N = 2048$, and we use an LA(8) DWT.

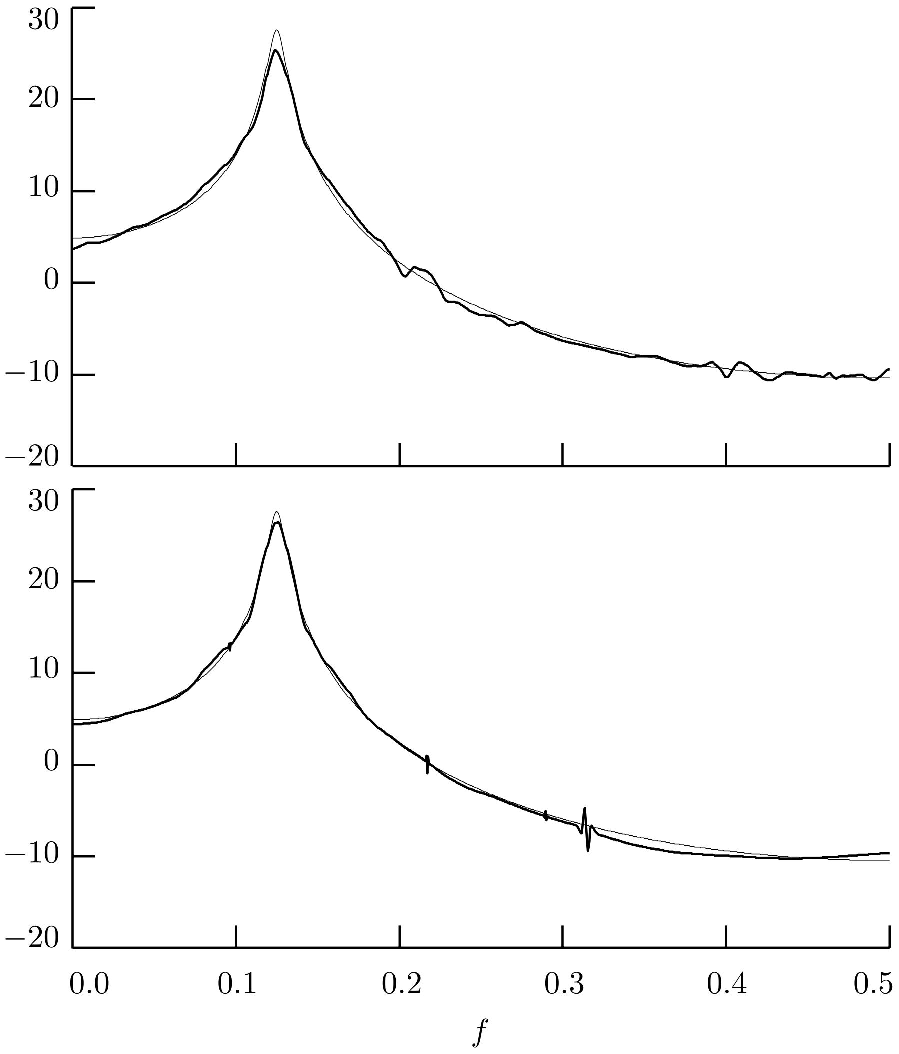

Figure 448. Estimated SDFs (thick curves) and true SDF (thin) for the AR(2) process. Layout and parameters are as for Figure 447.

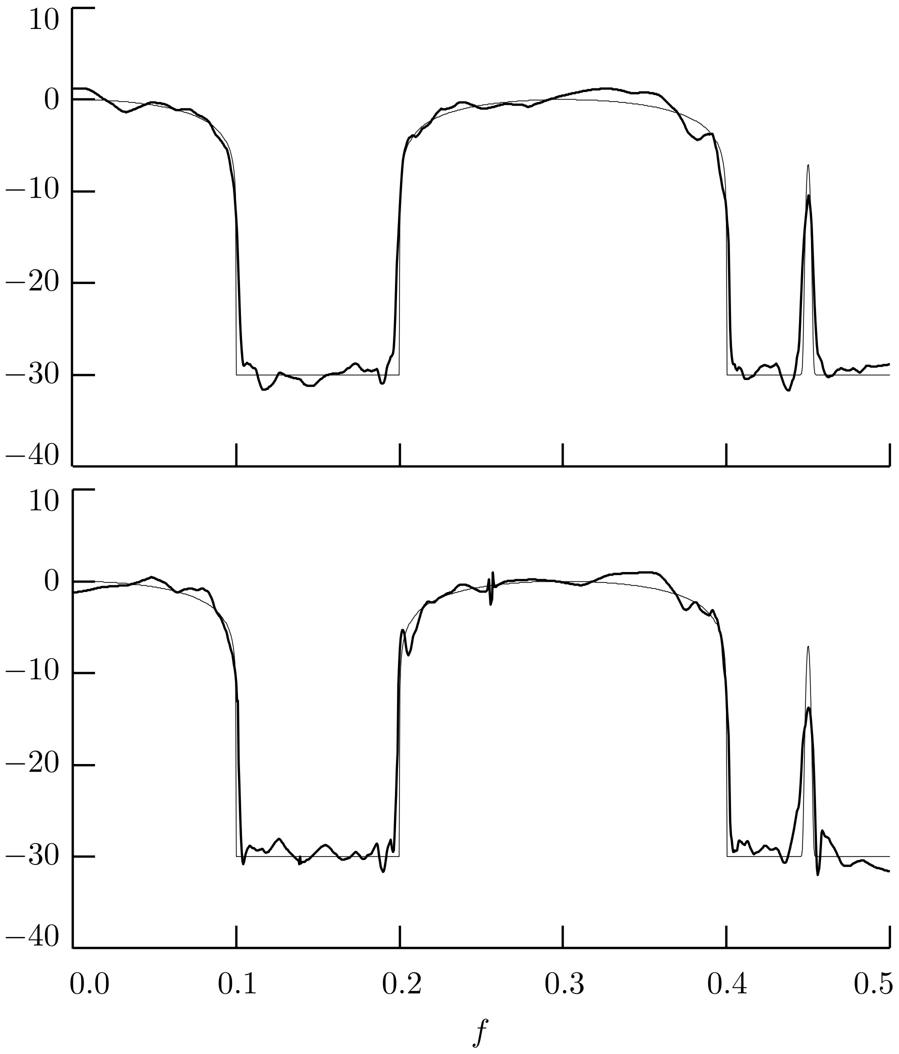

Figure 449. Estimated SDF (thick curve) and true SDF (thin curve) for the mobile radio communications process. Layout and parameters are as for Figure 447.

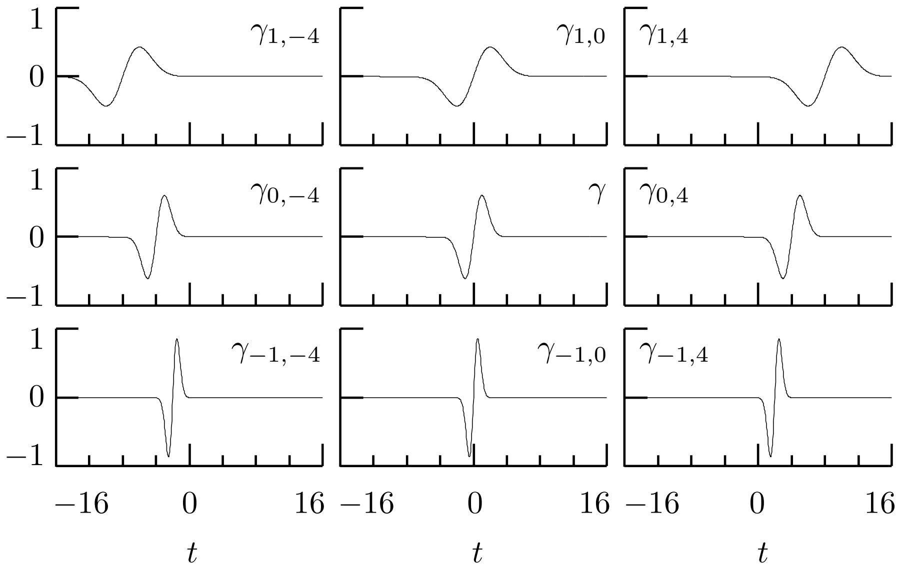

Figure 458. Translation and dilation of the function defined by $\gamma(t) = t\exp(-t^2/2)$.

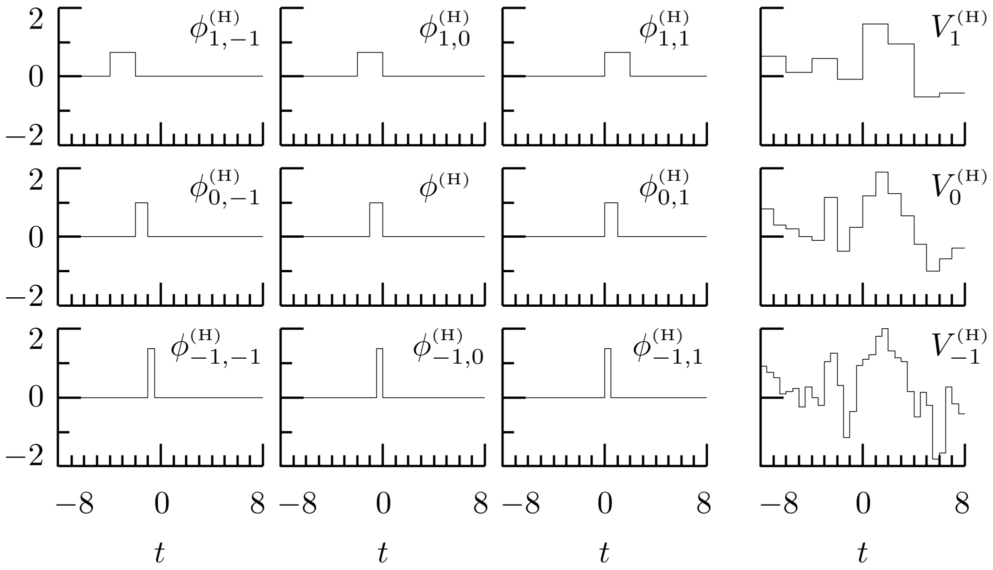

Figure 461. The Haar scaling function $\phi^{(\mathrm{H})}(\cdot)$ and corresponding approximation spaces. The first three plots on the middle row show three of the basis functions for the Haar approximation space $V_0^{(\mathrm{H})}$, namely, from left to right, $\phi_{0,-1}^{(\mathrm{H})}(\cdot)$, $\phi^{(\mathrm{H})}(\cdot)$ and $\phi_{0,1}^{(\mathrm{H})}(\cdot)$. The right-most plot on this row is an example of a function contained in $V_0^{(\mathrm{H})}$. The top and bottom rows show, respectively, corresponding plots for the Haar approximation spaces $V_1^{(\mathrm{H})}$ (a coarser approximation than $V_0^{(\mathrm{H})}$) and $V_{-1}^{(\mathrm{H})}$ (a finer approximation than $V_0^{(\mathrm{H})}$). The right-most column of plots can be regarded as three Haar approximations of a single $L^2(\mathbb{R})$ function, with the associated scales of 2, 1 and 1/2 (top to bottom).

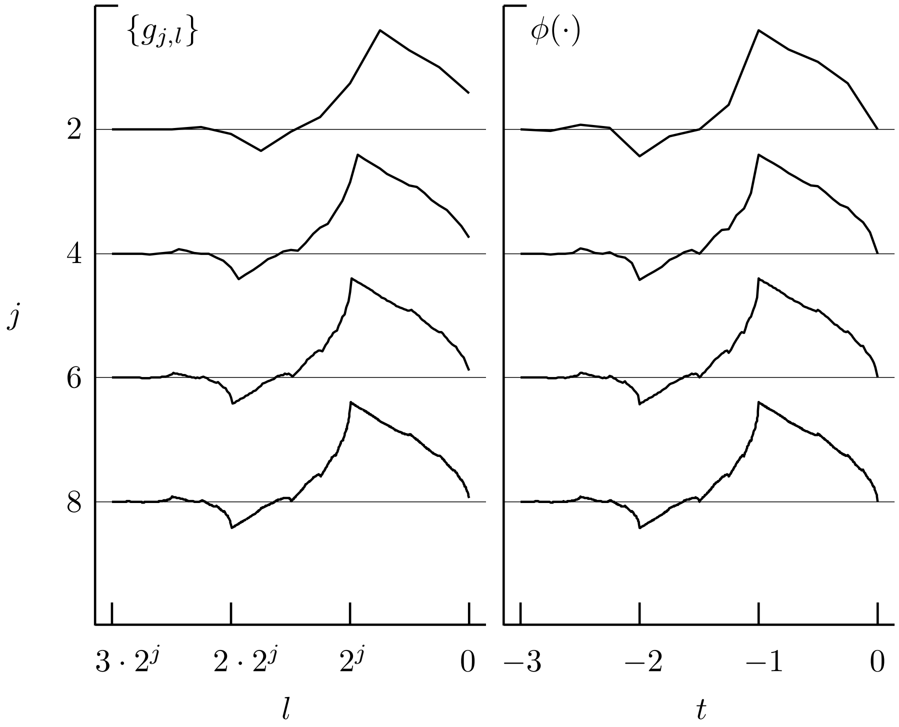

Figure 471. Level j equivalent D(4) scaling filters $\{g_{j,l}\}$ (left-hand column) and the D(4) scaling function $\phi(\cdot)$ evaluated over the grid defined by $\frac{l}{2^j}$, $l = -3 \cdot 2^j, \ldots, -1, 0$ (right-hand) for $j = 2, 4, 6$ and 8 (top to bottom). For a given j, the two plotted sequences consist of $3 \cdot 2^j + 1$ values connected by line segments. In the right-hand column, the function $\phi(\cdot)$ is plotted at values $t = -3.0$ to $t = 0$ in steps of, from top to bottom, 0.25, 0.0625, 0.015625 and 0.00390625. The filters in the left-hand column are plotted in such a manner as to illustrate the approximation of Equation (469), whose validity increases with increasing j.

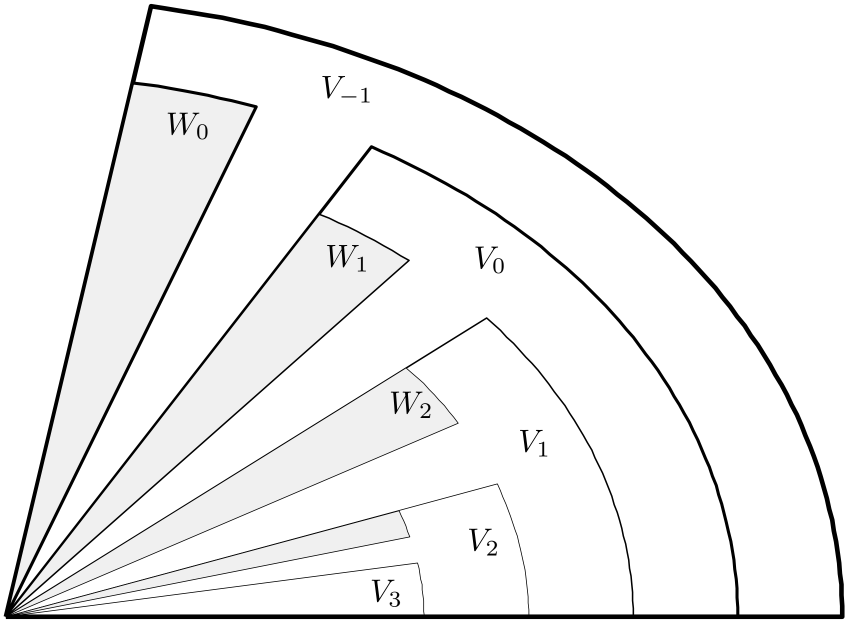

Figure 473a. Venn diagram illustrating the nesting of subspaces V_j and W_j. There are five arcs emanating from the baseline. Starting at each end of an arc, there is a line segment that continues to the lower left-hand corner of the plot. The area enclosed by a given arc and the two line segments emanating from its ends represents an approximation space V_j. The largest such area outlines the entire figure and represents V_{-1}, while the smallest area represents V_3 (note that $V_3 \subset V_2 \subset V_1 \subset V_0 \subset V_{-1}$, as required). The shaded areas represent the detail spaces W_j. Note that $W_0 \subset V_{-1}$, $W_1 \subset V_0$, $W_2 \subset V_1$ and $W_3 \subset V_2$ (there is no label for W_3 due to lack of space). Note also that, while $V_0 \subset V_{-1}$ and $W_0 \subset V_{-1}$, it is the case that $V_0 \cup W_0 \neq V_{-1}$ because V_{-1} also contains linear combinations of functions that are in both V_0 and W_0 – such linear combinations need not be in either V_0 or W_0, but rather can be in the space disjoint to V_0 and W_0 and represented by the scythe-like shape bearing the label V_{-1}. Finally, note that all the V_j and W_j intersect at a single point (represented by the lower left-hand corner of the plot) because all these spaces must contain the null function.

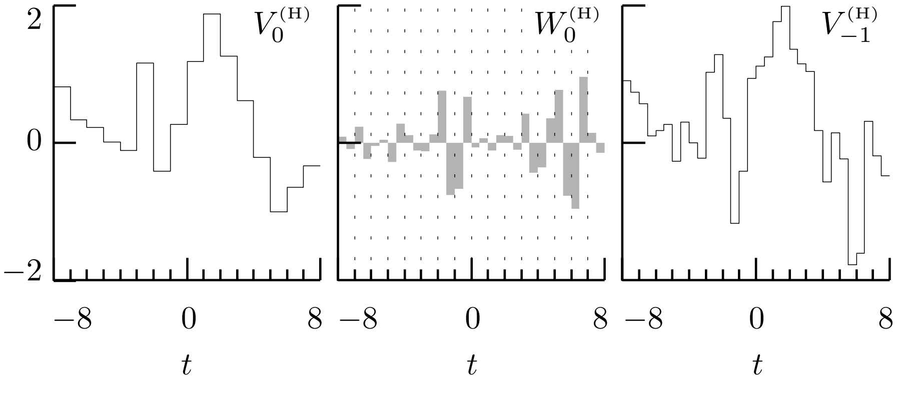

Figure 473b. Examples of functions in $V_0^{(\mathrm{H})}$, $W_0^{(\mathrm{H})}$ and $V_{-1}^{(\mathrm{H})}$. Note that, while the function in $V_0^{(\mathrm{H})}$ is constant over intervals of the form $(k-1, k]$ for $k \in \mathbb{Z}$, the function in $W_0^{(\mathrm{H})}$ integrates to zero over such intervals (the ends of these intervals are indicated in the middle plot by the vertical dotted lines). The function in $V_{-1}^{(\mathrm{H})}$ is in fact formed by point-wise addition of the functions in the other two spaces.

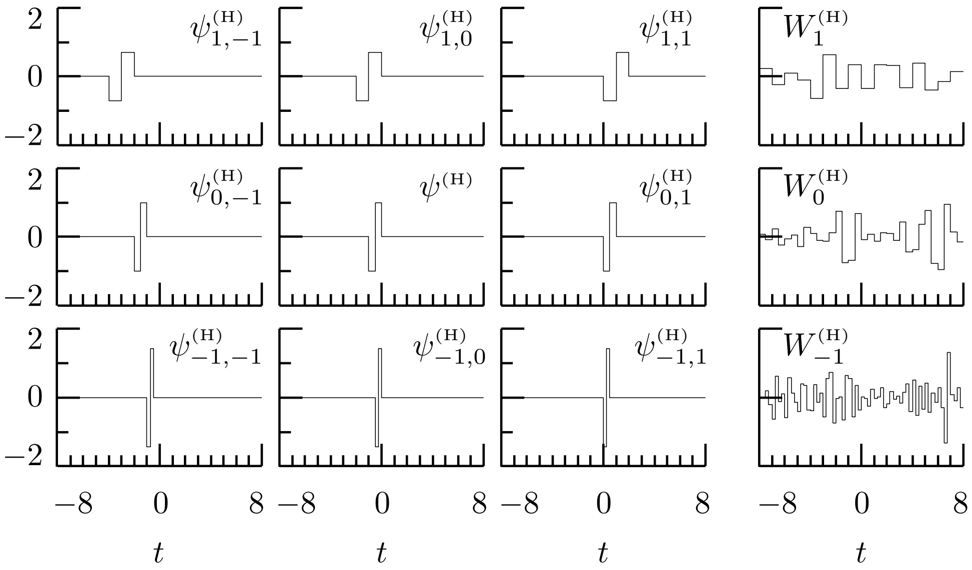

Figure 475. The Haar wavelet function $\psi^{(\mathrm{H})}(\cdot)$ and corresponding detail spaces. The first three plots on the middle row shows three of the basis functions for the Haar detail space $W_0^{(\mathrm{H})}$, namely, from left to right, $\psi_{0,-1}^{(\mathrm{H})}(\cdot)$, $\psi^{(\mathrm{H})}(\cdot)$ and $\psi_{0,1}^{(\mathrm{H})}(\cdot)$. The right-most plot on this row is an example of a function contained in $W_0^{(\mathrm{H})}$. The top and bottom rows show, respectively, corresponding plots for the Haar detail spaces $W_1^{(\mathrm{H})}$ and $W_{-1}^{(\mathrm{H})}$ (Figure 461 shows the corresponding Haar scaling function and approximation spaces).

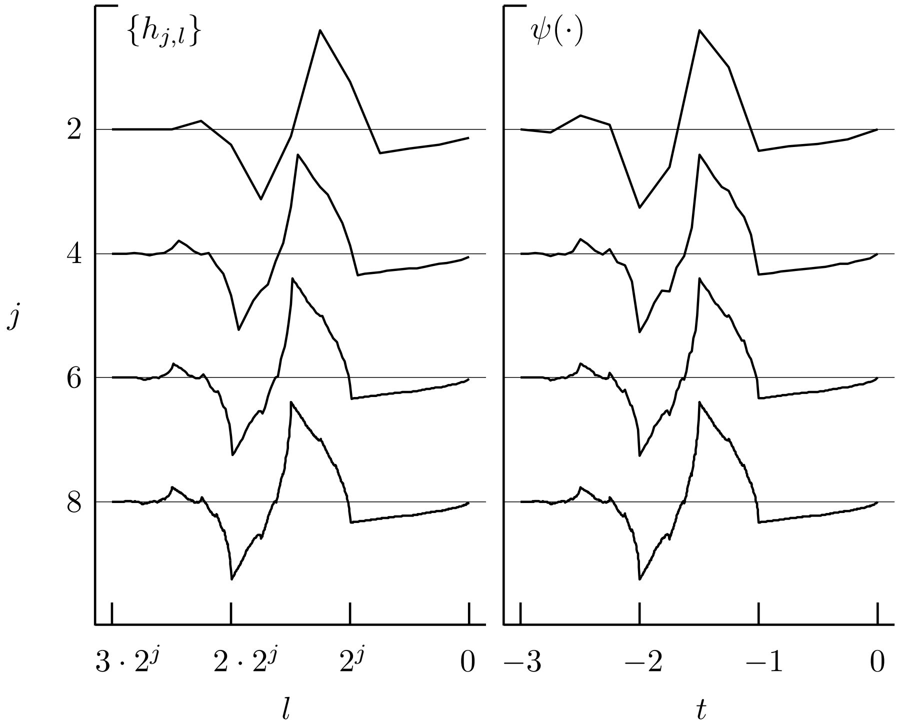

Figure 478. Level j equivalent D(4) wavelet filters $\{h_{j,l}\}$ (left-hand column) and the D(4) wavelet function $\psi(\cdot)$ evaluated over the grid defined by $\frac{l}{2^j}$, $l = -3 \cdot 2^j, \ldots, -1, 0$ (right-hand) for $j = 2, 4, 6$ and 8 (top to bottom). For details on the layout, see the caption for the analogous Figure 471.

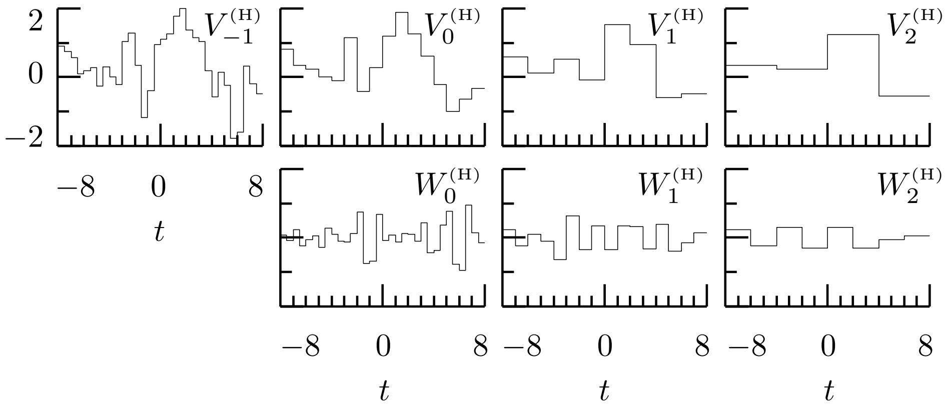

Figure 482. Multiresolution analysis of a function $x(\cdot) \in V_{-1}^{(\mathrm{H})}$ (upper left-hand plot), yielding three approximations, namely, $s_0(\cdot) \in V_0^{(\mathrm{H})}$, $s_1(\cdot) \in V_1^{(\mathrm{H})}$ and $s_2(\cdot) \in V_2^{(\mathrm{H})}$ (remaining plots on top row, from left to right), along with corresponding details $d_0(\cdot) \in W_0^{(\mathrm{H})}$, $d_1(\cdot) \in W_1^{(\mathrm{H})}$ and $d_2(\cdot) \in W_2^{(\mathrm{H})}$ (bottom row, from left to right).

$h_l \equiv \bar{h}_{-l},\, l = 0, \ldots, L-1$	$g_l \equiv \bar{g}_{-l},\, l = 0, \ldots, L-1$
$\bar{h}_l = (-1)^l \bar{g}_{1-l-L}$	$\bar{g}_l \equiv (-1)^{l+1} \bar{h}_{1-l-L}$
$\{\bar{h}_l\} \longleftrightarrow \overline{H}(\cdot)$	$\{\bar{g}_l\} \longleftrightarrow \overline{G}(\cdot)$
$\{h_l\} \longleftrightarrow H(\cdot)$	$\{g_l\} \longleftrightarrow G(\cdot)$
$H(f) = \overline{H}(-f)$	$G(f) = \overline{G}(-f)$
$\overline{H}(0) = 0$	$\overline{G}(0) = \sqrt{2}$
$\overline{H}(f) = -e^{i2\pi f(L-1)}\overline{G}(\frac{1}{2} - f)$	$\overline{G}(f) = e^{i2\pi f(L-1)}\overline{H}(\frac{1}{2} - f)$
$\overline{H}^{(m)}(0) = 0,\, m = 0, \ldots, r-1$	$\overline{G}^{(m)}(\frac{1}{2}) = 0,\, m = 0, \ldots, r-1$
$\bar{h}_l = \int \phi(t-l) \frac{\psi(\frac{t}{2})}{\sqrt{2}}\, dt$	$\bar{g}_l = \int \phi(t-l) \frac{\phi(\frac{t}{2})}{\sqrt{2}}\, dt$
$\int \psi(t) dt = 0$	$\int \phi(t)\, dt = 1$
$\text{support}\,\{\psi(\cdot)\} \subset (-(L-1), 0]$	$\text{support}\,\{\phi(\cdot)\} \subset (-(L-1), 0]$
$\psi(\cdot) \longleftrightarrow \Psi(\cdot)$	$\phi(\cdot) \longleftrightarrow \Phi(\cdot)$
$\Psi(-2^j f) \approx \widetilde{H}_j(f)$	$\Phi(-2^j f) \approx \widetilde{G}_j(f)$
$\psi(-\frac{l}{2^j}) \approx 2^j \tilde{h}_{j,l} = 2^{j/2} h_{j,l}$	$\phi(-\frac{l}{2^j}) \approx 2^j \tilde{g}_{j,l} = 2^{j/2} g_{j,l}$
$\Psi(f) = \Phi(\frac{f}{2}) \frac{\overline{H}(\frac{f}{2})}{\sqrt{2}}$	$\Phi(f) = \Phi(\frac{f}{2}) \frac{\overline{G}(\frac{f}{2})}{\sqrt{2}}$
$\Psi(f) = \frac{\overline{H}(\frac{f}{2})}{\sqrt{2}} \prod_{m=2}^{\infty} \frac{\overline{G}(\frac{f}{2^m})}{\sqrt{2}}$	$\Phi(f) = \prod_{m=1}^{\infty} \frac{\overline{G}(\frac{f}{2^m})}{\sqrt{2}}$
$\psi_{j,k}(t) \equiv \psi(\frac{t}{2^j} - k)/\sqrt{2^j}$	$\phi_{j,k}(t) \equiv \phi(\frac{t}{2^j} - k)/\sqrt{2^j}$
$\psi(t) = \sqrt{2} \sum_l \bar{h}_l \phi(2t - l)$	$\phi(t) = \sqrt{2} \sum_l \bar{g}_l \phi(2t - l)$
$w_{j,k} = \int x(t) \psi_{j,k}(t)\, dt$	$v_{j,k} = \int x(t) \phi_{j,k}(t)\, dt$
$w_{j,k} = \sum_l h_l v_{j-1,2k-l}$	$v_{j,k} = \sum_l g_l v_{j-1,2k-l}$

Table 499. Key relationships involving (i) wavelet and scaling filters $\{h_l\}$ and $\{g_l\}$ and their time reverses $\{\bar{h}_l\}$ and $\{\bar{g}_l\}$ and (ii) wavelet functions $\psi(\cdot)$ and scaling functions $\phi(\cdot)$.

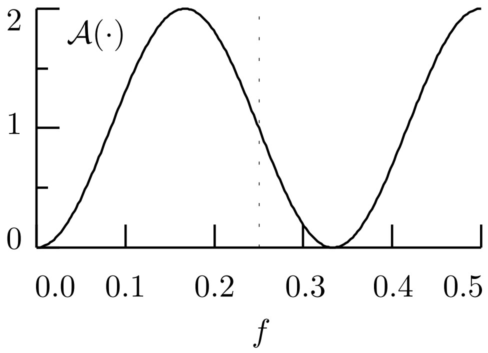

Figure 519. Squared gain function $\mathcal{A}(\cdot)$ for the filter $\{a_0 = -1/\sqrt{2}, a_1 = 0, a_2 = 0, a_3 = -1/\sqrt{2}\}$.

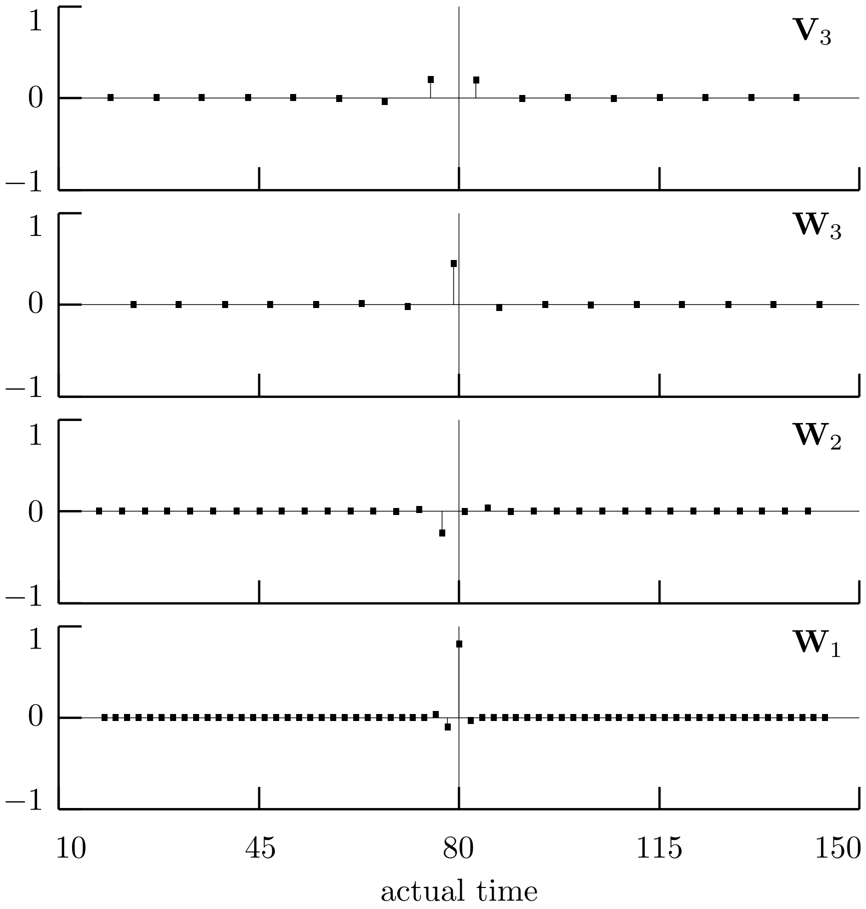

Figure 524. Wavelet and scaling coefficients for a level $J_0 = 3$ partial LA(8) DWT of a time series $\{X_t : t = 0, \ldots, 127\}$ that is zero everywhere for $X_{63} = 1$. The tth value of X_t is associated with actual time $t + 17$, so X_{63} is associated with actual time 80, which is indicated by the thin vertical lines in the plots above.